ULTRASONIC IMAGING
FOR THE CHARACTERIZATION OF DEFECTS
IN STEEL COMPONENTS

PROEFSCHRIFT

ter verkrijging van de graad van doctor
aan de Technische Universiteit Delft,
op gezag van de Rector Magnificus,
professor drs. P.A. Schenck,
in het openbaar te verdedigen
ten overstaan van een commissie,
aangewezen door het College van Dekanen,
op dinsdag 15 juni 1993 te 16.00 uur door

MAARTEN LORENZ

geboren te Rijswijk (Z-H)

natuurkundig ingenieur

Dit proefschrift is goedgekeurd door de promotor:

Professor dr. ir. A.J. Berkhout

Toegevoegd promotor:

Dr. ir. C.P.A. Wapenaar

Promotiecommissie:

Professor dr. K.J. Langenberg (*Elektrotechnik, Universität Kassel*)
Professor dr. ir. H. Blok (*Elektrotechniek, TU Delft*)
Professor dr. ir. J.T. Fokkema (*Mijnbouwkunde, TU Delft*)
Professor ir. L.B. Vogelesang (*Lucht- en Ruimtevaarttechniek, TU Delft*)
Dr. R. Hunik (*KEMA, Arnhem*)
Professor dr. ir. J.W. Verheij (*reservelid, TU Eindhoven*)

Preface

Table of Contents

1

General Introduction

1.1 Nondestructive Inspection of Steel Components

The safe and economical operation of steel pipeline networks and steel pressure vessels in gas, chemical and electricity plants is of great concern to industry and to society in general. Therefore, considerable investments have been made in the development of suitable nondestructive inspection systems for quality assessment and control. These systems are applied during the construction of installations and fabrication of components, as well as during the time they are in operation. In the last decades, the introduction of fast computers facilitated the development of more advanced nondestructive inspection techniques. However, these advanced techniques have to remain practicable in order to be economically applied in industry. It should also be noticed, that every NDI problem requires the *appropriate* inspection method to be applied. Of course, this method has to be implemented *correctly* in order to be successful or, as Harker (1988) puts it, "the physics must be right". For this reason, the work presented in this thesis will emphasize both practical applicability and the underlying physical principles.

Although the term 'nondestructive testing, NDT' is widely used in practice, the term *'nondestructive inspection, NDI*' should be preferred, since the applied nondestructive measuring methods are generally concerned with inspecting rather than testing a component. The result of nondestructive inspection ideally is a detailed characterization of the detected inhomogeneity. Whether or not the presence of this inhomogeneity affects the integrity of the construction is based on either standard acceptation/rejection criteria or fracture mechanics. Therefore, the term *'nondestructive evaluation, NDE*' refers to the total procedure of inspection and assessment of the inspection results. In this thesis the neutral term *'inhomogeneity*' will be used for any flaw which is not (yet) rejected, as the EC has ruled that the term *'defect*' should signify an unacceptable inhomogeneity.

1.1.1 NDI-methods

Radiographic, ultrasonic, magnetic, electrical and penetrant methods can be considered as the major nondestructive inspection methods applied in practice on steel components. Table 1.1 gives

a general overview of the physical principles, the main application, the advantages and disadvantages of each method (Wenk and McMaster, 1987). Recent developments in the field of NDI now provides one with an even wider choice of methods, including acoustic emission, thermography and shearography (Halmshaw, 1987). Furthermore, the application of fast computers allows complex processing of the measured data, which may improve the interpretability of NDI results considerably. However, the general problem with NDI is, that there is generally too large a choice of methods and techniques and too little quantitative information on their performance. Yet, as the application of NDI in practice is a balance between costs and safety, it is very important to know the range of application, running costs, speed of operation and reliability of different NDI techniques.

Table 1.1: *The five major NDI methods for steel components and their characteristics.*

NDI method (technique)	physical principle	main application	advantages	disadvantages
radiography (X-ray)	attenuation of X-rays (density variations)	weld defects and cracks	high-resolution; 1:1 projection image of inhomo-geneity	radiation hazard; cracks must be oriented parallel to beam; access to opposite side required
ultrasonics (pulse-echo)	scattering of elastic waves (reflectivity)	weld defects, cracks and delami-nations	suitable for in-ser-vice inspection; highly sensitive for small scatterers	coupling required; interpretation of measurements is often difficult
magnetic methods (static magnetic field)	perturbations of mag-netic field (magnetic permeability)	surface and sub-surface flaws	non-contact tech-nique; fast application	only sensitive for near-surface inho-mogeneities; qualitative results
electrical methods (eddy current)	inductive reactance to magnetic field of induced eddy current (conductivity, electri-cal permeability)	surface and sub-surface flaws	non-contact tech-nique; fast application	most sensitive for near-surface inho-mogeneities; requires special probes for object; qualitative results
penetrant methods (liquid penetrant)	liquid penetrating in surface-connected cracks (capillarity)	surface-connected cracks	inexpensive; fast application; highly sensitive	porosity of surface may mask indica-tions; only sensi-tive to surface-connected defects; qualitative results
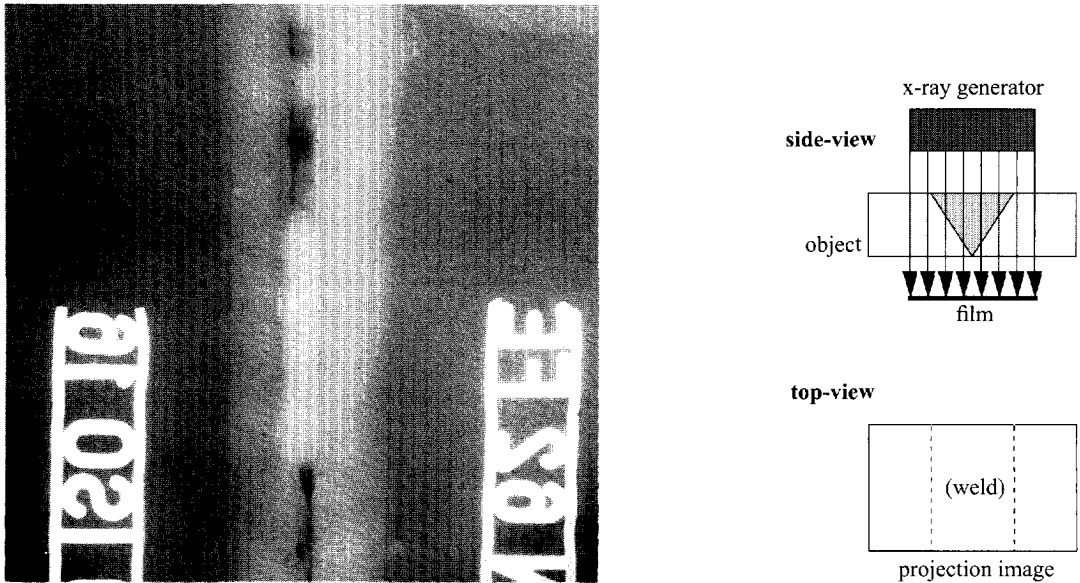
Figure 1.1: *A radiographic (X-ray) projection image of a lack-of-penetration defect in a V-shaped weld which connects two flat steel plates of 13 mm thickness.*

All nondestructive inspection methods have special benefits and drawbacks, and none of them is generally regarded as the perfect method in a certain situation. Radiography, for instance, may provide very high-resolution projection images of inhomogeneities when applied to thin steel objects (see figure 1.1). However, since it is typically a transmission method, the component should normally be taken out of service for inspection. With the penetrant dye technique very small surface-breaking cracks can be detected, but the application of this method is confined strictly to the accessible surface of the component. Ultrasonics, as a reflection method, can be applied as an in-service inspection technique and its application is not confined to the near-surface region of the component. However, the relation between the recorded ultrasonic responses and the characteristics of a reflecting inhomogeneity may become very complicated and, consequently, ultrasonic measurement results may be hard to evaluate (see figure 1.2).

The reliability of nondestructive inspection can be improved substantially by combining different methods and techniques. Moreover, appropriate processing of the different nondestructive measurement results may improve the extraction and combination of information contained in these results. Consequently, this will lead to more consistent and reliable information on the condition of a component.

1.1.2 Acceptance standards

The results of nondestructive inspection have to be interpreted in order to determine the condition of the component that has been inspected. This judgement is generally based on more information than provided by NDI, such as the material, the geometry, and the loading of the component. Over the years, many codes have been written containing acceptance/rejection criteria based on measurement results. Most of these acceptance codes were written originally for radiographic inspection as this was the earliest NDI method capable of detecting inhomogeneities throughout the volume of a material. As radiography was typically applied for the inspection of welds in steel, most of the codes produced referred to weld defects.

From *fracture mechanics* considerations it is well established that planar defects, such as cracks and lack of fusion, affect the strength of a construction the most. Volumetric defects, such as gas holes or slag inclusions, are regarded less serious. Furthermore, it is clear that the through-thickness dimension of a defect (so-called *defect height*) is more significant than the defect length and that surface-breaking defects are more serious than internal defects. Because of the studies in the field of fracture mechanics, the acceptance levels are constantly changing and subject to much discussion and controversy. For instance, a degree of perfection of welds is often demanded that exceeds by far the perfection of the adjacent base material.
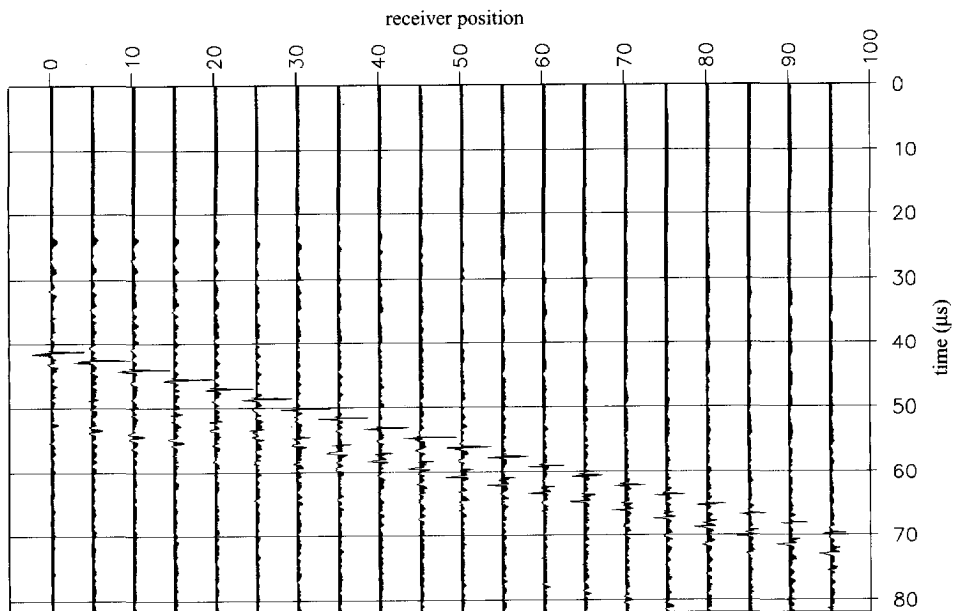
Figure 1.2: *The ultrasonic B-scan data from a real lack-of-fusion defect in a U-shaped weld connecting two flat steel plates of 30 mm thickness.*

Although some codes do not allow any defects to be present, in many codes certain acceptable defect dimensions and positions are specified, usually with respect to the nominal thickness of the object. The latter codes contain criteria which are mainly meant to act as guidance to contracting parties in the industry and are known as *good-workmanship* criteria. In case the criteria are based on the rules of fracture mechanics they are known as *fitness-for-purpose* criteria. A correct fitness-for-purpose analysis requires the knowledge on the applied stresses in service *and* a full characterization of the inhomogeneity. Therefore, employing fitness-for-purpose criteria makes high demands upon the applied NDI techniques. In any case, for both types of criteria it is necessary to identify the nature of an inhomogeneity. By radiography this is usually easy to accomplish, as the location, length and width of the inhomogeneity can be measured directly on film. In ultrasonic inspection the situation is much more complex, as the nature of an inhomogeneity cannot always be uniquely identified.

1.2 From Detection to Characterization

1.2.1 Qualitative and quantitative NDI

During repair or after destructive inspection of components containing inhomogeneities, which were detected by NDI and classified as defects by the acceptance codes, it appeared quite often that (regarding the nature of the inhomogeneity) taking action would not have been necessary at all. As repairing or replacing components may be quite expensive, it is not surprising that the current acceptance codes – based on good-workmanship criteria – are in many cases found to be too stringent. These acceptance codes may be adjusted, but a general tendency towards the formulation and application of fitness-for-purpose criteria is noticeable.

As has been mentioned in the previous section, the application of criteria based on fracture mechanics considerations require a full *characterization* of the inhomogeneity. This means, that the *exact location, orientation, size* and *shape* of the inhomogeneity must be known. Consequently, *qualitative NDI* (detection and approximate localization) has to be followed by *quantitative NDI* (characterization). This may be achieved by applying alternative techniques and/ or by appropriate processing of the measured data. Although many NDI methods may be chosen for defect characterization purposes, it is found that ultrasonics offers the best potential, since the technique may be operated while the component remains in service and the inspection is not confined to the near-surface region of the component. As stated before, however, ultrasonic measurements do not directly reveal the characteristics of an inhomogeneity. Therefore, special processing techniques should be applied in order to extract the characteristic features of such an inhomogeneity from the ultrasonic measurements.

1.2.2   The ultrasonic imaging approach

Ultrasonic experiments result in measurements of echo-acoustic responses in terms of amplitudes and travel times. In case the wave velocity is accurately known throughout the medium, the relation between travel time and travelled distance (path length) of an ultrasonic pulse is uniquely defined. Consequently, the position of the scatterer can be determined approximately. When the scattering response is recorded at several different positions along the inspection surface of an object, resulting in a so-called *B-scan*, it is possible to locate the scatterer by a kind of cross-bearing. Such a localization method has been developed initially for radar and is called Synthetic Aperture Focusing Technique or *SAFT* (Flaherty et al., 1967; Seydel, 1982).

With conventional SAFT the measured data are processed to obtain a focused spatial image of a certain region of interest (*ROI*), which may contain indications marking the scattering surfaces. The heuristically derived SAFT-algorithm is a *back-propagation* technique and is merely based on the elimination of the propagation effects from the measured ultrasonic data. Actually, it equals a simplified version of the *imaging procedure* as defined by general wave theory (Berkhout, 1987; Langenberg, 1987). Acoustic imaging is being applied in different fields, such as seismic exploration, medical diagnostics and underwater acoustics.

Ideally, a two-dimensional ultrasonic imaging result would feature an exact image of the surface of the scatterers. However, this may only be accomplished when sources and receivers can be positioned on a closed surface completely surrounding the scatterer, such as in tomography for example. In practice, the *inspection aperture* (defining the positions along the surface of the object where data can be recorded) is restricted due to limited accessibility and consequently the image resolution is limited. In other words, the image resolution depends on the spatial frequency bandwidth of the recorded B-scan data. Moreover, in case no temporal deconvolution of the ultrasonic data with the source wavelet is applied, the image resolution also depends on the length of the ultrasonic response, i.e. the temporal frequency bandwidth.

In many research projects it has been demonstrated (Barna and Johnson, 1983; Doctor et al., 1986; Burch, 1987; Ozaki et al., 1988), that due to the limitation of the image resolution *conventional* SAFT imaging is not generally suitable for the *characterization* of defects for NDI. However, because conventional SAFT imaging is relatively simple in comparison with the imaging processes that have been developed and applied in seismic exploration, it appeared that imaging in NDI could be improved considerably. For this reason, a research project has been initiated in 1988 by the TNO Institute of Applied Physics and the Delft University of Technology to improve and evaluate the application of SAFT for defect characterization in NDI of steel components. This research project has been supported by the Dutch Electric Power Institute (KEMA), Billiton/Shell Research and the Dutch Gas Company (Gasunie) and led eventually to
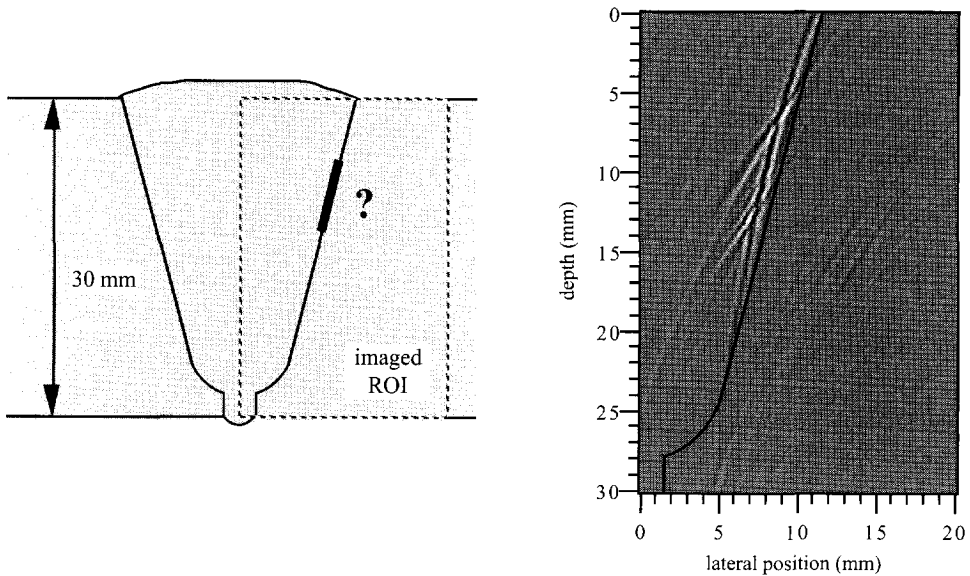
Figure 1.3: *The configuration of a real lack-of-fusion defect in a U-shaped weld connecting two flat steel plates of 30 mm thickness and its combined Multi-SAFT imaging result; the* approximate *weld preparation geometry is indicated in the image (see section 8.3.1 for more details).*

the writing of this thesis.

The improved version of SAFT is based on the employment of *primary* as well as *multiple surface-related* insonification and scattering for imaging. As the employment of multiple responses actually implies the employment of multiple synthetic apertures, the improved version of SAFT is referred to as *Multi-SAFT*. A combined Multi-SAFT imaging result consists of a superposition of different images from different (diffraction and reflection) responses. As an example, figure 1.3 shows the combined Multi-SAFT image of a real lack-of-fusion defect in a U-shaped weld, computed from the data shown in figure 1.2.

1.3 Outline of this Thesis

In *chapter 2*, the *acoustic* imaging procedure is derived with the aid of the one-way wave equation via a formulation of the forward model describing the propagation of acoustic waves. For the explanation of the underlying physical principles the matrix notation, as introduced by Berkhout (1985) in seismics, is used which clearly indicates the similarities and differences between *reflectivity imaging* in seismic exploration and NDI. It is also demonstrated, that the imaging algorithm can be applied in the *elastic* situation for all different elastic wave components

(PP, PS, SP and SS) individually in case these are considered to be uncoupled during propagation. Finally, it is shown that the heuristically derived SAFT-algorithm is actually a simplified version of the imaging algorithm derived from wave theory, as it does not take into account any amplitude effects. Nevertheless, this algorithm may be applicable in practice because only structural information on the inhomogeneities is extracted from the imaging results.

The imaging algorithm derived with the aid of wave theory, however, clearly indicates how the conventional SAFT-algorithm can be improved. For instance, the image resolution can be improved considerably by performing and combining multi-shot experiments (applying many different source positions), as is common practice in seismic exploration. If necessary, the material characteristics of the scatterer may even be extracted from the reflectivity information by handling the amplitudes correctly and performing a parametric inversion on the imaging results (Lörtzer, 1990; De Bruin, 1992).

The practical aspects of ultrasonic imaging for NDI are expla ned in *chapter 3*. The types of objects and defects of interest are described as well as the applied transducers and data-acquisition configurations. The practical constraints on the application of the ultrasonic imaging theory are summarized and the image resolution is defined. In the last section, the conventional SAFT imaging algorithm is described and its imaging performance evaluated.

Chapter 4 presents the Multi-SAFT philosophy and describes the effects of the practical aperture limitation on the spatial resolution. The Multi-SAFT imaging algorithm is formulated for a flat plate geometry as well as for a cylindrical pipe geometry. The assumptions, which are made regarding the application of Multi-SAFT in practice, are presented and discussed. In *chapter 5*, the effects of single-mode, bounded-beam transducers (such as being applied in practice) and of the limitation of the inspection aperture on the Multi-SAFT imaging results are illustrated with the aid of finite-difference modelling experiments.

In order to obtain an optimum imaging result, the data-acquisition procedure should be carefully optimized as described in *chapter 6*. It is demonstrated, that the application of separate source and receiver transducers is absolutely necessary in case the imaging of vertically oriented (with respect to the normal on the inspection surface) defects is concerned. Avoiding the fixed source transducer to obstruct the scanning receiver transducer, a special data-acquisition configuration is proposed called the *lateral split angle configuration*. As reflectivity imaging of shear wave responses is concerned throughout this thesis, the angle dependent shear wave reflectivity is studied in this chapter, including polarization effects. Finally, the combination of diffraction and reflection images is addressed.

Chapter 7 deals with the image accuracy of Multi-SAFT imaging, which is defined as the extent to which indications are positioned correctly, imaged completely and correspond to true inhomogeneities. The influence of uncorrelated noise and interfering ultrasonic responses on the imaging result is discussed, as well as the influence of errors in the imaging parameters (transducer positions, wave velocity, etc.) and of certain medium characteristics (homogeneity, isotropy). In this chapter the qualitative effects of defect-surface roughness on the accuracy are illustrated with the aid of finite-difference modelling results.

In *chapter 8*, a series of experimental imaging results are presented. The experiments have been performed on artificial and real weld defects in either flat plate or cylindrical pipe objects. Some objects have been destructively inspected and the real cross-sections are directly compared to the ones obtained by ultrasonic imaging. The Multi-SAFT imaging and characterization performance is evaluated using the experimental results. The experiments involved have all been performed with a workstation that was especially developed for Multi-SAFT and is described in Appendix C.

Because of the limited inspection aperture, the shape of the imaged inhomogeneities cannot always be identified uniquely. Therefore, *chapter 9* is devoted to the first step towards the application of neural networks for the classification of defects. It is described, how neural networks could be applied to determine the shape of a defect from properly pre-processed ultrasonic B-scan data and the classification performance is evaluated using modelled as well as experimental ultrasonic data. Finally, *chapter 10* gives the conclusions of the work presented and a discussion on the role of Multi-SAFT, (elastic) modelling and artificial intelligence in future NDI.

Throughout this thesis many modelled data sets have been used to demonstrate certain effects. In case the modelling technique is not specified, data have been modelled using a simple acoustic ray-tracing algorithm.

Ultrasonic Imaging and Wave Theory

2.1 Introduction

Ultrasonic imaging of inhomogeneities in steel components is primarily based on the elimination of the wave propagation effects (source→inhomogeneity and inhomogeneity→receiver) from the recorded echo-acoustic data. Hence, imaging is an inverse problem and results in a spatial reflectivity distribution containing information on the structure and the composition of an inhomogeneity. To be able to formulate the inversion process of recorded echo-acoustic data, the process of generating and recording wave fields has to be described first. This measurement process is referred to as the forward model. The forward propagation operators (quantifying the wave propagation effects to and from the inhomogeneities) is then derived; the result is used to define the inverse propagation operators needed for the elimination of the propagation effects.

Traditionally, forward models are based on the two-way wave equation, where two-way means that the *total* wave field is addressed. In the two-way description the medium is defined by the *density* and *wave velocity* (generally with respect to a reference or back-ground medium). However, the forward model can also be represented by one-way wave equations, separately describing the propagation of the generated wave field from the source to the inhomogeneity, the reflection of the wave field, and the propagation of the reflected wave field from the inhomogeneity to the receiver. In this description the medium is defined by *reflectivity*. As the reflectivity is paramount in the imaging process, a representation of the wave phenomena by one-way wave equations is preferred and therefore applied throughout this thesis.

It will be demonstrated, that the acoustic formulation of the imaging process (as presented in this chapter) is also valid for the individual elastic wave components in case these components are considered to be uncoupled *during propagation* (of course, they are coupled during reflection). The acoustic imaging process may consequently be applied in practice, where elastic (steel) media are inspected. In the last section of this chapter it will be shown, that the heuristically derived imaging algorithm called SAFT is closely related to the imaging algorithm derived with the aid of acoustic wave theory. SAFT is not designed to handle the amplitudes correctly, because this is not essential for the extraction from the image of structural information only.

2.2 Measurements: The Forward Model

In order to be able to record ultrasonic responses from inhomogeneities in the material, a source wave field has to be generated to interact with those inhomogeneities. Generally, this generated wave field will have broadband frequency characteristics, preferably with the minimum phase property, to assure temporal resolution. In this section a model is presented which describes the interaction of a generated wave field with an inhomogeneity and the object boundaries in acoustic as well as elastic media. This so-called *forward model* describes the measurements (in terms of the sub-processes of generation, propagation, reflection and recording of wave fields) obtained through an ultrasonic inspection experiment. The forward model will provide the basis for the inversion of ultrasonic data.

When regarding stress-free media, such as (ideal) gases and fluids, only compressional waves may exist and these media will be called *acoustic* media. The forward model for acoustic media will be mathematically described in terms of matrix operators, similar to those introduced by Berkhout (1985) in seismic wave theory. For an up-to-date version the reader is referred to Berkhout (1993). The matrix operators quantify the physical processes of generation, propagation, reflection and detection of the wave field. All matrices will be represented in the frequency domain, describing the processes for one single temporal Fourier component (frequency). This makes the formulation of the forward problem relatively simple and may thus improve the understanding of the underlying physical processes.

The basic elements of the one-way matrix model are the propagation and the reflectivity. The wave field at the inspection surface P_n can therefore be represented by:

$$P_n = \sum_m W_{n,m} R_m P_m \ ,$$
(2.1)

where P_m describes the incident wave field at the inhomogeneity m, which possesses a reflectivity R_m, and $W_{n,m}$ describes the propagation of the scattering wave field towards the inspection surface. Notice, that the summation of equation (2.1) indicates that the wave field at the inspection surface may consist of many scattering responses.

2.2.1 The insonifying wave field

A source distribution along the inspection surface may be generated by a transducer, which is activated through an electric pulse. The resulting source wave field along the *inspection surface* ζ_0 of the object will be represented by the vector $\underline{S}^+(\zeta_0)$:

$$\underline{S}^+(\zeta_0) = \mathbf{D}_s(\zeta_0)\underline{S}(\zeta_0) \ ,$$
(2.2)

where $\underline{S}(\zeta_0)$ is a vector consisting of the distribution of stresses (defining position, complex amplitude and directivity) as generated by the source transducer along the inspection surface and $\mathbf{D}_S(\zeta_0)$ is a transformation matrix containing the surface conditions (acoustic impedance contrast, coupling). The elements of the vector $\underline{S}^+(\zeta_0)$ represent the monochromatic source wave field at every position along the inspection surface.

Before interacting with an inhomogeneity, the wave field has to propagate towards it. The *primary* insonifying wave field along the surface of the scatterer $\underline{P}_0^+(\zeta_d)$ can be formulated as:

$$\underline{P}_0^+(\zeta_d) = \mathbf{W}^-(\zeta_d,\zeta_0)\underline{S}^+(\zeta_0) , \tag{2.3}$$

where ζ_d indicates the surface of the possible defect and the '$^+$'-sign denotes that the wave field is propagating *towards* the possible defect. The matrix $\mathbf{W}$ represents the *propagation operator* and $\mathbf{W}^+(\zeta_m, \zeta_k)$ represents the propagation of the insonifying wave field from the surface ζ_k towards the surface ζ_m. Every column of the matrix $\mathbf{W}^+(\zeta_m, \zeta_k)$ equals the monochromatic response along the surface ζ_k due to a point source positioned at surface ζ_m. This is illustrated in figure 2.1 for $\mathbf{W}^+(\zeta_d, \zeta_0)$.
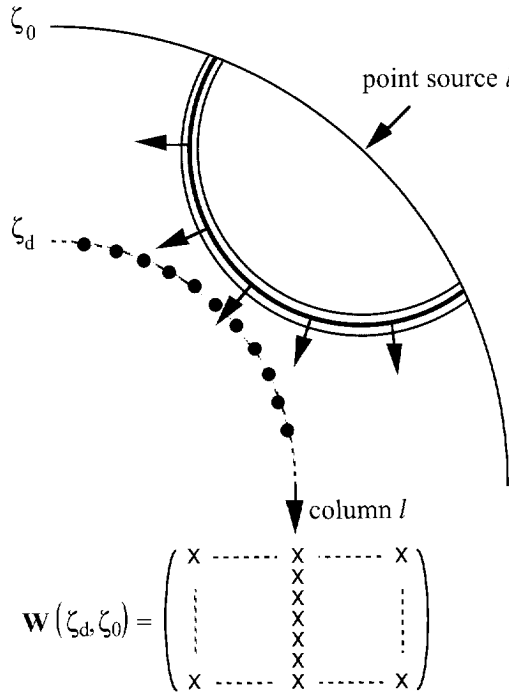
Figure 2.1: *The matrix W^+ represents the propagation operator and $W^+(\zeta_d, \zeta_0)$ represents the propagation of the insonifying wave field from the surface ζ_0 towards the surface ζ_d.*

In general, the total insonifying wave field will consist of the primary wave field as well as the indirectly insonifying wave field via the boundaries of the object and/or via other internal inhomogeneities. Using equation (2.3) for the primary wave field, the total insonifying wave field along the surface of the inhomogeneity (up to first order in $\mathbf{R}(\zeta_k)$) can therefore be formulated as:

$$\underline{P}^+(\zeta_d) = \underline{P}_0^+(\zeta_d) + \sum_k \mathbf{W}^+(\zeta_d, \zeta_k)\, \mathbf{R}(\zeta_k)\, \underline{P}_0^+(\zeta_k) \quad , \tag{2.4}$$

where $\underline{P}_0^+(\zeta_k)$ represents the primary insonifying wave field at the inhomogeneity k. The matrix $\mathbf{R}$ represents the *reflectivity matrix* and $\mathbf{R}(\zeta_k)$ describes the reflectivity of the surface ζ_k, where each column of this matrix contains the monochromatic response along that surface due to a point source positioned at that *same* surface (see figure 2.2).

Following Berkhout's terminology, when the inhomogeneity k is related to the object boundaries, its contribution to the insonifying wave field will be called the *surface related insonification*. In case the inhomogeneity k is an internal scatterer, its contribution to the insonifying wave field will be called *internally deflected insonification*. In this thesis only the surface related insonification will be taken into account. Consequently, the second term in equation (2.4) can be substituted by two terms resulting from reflections via the inspection and back-wall surfaces.
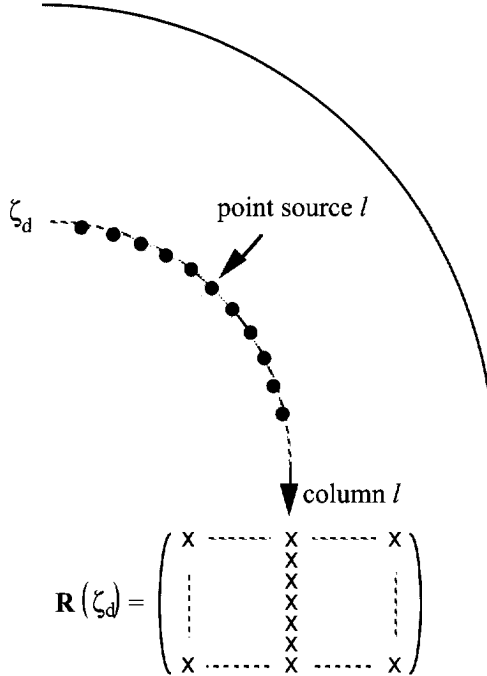
Figure 2.2: *The matrix* **R** *represents the reflectivity matrix and* **R**(ζ_d) *describes the reflectivity of the surface* ζ_d.

For practical reasons, equation (2.4) will now be rewritten in terms of wave paths. In NDI bounded media are considered and thus the wave field will reach the inhomogeneity directly as well as after a number of reflections with the (free-surface) object boundaries. Two surfaces may be distinguished, namely the inspection surface ζ_0 and the opposite or back-wall surface ζ_1 (the latter one does *not* exist in the seismic problem). When the total insonifying wave field along the surface of the scatterer $\underline{P}^+(\zeta_d)$ is described by:

$$\underline{P}^+(\zeta_d) = \mathbf{W}^+(\zeta_d,\zeta_0)\,\underline{S}^+(\zeta_0) \;, \tag{2.5}$$

the propagation matrix $\mathbf{W}^+(\zeta_d,\zeta_0)$ may be written as:

$$\mathbf{W}^+(\zeta_d,\zeta_0) = \sum_{n=0}^{\infty} \mathbf{W}^+_n(\zeta_d,\zeta_0) \;. \tag{2.6}$$

Here, $\mathbf{W}_n^+(\zeta_d,\zeta_0)$ represents the nth *order* of propagation of the insonifying wave field towards the surface of the inhomogeneity (containing n reflections at the object boundaries ζ_0 and ζ_1). Consequently, these matrices can be written as:

$$\mathbf{W}^+_n(\zeta_d,\zeta_0) = \mathbf{W}^+(\zeta_d,\zeta_0)\left[\mathbf{Y}^+(\zeta_0)\right]^{n/2} \;; \qquad n = 0 \text{ or even}, \tag{2.7a}$$

$$\mathbf{W}^+_n(\zeta_d,\zeta_0) = \mathbf{W}^+(\zeta_d,\zeta_1)\,\mathbf{R}(\zeta_1)\,\mathbf{W}^+(\zeta_1,\zeta_0)\left[\mathbf{Y}^+(\zeta_0)\right]^{(n-1)/2} \;; \qquad n = \text{odd}, \tag{2.7b}$$

with:

$$\mathbf{Y}^+(\zeta_0) = \mathbf{R}(\zeta_0)\,\mathbf{W}^+(\zeta_0,\zeta_1)\,\mathbf{R}(\zeta_1)\,\mathbf{W}^+(\zeta_1,\zeta_0) \;. \tag{2.7c}$$

The operator $\mathbf{Y}^+(\zeta_0)$ describes, respectively, the propagation of the primary wave field towards the back-wall surface, the reflection at the back-wall surface, the propagation of the back-wall surface related reflection towards the inspection surface, and the reflection at the inspection surface.

2.2.2 The scattering wave field

After none or several reflections at the object boundaries ζ_0 and ζ_1, the wave field may reach the inhomogeneity and reflection will take place. This interaction is represented by the reflectivity matrix $\mathbf{R}(\zeta_d)$, describing the monochromatic angle dependent reflectivity properties of each point on the surface ζ_d of the inhomogeneity. After this interaction the wave field may propagate from the inhomogeneity towards the receiver distribution at the inspection surface.

Analogously to equation (2.3), the *primary* scattering wave field at the inspection surface $\underline{P}_0^-(\zeta_0)$ can be formulated as:

$$\underline{P}_0^-(\zeta_0) = \mathbf{W}^-(\zeta_0,\zeta_d)\,\underline{P}_0^-(\zeta_d) \ , \tag{2.8}$$

where the '$^-$'-sign denotes that the reflected wave field is propagating away from the inhomogeneity. In general, the total scattering wave field will consist of the primary scattering wave field and the higher-order scattering wave field via the boundaries of the object and/or via other internal inhomogeneities. Using equation (2.8) for the primary scattering wave field, the total scattering wave field (up to first order in $\mathbf{R}(\zeta_k)$) along the inspection surface can therefore be formulated as:

$$\underline{P}^-(\zeta_0) = \underline{P}_0^-(\zeta_0) + \sum_k \mathbf{W}^-(\zeta_0,\zeta_k)\,\mathbf{R}(\zeta_k)\,\underline{P}_0^-(\zeta_k) \ , \tag{2.9}$$

where $\underline{P}_0^-(\zeta_k)$ represents the primary scattering wave field at the inhomogeneity k.

When the inhomogeneity k is related to the object boundaries, its contribution to the scattering wave field will be called the *surface related scattering*. In case the inhomogeneity k is an internal scatterer, its contribution to the scattering wave field will be called *internally deflected scattering*. In this thesis only the surface related scattering will be taken into account. Consequently, the second term in equation (2.9) can be substituted by two terms resulting from reflections via the inspection and back-wall surfaces.

As for equation (2.4), equation (2.9) will also be rewritten in terms of wave paths. When the total scattering wave field along the inspection surface $\underline{P}^-(\zeta_0)$ is described by:

$$\underline{P}^-(\zeta_0) = \mathbf{W}^-(\zeta_0,\zeta_d)\,\underline{P}^-(\zeta_d) \ , \tag{2.10}$$

the propagation matrix $\mathbf{W}^-(\zeta_0,\zeta_d)$ may be written as:

$$\mathbf{W}^-(\zeta_0,\zeta_d) = \sum_{m=0}^{\infty} \mathbf{W}^-_m(\zeta_0,\zeta_d) \ , \tag{2.11}$$

where the matrix $\mathbf{W}^-_m(\zeta_0,\zeta_d)$ represents the mth *order* of propagation of the scattering wave field towards the inspection surface (containing m reflections at the object boundaries ζ_0 and ζ_1), which is defined by:

$$\mathbf{W}^-_m(\zeta_0,\zeta_d) = \left[\mathbf{Y}^-(\zeta_0)\right]^{m/2}\mathbf{W}^-(\zeta_0,\zeta_d) \ ; \qquad\qquad m = 0 \text{ or even,} \tag{2.12a}$$

$$\mathbf{W}^-_{m}(\zeta_0,\zeta_d) = \left[\mathbf{Y}^-(\zeta_0)\right]^{(m-1)/2} \mathbf{W}^-(\zeta_0,\zeta_1)\,\mathbf{R}(\zeta_1)\,\mathbf{W}^-(\zeta_1,\zeta_d)\ ; \qquad m = \text{odd}, \qquad (2.12b)$$

with:

$$\mathbf{Y}^-(\zeta_0) = \mathbf{W}^-(\zeta_0,\zeta_1)\,\mathbf{R}(\zeta_1)\,\mathbf{W}^-(\zeta_1,\zeta_0)\,\mathbf{R}(\zeta_0)\ . \qquad (2.12c)$$

The operator $\mathbf{Y}^-(\zeta_0)$ describes, respectively, the reflection of the primary scattering wave field at the inspection surface, the propagation of the inspection surface related reflection towards the back-wall surface, the reflection at the back-wall surface, and the propagation of the back-wall surface related reflection towards the inspection surface.

The number n from equation (2.7) and the number m from equation (2.12) denote, respectively, the number of reflections of the wave field *before* and *after* scattering at the inhomogeneity. In case n and m are *both* 0, even or odd, the reflected wave field is called *back scattering*, while for other combinations the reflected wave field is called *forward scattering*. In chapter 4 the characteristics of these two types of wave paths are discussed.

2.2.3 Formulation of the forward model

The scattered wave field arriving at the inspection surface is represented by $\underline{P}^-(\zeta_0)$, which will be transformed into electric pulses to be recorded. This transformation is represented by the matrix $\mathbf{D}_r(\zeta_0)$ which contains the characteristics of the receiver transducer(s) and the surface conditions. Using the formulation of the insonifying (2.5) and scattering wave field (2.10), the total forward model is given by:

$$\underline{P}(\zeta_0) = \mathbf{D}_r(\zeta_0)\,\mathbf{X}(\zeta_0,\zeta_0)\,\mathbf{D}_s(\zeta_0)\big]\,\underline{S}(\zeta_0)\ , \qquad (2.13a)$$

with:

$$\mathbf{X}(\zeta_0,\zeta_0) = \sum_{m=0}^{\infty}\sum_{n=0}^{\infty}\mathbf{W}^-_{m}(\zeta_0,\zeta_d)\,\mathbf{R}(\zeta_d)\,\mathbf{W}^+_{n}(\zeta_d,\zeta_0)\ . \qquad (2.13b)$$

Because of the characteristic elements of propagation and reflection, this formulation of the forward model is called the '*WRW-model*'. Equations (2.13a,b) describe the forward model for a single monochromatic experiment, including n insonifying wave paths and m scattering wave paths. The forward model is schematically illustrated in figure 2.3 for the primary insonification and scattering only ($n=m=0$):
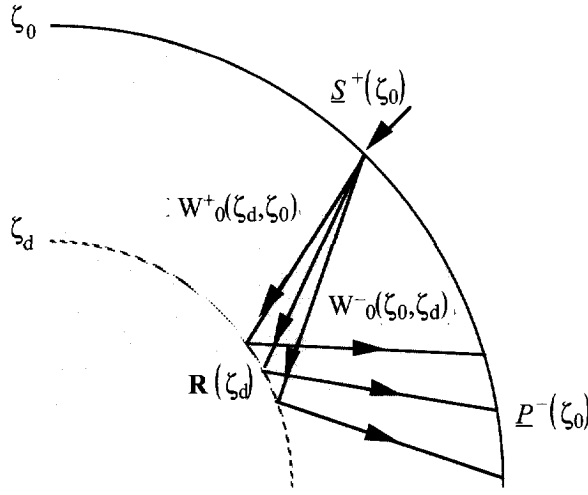
Figure 2.3: *The forward model for primary insonification and scattering.*

$$\underline{P}(\zeta_0) = \left[\mathbf{D}_r(\zeta_0)\, \mathbf{X}_{0,0}(\zeta_0, \zeta_0)\, \mathbf{D}_s(\zeta_0) \right] \underline{S}(\zeta_0) \ . \tag{2.13c}$$

The matrix formulation is very well suited to represent multiple experiments, as is particularly useful in seismics (Wapenaar and Berkhout, 1989). The vectors $\underline{S}$ and $\underline{P}$ should then be replaced by matrices, where each column of these monochromatic matrices is related to a single experiment. This will lead to a formulation of the forward model similar to (2.13a) and reads:

$$\mathbf{P}(\zeta_0) = \mathbf{D}_r(\zeta_0)\, \mathbf{X}(\zeta_0, \zeta_0)\, \mathbf{D}_s(\zeta_0)\, \mathbf{S}(\zeta_0) \ . \tag{2.14}$$

Notice that the formulation presented above holds for 2-D as well as 3-D acoustic situations. An equivalent matrix formulation can be used in the elastic situation, where the matrices (in the general 3-D case) will exist of nine sub-matrices due to the combinations of a single compressional (P) and two shear (S) wave components.

2.3 The Propagation Operator

The propagation operator $\mathbf{W}$ plays a key role in the data-acquisition process as it represents the transfer of information through the medium. Even if the medium is generally inhomogeneous and anisotropic, properly designed propagation matrices will still describe the propagation of the wave field correctly. In most cases in NDI of steel components the medium may be regarded as
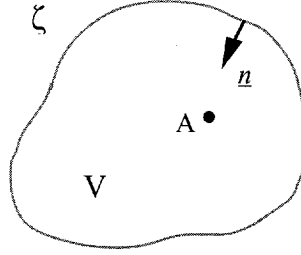
Figure 2.4: *The configuration of the pressure P in a point A inside a source-free volume V surrounded by the surface ζ for the Kirchhoff-Helmholtz integral formulation.*

being homogeneous and isotropic. For this relatively simple homogeneous and isotropic case it is fairly easy to describe the wave propagation mathematically. The wave fields will be presented here in the space-frequency domain unless stated otherwise. The mathematical description of the propagation operator will be given for the acoustic situation and is based on Berkhout (1987).

2.3.1 The Kirchhoff-Helmholtz integral formulation

With the aid of the theorem of Gauss and the second theorem of Green, the Kirchhoff-Helmholtz integral may be formulated for the pressure P in a point A inside a source-free volume V surrounded by the surface ζ (see figure 2.4):

$$P_A = \frac{1}{4\pi} \oint_\zeta \left[P \frac{\partial G}{\partial n} - \frac{\partial P}{\partial n} G \right] d\zeta \;, \tag{2.15}$$

where $\partial/\partial n$ stands for $\underline{n} \cdot \nabla$, with $\nabla = (\partial/\partial x, \partial/\partial y, \partial/\partial z)$ and the unit vector $\underline{n}$ pointing inward on the surface ζ. The function P describes the compressional wave field which is generated by sources *outside* surface ζ. For all points *inside* ζ, P satisfies the homogeneous wave equation:

$$\nabla^2 P + k^2 P = 0 \;. \tag{2.16}$$

Here k denotes the wave number, which is defined by the ratio of the angular frequency ω and the wave velocity c. The function G describes the compressional wave field that would be generated by a source at A *inside* the surface ζ. It is the so-called *Green's function*, describing the impulse response of the actual acoustic medium under inspection. This Green's function satisfies the

inhomogeneous acoustic wave equation:

$$\nabla^2 G + k^2 G = -4\pi\, \partial(\underline{r}-\underline{r}_A) \; , \tag{2.17}$$

with a monopole source in point A inside ζ, which is indicated by the vector $\underline{r}_A = (x_A, y_A, z_A)$, and $\underline{r} = (x,y,z)$ the observation point. The solution for this inhomogeneous differential equation is well known and defines the Green's function for a homogeneous acoustic medium:

$$G = \frac{\exp(-jk\Delta r)}{\Delta r} \; , \tag{2.18}$$

where $\Delta r = \sqrt{(x-x_A)^2 + (y-y_A)^2 + (z-z_A)^2}$ is the distance between the Green's point source indicated by $\underline{r}_A$ and observation point indicated by $\underline{r}$.

The Kirchhoff-Helmholtz integral (2.15) states, that the pressure in a point A *inside* a source-free volume V can be computed from the measurements of the pressure and the normal component of the particle velocity V_n (which is related to P according to $\partial P / \partial n = -j\omega\rho V_n$) *on* the closed surface ζ surrounding the volume V. As long as it satisfies the inhomogeneous acoustic wave equation (2.17), the Green's function may be chosen arbitrarily, which makes it possible to change (2.15) into:

$$P_A = \frac{1}{4\pi} \oint_\zeta P \frac{\partial G_f}{\partial n} d\zeta \; , \tag{2.19}$$

for such a Green's function that $G_f = 0$ at every point on ζ. This means, that the pressure in point A may be computed from measurements of the pressure along the surface ζ only. In this case the Green's function satisfies the so-called *Dirichlet* boundary condition, which means that ζ is a perfectly reflecting *free surface*. For an arbitrarily shaped inspection surface ζ the function G_f may become very complicated.

2.3.2 The Rayleigh II integral formulation

When a half-space geometry is considered according to figure 2.5, the closed surface ζ consists of a flat surface $z=z_0$ and a hemi-sphere ζ_1 in the lower half-space $z \geq z_0$, with midpoint A and radius r_1. When the sources of the acoustic wave field P are assumed to be situated in the upper half-space $z < z_0$, then the contribution of the Kirchhoff-Helmholtz integral over ζ_1 to the acoustic pressure at A vanishes in case r_1 is going to infinity. For this special case that ζ reduces to a plane surface $z=z_0$ the *Rayleigh II* integral may be formulated for the determination of the pressure P in point A:
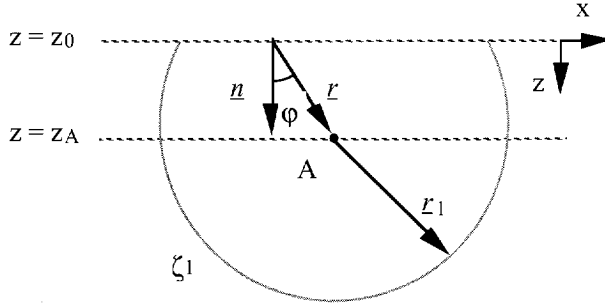
Figure 2.5: *Half-space geometry for the derivation of the Rayleigh II integral.*

$$P_A = \frac{1}{2\pi} \int\int\limits_{-\infty}^{+\infty} P \frac{\partial}{\partial n} \left\{ \frac{\exp(-jk\Delta r)}{\Delta r} \right\} dxdy$$

$$= \frac{1}{2\pi} \int\int\limits_{-\infty}^{+\infty} P \left[\frac{1 + jk\Delta r}{\Delta r^2} \right] \cos\varphi \, \exp(-jk\Delta r) \, dxdy \quad , \tag{2.20}$$

with:

$$\cos\varphi = \frac{z_A - z_0}{\Delta r} \quad . \tag{2.21}$$

Here φ and Δr are defined as the angle (with respect to the normal on $z=z_0$) and the length of the vector pointing from a point on the plane surface $z=z_0$ to the observation point A ($\Delta r=|\underline{r}|$, see figure 2.5). This result states, that any pressure field may be computed from a *dipole* distribution on a plane $z=z_0$, the related force per unit area of each dipole being given by P. This formulation is known as *Huygens' principle*.

2.3.3 Formulation of the forward propagation operator

The Rayleigh II integral of equation (2.20) can be written as:

$$P(x,y,z_n) = \frac{1}{2\pi} \int\int\limits_{-\infty}^{+\infty} W(x-x',y-y',\Delta z_n;\omega) \, P(x',y',z_0) \, dx'dy' \quad , \tag{2.22}$$

where $W(x-x',y-y',\Delta z_n;\omega)$ represents the propagation operator, which extrapolates the wave field P from the plane surface $z=z_0$ to the parallel plane surface $z=z_n$, defined by:

$$W(x,y,\Delta z_n;\omega) = \frac{\partial}{\partial n}\left\{\frac{\exp(-jkr)}{r}\right\}$$

$$= \left[\frac{1 + jkr}{r^2}\right]\cos\varphi\,\exp(-jkr)\ , \tag{2.23}$$

with:

$$r = \sqrt{x^2 + y^2 + (z_n - z_0)^2}\ , \tag{2.24}$$

the distance between a point on the surface $z=z_0$ and a point on the surface $z=z_n$. In this way the propagation (forward extrapolation) process is described by a spatial convolution integral. For digital processing, discretized propagation operators are applied and therefore the spatial convolution integral equation (2.22) can be conveniently written in terms of matrices:

$$\underline{P}(z_n) = \mathbf{W}(z_n,z_0)\,\underline{P}(z_0)\ . \tag{2.25}$$

The elements of one column of $\mathbf{W}(z_n,z_0)$ describe the wave field along the discretized surface $z=z_n$ due to a dipole (point) source positioned at the surface $z=z_0$ (equivalent to figure 2.1).

Equation (2.23) describes the forward propagation operator in terms of an amplitude and a phase factor. Note, that both factors are depending on frequency and path length, and that the amplitude factor is only exact for parallel surfaces. As practice deals typically with (arbitrarily) curved surfaces and the amplitude factor is not *essential* for the imaging process, this amplitude factor is often neglected by conventional imaging systems for NDI. However, amplitudes *do* influence the image resolution and should therefore be handled properly (see chapter 3). The phase factor (equal to a time shift in the time domain) is truly essential for the imaging process and plays a central role in the inversion scheme. In the next section the forward propagation operator will be used to define the inverse propagation operator which governs the imaging process.

2.4 Imaging: The Inverse Reflectivity Problem

The process of reconstructing the reflecting boundaries of an inhomogeneity in terms of reflectivity from echo-acoustic data is called *imaging*. Such a reconstruction is based on inverse wave field extrapolation and is referred to as the *inverse reflectivity problem*. This inversion again is based on the forward model (2.14) as described in section 2.2. Inversion for the general elastic

case is very complicated and therefore the expressions for the inversion operators will be derived in this section for the relatively simple homogeneous and isotropic acoustic situation. Later on it will be made plausible that the inversion operators may be applied for imaging purposes of real ultrasonic data (from elastic media) as well.

2.4.1 Reflectivity imaging

The actual information on the inhomogeneity in the forward model is contained in the reflectivity matrix $\mathbf{R}(\zeta_d)$. Equation (2.13b) gives the relation between the measured echo-acoustic data $\mathbf{P}(\zeta_0)$ and the reflectivity of the scattering surface of the inhomogeneity $\mathbf{R}(\zeta_d)$. A perfect imaging process involves the elimination of $\mathbf{D}_s(\zeta_0)$ and $\mathbf{D}_r(\zeta_0)$, as well as the elimination of the propagation effects $\mathbf{W}^+(\zeta_d,\zeta_0)$ and $\mathbf{W}^-(\zeta_0,\zeta_d)$. In this section the elimination of $\mathbf{D}_s(\zeta_0)$ and $\mathbf{D}_r(\zeta_0)$ will be left out of consideration, because it is generally not essential for the imaging process[1] and very hard to accomplish in practical situations.

The elimination of the propagation effects is called *inverse extrapolation* or back-propagation (Langenberg, 1987) and is performed for every reference level[2] ζ_n in the region to be imaged. The result of this operation in the Fourier domain is a secondary source distribution along the reference level ζ_n in terms of reflectivity matrices $\mathbf{R}(\zeta_n)$. The actual imaging in the frequency domain of the secondary source distribution is done for every reference level ζ_n by performing the *imaging step*: averaging the reflectivity $\mathbf{R}(\zeta_n)$ over all frequency components. This yields a space domain result which may contain a reconstruction of the scattering surface ζ_d of an inhomogeneity in terms of the weighted (by $\mathbf{D}_s$ and $\mathbf{D}_r$) local reflectivity, consisting of the diagonal elements of $\mathbf{R}(\zeta_n)$ (see De Bruin (1992) for a more detailed discussion of reflectivity).

Neglecting the influence $\mathbf{D}_s$ and $\mathbf{D}_r$ and regarding the primary wave field only, it follows from equation (2.14) that the elimination of the propagation effects may be described by:

$$\mathbf{R}(\zeta_n) = \left[\mathbf{W}^-(\zeta_0,\zeta_n)\right]^{-1} \mathbf{P}(\zeta_0) \left[\mathbf{W}^+(\zeta_n,\zeta_0)\right]^{-1} \left[\mathbf{S}(\zeta_0)\right]^{-1}$$

$$= \mathbf{F}^-(\zeta_n,\zeta_0)\, \mathbf{P}(\zeta_0)\, \mathbf{F}^+(\zeta_0,\zeta_n) \left[\mathbf{S}(\zeta_0)\right]^{-1} \qquad , \qquad (2.26a)$$

with $\mathbf{F}^+$ and $\mathbf{F}^-$ the inverse propagation operators and $[\mathbf{S}(\zeta_0)]^{-1}$ the deconvolution with the source characteristics. Of course, the inversion of equation (2.26a) should be carried out in a stable sense. The spatial deconvolution process of equation (2.26a) is totally based on the knowledge of the background medium parameters, in particular the wave velocity. Equation (2.26a) can be written

---

1   In chapter 7 it will be shown, however, that laterally varying phase changes of the received signals may occur due to surface and coupling conditions; they are disastrous to the imaging process and should be either avoided or eliminated.

2   These reference levels do not necessarily have to correspond to real surfaces.

as a symbolic expression, which facilitates the interpretation, yielding:

$$R(\zeta_n) = \frac{F^-(\zeta_n,\zeta_0)\,P(\zeta_0)}{W^+(\zeta_n,\zeta_0)\,S(\zeta_0)} \ . \tag{2.26b}$$

From equation (2.26b) it becomes clear, that the elimination of the propagation effects involves the *inverse* extrapolation of the recorded wave field and the *forward* extrapolation of the source wave field towards the surface ζ_n. This process will be illustrated in section 2.6.

2.4.2 Formulation of the inverse propagation operator

If no reflections of the wave field at the object boundaries take place, the inverse propagation operators may be written as (see equations (2.7) and (2.12)):

$$F^+(\zeta_0,\zeta_n) = \left[W^+(\zeta_n,\zeta_0)\right]^{-1} \ , \tag{2.27a}$$

$$F^-(\zeta_n,\zeta_0) = \left[W^-(\zeta_0,\zeta_n)\right]^{-1} \ . \tag{2.27b}$$

However, these inverse propagations operators F^+ and F^- are unstable for evanescent waves. When only propagating waves are considered and the surfaces ζ_0 and ζ_n are plane and parallel (indicated by $z=z_0$ and $z=z_n$, respectively), then the *matched filter approach* may be applied (Berkhout, 1987) resulting in:

$$F^+(z_0,z_n) = \left[W^+(z_n,z_0)\right]^H \ , \tag{2.28a}$$

$$F^-(z_n,z_0) = \left[W^-(z_0,z_n)\right]^H \ , \tag{2.28b}$$

where 'H' denotes Hermitian (complex conjugated and transposed). For parallel surfaces $z=z_0$ and $z=z_n$ the elements of F^+ and F^- are equal and can be defined as the complex conjugate of the elements of W in (2.23) resulting in:

$$F(x,y,\Delta z_n;\omega) = \frac{\partial}{\partial n}\left[\frac{\exp(jkr)}{r}\right]$$

$$= \left[\frac{1 - jkr}{r^2}\right]\cos\varphi\,\exp(jkr) \ . \tag{2.29}$$

This expression holds for all real k (i.e. no absorption) in the 3-D situation where the pressure is measured along a plane inspection surface $z=z_0$ and the pressure is reconstructed along a plane surface parallel to that inspection surface.

For direct scattering (*primary*) wave fields the inverse propagation operators are relatively simple. If the primary *and* all multiple reflections at the object boundaries should be taken into account, the inverse propagation operators would become very complex. Therefore, this total inversion process will be subdivided to be applied on wave fields of different order of insonification and scattering. Consequently, the measured echo-acoustic data will be inverted assuming that the insonified wave field reflected a certain number of n times at the object boundaries before reaching the inhomogeneity (n^{th} order insonification) and that all scattered responses did reflect also a number of m times at the object boundaries before reaching the receivers (m^{th} order scattering). Moreover, it is assumed that no interactions between secondary sources, that make up the scattering geometry, take place. Of course, these assumptions may lead to spurious (focused) indications in the image. These assumptions will be discussed in chapter 4 and the effects on the imaging process will be discussed in chapter 7.

By applying inverse propagation operators on recorded ultrasonic data, the scattering geometry may be imaged. To obtain a good image resolution, however, many frequency components should be included. This means, that a broad-band frequency signal has to be applied as a source wave field, thus providing the necessary *frequency diversity*. Furthermore, all points lying on the surface of the inhomogeneity should be able to act as secondary sources, which implies that the source wave field has to insonify the scatterer from every possible angle. The scattered wave field has also to be recorded at every possible angle. This means, that for high-resolution imaging sources as well as receivers have to be applied along a closed surface surrounding the scatterer, thus providing the necessary *angular diversity* (Langenberg, 1987). Thus, multi-shot experiments should be performed, as is common practice in seismic exploration. In chapter 4 the spatial resolution of the image will be discussed in terms of frequency and angular diversity.

2.5 Elastic and Acoustic Wave Equations

In practice, steel components will be inspected and therefore *elastic* instead of *acoustic* media should be considered. The general theory of propagation of waves in arbitrarily inhomogeneous and anisotropic solids is very complicated due to the coupling of different modes and is extensively treated in the literature (Achenbach, 1973; Auld, 1973). Following Wapenaar and Berkhout (1989) and Harker (1988) it will be demonstrated in this section, that the wave propagation operator (as derived in section 2.3) may also be applied to the different elastic wave components individually.

2.5.1 Decomposition of the elastic wave field

The law of conservation of momentum in combination with the constitutive equation (stress-

strain relationship) gives the general equation of dynamic elasticity in terms of displacements $\underline{u}$. For a source-free homogeneous isotropic solid this equation reads (in the time-domain):

$$\left(\lambda + 2\mu\right) \nabla \nabla \cdot \underline{u} - \mu \nabla \times \nabla \times \underline{u} - \rho \frac{\partial^2 \underline{u}}{\partial t^2} = 0 \ , \tag{2.30}$$

with λ and μ the Lamé constants and ρ the mass density of the medium. This equation illustrates the complexity of elastic wave propagation, as it couples the various components of displacement. It is therefore more convenient to introduce wave potentials and to relate the displacements to the derivatives of these potentials. Conventionally, the scalar ϕ and vector $\underline{\psi}$ wave potentials are defined by:

$$\underline{u} = \nabla \phi + \nabla \times \underline{\psi} \ . \tag{2.31}$$

This equation relates the three components of $\underline{u}$ to four functions (ϕ and the three components of $\underline{\psi}$), which calls for an additional condition:

$$\nabla \cdot \underline{\psi} = 0 \ . \tag{2.32}$$

Substituting (2.31) and (2.32) into the wave equation (2.30) and grouping terms yields:

$$\nabla \left\{ \left(\lambda + 2\mu\right) \nabla^2 \phi - \rho \frac{\partial^2 \phi}{\partial t^2} \right\} + \nabla \times \left\{ \mu \nabla^2 \underline{\psi} - \rho \frac{\partial^2 \underline{\psi}}{\partial t^2} \right\} = \underline{0} \ , \tag{2.33}$$

where the following identity has been used:

$$- \nabla \times \nabla \times \underline{\psi} + \nabla \left(\nabla \cdot \underline{\psi}\right) = \nabla^2 \underline{\psi} \ . \tag{2.34}$$

This equation will be satisfied when each of the terms in braces is zero:

$$\nabla^2 \phi - \frac{\rho}{\left(\lambda + 2\mu\right)} \frac{\partial^2 \phi}{\partial t^2} = 0 \ , \tag{2.35}$$

and:

$$\nabla^2 \underline{\psi} - \frac{\rho}{\mu} \frac{\partial^2 \underline{\psi}}{\partial t^2} = \underline{0} \ , \tag{2.36}$$

In the Fourier domain, expressions (2.35) and (2.36) transform into:

$$\nabla^2 \Phi + \frac{\omega^2}{c_p^2} \Phi = 0 \ , \tag{2.37}$$

and:

$$\nabla^2 \underline{\Psi} + \frac{\omega^2}{c_s^2} \underline{\Psi} = \underline{0} .$$
(2.38)

The equations (2.37) and (2.38) have the characteristic form of the acoustic wave equation, with characteristic wave velocities:

$$c_p = \sqrt{\frac{(\lambda + 2\mu)}{\rho}} ,$$
(2.39)

$$c_s = \sqrt{\frac{\mu}{\rho}} .$$
(2.40)

As the scalar (P) and vector (S) wave potential are both satisfying the 'acoustic' wave equation, it follows from sections 2.3 and 2.4 that forward propagation operators W_p and W_s (according to (2.7) and (2.12)), as well as inverse propagation operators F_p and F_s (according to (2.27)), may be related to these elastic wave components.

2.5.2   Identifying the elastic wave components

As $\nabla \times \nabla \Phi = 0$, the scalar wave potential Φ describes a compressional (P) wave field in the solid propagating with the wave velocity c_p. On the other hand, the relation $\nabla \cdot (\nabla \times \underline{\Psi}) = 0$ implies that no volume changes take place (pure translation) and thus the vector wave potential $\underline{\Psi}$ describes a shear (S) wave field in the solid[3]. In ideal gases and fluids the Lamé constant μ is zero and only equation (2.37) will hold because a shear wave field does not exist.

The vector potential wave equation (2.38) may be decomposed into three scalar potential wave equations related to the three Cartesian coordinates:

$$\nabla^2 \Psi_x + \frac{\omega^2}{c_s^2} \Psi_x = 0 ,$$
(2.41a)

$$\nabla^2 \Psi_y + \frac{\omega^2}{c_s^2} \Psi_y = 0 ,$$
(2.41b)

$$\nabla^2 \Psi_z + \frac{\omega^2}{c_s^2} \Psi_z = 0 .$$
(2.41c)

---

3   Compressional and shear waves are often referred to as, respectively, longitudinal and transversal waves which may lead to confusion. For the components of the displacement of a P wave, which are not oriented parallel to the propagation direction, as well as those components of an S wave, which are not oriented perpendicular to the propagation direction, will only vanish in the far field of the source in a homogeneous and isotropic medium.

The potentials Ψ_x, Ψ_y and Ψ_z will lead to particle displacements u in the x-, y-, and z-direction according to:

$$U_x \sim -\frac{\partial \Psi_y}{\partial z} , \tag{2.42a}$$

$$U_y \sim \frac{\partial \Psi_x}{\partial z} - \frac{\partial \Psi_z}{\partial x} , \tag{2.42b}$$

$$U_z \sim \frac{\partial \Psi_y}{\partial x} . \tag{2.42c}$$

The Cartesian coordinate system has been chosen in such a way that the scattering surface lies in the x-y plane and the incident shear wave propagates in the x-z plane (see figure 2.6). For any elliptically polarized shear wave, incident under an arbitrary angle α on the scattering x-y plane, two orthogonal shear-wave components (displacements normal to the propagation direction) may be defined. The polarization of these components will be defined here *with respect to the x-z plane* which will be called the *sagittal* plane.

The particle-displacement component u_y normal to the x-z plane will be called the *horizontally polarized* shear wave component (SH). The particle-displacement component in the x-z plane and composed of u_x and u_z will be called the *vertically polarized* shear wave component (SV). Because P waves generate particle displacements in the x-z plane only it can be shown that P and SV waves are coupled at scattering boundaries, i.e. that *mode-conversion* may take place on reflection at an inhomogeneity, while SH waves are totally uncoupled and will interact with inhomogeneities without being subject to mode-conversion. In chapter 6 the effects of shear wave
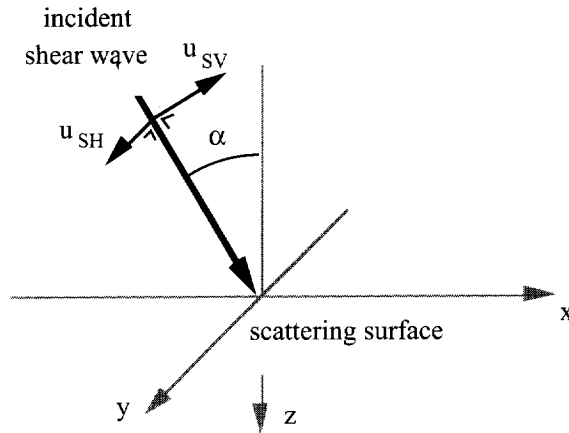
Figure 2.6: *The configuration for the definition of shear wave polarization.*

reflectivity and polarization will be discussed in detail.

In this section it has been demonstrated, that the elastic wave equation may be decomposed into acoustical types of wave equations which are coupled through the boundary conditions at the scattering surfaces. The acoustic inversion process of section 2.4 will only hold independently for each of the four components (PP, PS, SP and SS) of a primary elastic wave field in case they are considered to be uncoupled during propagation. As real ultrasonic data may contain a mixture of these components, errors will be made when the acoustic inversion process is applied for one of the four components only. This may affect the image quality and will be discussed in chapter 7.

2.6 SAFT: Imaging through Back-Propagation

In section 2.4 it has already been observed that the process of reconstructing the scattering geometry is mainly concerned with back-propagation of the recorded wave field by the inverse propagation operator F. In this section the inversion process will be interpreted geometrically with the aid of an example. It will be shown that a heuristic approach of the inversion process will lead to the conventional imaging method generally known as the *Synthetic Aperture Focusing Technique (SAFT)* and that this technique is a simplified version of the general 'WRW-model'.

2.6.1 The conventional SAFT-algorithm

Figure 2.7 shows the configuration of a point diffractor in an otherwise homogeneous and isotropic (acoustic) medium. A single point source is applied at $t=t_0$ and an array of receivers are recording the wave field (with respect to $t=t_0$). This recorded wave field will contain the direct source wave field and the scattered wave field, as shown in figure 2.8. The travelled distance of a certain response can be easily computed from the travel times of the recorded responses and the wave velocity of the medium. From this travelled distance and the positions of the source and the
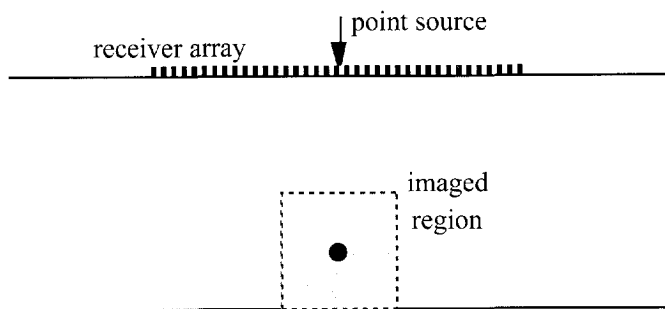
Figure 2.7: *The model of a point diffractor as used for the demonstration of the imaging process.*

receiver position
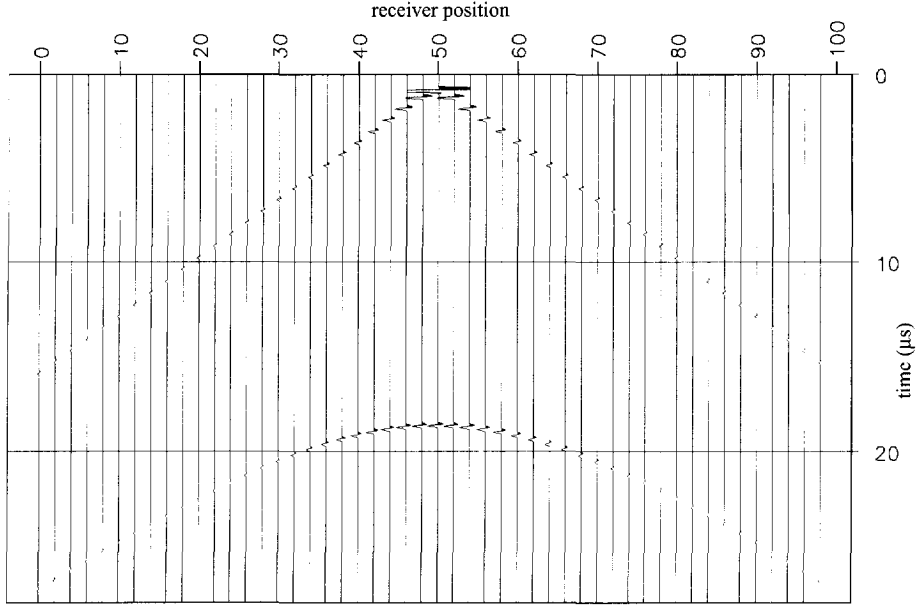
Figure 2.8: *Modelled B-scan recording of the direct source wave field and the secondary scattered wave field using the model of figure 2.7.*

receivers, secondary source distributions can be reconstructed in space (see figure 2.9). A secondary source distribution is an ellipsoid in space and an ellipse in a plane, indicating all positions where the recorded scattered response may have originated from. Such ellipses are sometimes called *imaged back-propagated responses*.

If such secondary source distributions are reconstructed for all receiver positions and superimposed on each other, they will generally only interfere constructively at those points, which correspond to true secondary sources (see figure 2.10). This imaging process appears to be a kind of *spatial averaging* of imaged back-propagated responses, resulting in the secondary source distribution indicating (a part of) the reflecting surface of an inhomogeneity. The process of imaging through back-propagation applies to any distribution of point diffractors forming an extended inhomogeneity.

The described process of reconstructing a two-dimensional image $\Omega(x,z)$ of an inhomogeneity in the x-z plane of a Cartesian coordinate system may be written as:

$$\Omega(x,z) = \sum_{i=1}^{N} p\left(x_{R,i}, x_S; t = t_0 + \frac{1}{c}\left\{\sqrt{(x-x_S)^2 + (z-z_0)^2} + \sqrt{(x-x_{R,i})^2 + (z-z_0)^2}\right\}\right) , \qquad (2.43)$$

lateral direction
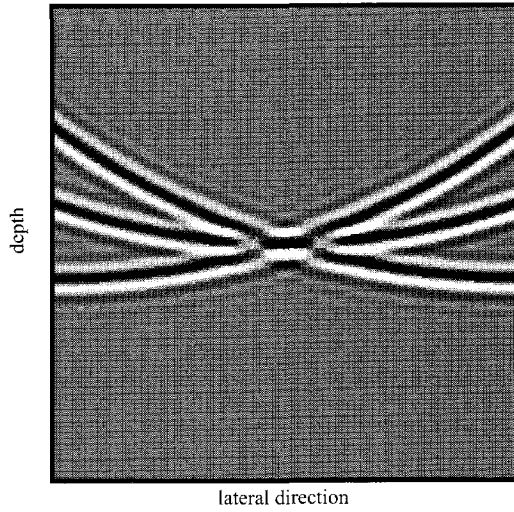
Figure 2.9: *The imaged region as indicated in the model of figure 2.7 with three imaged back-propagated responses.*

where p is the recorded wave field, with x_S the fixed position of the source, $x_{R,i}$ the position of receiver *i* at one of the *N* positions along the aperture on the plane inspection surface $z=z_0$, and c the wave velocity of the medium. In practice, the wave field is recorded along an aperture by scanning with a single receiver transducer. This heuristically derived reconstruction algorithm described by equation (2.43), which discards any amplitude effects, is known as the *Synthetic Aperture Focusing Technique (SAFT)* (Flaherty, 1967). SAFT originates from radar imaging and is currently also being applied in NDI and medical diagnostics (Seydel, 1982).

lateral direction
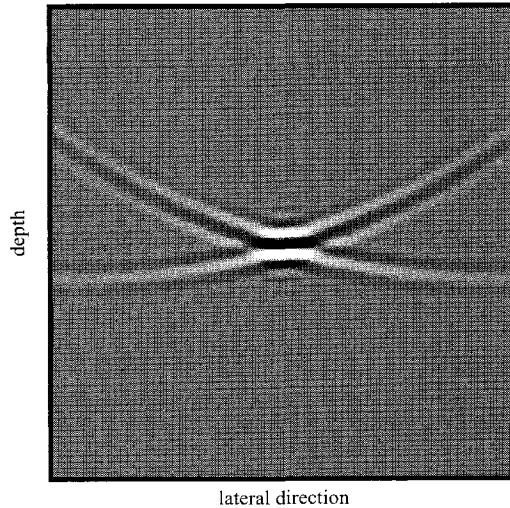
Figure 2.10: *The image of the point diffractor from the model shown in figure 2.7 for a limited linear receiver aperture.*

2.6.2 SAFT in terms of the 'WRW-model'

The SAFT-algorithm of equation (2.43) is very similar to the inversion process (2.26) determined with the aid of wave theory. It also involves the forward extrapolation of the source wave field (first term between braces in equation (2.43)) and the inverse extrapolation of the recorded wave field (second term between braces in equation (2.43)). The monochromatic phase shifts of the inverse propagation operators F^+ and F^- of equation (2.26a) in the frequency domain equal the time shifts of equation (2.43) in the time domain. An imaged back-propagated response, as shown in the image of figure 2.9, is the result of imaging the reflectivity for one receiver position on every depth level, for every frequency component contained in the recorded data. The experiment described in section 2.6.1 involves one single source position. The recorded signals of all receivers for this single-shot experiment are contained in the vector $\underline{P}(\zeta_0)$. By multiplying the matrices of equation (2.26a) the contributions to the reflectivity of a certain depth level are summed over all receivers. Thus, the *spatial averaging process* mentioned previously is actually a *spatial deconvolution process*. The focused image of figure 2.10 is the result of applying the inversion process of equation (2.26a) (and the imaging of reflectivity) for all depth levels and frequencies.

It should be noted, that in practical situations the insonifying wave field may often be considered as a local plane wave at the surface of the scatterer. This means that for a single-shot experiment the reflectivity matrix $\mathbf{R}$ may be replaced by a diagonal matrix $\mathbf{R}_{dia}$ of plane wave reflection coefficients. In this thesis the diagonal reflectivity matrix $\mathbf{R}_{dia}$ will be used and the scatterer is assumed to be '*locally reacting*'.

When the recorded responses are true δ-pulses and when the sources and receivers are positioned over a closed surface surrounding the scatterer, the scattering geometry can be reconstructed exactly. From figure 2.10 it can be seen, however, that the scattering geometry is not reconstructed by a sharp discontinuity but by a distribution of energy in space. This energy distribution is related to the shape of the wavelet (temporal frequency bandwidth) and the source/receiver distributions (spatial frequency bandwidth). The influence of the source wavelet on the imaging result of figure 2.10 is due to the fact that the reflectivity has not been deconvolved with the source wavelet $\underline{S}(\zeta_0)$, as is actually prescribed by the inversion process of equation (2.26a). In chapter 3 the effects of the limited temporal and spatial bandwidths on the image resolution will be discussed in detail.

2.6.3 Possible improvements of SAFT

From the comparison between the inversion process derived with the aid of wave theory and the heuristically derived SAFT-algorithm it becomes clear, that the imaging performance of the

SAFT-algorithm will be limited due to the neglecting of amplitude effects and the handling of primary responses of single shot experiments only. In this thesis the conventional SAFT-algorithm of equation (2.43) will form the starting-point for an improved imaging procedure resulting in Multi-SAFT. The general objective of the application of ultrasonic imaging in NDI is to reconstruct the scattering geometry of a detected inhomogeneity in order to be able to characterize it. For extracting this structural information, the amplitudes do not have to be correct and therefore it is generally justified that the amplitudes will not be handled *correctly*. In order to obtain the highest possible image resolution, however, amplitudes do have to be handled *properly* (see chapter 3). Table 2.1 indicates the possible improvements of SAFT. It should be realized, that the temporal and spatial bandwidths will always be limited in practice and that no assumptions on the reflectivity **R** are needed.

Table 2.1: *The features of SAFT, Multi-SAFT and the possible further improvements.*

features	conventional SAFT	Multi-SAFT	further extensions
modes	single-mode	single-mode	multi-mode
S-wave polarization	only SV	SV and SH	–
responses	primary only	primary and multiple	–
data-acquisition configuration	pulse-echo	pitch-catch (single-shot)	pitch-catch (multi-shot)
amplitude handling	no	to a certain extent	exact
object geometry	flat plate	flat plate and cylindrical pipe	arbitrary

3

Ultrasonic Imaging and Practical Aspects

In this chapter the practical constraints, which are imposed on the imaging theory of chapter 2 by the object geometry, the characteristics of the defects and applied transducers, are described. It is explained, that actually these practical constraints lead to the application of such a simple imaging algorithm as SAFT. Some poor imaging results of conventional pulse-echo SAFT for the important class of vertically oriented defects are shown and discussed. The limitation of the inspection aperture in practical situations is shown to be the reason for the reduced image resolution which seems to be inherent to practical ultrasonic imaging for NDI.

3.1 Objects, Defects and Transducers

The objects to be inspected, the defects to be characterized and the instruments to be applied to acquire the ultrasonic data determine to a large extent the success of ultrasonic imaging. Their characteristics will put certain constraints on the theory of ultrasonic imaging, as described in the previous chapter. The implications of these constraints will be discussed in the next section. In this section, an overview is given of the types and characteristics of the objects, the defects and the transducers which are of interest in NDI of steel components.

3.1.1 Objects of interest in practice

As has already been mentioned in the introduction of this thesis, NDI of steel components mainly involves objects such as pipes and pressure vessels. Ultrasonic inspection is preferred over other NDI-techniques as it may be applied to active components with single-sided access, i.e. for *in-service* inspection. Moreover, ultrasonic inspection is not confined to the near-surface region and may cover the total volume of the object. Although defects can be encountered anywhere in a steel construction, special attention is paid to the (welded) joints and connections.

Critical parts of constructions, which are of particular interest to the gas companies, the petrochemical industry and the electricity companies, are for example girth welds in pipes, split-tees on piping and welds in nozzles of (large, heavy steel) pressure vessels (figure 3.1). The
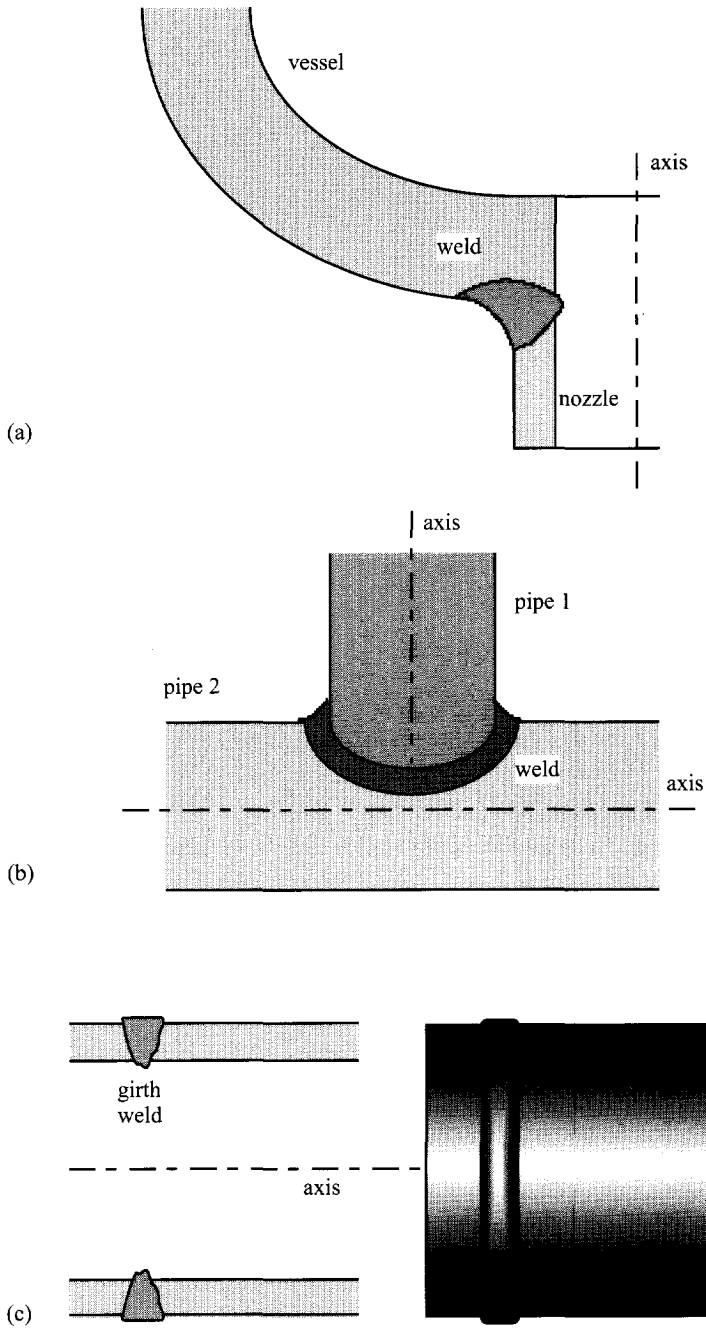
Figure 3.1: *Critical parts of constructions are, for instance, welds in nozzles (a), split-tees on piping (b) and girth welds in pipes.*
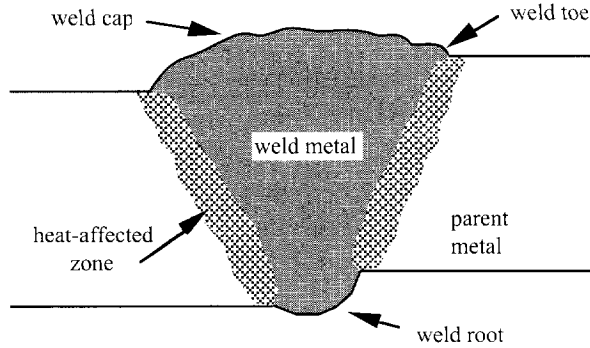
Figure 3.2: *The configuration of a V-shaped weld in a high-low situation; the different parts of the welded region are indicated.*

material used is mostly low-carbon steel, which can be considered fairly homogeneous and isotropic. However, more anisotropic and inhomogeneous types of steel are also used, such as austenitic or stainless steel. The thickness of the objects may range from about 10 mm for piping up to more than 200 mm for pressure vessels. The wave velocities in steel vary, but they are typically 5900 m/s for compressional and 3250 m/s for shear waves, while the density is approximately 7700 kg/m^3.

The surface of the steel components to be inspected in practice will be often corroded and certainly never really smooth (polished). At the position of a weld, the surface is irregularly shaped due to the presence of the weld cap (see figure 3.2). In most cases, cleaning or even grinding is permitted to smoothen the inspection surface, though it is rarely allowed to remove the weld cap totally.

In case of special weld configurations, such as the high-low situation shown in figure 3.2, spurious defect echo's may be recorded which are caused by 'discontinuities' in the weld geometry. Thus, it is of great importance that the weld geometry is known or has been determined before inspection in order to be able to distinguish between real and false defect responses. This also holds for a component consisting of combinations of different types of steel. For instance, special (stainless) steel cladding layers may be applied at the inner surface of an object to prevent chemicals affecting the low-carbon steel vessel.

Although the objects of interest in practice are curved without exception, the attention in this thesis will be primarily focused on plane objects for evaluating the performance of ultrasonic imaging. It will be made clear in section 3.3. that in spite of fairly complex inspection and processing the imaging performance for curved objects should be as good as, or even better than for plane objects.

3.1.2 Defect geometries and orientations

As stated above, the welded joints are of particular interest for ultrasonic NDI. Inhomogeneities in or near welds do arise through different causes. Imperfections during the welding procedure may lead to deformations of the weld geometry, which again may result into a decrease in strength of the welded joint. Furthermore, small inhomogeneities or cracks may be incorporated in the weld by negligent welding, which may grow to serious defects when the weld is put under load. Whether or not an inhomogeneity has to be regarded a defect is determined by fracture mechanics. It depends on the extent to which the presence of an inhomogeneity affects the integrity of a construction. The function of the construction, its dimensions and the material it consists of should all be taken into account. For a proper *fitness-for-purpose analysis* of components, the welding process and welding material have to be taken into account as well (Tielsch, 1967).

As shown by the examples of figure 3.3, weld defects may have many different geometries and

sound weld	slag inclusion
lack of side wall fusion	internal lack of fusion
lack of penetration	single-sided lack of penetration
external undercut	cracking
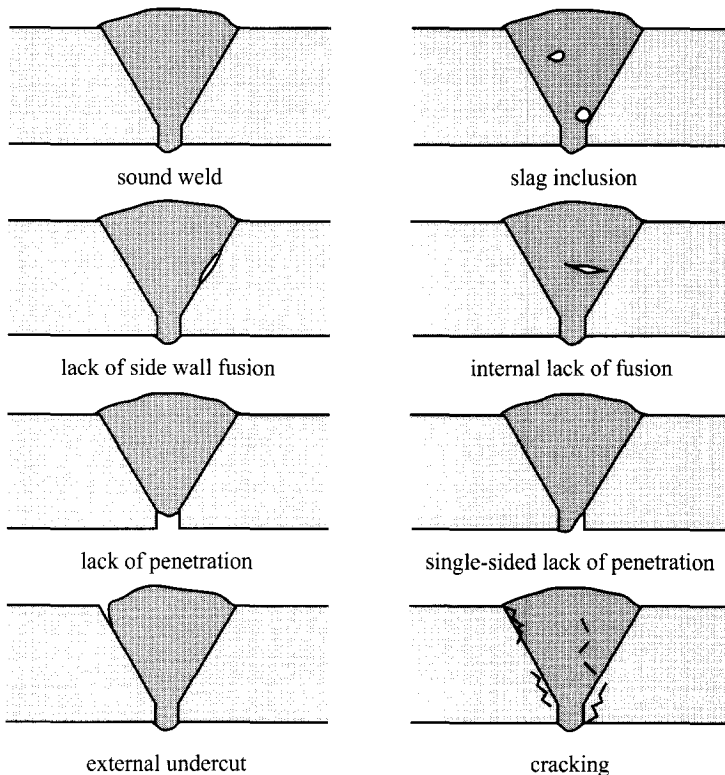
Figure 3.3: *A V-shaped weld in sound condition and with different weld defects.*

orientations. Lack of fusion, lack of penetration, slag inclusions and cracking are the most frequently encountered types of inhomogeneities in welds. In general, inhomogeneities in welds or other parts of steel components exhibit a large contrast in acoustic impedance and may therefore be regarded in general as perfectly reflecting stress-free surfaces.

Weld defects can be divided into *planar* and non-planar (*volumetrical*) defects. This distinction is based on the theory of fracture mechanics which states, that a planar defect is generally more dangerous to a construction than a volumetrical defect because stresses will be concentrated in its extremities, inducing defect growth (Harker, 1988). Furthermore, defects may be classified as 'smooth', 'rough' or irregular, all in relation to the applied ultrasonic wave length (Ogilvy, 1991). With respect to the widely applied wave length of 1 mm (~3 MHz shear wave in steel), the surfaces of lack-of-fusion and lack-of-penetration defects (see figure 3.3) may usually be regarded as 'smooth' and are therefore very well-reflecting. Cracks, on the contrary, are mostly 'rough' or even irregularly shaped (see figure 3.3) and will diffract most of the echo-acoustic energy or reflect it in different directions. In chapter 7 the effects of defect roughness on the image are illustrated.

Planar defects are generally oriented in every possible direction. This holds especially for all kinds of cracking. There are types of defects, however, which have a certain preferential orientation. The orientations of lack-of-fusion or lack-of-penetration defects, for instance, are strongly related to the angle of the prepared fusion faces of the welded objects (see figure 3.4). Another example is *Hydrogen Induced Cracking* (HIC) which is caused by the diffusion of hydrogen in low-carbon steel. When this type of cracking develops in the parent metal, i.e. not in the weld, it is oriented parallel to the surface of the object and becomes potentially dangerous when it gets interconnected to other parallel cracks, such as shown in figure 3.5.

Weld defects which arise during the manufacturing or repairing processes should, but may not
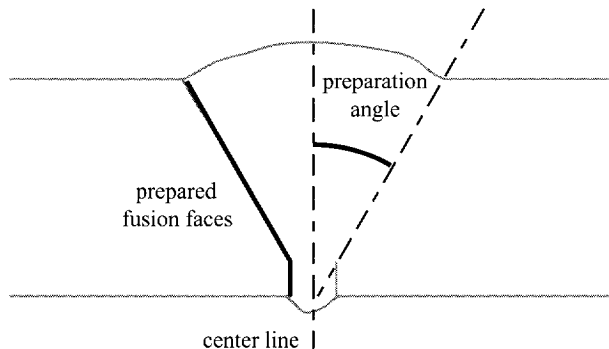
Figure 3.4: *The configuration of a V-shaped weld with the geometry of the objects to be welded (preparation geometry).*

39
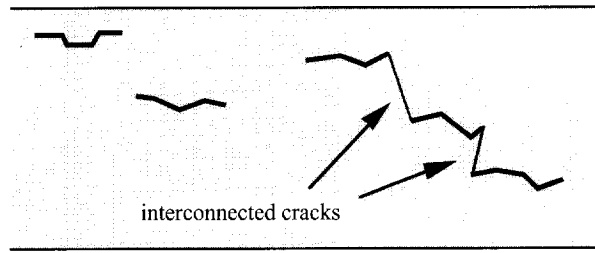
Figure 3.5: *Typical geometry of Hydrogen Induced Cracking (HIC).*

always be detected, as the construction may not permit two-sided access, even though it might be out of service. As soon as a component is in service, defects can be formed through excessive loading or chemical reactions. Defects induced by in-service conditions (stress-loading, high pressures/temperatures, chemicals) will often have the shape of cracks. Small inhomogeneities in the weld, which originate from the welding process, may initiate such defects. Cracks do not only occur in welds or in their heat-affected zone, but do also appear in other parts of the component (see figure 3.6). In some cases, external stress loading can lead to partially or totally closed cracks which may be (partially) transparent for P and SV waves (see figure 3.6).

In practice, cracks are considered as the most dangerous and should be identified as soon as they arise. Especially in thin steel components (~10 mm thickness) or components which are heavily loaded, very small (weld) defects may already be considered hazardous to the construction. This means, that in some cases defects of 1 mm in length already have to be characterized as such by ultrasonic imaging. Whether or not this is possible depends on the feasible image resolution and will be discussed in section 3.2.
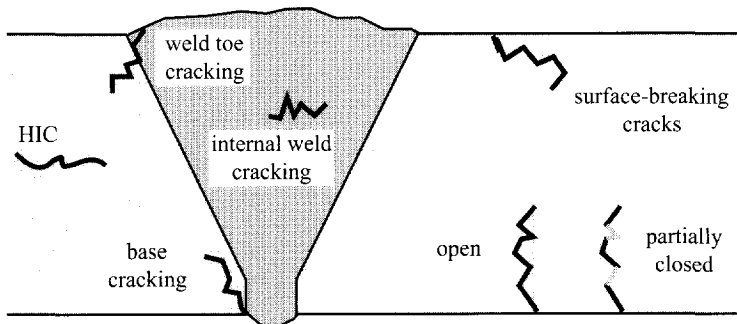
Figure 3.6: *Different types of cracking in the welded region and in the welded parts.*

3.1.3   Source and receiver transducers in NDI

Ultrasonic waves in steel may be generated and detected by applying different physical principles (Halmshaw, 1987). The *EMAT* (ElectroMagnetic-Acoustic Transducer), for instance, generates and detects ultrasonic waves by employing Lorentz forces induced by eddy currents in a steady magnetic field. This type of transducer operates in the vicinity of the inspection surface and is a so-called *non-contact* technique. Another non-contact NDI-method is *opto-acoustics*, where lasers are used to generate and detect ultrasonic waves (White, 1963; Monchalin, 1986; Lorenz, 1988). Both EMAT and opto-acoustic NDI-methods are currently developed for practical applications (De Jong and Stelwagen, 1992). Most widely used in ultrasonic NDI, however, are piezo-electric transducers. They are based on the piezo-electric principle that an electric voltage causes deformation of the piezo-material and vice versa, and are preferably applied in contact with the inspection surface.

As piezo-electric transducers have been developed into suitable ultrasonic sources and receivers, commercially available in many different designs, they are the most commonly used transducers in the NDI practice. The evaluation of ultrasonic imaging for NDI described in this thesis has for this reason been performed with the aid of piezo-electric transducers[1]. The influence of the characteristics of piezo-electric transducers on the ultrasonic imaging performance, however, should be studied properly and taken into consideration.

An electronically triggered piezo-electric disc may give rise to deformations oriented parallel or perpendicular to its surface. A piezo-electric transducer is a piece of piezo-material which is fit into a housing with an appropriate backing in order to damp the response and a surface layer in order to match the inspected material (Silk, 1984). When the surface of such a transducer is put in contact with the inspection surface it may apply stresses parallel or perpendicular to that surface. These stresses will only lead to an effective generation of, respectively, ultrasonic shear and compressional waves in case the energy coupling between the transducer and the steel object is sufficiently high. An air layer between the transducer and the inspection surfaces reduces the transmission of acoustic energy considerably. Therefore, a coupling medium has to be applied between the transducer and inspection surface in order to overcome the large discontinuity in acoustic impedance caused by the presence of an air layer.

To generate or detect compressional waves in steel, a water-based coupling fluid will suffice, for it is well-known that compressional waves do propagate in fluids. When shear waves have to be generated or detected, the coupling medium should transfer shear stresses and therefore possess a rather high viscosity. In practice, a very sticky treacle is applied which makes scanning with the transducer almost impossible. As shear waves are favorably used in ultrasonic NDI this seems a

---

1   It has to be recognized that other types of transducers may be fit for ultrasonic imaging purposes as well.
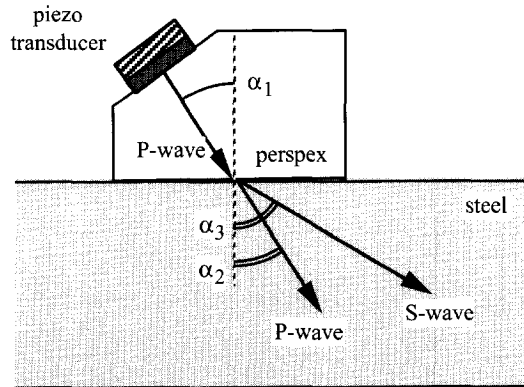
Figure 3.7: *A piezo-electric wedge transducer as commonly applied in practice; a P-wave is generated in the wedge material and is partially transmitted as a P-wave and partially as an S-wave; the angles α_2 and α_3 depend on the angle α_1 and the velocity contrast between the steel and wedge material.*

definite drawback of piezo-electric transducers.

Practical source and receiver transducers posses a certain directivity pattern with a distinct main lobe. In order to be able to manipulate this directivity, special wedges are being applied (see figure 3.7). The wedge material is chosen to match the acoustic impedance of steel as closely as possible so that most of the acoustic energy generated in the wedge will be transmitted into the steel object. For this reason, most wedges are made of perspex, although perspex does attenuate ultrasonic waves to a certain extent. The transducer is mounted on the wedge under such an angle that the generated wave field is propagating mainly in the desired direction in the steel object. It has to be noticed, that the directivity and beam width of a wedge transducer are always frequency dependent (see figure 3.8).

Commonly, compressional wave transducers are being applied on wedges. Because of mode-conversion effects at the wedge-steel interface, compressional as well as shear waves will be generated and detected. The angle of incidence for the compressional waves in the wedge can be chosen such that the transducer is only generating or detecting shear waves in the steel medium. In this way a scanning shear wave transducer will be realized which eliminates the drawback of piezo-electric shear wave transducers as mentioned earlier. It has to be noted, that when the inspection surface is defined as the x-y plane, the shear waves that are generated and detected by scanning wedge transducers in practice are pure SV waves, i.e. the particle-displacement components are polarized in the x-z plane. This is a direct result of the fact that P and SV waves are coupled and thus no particle-displacement component parallel to the inspection surface can be generated or detected.
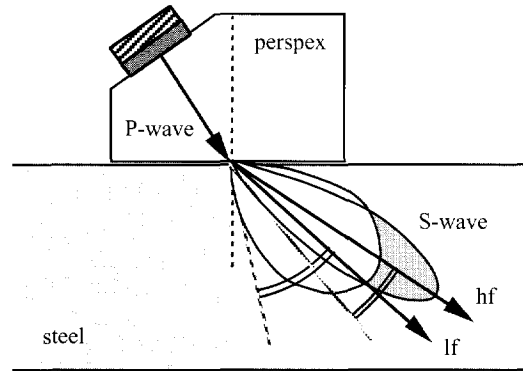
Figure 3.8: *The directivity pattern of a piezo-electric wedge transducer is frequency dependent; 'lf' indicates the beam of a low and 'hf' of a high frequency component, both having different main directions and beam widths.*

The center frequency and bandwidth of a piezo-electric transducer depend on the thickness of the applied piezo-material, the type and construction of its backing (damping), and possibly on the frequency dependent absorption of the wedge material (Silk, 1984). In practice, piezo-electric transducers are being applied to generate and detect ultrasonic frequencies up to about 10 MHz successfully, for most types of steel will attenuate higher frequencies to a great extent (Reynolds and Smith, 1984). The frequency bandwidth is related to the transducer's sensitivity and may vary in practice from 1 to 4 MHz (for −6 dB in reflection). It has to be noted here that the frequency contents of a recorded ultrasonic response also depends on the pulser and amplifier characteristics (Green, 1990).

As mentioned above, shear waves are favorably applied in ultrasonic NDI. The reason for this lies in the fact that the shear wave velocity is about half the compressional wave velocity in most solids, which makes the wave length (for a certain frequency) of shear waves about half that of compressional waves. This results in a temporal resolution which is twice as high for shear waves as for compressional waves. The transducers used for the experiments described in this thesis are all angled (45° and 60°) shear wave transducers of around 4 MHz center frequency with a 3-4 MHz (−6 dB) bandwidth.

3.1.4 Data-acquisition configurations in NDI

Ultrasonic data may be acquired by scanning the source and/or receiver transducer(s) along the inspection surface. In practice, four different data-acquisition configurations are known[2] (see also

---

2 Of course, the positions of the source and receiver may be interchanged as the result of reciprocity (Wapenaar, 1989).

figure 3.9):

a.   *pulse-echo*: the source and receiver are physically one single transducer which is scanned along the available aperture; this configuration is also called *zero-offset* (seismics) or *monostatic* (radar);

b.   *tandem*: the source and receiver transducers are separated by a fixed distance and are scanned simultaneously; this configuration is also known as *common-offset* (seismics);

c.   *pitch-catch*: the source transducer is placed at a fixed position and the receiver transducer is scanned; this configuration is also known as *common-shot* (seismics) or *bistatic* (radar);

d.   *multistatic*: the receiver transducer is scanned along the inspection surface for every position of the scanning source transducer; this configuration is also known as *multi-shot, multi-offset* (seismics).

For conventional ultrasonic inspections the pulse-echo configuration is most frequently used. Because of the more complex scanning system required for the scanning of two transducers simultaneously, a tandem configuration is generally not preferred in NDI practice. As the multistatic configuration results in an enormous amount of ultrasonic data, it is not applied in NDI practice (yet...). Consequently, only the pulse-echo and pitch-catch data-acquisition configurations will be considered in this thesis.
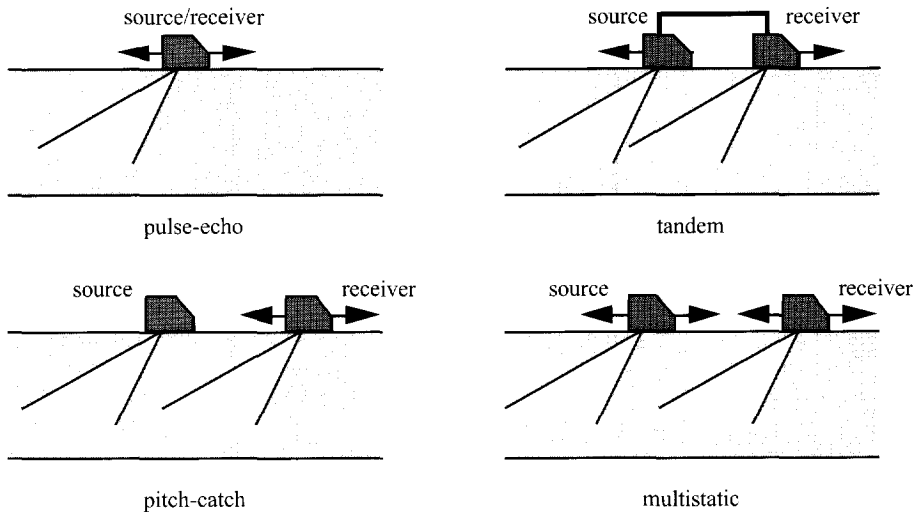
Figure 3.9: *The four different data-acquisition configurations which are generally known in practice; the pitch-catch configuration will be considered throughout this thesis.*

3.2 Practical Constraints and their Implications on Imaging

The intrinsic characteristics of the objects, defects and transducers as described in the previous section put certain constraints on the imaging theory presented in chapter 2. As will be demonstrated in this section, these practical constraints may in some cases affect the image quality considerably.

3.2.1 Practical constraints

The most important practical constraint has to do with the available inspection surface. General imaging theory prescribes ultrasonic waves to be generated and recorded along a closed surface surrounding an inhomogeneity entirely. The description of the object geometries in section 3.1. plainly illustrates that this cannot be achieved in practice, especially not when in-service inspection has to be performed. Moreover, the presence of a weld cap over a potential defect area (welded joint) makes it impossible to apply piezo-electric transducers in this region of the inspection surface. Thus, the object geometry gives rise to a considerable source as well as receiver aperture limitation. Apart from that, the objects of interest are strictly bounded which results in the presence of multiple responses in the recorded data which can lead to spurious indications in the image.

The inverse propagation operator derived in chapter 2 for reconstructing the scattering surface of an inhomogeneity is only valid for 3-D wave fields measured at a plane inspection surface and reconstructed at a surface oriented parallel to that inspection surface. In practice, inspection surfaces will often be curved which means that instead of the Rayleigh II integral the general Kirchhoff-Helmholtz integral has to be applied. This again implies that both the pressure and the normal component of the particle velocity have to be measured. When for practical reasons the Rayleigh II integral – and thus the inverse propagation operator – is applied on data measured along curved inspection surfaces anyhow, the scattering geometry will still be reconstructed correctly but the amplitude of the imaged indications will be incorrect. As this amplitude error does not affect the shape of the reconstructed scattering geometry and because no parametrical inversion has to be performed on the imaging result (as is the case in seismics, for instance), the amplitude corrections contained in the inverse propagation operator will generally be neglected.

The transducers applied in practice may be sensitive to compressional as well as shear waves. This means, that the recorded wave field may consist of different types of waves and that acoustic inversion can consequently lead to spurious indications in the image. Furthermore, the dimensions of real transducers will also contribute to the limitation of the source and receiver aperture. Because real transducers possess bounded beams, the information recorded at the limited inspection surface will be restricted even more.

Planar inhomogeneities reflect an incident wave in a well-defined direction which is related to their orientation with respect to the incident wave field. This means, that in some cases the transducer aperture limitation may be responsible for the fact that planar inhomogeneities, oriented in some particular direction, cannot be imaged properly. A combination of the aperture limitation and the directivity of a piezo-electric transducer may result into situations in which an inhomogeneity cannot be insonified at all. These so-called '*worst-case defects*' (Green, 1989) will definitely not be detected by ultrasonic means, let alone be characterized by ultrasonic imaging.

Another most important practical constraint is simply *time*. In practice, NDI should often be applied in a restricted amount of time (in the order of hours). Yet, imaging theory prescribes a series of experiments (*scans*) involving many different source positions in order to insonify the inhomogeneity and collect scattered waves from all directions. Performing numerous experiments in practice would be very time-consuming (in the order of days) and therefore in most situations undesired. Also complex (elastic) processing of recorded ultrasonic data still leads to unacceptable long inspection times. Therefore, both the imaging procedure and algorithm have to be designed to be as simple as possible, without causing intolerable errors (errors leading to mis-interpretations).

3.2.2 Image quality: resolution and accuracy

Both the resolution and accuracy of the image determine the image *quality* and the success of ultrasonic imaging for defect characterization in NDI. The image (spatial) *resolution* may typically be defined as the minimum distance at which two point diffractors may be observed separately. The extent to which indications are positioned correctly, imaged completely and correspond to true inhomogeneities will be defined here as the image *accuracy*. Consequently, the image accuracy depends mainly on errors in the object and data-acquisition parameters, such as the wave velocity, object geometry and transducer positions. The effects of these errors on the image accuracy will be described extensively in chapter 7. Here only the image resolution will be discussed.

Ideally, when sources and receivers can be applied along a closed aperture surrounding the inhomogeneity, the resolution of the reconstructed scattering surface in the image will be determined by the shape of the employed wavelet. This means, that only the frequency contents of the recorded responses determines the so-called *point-spread function* (PSF) in the image, which is independent of position for closed inspection surfaces. This is illustrated in figure 3.10a, where two point inhomogeneities have been imaged using modeled ultrasonic data recorded along a closed aperture surrounding the imaged region (pulse-echo configuration). In this case, the resolution (obtained by SAFT) may be typically defined in the order of half the wave length of the maximum frequency present in the recorded responses (Born and Wolf, 1975).
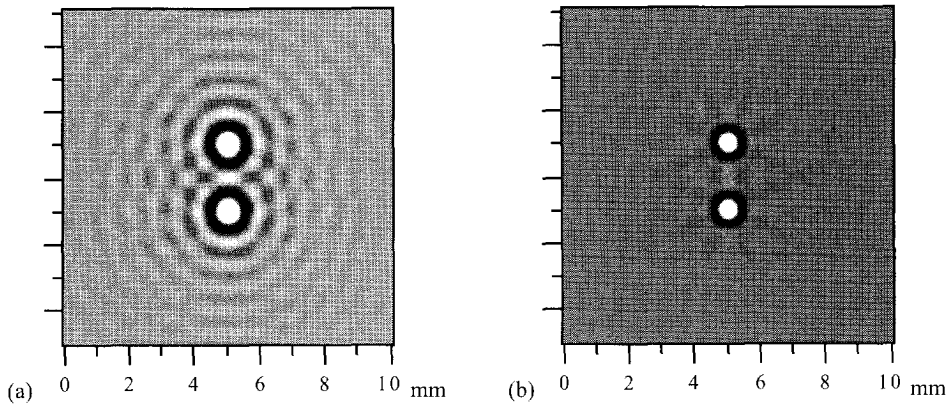
Figure 3.10: *The images without (a) and with (b) proper temporal frequency tapering of pulse-echo data recorded along an aperture surrounding two point diffractors completely; the maximum frequency component has a wave length of approximately 0.8 mm.*

The shape of the PSF depends on the frequency bandwidth and the maximum frequency of the recorded responses. The larger the frequency bandwidth, the lower the side-lobe levels of the PSF will be and the more narrow the shape of the PSF will become (approaching the delta pulse). Yet, the shape of the frequency spectrum will also influence the shape of the PSF. As is illustrated in figure 3.10b, a properly (cosine-shaped) filtered frequency band results in considerably lower side-lobe levels (Berkhout, 1984). Lower side-lobe levels improve the image resolution and avoid the possible formation of spurious indications.

In case transducers can be positioned along a closed aperture surrounding the inhomogeneity, responses can be recorded from every possible direction and the image resolution will be fully determined by its temporal frequency contents. However, when the transducer apertures are restricted, the limited spatial frequency bandwidth will also affect the image resolution, as is shown in figure 3.11a. For a restricted inspection aperture the image resolution becomes position-dependent, as the spatial frequency bandwidth (angular diversity) at a point in space is depending on the distance from that point to the inspection aperture.

The imaged point diffractors in figure 3.11a exhibit the so-called 'focusing-cross' (Berkhout, 1984). This is due to the absence of destructive interference by imaged back-propagated responses from outside the inspection aperture. This effect is similar to the presence of side-lobes in the PSF. Thus, in case the spatial frequency spectrum is not rectangularly shaped but properly (cosine-shaped) filtered, the effects of the focusing-cross will be suppressed (see figure 3.11b). Note that due to the spatial filtering the spatial resolution is slightly reduced.

The practical constraints imposed by the transducer characteristics and the limitation of the
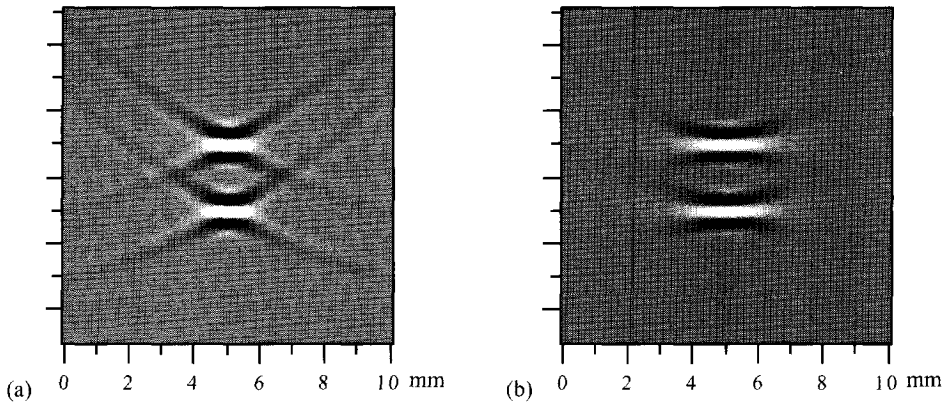
Figure 3.11: *The images without (a) and with (b) proper spatial frequency tapering of pulse-echo data recorded along a limited aperture positioned above two point diffractors.*

inspection aperture as well as the number of experiments ('shots') will lead to a restriction of the ultrasonic information to be collected. Consequently, this will result into a reduction of the image resolution. It seems that this reduced image resolution is inherent to practical ultrasonic imaging for NDI. This will be illustrated by results of conventional SAFT-imaging in the next section.

3.3 Conventional SAFT Imaging

The Synthetic Aperture Focusing Technique originates from radar technology and was first applied in NDI of steel components in 1967 (Flaherty et al., 1967). In 1974 the US Nuclear Regulatory Commission initiated the development of SAFT for NDI at the University of Michigan (Vandenbroek et al., 1980). The first SAFT imaging systems date from the period 1978-1982 (Corl et al., 1978; Bruck et al., 1982). With the steadily increase of computing power SAFT gradually developed during the 1980's and numerous research and evaluation projects were performed (Hamlin, 1985; Schmitz, 1986a; Hall et al., 1987; Van Dijk et al., 1989; Chinn and Dieterman, 1993). The results of these projects were not very promising due to specific assumptions and modification of the conventional SAFT algorithm. In this section the structure of this algorithm and its performance are described, identifying the problems related to conventional SAFT imaging.

3.3.1 The conventional SAFT-algorithm

Conventional SAFT is applied on flat plates, using a single scanning transducer in pulse-echo and a linear scanning aperture. A two-dimensional image is reconstructed using a modified form of equation (2.26a):

$$\Omega(x,z) = \sum_{i=1}^{N} P\left(x_{S/R,i}; t = t_0 + \frac{2}{c}\sqrt{(x - x_{S/R,i})^2 + (z - z_0)^2}\right) , \tag{3.1}$$

with $x_{S/R,i}$ indicating the ith position of the source/receiver (S/R) transducer on a plane inspection surface $z = z_0$. This algorithm is able to image only directly insonified and scattered responses correctly and will not take into account any reflections of the waves at the object boundaries. Furthermore, no amplitude correction is applied and imaging is performed in the time domain by picking samples from the recorded data.

The image reconstruction is usually conducted from an image point (Thomson, 1984), i.e. considering a point in the region of interest (*ROI*) to be imaged, the amplitude values of the time samples calculated according to (3.1) are taken from the ultrasonic data, summed and assigned to that point in the image. To reduce the processing time considerably, the image reconstruction is sometimes conducted from only those samples in the recorded ultrasonic data which exceed a certain threshold (Doctor et al., 1986). Both principles are illustrated in figure 3.12. Because the recorded data is discretized in time, the correct travel time does not generally correspond to the sample being picked. The rounding-off process will result in small errors in the image, but may be negligible in case the data is sufficiently (two times or more) oversampled (Seydel, 1982). By transforming the (x,t) data to the (temporal) frequency (x,ω) domain, this rounding-off process is avoided and continuous phase shifts instead of discrete time shifts are applied (Fortunko et al., 1984; Langenberg et al., 1986).
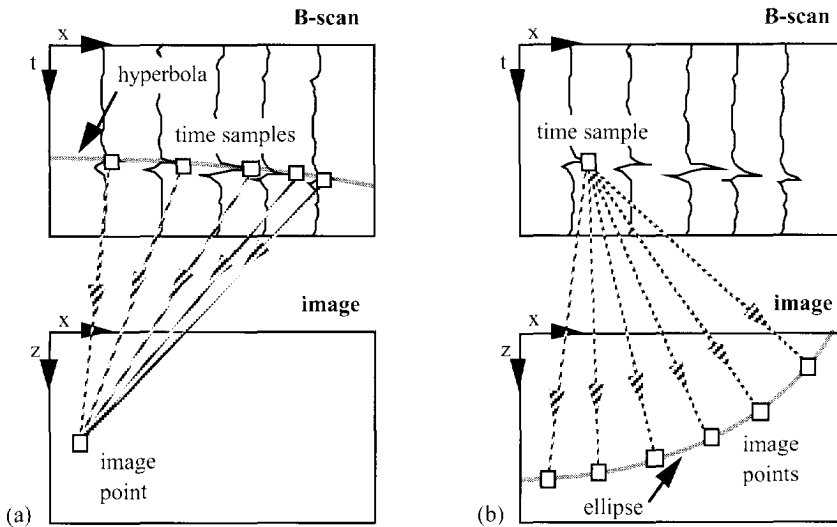
Figure 3.12: *The image reconstruction procedure conducted from an image point (a) and from a time sample (b).*
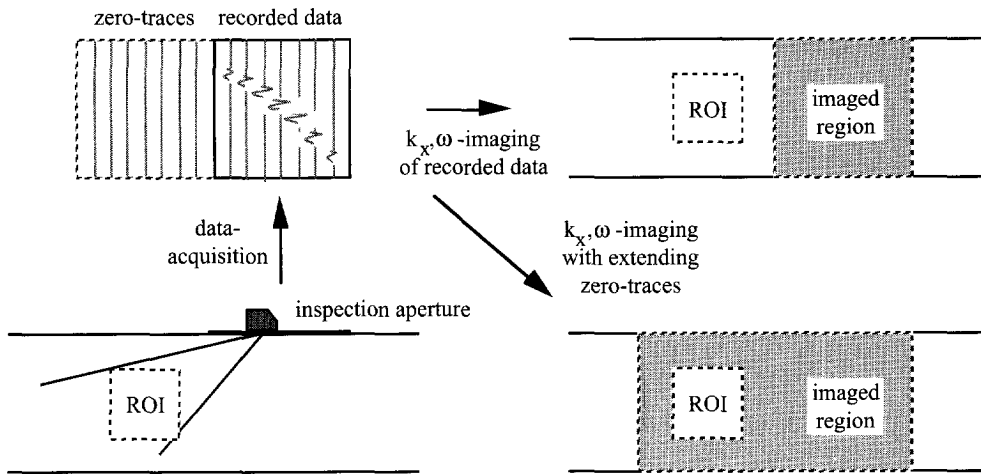
Figure 3.13: *Imaging with angled beam transducers in the (k_x, ω) domain.*

Imaging can also totally be performed in the (k_x,ω) domain with the aid of the so-called mapping algorithm (Berkhout, 1987; Mayer, 1990). For pulse-echo data this algorithm is very efficient and does not suffer from any errors caused by the discrete time sampling. A drawback of the (k_x,ω) domain processing is that the region to be imaged is defined by the position of the inspection aperture. In cases in which angled beam transducers are applied, the ROI is often situated out of this imaged region. In such situations the aperture has to be extended by adding traces (containing zeroes) over the ROI as indicated in figure 3.13. The mapping algorithm cannot simply be applied on pitch-catch data.

Although conventional SAFT has been applied almost only on flat structures (plates), some cylindrical versions of the algorithm (3.1) in the time (x,t) and frequency (x,ω) domain have been developed during the 1980's (Schmitz et al., 1986b). However, from the literature it may be generally concluded that during the last decade most effort has been put in decreasing the processing time and working towards real-time imaging systems (Hall et al., 1987; Ozaki et al., 1988) instead of in the necessary improvements of the imaging performance.

3.3.2 Conventional SAFT imaging performance

For the first SAFT images the ultrasonic data was obtained in a water tank with the transducer scanning in pulse-echo over an immersed object (Vandenbroek et al., 1980) as shown in figure 3.14. In case of applying straight beams in such an *immersion* experiment, the image would suffer from strong disturbing indications due to the high-amplitude reflections from the water-steel
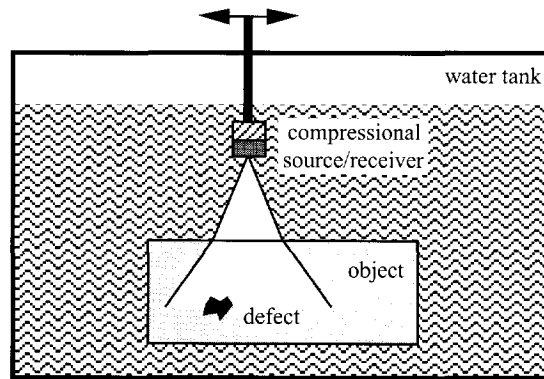
Figure 3.14: *The configuration of an immersion NDI experiment.*

interface. Consequently, the coupling of ultrasonic energy into the steel object and vice versa was often quite poor. In most experiments compressional waves were employed in the medium to be inspected, which means that the image resolution was not optimum.

The model defect being very popular for evaluating the imaging performance is the *flat-bottom hole*, as shown in figure 3.15. Drilled perpendicularly to the back-wall or under an angle, the flat bottom of these holes are imaged to determine the image quality. Figure 3.16a shows that the image of the flat top is very accurate when the *direct* pulse-echo data, as acquired in situation II of figure 3.15, are employed for imaging. Flat-bottom holes, however, are not particularly good models for real (weld) defects in steel components. For instance, the sides of the holes are not imaged at all and the images suggest an isolated horizontally oriented planar defect inside the material.

Flat-bottom holes drilled parallel to the back-wall are also used to test conventional SAFT
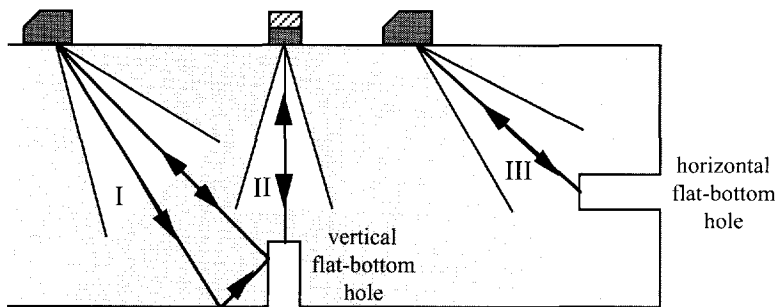
Figure 3.15: *Vertically and horizontally oriented flat-bottom holes for the conventional determination of image quality; three different data-acquisition situations are indicated.*
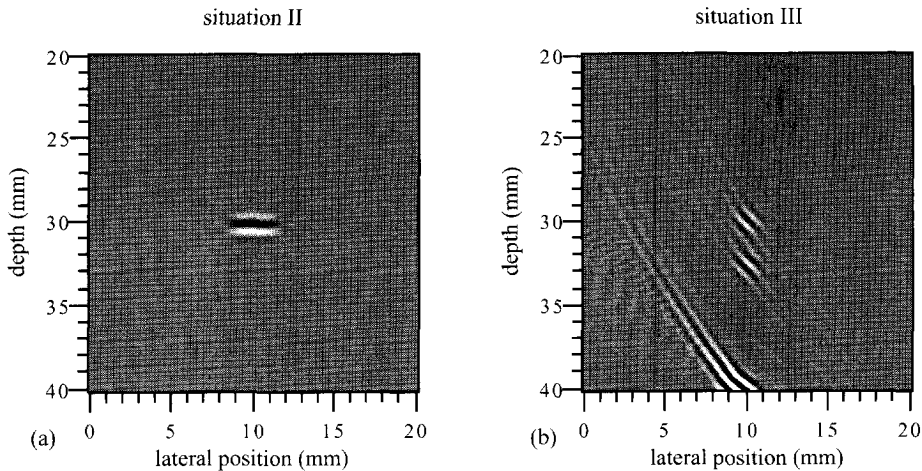
Figure 3.16: *The images of a 2 mm diameter vertical (a) and horizontal (b) flat-bottom hole computed from pulse-echo data recorded along a limited aperture positioned at 30 mm above the holes; the data-acquisition situations are indicated in figure 3.15.*

imaging. The imaging results of this type of (more realistic) model defect immediately show the weakness of conventional (pulse-echo) SAFT, as is illustrated by the image in figure 3.16b. Here the *direct* pulse-echo data, as acquired in situation III of figure 3.15, are employed for imaging. Only the diffracting edges of the defect are imaged and the responses of indirectly reflecting waves (propagating via the back-wall) cause spurious indications in the image, which consequently troubles the interpretation of the image.

Experimental imaging results obtained with conventional SAFT on *vertically oriented defects*, i.e. defects oriented perpendicularly to the back-wall of the object, are very poor (Van Dijk et al., 1988). Generally, only the (diffracting) top of the defect can be imaged correctly when *direct* pulse-echo data, as acquired in situation I of figure 3.15, are employed for imaging. In most cases, however, the image will only show spurious indications, as is shown in figure 3.17a. Evidently, the responses of *indirectly* reflecting waves should be employed for imaging in this situation, but the quality of these imaging results for conventional SAFT are even worse (see figure 3.17b).

As vertically oriented defects (cracking, lack of penetration, lack of fusion) may generally be considered as being dangerous to a construction, conventional SAFT imaging is justly found to be inadequate and not suitable for characterizing these important defects in steel components. Processing ultrasonic data acquired with a tandem configuration results in better images of vertically oriented defects, but the required scanning facilities are more complex and the available scanning space will be reduced even more. Probably for the reasons described here, the efforts in developing and introducing ultrasonic imaging for NDI have been greatly diminished at the end of the 1980's.
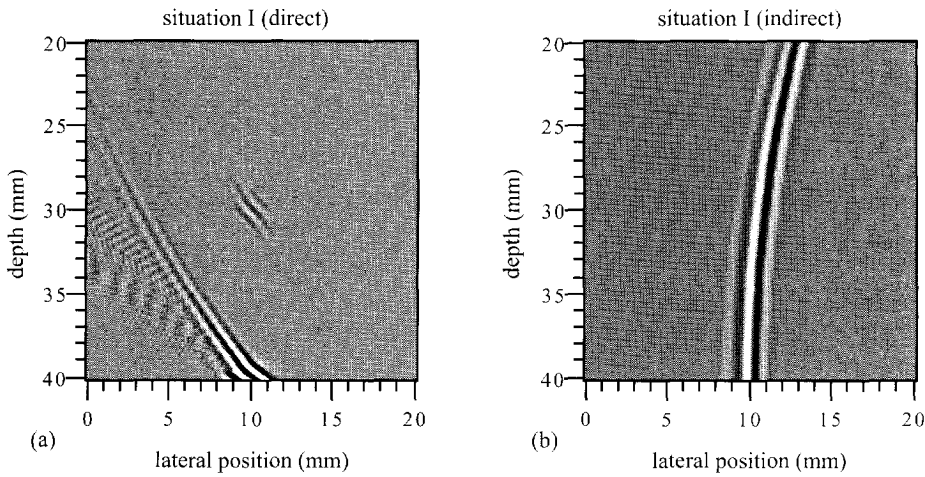
Figure 3.17: *The images of a 2 mm diameter vertical flat-bottom hole computed from direct (a) and indirect (b) pulse-echo data recorded along a limited aperture positioned at 30 mm above the holes; the data-acquisition situation I is indicated in figure 3.15.*

Around that time it was recognized, that specific improvements were absolutely necessary in order to be able to apply ultrasonic imaging as a defect characterization method in NDI (Van Dijk et al., 1988). The implications of the aperture limitation and of the pulse-echo data-acquisition configuration on the imaging result gradually became clear and the development of ultrasonic imaging for NDI started to concentrate on the optimization of both data-acquisition and processing. The evaluation study of ultrasonic imaging for NDI, as presented in this thesis, has been the direct consequence of the conclusions described in this section.

4

Imaging with Multi-SAFT

4.1 Introduction

The availability of only a limited inspection aperture makes it absolutely necessary to employ different wave paths for imaging. In this chapter the Multi-SAFT philosophy will presented and the contributions to the imaging result of forward and back scattering wave fields will be discussed for the pulse-echo as well as the pitch-catch data-acquisition configuration. The simplified inverse propagation operator for Multi-SAFT, neglecting amplitude effects, will be given and time-domain processing will be proposed.

To justify the applicability of a simplified imaging algorithm, a number of eight assumptions will be made which concern the nature of the wave field, the media to be inspected and the transducers applied in practice. It is argued that, due to neglecting amplitude effects, the inverse problem is more or less reduced to a geometrical problem concerning the determination of the length of wave paths in bounded media. Analytical expressions for the path lengths of directly and indirectly reflecting waves are presented for the flat plate and cylindrical pipe geometries.

4.2 The Multi-SAFT Philosophy

4.2.1 Virtual aperture enlargement

The main reason for the poor results of conventional SAFT-imaging for NDI is the availability of only a limited inspection aperture. In order to improve the image resolution this aperture should be extended in some way. The bounded nature of the objects to be inspected gives rise to the presence of multiple wave paths. By employing these multiple reflecting waves for imaging the inspection aperture may be virtually enlarged. This is illustrated in figure 4.1 for a simple flat plate geometry. The use of the scattered wave field, reflecting via the back wall of the plate towards the receivers, actually implies a virtual receiver aperture on a fictive surface opposite to the back wall. This *virtual aperture enlargement* does also apply to other possible (insonifying and scattering) wave paths.
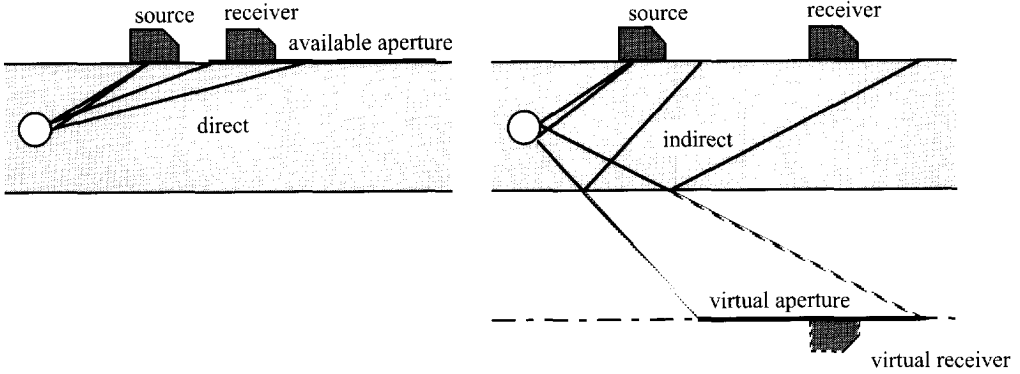
Figure 4.1: *The basis of the Multi-SAFT philosophy: virtual enlargement of the inspection aperture by employing multiple reflecting waves.*

Applying SAFT on responses from multiple wave paths implies more or less the employment of multiple synthetic apertures for imaging. Consequently, the multiple-SAFT procedure has been named *Multi-SAFT*. In figure 4.2 and 4.3 the Multi-SAFT principle is demonstrated for a model crack inspected with the pitch-catch data-acquisition configuration. The benefits of applying Multi-SAFT are obvious for this type of defect, particularly when the combined wave-path image is compared to the conventional pulse-echo imaging result.
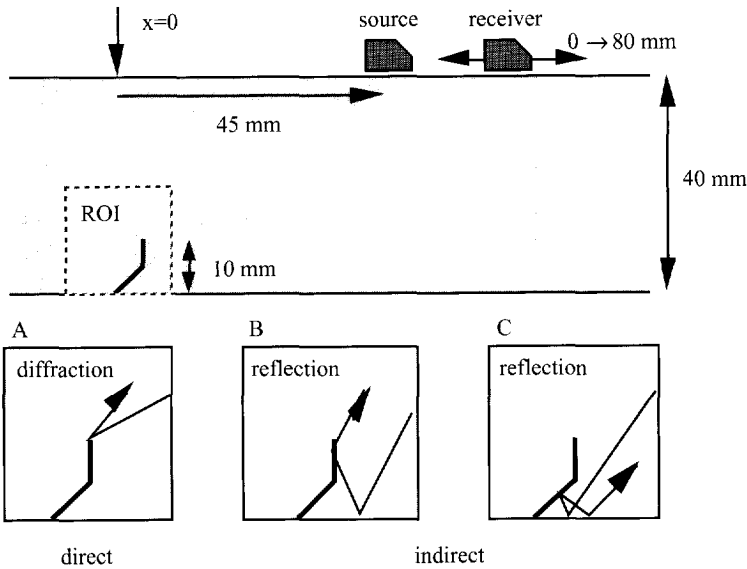
Figure 4.2: *Multi-SAFT: combining the information of multiple wave paths from one single-shot experiment; direct diffraction (A) as well as indirect reflection (B,C) responses are employed for imaging.*
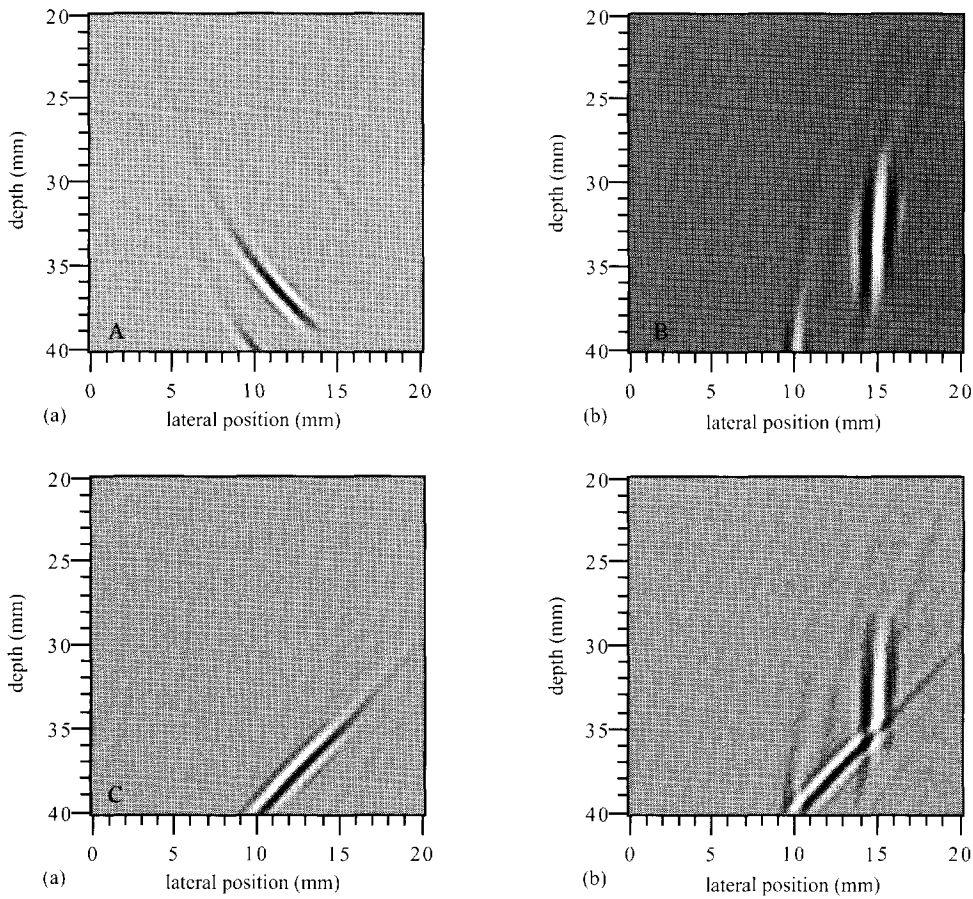
Figure 4.3: *The diffraction image (a), the reflection images (b,c) and the combined Multi-SAFT image of the model crack of figure 4.2.*

4.2.2 Spatial resolution

That the indirectly insonifying and scattering waves do indeed contain extra structural information can be illustrated in the wave number domain. Figure 4.4 shows the configuration of an insonifying plane wave $\underline{k}_i$ and a scattering plane wave $\underline{k}_s$ for the so-called *forward scattering* and *back scattering* situations (Berkhout, 1987[1]). In order to obtain a good spatial resolution a sufficient range of $\underline{k}_i\text{--}\underline{k}_s$ vectors are needed to fill the (k_x,k_z) plane in such a way, that spatially broad-band data is available for the inversion process. In figure 4.5 it is shown how the $\underline{k}_i\text{--}\underline{k}_s$ vectors are constructed for a point diffractor as indicated in figure 4.4 and for a range of incident angles.

---

1   In Berkhout (1987) the figure of the forward and back scattering situations have been erroneously interchanged.
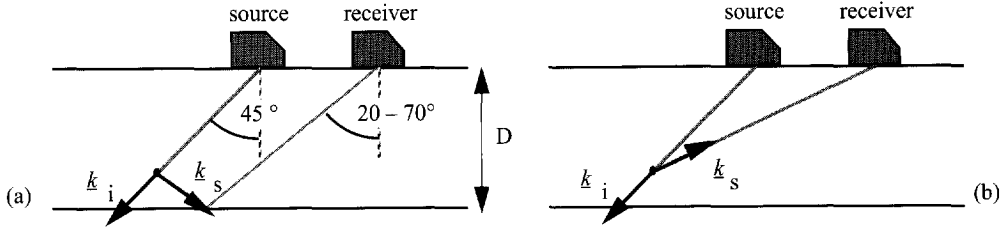
Figure 4.4: *The configuration of a point diffractor with an insonifying plane wave $\underline{k}_i$ and scattering plane wave $\underline{k}_s$ for the forward (a) and back scattering (b) situations.*

In figure 4.6 the part of the (k_x,k_z) plane is indicated which is filled for the forward and back scattering situations in the case that pitch-catch data-acquisition is applied. It has been assumed that the data is temporally broadband, that the point diffractor is positioned at a depth of 30 mm in a 40 mm thick plate, and that the insonification angle α is $45°$. The angles β under which the scattering wave field has been recorded are ranging between $20°$ and $70°$ (see figure 4.5). From figure 4.6 it can be seen, that the forward scattering waves do fill another part of the (k_x,k_z) plane than the back scattering waves and will therefore be expected to contribute positively to the image resolution.

In case the pulse-echo configuration is applied, the length of the vector $\underline{k}_i - \underline{k}_s$ will be simply $2\underline{k}_i$ for the back scattering problem, which results in the (k_x,k_z)-plane image shown in figure 4.7a. For the pulse-echo forward scattering situation (*round-trip* wave path) the resulting length of the vector $\underline{k}_i - \underline{k}_s$ will depend on the depth of the scatterer. For a scatterer at the position of the back-wall (mirror plane), the length of the resulting vector $\underline{k}_i - \underline{k}_s$ for forward scattering waves will also be exactly $2\underline{k}_i$, but this vector will always be pointing in the k_x-direction. This will result in a good resolution in the x-direction, but in the z-direction no resolution will be obtained. For a scatterer
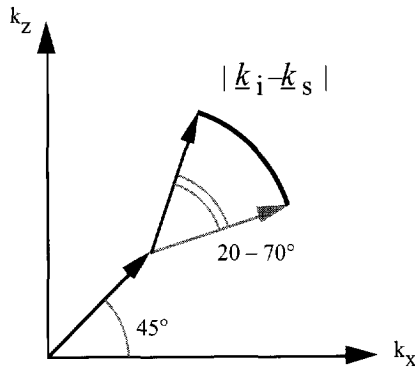
Figure 4.5: *The construction of the range of a monochromatic vector $|\underline{k}_i - \underline{k}_s|$ in the (k_x,k_z)-plane for a fixed angle of insonification ($\alpha=45°$) and different angles of recording ($20°\leq\beta\leq70°$).*
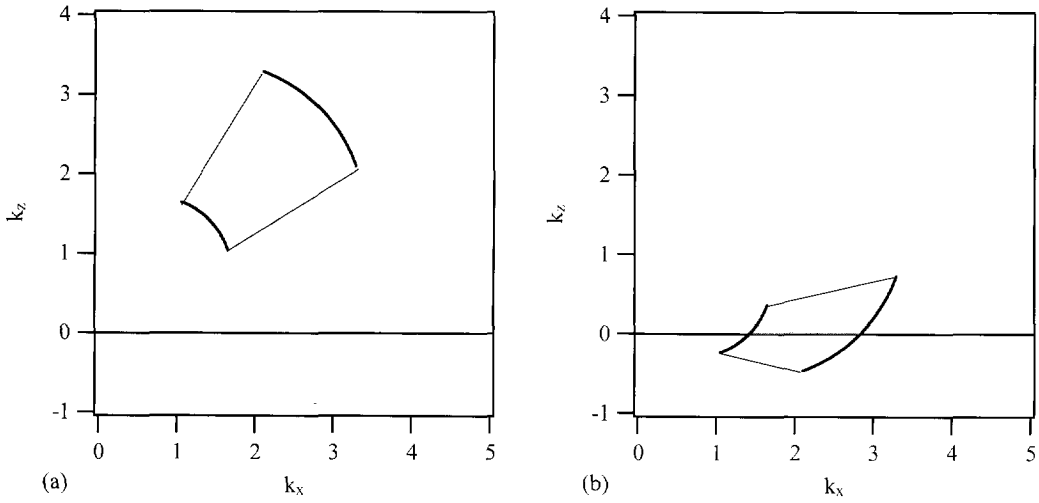
Figure 4.6: *The sections filled by the vector $|\underline{k}_i - \underline{k}_s|$ in the (k_x, k_z)-plane of back scattering (a) and forward scattering (b) plane waves for a broadband* pitch-catch *experiment, with $\alpha=45°$, $20°{\leq}\beta{\leq}70°$ and a diffractor at a depth of $0.75*D$ (see figure 4.5).*
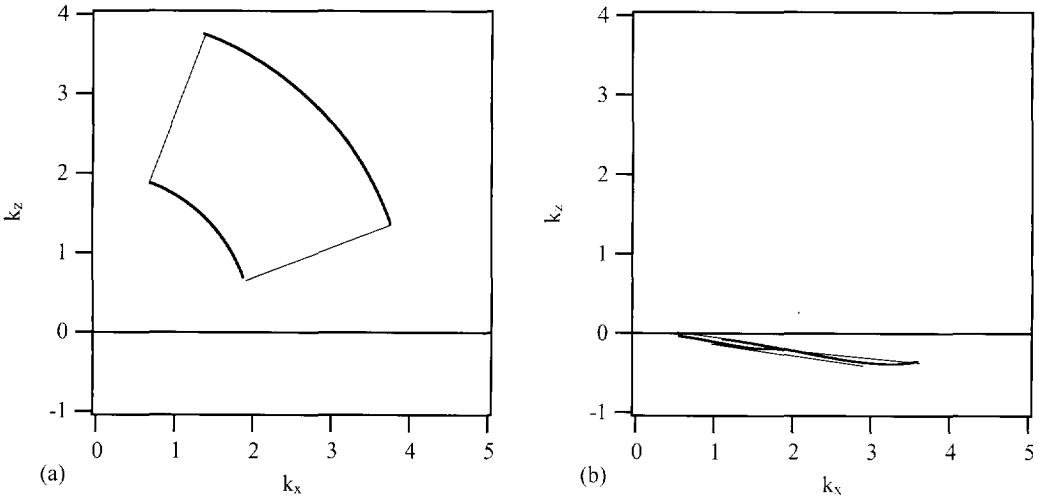
Figure 4.7: *The sections filled by the vector $|\underline{k}_i - \underline{k}_s|$ in the (k_x, k_z)-plane of back scattering (a) and forward scattering (b) plane waves for a broadband* pulse-echo *experiment, with $20°{\leq}\alpha, \beta{\leq}70°$ and a diffractor at a depth of $0.75*D$ (see figure 4.5).*

located somewhere between the inspection surface and the back-wall, the resulting forward scattering vector $\underline{k}_i - \underline{k}_s$ will only fill up a very small part of the (k_x, k_z) plane, as indicated in figure 4.7b.
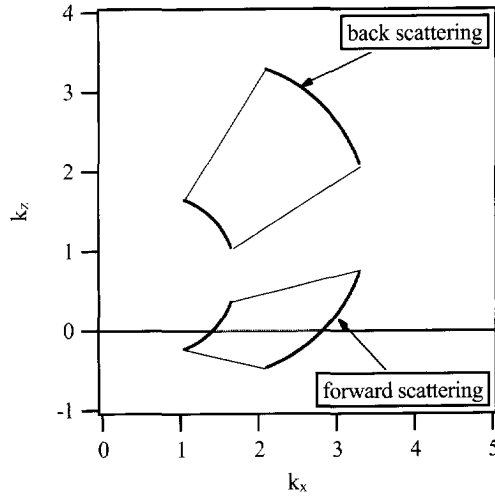
Figure 4.8: *The total section filled by the vector $|\underline{k}_i - \underline{k}_s|$ in the (k_x,k_z)-plane of both back scattering and forward scattering plane waves for a broadband pitch-catch experiment, with $\alpha=45°$, $20°\leq\alpha,\beta\leq70°$ and a diffractor at a depth of 0.75*D (see figure 4.5).*

From these results can be concluded that in general no spatial resolution in the z-direction can be obtained in case pulse-echo data-acquisition is applied *and* forward scattering waves are employed for imaging. This is also the explanation for the poor imaging result, as shown in the previous chapter, for conventional SAFT applied on forward (indirectly) scattering waves. The implication of this conclusion will be discussed in chapter 6, where the imaging of vertically oriented defects will be studied.

As has been illustrated in figure 4.3, imaging the recorded ultrasonic data (containing multiple responses) for different wave paths, thus virtually extending the source and receiver apertures, will generally result into a better spatial resolution than may be obtained by applying directly back scattering waves only. This is made clear in the (k_x,k_z)-plane image shown in figure 4.8 for the pitch-catch situation. Here the ultrasonic information of the forward and back scattering wave paths of the configuration shown in figure 4.4 have been combined. It can be observed from figure 4.8 that a considerable coverage of the (k_x,k_z) plane is obtained by only one single shot experiment in case multiple reflections are taken into account.

Responses of both forward and back scattering waves are present in the ultrasonic data to be imaged. To avoid interfering indications in the images, as the result of responses corresponding to different wave paths, the data-acquisition procedure should be carefully optimized. This optimization will be extensively described in chapter 6.
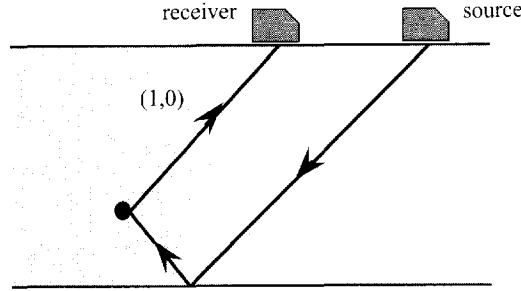
Figure 4.9: *An illustration of a (1,0) wave path.*

It is convenient to define a short-hand notation to designate the different wave paths that may exist in a bounded object. A wave may reflect a number of times at the front and/or back wall of the object before and/or after scattering at an inhomogeneity. Such a wave will be denoted as '*(k,l)*', where *k* and *l* denote the total number of reflections of the wave with the object boundaries for the insonifying and scattering waves, respectively. Thus, the (1,0) wave path implies one reflection (at the back wall) of the insonifying wave before and no reflection after scattering at an inhomogeneity (see figure 4.9) and may be referred to as a forward scattering wave path. The wave paths (0,0) and (1,3), for instance, are both back scattering wave paths according to the configuration of figure 4.4.

4.3 The Multi-SAFT Imaging Algorithm

4.3.1 The inverse propagation operator

The Multi-SAFT algorithm is based on the conventional SAFT algorithm (2.35) neglecting any amplitude effects. Therefore, the applied inverse propagation operator F' is a simplified version of (2.29) and reads in the frequency domain:

$$F'(x,y;z_0,z_n) = j\omega \exp(jk\Delta r) = j\omega \exp(j\omega\Delta t) \ , \tag{4.1}$$

where Δr is the distance from the (source or receiver) transducer position to a point in the imaged region of interest (*ROI*) and $\Delta t = \Delta r/c$ is the travel time corresponding to that distance. This inverse propagation operator F' contains a '$j\omega$' factor, which corresponds to a high-pass frequency filter. In the time domain this '$j\omega$' factor corresponds to a time derivative ($\partial/\partial t$). This simple amplitude correction arises from wave theory.

According to the Kirchhoff-Helmholtz integral, the pressure in a point A in space can be determined from the integral over the sum of the products $P[\partial G/\partial n]$ and $G[\partial P/\partial n]$, where P is the

pressure measured along an inspection surface surrounding the point A and G is the Green's function describing the impulse response of the background medium. Both products involve the factor 'jk' which originates from the derivative with respect to the normal on the inspection surface ($\partial/\partial n$). This factor results in the high-pass frequency filter of (4.1) and may be interpreted as a compensation for the low-pass frequency filtering effect as the result of the integration along the inspection surface. Note that the '$j\omega$' factor is only exact for 3-D parallel surfaces.

Multi-SAFT is applied in the time domain using the pitch-catch data-acquisition configuration (fixed source, scanning receiver) and thus the algorithm in the time domain will read, using the definition of the inverse propagation operator of equation (4.1):

$$\Omega(x,y,z) = \sum_{i=1}^{N} \frac{\partial}{\partial t} P\left(x_{R,i},x_S;y_{R,i},y_S;t = \frac{1}{c}(\Delta r_{R,i} + \Delta r_S) - \tau\right) , \tag{4.2}$$

with ($x_{R,i},y_{R,i}$) and (x_S,y_S) the positions, respectively, of the receiver and source transducers along the inspection surface, $\Delta r_{R,i}$ and Δr_S the lengths of the one-way (scattering and insonifying, respectively) wave paths, and τ the total wedge delay with respect to the source trigger pulse. For two-dimensional images the y-coordinate of Ω is a constant. The path length Δr depends on the type of wave path chosen for imaging.

4.3.2 Time domain processing

The actual imaging of the SAFT algorithm equation (4.2) has been implemented to process the data in the time domain. The application of the '$j\omega$' factor and frequency filtering are done in the frequency domain prior to imaging. Before applying a temporal Fourier transformation on the recorded ultrasonic data in order to perform these operations, the DC-component is removed and a time window is applied in order to assure continuity of the recorded signals in time. The main reason for the image reconstruction to take place in the time domain is that for general data-acquisition configurations, such as pitch-catch, time domain processing is much faster. This is caused by the fact, that image reconstruction in the frequency domain involves a phase shift for every frequency component, for every recorded trace, *and* for every position in the image. In the time domain the image reconstruction involves only a time shift for every recorded trace, for every position in the image. Especially computing the time-consuming complex exponentials for the phase shifts, which have to be calculated for every frequency (inner loop!), makes frequency domain imaging so much slower (Lorenz, 1990).

In the frequency domain, however, exact *phase shifts* can be applied instead of rounded off *time shifts* in the time domain. The errors made in the time domain depend on the sampling frequency

and may be reduced to negligible proportions through oversampling of the recorded ultrasonic data (Seydel, 1982). The recorded data should be sampled with a sampling time Δt, satisfying the *temporal anti-aliasing criterion* according to (Berkhout, 1985):

$$\Delta t \leq \frac{1}{2\ f_{max}}\ , \tag{4.3}$$

where f_{max} is the maximum frequency present in the recorded data. The ultrasonic data, as presented in this thesis and recorded to be processed with the Multi-SAFT time-domain algorithm, contain frequencies up to approximately 6 MHz (–20 dB). They should therefore be sampled with a sampling frequency of at least 12 MHz, but by applying a sampling frequency of 25 MHz the errors, due to rounding off the time shifts, will be reduced to 20 ns maximum. This corresponds to a maximum phase error of $\pi/4$, which may be considered acceptable.

As already mentioned in the previous chapter, ultrasonic pulse-echo data may also be processed in the wave number domain by applying the mapping algorithm containing the c/2-operator (Berkhout, 1985). This algorithm is superior in processing speed over the time and frequency domain algorithms. However, it is only capable of imaging data in the region located directly below a plane or circular inspection aperture (though this aperture may be virtually extended, see figure 3.13). An attractive feature of time and frequency domain processing in particular is that the ROI to be imaged, as well as the type of wave path, may be chosen arbitrarily and the inspection aperture may have any shape.

4.3.3 Time-efficient processing

The processing time needed for imaging a certain ROI depends on the number of recorded traces and the dimensions of the image. The sampling distances Δx and Δz in the image should satisfy the *spatial anti-aliasing criterion* and consequently depend on the maximum wave number k_{max} as present in the recorded ultrasonic data to be imaged, according to (Berkhout, 1985):

$$\Delta x \leq \frac{\pi}{k_{max}\ \sin\ \alpha_{max}} = \frac{c}{2\ f_{max}\ \sin\ \alpha_{max}}\ , \tag{4.4a}$$

$$\Delta z \leq \frac{\pi}{k_{max}\ \cos\ \alpha_{max}} = \frac{c}{2\ f_{max}\ \cos\ \alpha_{max}}\ , \tag{4.4b}$$

with c the wave velocity in the medium to be imaged and α_{max} the maximum angle of the vector $\underline{k}_i-\underline{k}_s$ with respect to the normal on the plane inspection surface. For arbitrarily shaped inspection surfaces and forward scattering wave paths the angle α_{max} cannot always be easily determined and therefore the Multi-SAFT images will be reconstructed by using simply:

$$\Delta x = \Delta z \leq \frac{c}{2\ f_{max}} = \frac{\lambda_{min}}{2}\ . \tag{4.5}$$

Here λ_{min} is the minimum wave length and with the practical approximate values of $c = 3250$ m/s and $f_{max} = 6$ MHz the sampling distances Δx and Δz should be chosen smaller than 0.27 mm.

In case a large section has to be imaged, because the approximate location of the inhomogeneity is not known accurately enough, the number of samples to be imaged may become very large. Consequently, the processing time will become unacceptably long. For a fast and reasonably accurate determination of the location of the inhomogeneity, the imaged region could be sampled with a much larger sampling distance. This would, however, result into spatial aliasing caused by the higher frequencies contained in the recorded data. Yet, this spatial aliasing can be simply avoided by applying an appropriate low-pass frequency filter prior to imaging.

4.4 Assumptions for Practical Application

To assure the Multi-SAFT imaging procedure to be practicable, i.e. not too laborious and thereby time consuming, a number of eight important assumptions will be made concerning the data-acquisition and processing procedures. The first assumption has been made in the previous section and states that the error in the discrete time-shifting operation is tolerable in case the recorded ultrasonic data is (over)sampled with at least four times the maximum frequency. The other assumptions will follow below and have been arranged roughly into three groups, related to the characteristics of the responses, the medium and the transducers.

4.4.1 Recorded responses

The second assumption is that no multiple scattering has taken place between different point diffractors (secondary sources) making up one or more inhomogeneities. This means, that it is assumed that the insonifying wave field is scattered by a point diffractor and that this scattered wave field has not interacted with other parts of the inhomogeneity or with other inhomogeneities before being recorded. In practice, such multiple scattering is very well possible and the corresponding responses will give rise to spurious indications in the image (as will be shown in chapter 8).

The third assumption is that the imaging procedure may be performed for a certain wave path using the complete recorded dataset containing responses from every possible wave path. This implies, that responses from other wave paths will be imaged incorrectly and may reduce the image quality. It will be shown in chapter 7 that – due to the spatial averaging process for a certain wave path – the responses from other wave paths generally will not interfere constructively in the image, thus making this assumption reasonable.

The fourth assumption concerns the origin of the recorded responses. As a 2-D image is reconstructed, the responses are assumed to be originating from diffractors located in the reconstructed image plane. In chapter 6 it will be explained that the data-acquisition process can be optimized by applying a narrow source beam. Then only that (part of an) inhomogeneity which is located in the image plane may be insonified. In practice, the recording of responses from inhomogeneities located out of the image plane cannot always be avoided.

4.4.2 Homogeneous isotropic acoustic media

The fifth assumption which will be made concerns the (background) medium to be inspected. Apart from the possible isolated inhomogeneities, this medium is assumed to be perfectly homogeneous and isotropic. The wave velocity is determined by applying a straight-beam shear wave transducer with the aid of a coupling treacle to the inspection surface and measuring a series of back-wall reflection responses. Of course, the thickness of the object has to be known accurately in order to be able to compute the shear wave velocity in this way. The steel components as used in practice have been found to be considerably homogeneous and isotropic, although certain production processes (rolling of pipes) may induce slight anisotropy. The influence of errors made in practice by assuming the medium to be homogeneous and isotropic will be discussed in chapter 7.

The sixth assumption deals with the acoustic nature of the Multi-SAFT algorithm. It is assumed that only shear waves propagate through the medium to be inspected. This means, that the existence of other wave types is not taken into account. Because the angled-beam shear wave transducers – as applied for the experiments described in this thesis – are (almost) only sensitive for shear waves, this assumption seems to be justified. Of course, if a shear wave is converted into a pressure wave and back again into a shear wave, it might be recorded and may result into a false indication in the image.

The seventh assumption concerns the influence of reflections at the object boundaries on the wave field in case indirectly reflecting waves are employed for imaging. It is assumed that the changes in the amplitude and/or phase of the insonifying or scattering wave field do not influence the imaging result. Thus, no corrections will be made for the reflectivity of the object boundaries described by $\mathbf{R}(\zeta_0)$ and $\mathbf{R}(\zeta_1)$ in equations (2.7c) and (2.12c). In practice, reflection at the object boundaries may involve mode-conversion (which is merely an amplitude effect) or phase changing (for post-critical shear wave reflection, for instance). The influence of these effects on the imaging result will be discussed in chapter 7. For now it is assumed that the phase change upon reflection at the object boundaries is approximately constant and does not influence the image quality.

4.4.3 Transducers and index points

The eighth and last assumption is an important one and concerns the transducer positions. For all real experiments described in this thesis wedge transducers were applied to generate and receive only shear waves propagating under an angle with respect to the normal on the inspection surface. The *index point* of such angled beam transducers is the point on the coupling face of the transducer at which the waves leave or enter the wedge and is mainly depending on the orientation and size of the piezo-crystal (see figure 4.10a). In practice, it is determined by applying the transducer in pulse-echo on a standard calibration block with a cylindrically shaped end, as shown in figure 4.10b. By looking for the transducer position at which the response from the cylindrical boundary is maximum, the index point is found to be located at the center of the cylinder[2] (Krautkrämer and Krautkrämer, 1977).

Although the position of this index point is actually depending on the angle under which a plane wave is generated or received (due to Snell's law), it is chosen to be a fixed point. It is assumed that this fixed index point uniquely defines the positions of the source and receiver transducers, i.e. the source and receiver transducers are considered as single point distributions. The source distribution vector $\underline{S}(\zeta_0)$ in equation (2.2) will then contain only one non-zero component. Assuming fixed index points also means assuming fixed *wedge delay times*, i.e. the time in which the waves propagate in the source and receiver wedges is assumed to be constant for all angles of insonification and reception.

(a)   (b)
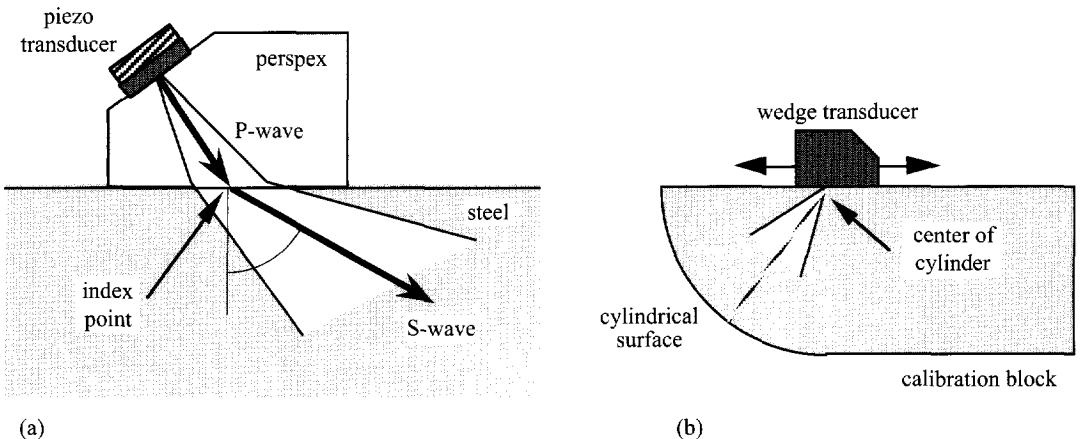
Figure 4.10: *The definition (a) and the determination (b) of the index point of a wedge transducer.*

---

2   For wedges with curved coupling faces to be applied on cylindrical pipes, for instance, the index point should actually be computed numerically; in practice, however, a sufficiently accurate estimation can often be made.
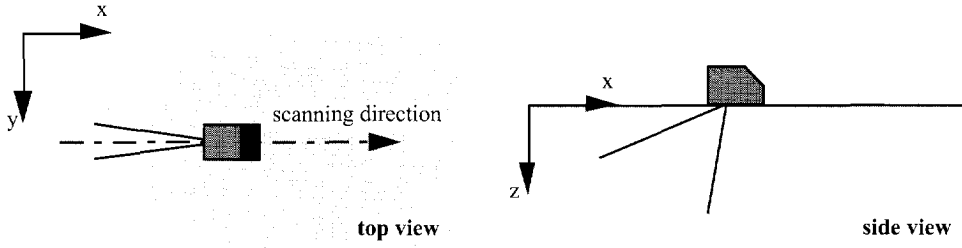
Figure 4.11: *The special directivity of the receiver transducer: a narrow beam in the x-y plane and a wide beam in the x-z plane.*

The total wedge delay for a set of transducers (source and receiver) is determined in practice by placing them with the coupling faces together in such a way, that the index points are in line. The time between the source trigger pulse and the received pulse is defined as the total wedge delay. The error that will be introduced in the imaging process by choosing fixed index points is depending on the direction of the generated or received waves and will be discussed in chapter 7.

The receiver has to record the scattered waves from as many directions as possible (for good spatial resolution, see section 4.2) and should therefore have a wide beam. To avoid – to a certain extent – the reception of scattering waves from directions other than from the image plane, the receiver transducer has been constructed to have a wide beam width in the plane defined by the linear scanning aperture and the z-axis, and a narrow beam width perpendicular to that plane (see figure 4.11). Although this optimization of the data-acquisition does not guarantee that the recorded responses are all originating from the image plane, it generally does suffice in practice.

4.5 Travel Time Calculation

As mentioned already in chapter 2, the time-shifting process is actually the essence of the imaging procedure. From the Multi-SAFT algorithm (4.2) it can be seen, that Δt is the total travel time which is determined by the wave velocity c and the total path length Δr, consisting of the insonifying and scattering wave path lengths. This illustrates that by neglecting any amplitude effects the imaging procedure has been more or less reduced to a geometrical problem, i.e. determining the lengths of wave paths in bounded media. In this section expressions for the wave path lengths for the flat plate and the cylindrical pipe geometries will be derived.

4.5.1 Flat plate geometry

In case of a flat plate geometry it is not very difficult to calculate the total path length Δr
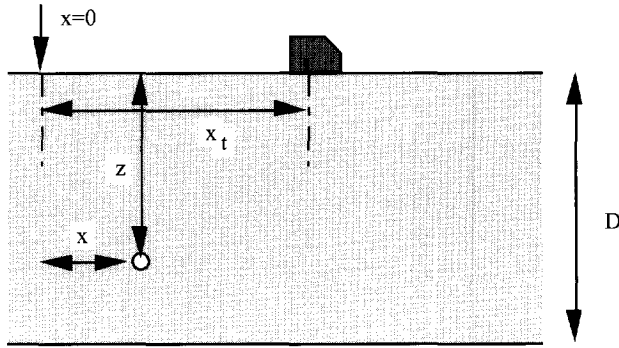
Figure 4.12: *The flat plate geometry as used for the calculation of direct and indirect wave path lengths.*

analytically. This total wave path does consists of two parts: the insonifying and the scattering wave path. These will both be designated as *one-way wave paths*, meaning wave paths from an image point to a transducer or vice versa. The length of a one-way wave path Δr_t (the index 't' stands for *type* of transducer) can be formulated analytically by making use of the object boundaries as mirror planes (see figure 4.12) and reads:

$$\Delta r_t = \sqrt{(x - x_t)^2 + (y - y_t)^2 + [(n_1 + n_2) D + n_3 z]^2} \quad , \tag{4.6}$$

with:

x,y,z- the coordinates of the point to be imaged;
x_t,y_t- the x- and y-coordinates of the transducer;
D- the thickness of the plate;
n_1- number of reflections at object boundaries;
n_2- factor, which is 0 when n_1 is 0 or even, and 1 when n_1 is odd;
n_3- factor, which is +1 when n_1 is 0 or even, and −1 when n_1 is odd.

The transducer is assumed to be located at the inspection surface $z=0$. The total travel time Δt is derived using the length of the two one-way wave paths and the known wave velocity c according to:

$$\Delta t = \frac{\Delta r_S + \Delta r_R}{c} \quad . \tag{4.7}$$

This total travel time is applied in the simplified inverse propagation operator defined by equation (4.1) for every image point, for every receiver position (pitch-catch configuration) to compute the imaging result.
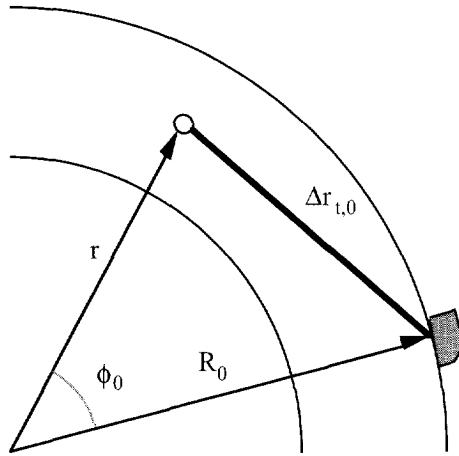
Figure 4.13: *The cylindrical pipe geometry used for the calculation of direct wave path lengths.*

4.5.2 Cylindrical pipe geometry

In case of a cylindrical pipe geometry the calculation of the length of a direct wave path (no reflection at the object boundaries) in a cross-section perpendicular to the pipe's axis is very straightforward. However, the calculation of the length of an indirect wave path (one or more reflections at the object boundaries) in such a cross-section happens to be quite complicated. In this section cylindrical coordinates will be used to indicate the positions of the transducer and the point to be imaged (*image point*).

For the length of a direct one-way wave path in a cylindrical pipe two parameters have to be known: the positions of the transducer and the image point. The angle between the radial vectors indicating the transducer position and the position of the image point is defined as ϕ_0. The length of the radius vector for the transducer position is equal to the outer radius of the pipe R_o, while for the position of the image point the length of the radius vector will vary and is indicated by r. The expression for the one-way direct path length $\Delta r_{t,0}(r,\phi_0)$ is derived using the geometry of figure 4.13 and reads:

$$\Delta r_{t,0}(r,\phi_0) = \sqrt{r^2 - 2rR_o\cos(\phi_0) + R_o{}^2} \ . \tag{4.8}$$

For the computation of the length of the indirect wave path (with *one* reflection at the inner surface of the pipe) *three* parameters have to known: the positions of the transducer and the image point, *as well as* the position at which the wave reflects at the inner surface of the pipe. This reflection will take place at a position indicated by the radius vector with length R_i, the inner
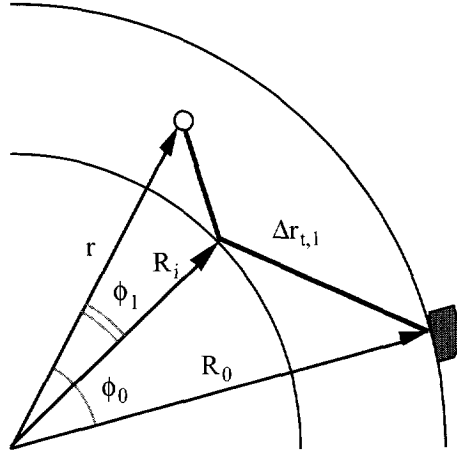
Figure 4.14: *The cylindrical pipe geometry used for the calculation of indirect wave path lengths.*

radius of the pipe, making an angle ϕ_1 with the radial position of the image point. Using figure 4.14, the expression for the one-way indirect path length $\Delta r_{t,1}(r,\phi_1,\phi_0)$ is:

$$\Delta r_{t,1}(r,\phi_1,\phi_0) = \sqrt{R_o^2 - 2R_oR_i\cos(\phi_0-\phi_1) + R_i^2} + \sqrt{r^2 - 2rR_i\cos(\phi_1) + R_i^2} \ . \tag{4.9}$$

From this equation it is not possible to compute the travel time as a function of r and ϕ_0, because the angle ϕ_1 is generally unknown. In the literature it is stated (Harker, 1988), that this angle ϕ_1 can only be determined by using a numerical method. Here a new method is proposed which results in a far more computational effective computation of indirect path lengths in cylindrical pipes. Applying the minimization theorem for $\Delta r_{t,1}(r,\phi_1,\phi_0)$ yields:

$$\frac{\partial \Delta r_{t,1}}{\partial \phi_1} = 0 \ , \tag{4.10}$$

which leads to:

$$\frac{r \sin(\phi_1)}{\sqrt{r^2 - 2rR_i\cos(\phi_1) + R_i^2}} + \frac{R_o\sin(\phi_0-\phi_1)}{\sqrt{R_o^2 - 2R_oR_i\cos(\phi_0-\phi_1) + R_i^2}} = 0 \ . \tag{4.11}$$

However, it is impossible to compute the value of ϕ_1 for certain values of ϕ_0 and r analytically from (4.11), because ϕ_1 cannot be written explicitly. Therefore, this equation is re-written[3] in the form of a second order equation in r:

---

3   This is allowed, because the arguments of the square roots in equation (4.11) will not become negative.

$$\left\{\sin^2(\phi_1)\left[R_o^2 - 2R_oR_i\cos(\phi_0-\phi_1) + R_i^2\right] - R_o^2\sin^2(\phi_0-\phi_1)\right\} r^2 +$$
$$+ \left\{2R_iR_o^2\sin^2(\phi_0-\phi_1)\cos(\phi_1)\right\} r +$$
$$- R_i^2R_o^2\sin^2(\phi_0-\phi_1) = 0 \quad . \tag{4.12}$$

Now it is possible to determine the value of r for certain values of ϕ_0 and ϕ_1 analytically. Notice, that when ϕ_1 runs from 0 to $\phi_0/2$, r will run from r=R_i to r=R_o, covering the entire radial section. Yet, by substituting the function $r(\phi_1,\phi_0)$ of (4.12) in equation (4.9), the result will become $\Delta r_{t,1}(\phi_1,\phi_0)$ instead of $\Delta r_{t,1}(r,\phi_0)$. Consequently, a total travel time $\Delta t(\phi_1,\phi_0)$ will be computed which is inconvenient, because imaging takes place for every image point indicated by (r,ϕ_0). To overcome this slight problem, the function $r(\phi_1,\phi_0)$ of equation (4.12) will be rearranged into a function $\phi_1(r,\phi_0)$ before it is substituted into equation (4.9). From (4.9) and the modified version of equation (4.12), the expression for the one-way indirect path length $\Delta r_{t,1}(r,\phi_0)$ can now be derived:

$$\Delta r_{t,1}(r,\phi_0) = \sqrt{R_o^2 - 2R_oR_i\cos\left[\phi_0-\phi_1(r,\phi_0)\right] + R_i^2} + \sqrt{r^2 - 2rR_i\cos\left[\phi_1(r,\phi_0)\right] + R_i^2} . \tag{4.13}$$

By using the method described here it is possible to compute the travel time of the total indirect wave path (being a function of r and ϕ_0) for every image point directly with (4.7), i.e. without applying a time-consuming numerical method. The resulting Multi-SAFT algorithm for cylindrical pipes proofs to be computationally very effective. The computation of the length of wave paths with more than one reflection at the object boundaries is based on the very same procedure as described here for the indirect wave path.

Equations (4.8) and (4.13) are derived for a two-dimensional geometry. However, the axial direction (y) may be included in the expressions for the one-way wave path length resulting into:

$$\Delta r_{t,n}(r,\phi_0;y) = \sqrt{\left[\Delta r_{t,n}(r,\phi_0)\right]^2 + (y-y_t)^2} \quad , \tag{4.14}$$

with n denoting the number of reflection at the object boundaries and y_t the y-position of the transducer. With the aid of equations (4.7) and (4.14) arbitrarily oriented plane cross-sections of cylindrical pipes may be imaged.

4.5.3 Geometrically feasible wave paths

It is important to notice that for a certain cylindrical pipe geometry some image points cannot be reached by the insonifying wave field propagating along a certain wave path. From figure 4.15 it is derived that for a direct wave path, as well as for an indirect wave path with only one reflection at the inner pipe surface (both wave paths coincide in this case), the maximum value of ϕ_0 for an
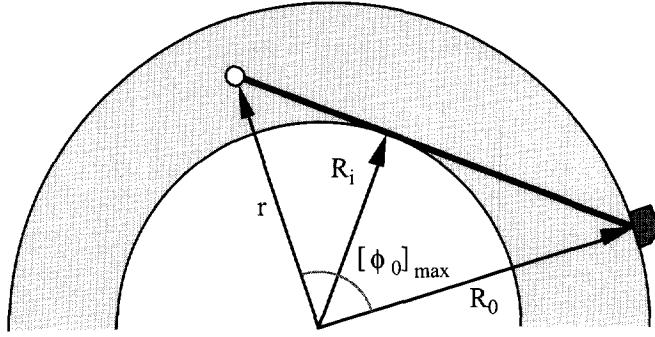
Figure 4.15: *The cylindrical pipe geometry used for the determination of feasible wave paths.*

image point indicated by $R_i \leq r \leq R_o$ is defined by:

$$[\phi_0]_{max} = \arccos\left(\frac{R_i}{R_o}\right) + \arccos\left(\frac{R_i}{r}\right) . \tag{4.15}$$

For indirect wave paths reflecting only once at the outer pipe surface, once at the inner *and* outer surface, or once at the outer and twice at the inner surface (these wave paths coincide in this case), the maximum value of ϕ_0 for an image point indicated by $R_i \leq r \leq R_o$ is defined as:

$$[\phi_{0}]_{max} = 3\arccos\left(\frac{R_i}{R_o}\right) + \arccos\left(\frac{R_i}{r}\right) . \tag{4.16}$$

For other wave paths similar expressions can be derived.

In this thesis the different possible wave paths will be indicated as *(k,l)*, as stated in section 4.2. In the case of cylindrical pipe geometries the wave path (1,0) actually implies one reflection of the insonifying wave field at the inner *or* outer pipe surface before reaching the inhomogeneity. Here it will be defined that the first reflection of an insonifying wave field will be assumed to take place at the inner pipe surface (back wall). Furthermore, for a sequence of reflections at the pipe's boundaries (like for the (0,3) wave path), the waves are assumed to reflect *alternately* at the inner and outer pipe surfaces.

Moreover, it has to be kept in mind that due to the transducer directivity certain image points will hardly be 'seen'[4] by the transducers, although direct or indirect wave paths to those image points are geometrically feasible.

---

4   Because of the 'sonic' nature of the problem it actually seems more appropriate to use 'heard' instead of 'seen'.

Modelled Experiments

5.1 Introduction

The transducers, which have been applied for the inspection of steel components in this thesis, do generate and record only one single wave type (mode) and possess a distinct directivity pattern. Because of these practical constraints, a relatively simple inversion scheme can be applied for imaging B-scan data. In case it would be possible to generate and record all wave types, the recorded ultrasonic data would contain more information on the inhomogeneity, but would also become very complicated and consequently difficult to invert. With modelled experiments it will be demonstrated in this chapter that some intrinsic filtering processes, which take place when applying angled shear wave transducers in practice, make ultrasonic imaging with a simplified inversion procedure like Multi-SAFT feasible.

To illustrate the wave phenomena which are likely to occur in practical inspection situations, the 2-D propagation of elastic and acoustic wave fields in a flat steel plate containing a cylindrical air-filled cavity is computed. With the aid of modelled experiments the effects of bounded beams, shear wave reflection and aperture limitation are described. The numerical method used for modelling the experiments described in this chapter is the finite difference modelling scheme (Rietveld, 1988). Finite difference methods were first introduced by Euler (1768) for one-dimensional problems and extended to two dimensions by Runge (1908). They have been in use for some time to solve elastic wave problems (Alterman, 1968), but it took until about 1973 before finite difference methods were applied to nondestructive testing problems by Harumi et al. (1973). For a detailed description of the finite difference scheme one is referred to the literature (Virieux, 1986).

The model which is used for the 2-D modelled experiments in this chapter is a flat steel plate of 40 mm thickness containing at its center a cylindrical air-filled cavity of 10 mm diameter (see figure 5.1). For the recorded data and the *snapshots*, displaying the wave phenomena in a plane cross-section of the medium at fixed instants of time, the z-component of the particle velocity (v_z-component) has been used. This component mainly contributes to the ultrasonic energy measured
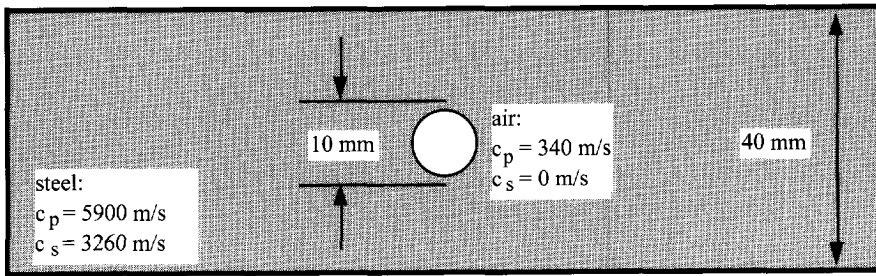
Figure 5.1: *The basic model as has been used throughout this chapter.*

at the inspection surface by *real* angled shear wave transducers. The applied ultrasonic source pulse is shown in figure 5.2, featuring a center frequency of 0.7 MHz, which is good enough for demonstrating the important wave phenomena. In case a center frequency of 4 MHz (as in real experiments) would have been chosen, the internal computer memory needed for the modelling scheme would have become very large and the processing time consequently unacceptably long, because of the stability criteria to be satisfied.

5.2 Single-Mode, Bounded-Beam Transducers

5.2.1 Stress-free boundaries

The first modelling experiment will illustrate the effects of elastic wave field scattering inside a bounded medium. The boundaries of the model of figure 5.1 will therefore be defined as *stress-*
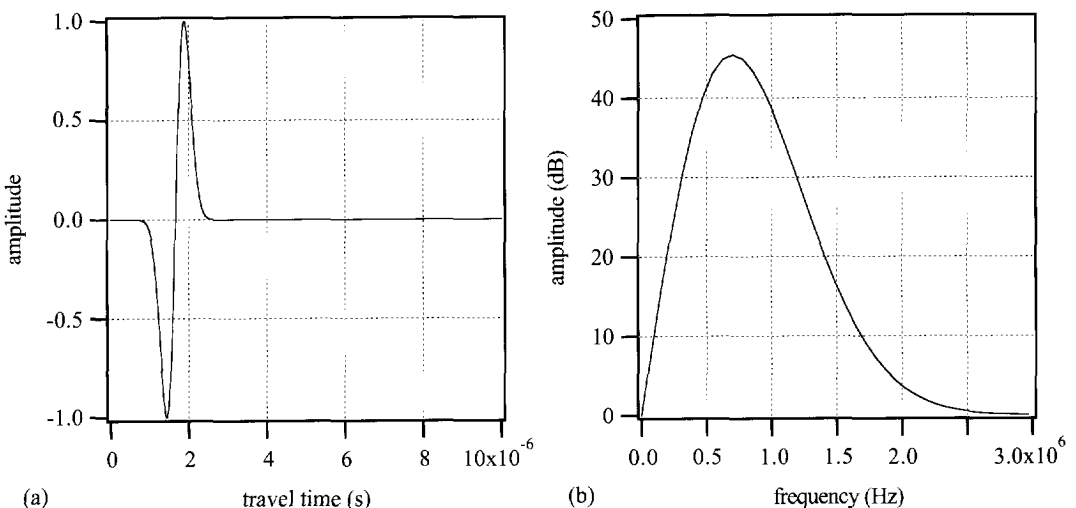
Figure 5.2: *The applied source wavelet and its temporal frequency spectrum.*
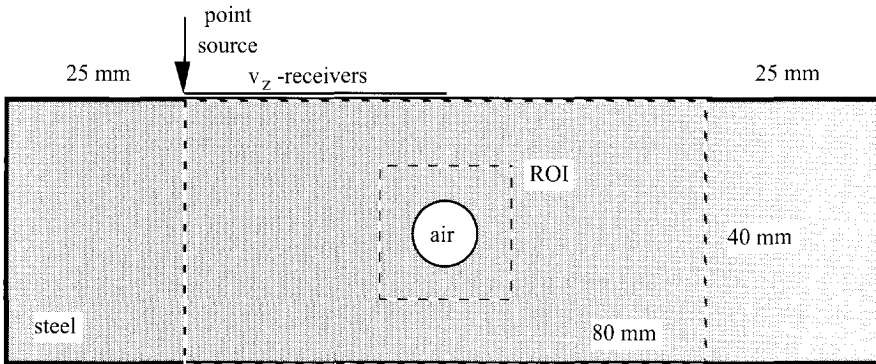
Figure 5.3: *The basic model of figure 5.1 with the position and dimension of the inspection aperture, the 40 mm by 80 mm region which is covered by the snapshots and the imaged ROI.*

free for all sides. A point source is applied generating compressional, shear and Rayleigh waves and it is positioned at the inspection surface 40 mm left of the center of the cavity (as shown in figure 5.3). In figure 5.4 a number of snapshots, taken 10, 15, 20 and 25 μs after triggering the source, are shown. As can be seen from the snapshots of figure 5.4, the bounded geometry of this elastic medium results in an enormous amount of responses to be recorded at the inspection surface in case a point source is applied. Point receivers are positioned at the inspection surface along the 40 mm between the source and the center of the cavity (see figure 5.3) and the recorded (v_z-component) data is shown in figure 5.5, featuring mainly the Rayleigh wave responses and the reflections from the back wall.

The limited receiver aperture, as shown in figure 5.3, corresponds to the practical situation of *single-sided in-service inspection*, i.e. an inhomogeneity can only be inspected ultrasonically from one side, along one of the two surfaces. Using the recorded data of figure 5.5, the direct (0,0) wave paths (assuming no reflection at the object boundaries) have been employed for imaging by Multi-SAFT. The imaging result is shown in figure 5.6a and looks very poor, as could be expected. The true indication of the cavity cannot be recognized because of the numerous false indications which are present in the image.

The main reason for the poor image quality is the presence of the strong source wave field (containing Rayleigh waves) in the recorded data. When this source wave field is eliminated from the recorded data by careful filtering, applying Multi-SAFT for the direct (0,0) wave path will result in the image shown in figure 5.6b. The true indication, resulting from focusing the real (0,0) responses, is marked in the image. The presence of several spurious indications in the image, originating from responses of other wave types and wave paths, makes characterization of the cavity clearly impossible. In case the images of several experiments would be combined, the image quality would certainly improve. Of course, the imaging result for this experiment is poor,
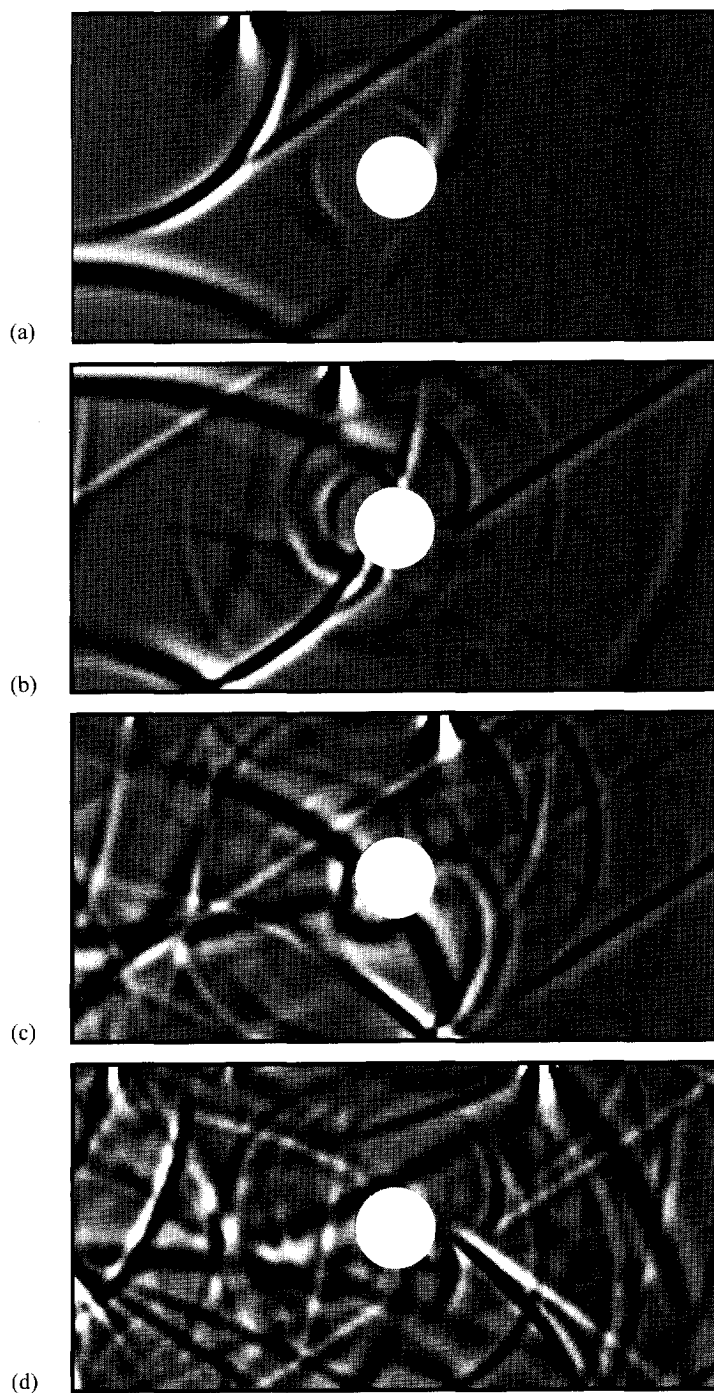
Figure 5.4: *The snapshots for the elastic model with stress-free boundaries at 10 μs (a), 15 μs (b), 20 μs (c) and 25 μs (d) after triggering the source.*
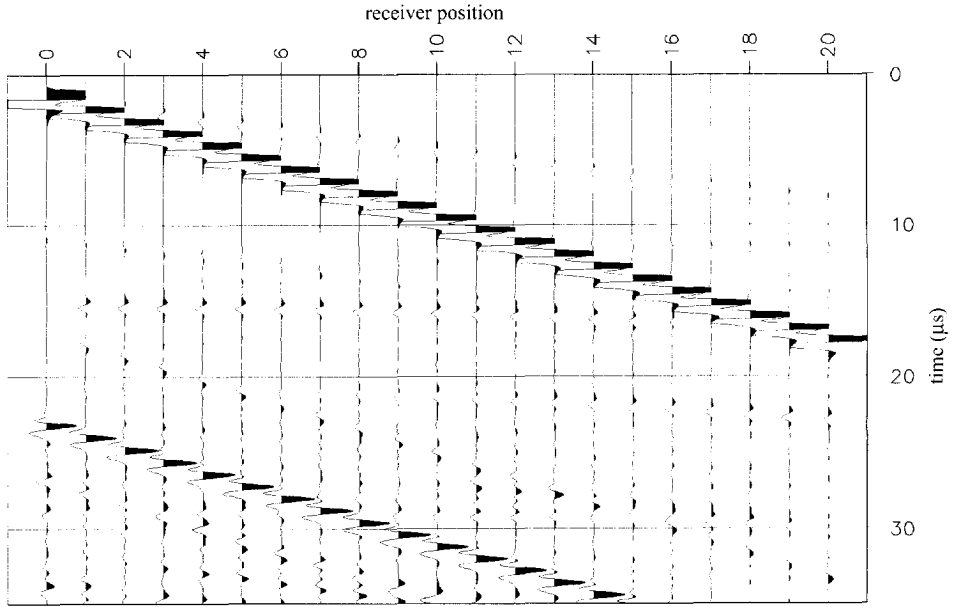
Figure 5.5: *The modelled B-scan data for the elastic model with stress-free boundaries (20 dB clipped).*

because Multi-SAFT has not been designed to invert full-elastic data. It will be shown in the next section that an unambiguous image can be obtained by applying Multi-SAFT on elastic data recorded by single-mode bounded-beam receivers.
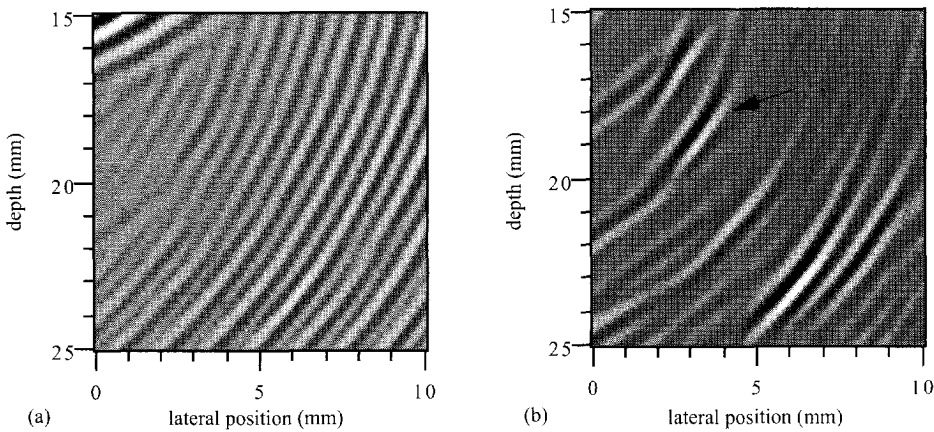
Figure 5.6: *The (0,0)-images of the cylindrical cavity with (a) and without (b) the presence of the direct source wave field in the B-scan data of the elastic model with stress-free boundaries; the imaged ROI is shown in figure 5.3; the correct indication is marked in the right image.*

77

(a)

(b)

(c)

(d)
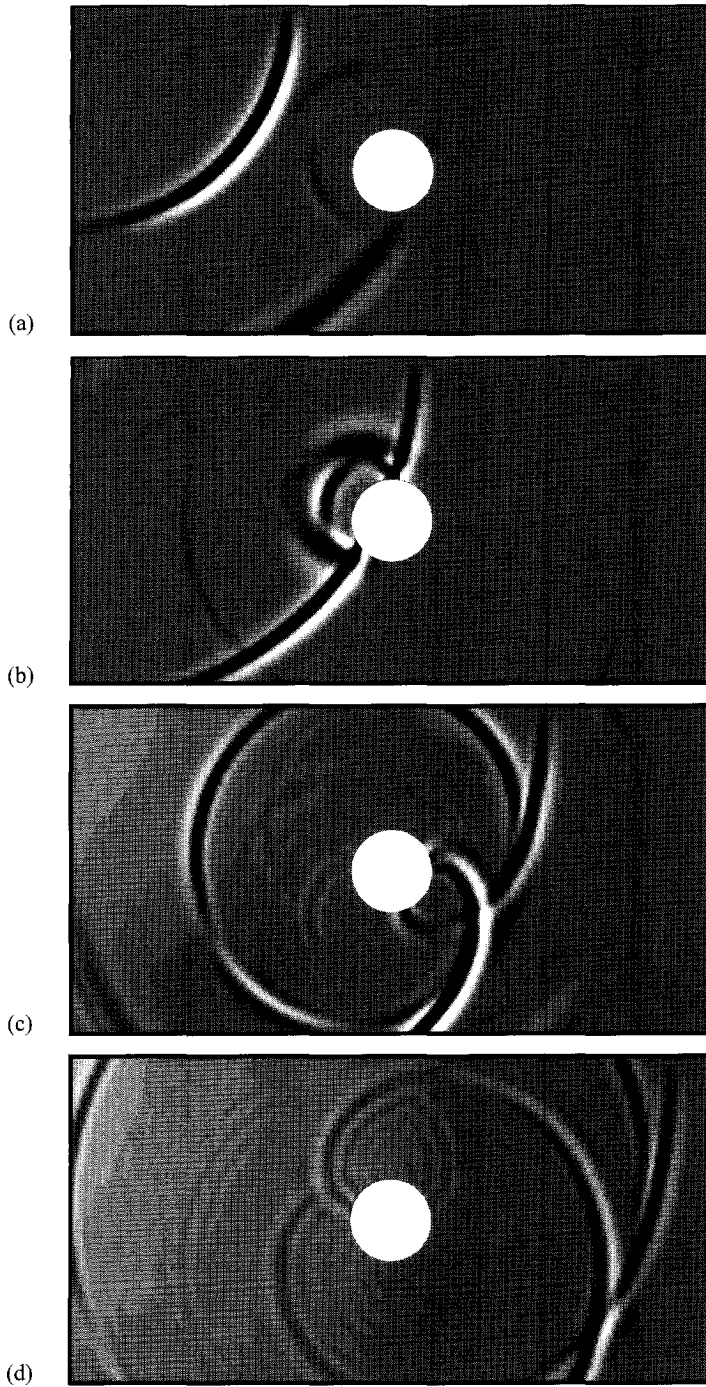
Figure 5.7: *The snapshots for the elastic model with absorbing boundaries at 10 μs (a), 15 μs (b), 20 μs (c) and 25 μs (d) after triggering the source.*

5.2.2 Absorbing boundaries

The angled shear wave transducers, as applied in practice, are so-called *single-mode, bounded-beam transducers*. They will neither record the direct source wave field, nor the strong reflections from the back wall. Furthermore, only one wave type will be generated and recorded. Therefore, the recorded wave field will be much less complex than the full-elastic one shown in figure 5.5 and will lead to better imaging results with Multi-SAFT. As bounded beams could not be modelled at the time this experiment was performed, the effect has been simulated by defining so-called *absorbing boundaries* (Randall, 1988) for all sides of the model. An insonifying shear wave field has been applied in this virtually infinite medium. The snapshots for this experiment, taken at the same points in time as those in the previous section, are shown in figure 5.7. The interaction of the source (shear) wave field with the cavity is now much better recognized, although the recorded data still contain numerous responses (figure 5.8).

When imaging the recorded data for the (0,0) wave path, the result clearly shows a small part of the surface of the cavity (figure 5.9). Most spurious indications have been eliminated due to the fact, that only one wave type has been employed and that the source may be regarded strongly directive (no other wave paths present). The imaging results of this section demonstrate that the application of angled shear wave transducers in practice, which introduces certain intrinsic filtering effects (single mode, bounded beams), justifies most of the assumptions made in chapter

Figure 5.8: *The modelled B-scan data for the elastic model with absorbing boundaries; the direct source wave field has been removed.*
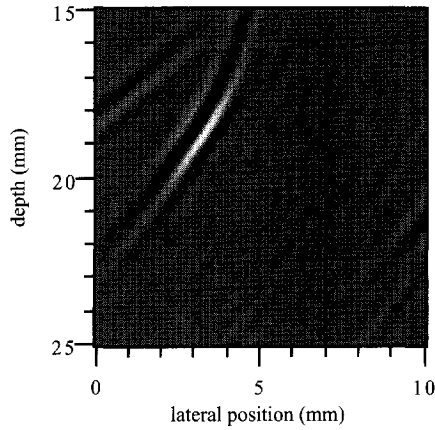
Figure 5.9: *The (0,0)-image of the cylindrical cavity without the presence of the direct source wave field in the B-scan data of the elastic model with absorbing boundaries; the imaged ROI is shown in figure 5.3.*

4. Therefore, it is possible to apply a simplified inversion scheme, such as Multi-SAFT, on ultrasonic B-scan data recorded from elastic media. The image of figure 5.9 does not show the entire cavity due to the use of a limited inspection aperture. The effects of the limitation of the inspection aperture are described in the next section.

5.3   Aperture Limitation

Although the location of the inhomogeneity may be estimated from the image of figure 5.9, its size and shape still cannot be determined. This is principally due to the limitation of the source and receiver aperture. At the end of this section it will be demonstrated, that a fairly good image of the cavity may be obtained when extending the inspection aperture virtually by employing indirect wave paths conform the Multi-SAFT principle. But first the effects of aperture limitation will be made explicitly clear by restricting little by little the data recorded for different source and receiver apertures, starting off with a closed inspection aperture surrounding the cavity entirely.

5.3.1   Conventional SAFT imaging

It has already been mentioned that the limitation of the inspection aperture in practice is the main reason for getting poor imaging results in ultrasonic NDI. In the first section of this chapter, the effects of the limited receiver aperture have been shown quite convincingly. There, only one single source position was applied (*single-shot experiment*) and only the direct (0,0) responses were employed (*conventional SAFT imaging*). For the modelled experiments in this section only shear waves will be generated and detected, and no coupling between elastic wave types is

assumed. This corresponds to some of the assumptions made for the Multi-SAFT algorithm to be applicable, as discussed in chapter 4.

The conditions described above are achieved for the modelled experiments by applying absorbing boundaries at all sides of the model of figure 5.1 and defining an acoustic medium with a wave velocity equal to the shear wave velocity in steel. For a point source, positioned at the upper left of the model, the snapshots (comparable to those of figures 5.4 and 5.7) are shown in figure 5.10 and the data recorded at the upper left aperture are shown in figure 5.11. Of course, the acoustic nature of the medium results in the absence of phenomena like creeping waves, but these are not essential for the effects of aperture limitation in this section.

To obtain a complete set of data, sources have been applied along a closed inspection aperture (indicated by the dashed lines in figure 5.3) surrounding the cavity entirely and data have been recorded (for each individual source position) along the same closed aperture. The series of recorded data have all been imaged for the direct (0,0) wave path and superimposed on each other, resulting in a single image. This final *tomographic* image (figure 5.12a) displays clearly the scattering geometry of the cavity, apart from the influence of the source wavelet. Of course, such an image obtained by applying a closed inspection aperture as actually prescribed in chapter 2, can generally not be realized in practice due to the geometry of the objects to be inspected (see chapter 3).

In most cases, the left and right sides of the model will not be accessible for source and receiver transducers. When the contributions related to these apertures are eliminated from the final image, the cavity may still be recognized (figure 5.12b). If only one surface is accessible, as is the case for in-service inspection, the aperture will be further reduced and the image will only indicate the top of the cavity (figure 5.12c). In case only a single-sided aperture (in this case left of the cavity) is available, the part of the cavity which is insonified and consequently imaged is reduced even more (figure 5.12d). Finally, when just one single source position is applied (single-shot experiment), as is often the case in practice, the imaged part of the cavity will become so small that it is impossible to be characterized (figure 5.12e).

The images in figure 5.12 clearly illustrate the serious effects of aperture limitation. Apparently, conventional single-shot imaging cannot generally be used for the characterization of inhomogeneities in practice in case the inspection aperture is limited to only a single side, with respect to the lateral position of the inhomogeneity, and to one surface (single-sided in-service inspection). In the next section it is shown that responses of other wave paths do indeed contribute positively to the image quality, as has been asserted in chapter 4, and may improve the interpretability.

(a)

(b)

(c)

(d)
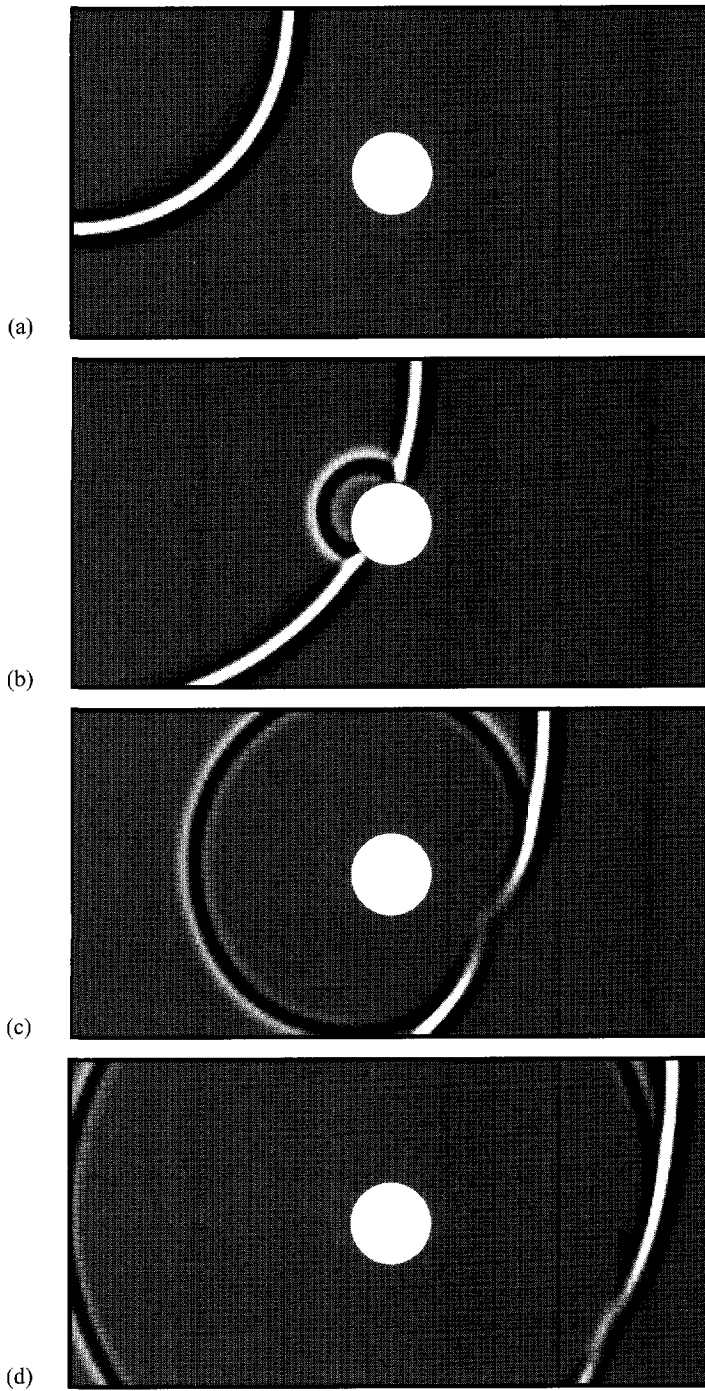
Figure 5.10: *The snapshots for the acoustic model with absorbing boundaries at 10 μs (a), 15 μs (b), 20 μs (c) and 25 μs (d) after triggering the source.*
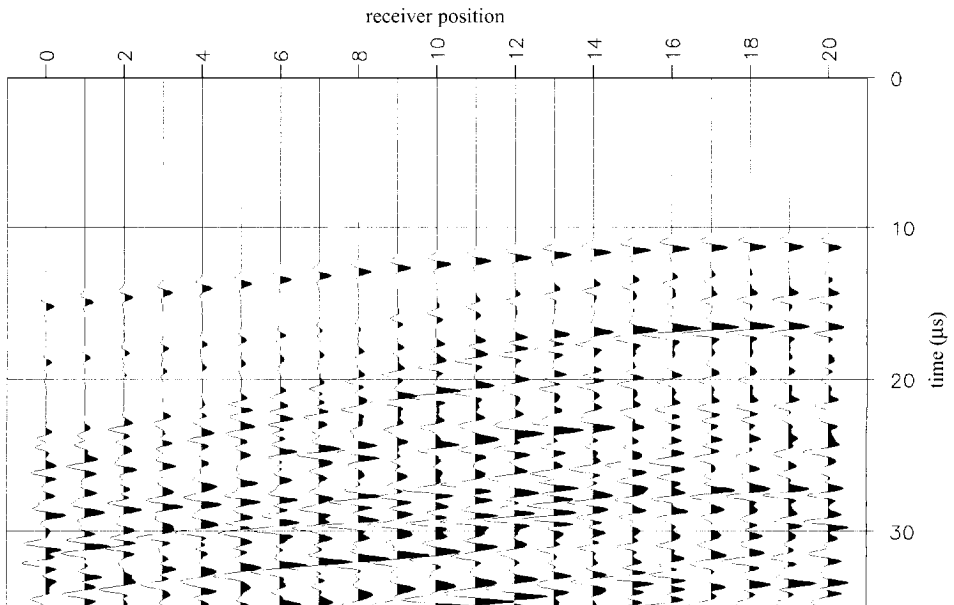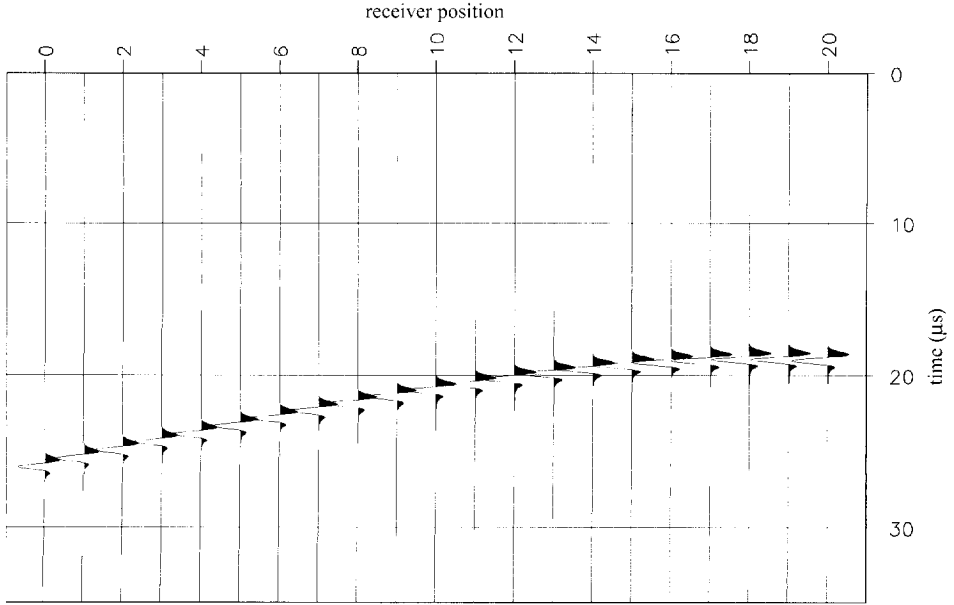
Figure 5.11: *The modelled B-scan data for the acoustic model with absorbing boundaries; the direct source wave field has been removed.*

5.3.2 Multi-SAFT imaging

In order to extend the inspection aperture virtually for a single-shot experiment, the responses which have been propagating along the indirect wave paths (1,0), (0,1) and (1,1) should also be employed for imaging. Therefore, the top and bottom boundaries of the model shown in figure 5.1 will be defined as stress-free, while the left and right boundaries will be defined as absorbing. Again, an acoustic medium is modelled with a wave velocity equal to the shear wave velocity in steel. A point source generates a wave field insonifying the cavity directly as well as indirectly via the back-wall and both the direct and indirect responses are recorded.

The reflections propagating along the (0,0), (1,0), (0,1) and (1,1) wave paths are marked in the four snapshots, taken at 10, 15, 20 and 25 μs, as shown in figure 5.13. Applying Multi-SAFT to the recorded single-shot data as shown in figure 5.14 for the four different wave paths results into four different images (figure 5.15). The lower spatial resolution of the images from the forward scattering wave paths (1,0) and (0,1) (see chapter 4) becomes apparent from these images. Nevertheless, different parts of the cavity can be imaged in this way. When the amplitudes in the four images of figure 5.15 are normalized between −1 and +1, it possible to combine (superimpose) the images. The *combined Multi-SAFT image*, resulting from superimposing the
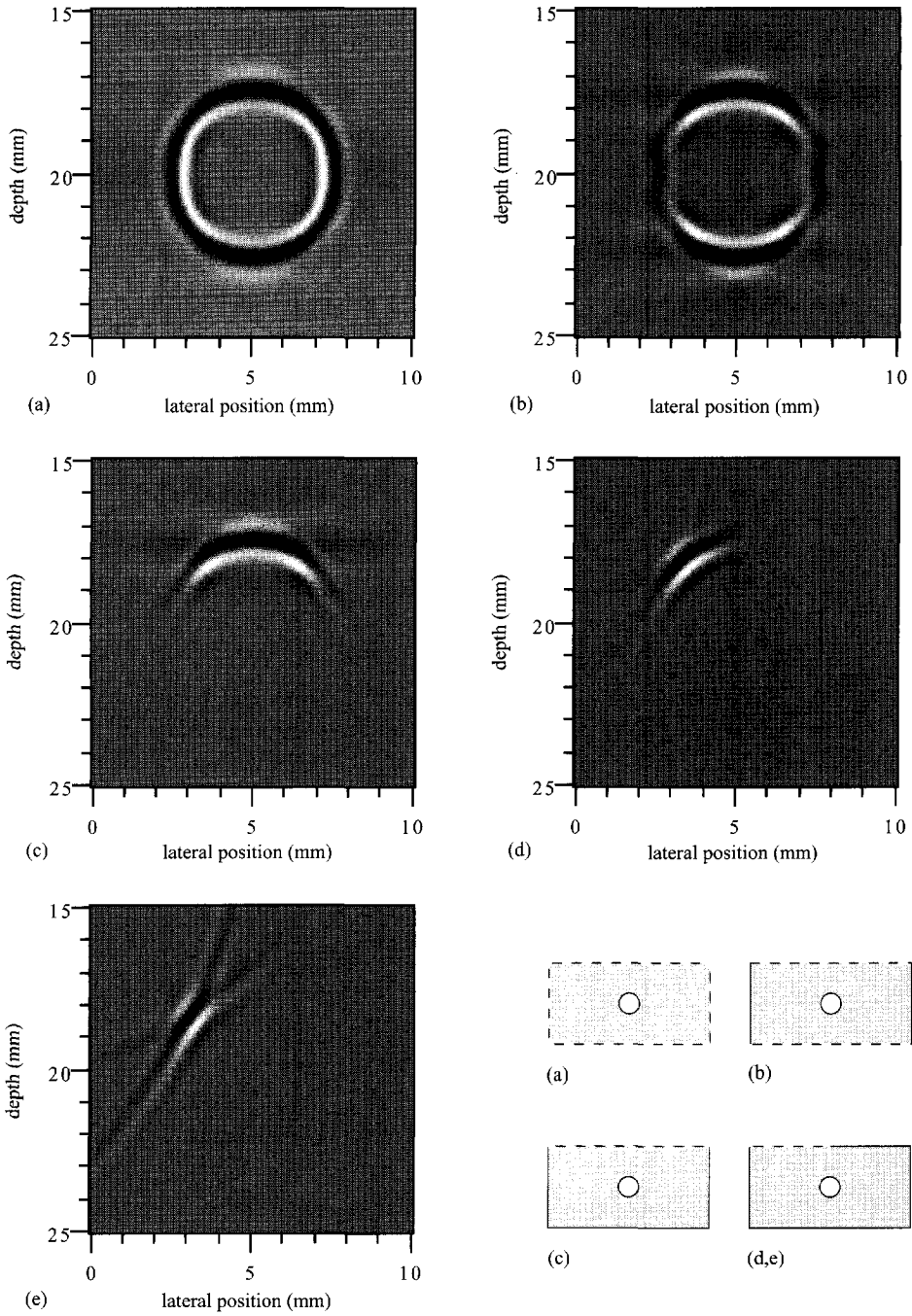
Figure 5.12: *The (0,0)-images of the cylindrical cavity of the acoustic model with absorbing boundaries for different degrees of aperture limitation; the imaged ROI is shown in figure 5.3; the receiver apertures are shown at the lower right; (d) is a multi-shot and (e) a single-shot image.*
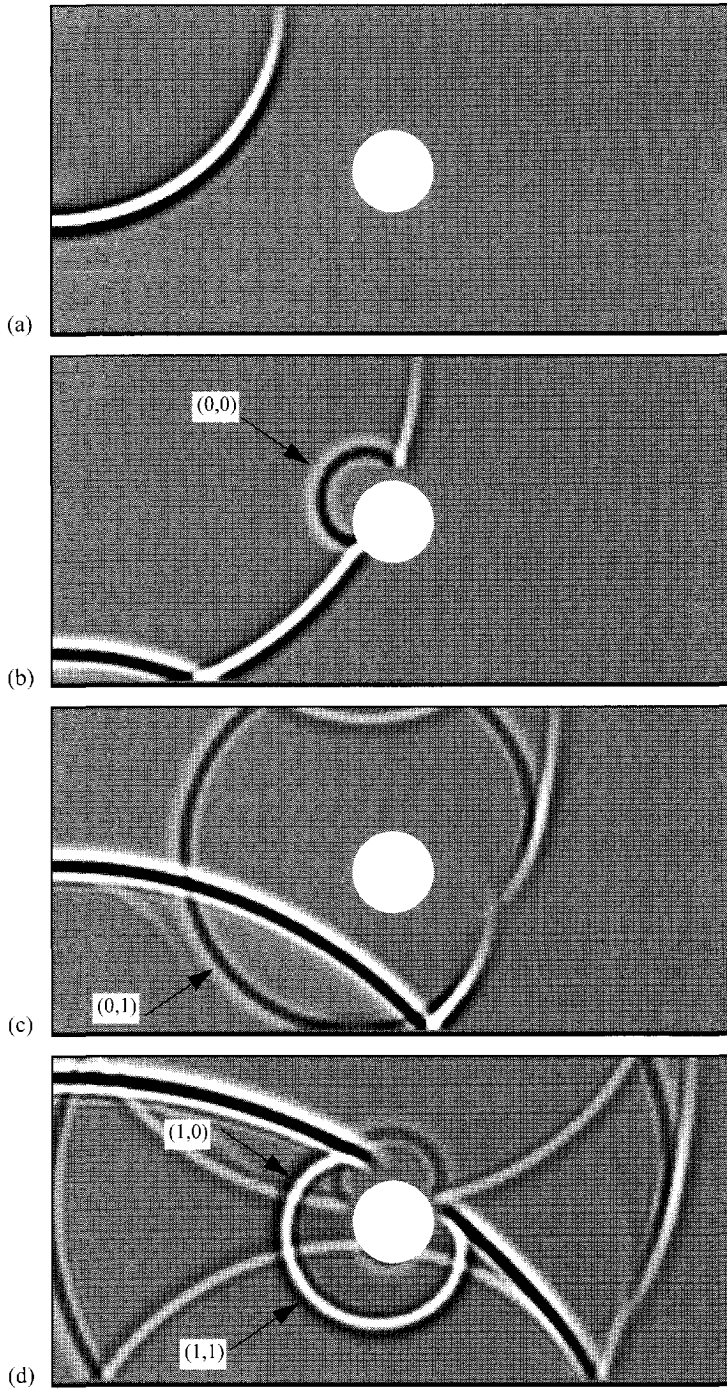
Figure 5.13: *The snapshots for the acoustic model with stress-free top/bottom and absorbing left/right boundaries at 10 μs (a), 15 μs (b), 20 μs (c) and 25 μs (d) after triggering the source.*
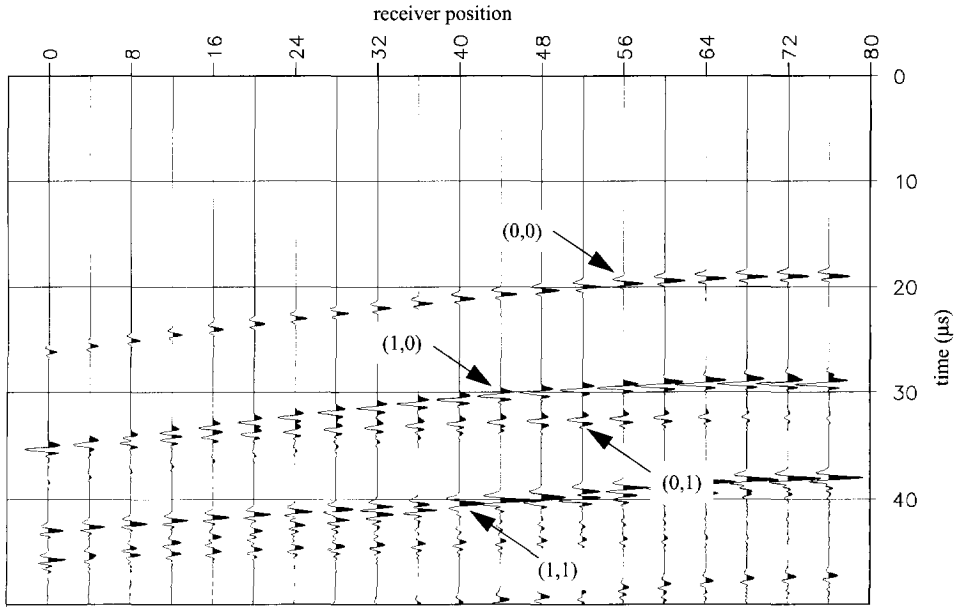
Figure 5.14: *The modelled B-scan data for the acoustic model with stress-free top/bottom and absorbing left/right boundaries; the direct source wave field has been removed; the responses from different wave paths are marked in the image.*

four images of figure 5.15, is shown in figure 5.16a and certainly reveals the presence of a circular cavity more clearly than the single-shot image of figure 5.12e. Of course, spurious indications are still present in the single-shot image (figure 5.16a) and the application of more source positions would surely improve the image quality. In case more source positions should be used (*multi-shot experiment*), the image would look like the one shown in figure 5.16b, which can be compared to the conventionally obtained image of figure 5.12d.

It has to be noticed, that due to the coupling of shear and compressional waves in practice, the real reflecting wave fields to be recorded will differ in amplitude from the ones shown in this section. This, of course, may lead into a slightly different imaging performance. In practice, the directivity of the source transducer is used to aim for only one or two wave paths by locating the source at a specified position with respect to the inhomogeneity. Furthermore, a specific position of the source can sometimes be preferred in order to avoid undesired mode-conversion effects. This all results in an optimization of the data-acquisition configuration (discussed in chapter 6), which leads to combined Multi-SAFT images of better image quality.
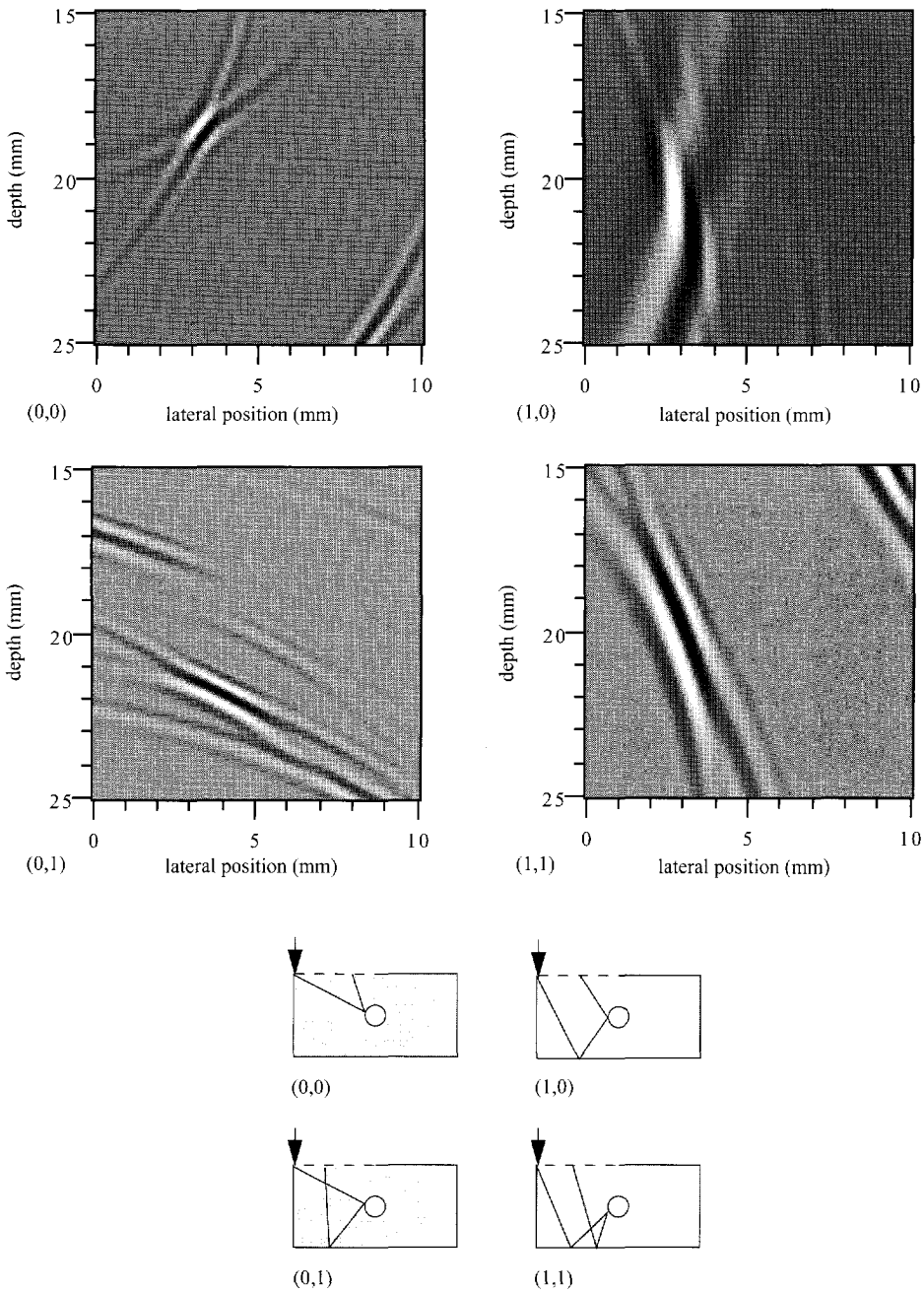
Figure 5.15: *The images of the cylindrical cavity of the acoustic model with stress-free top/bottom and absorbing left/right boundaries for different wave paths; the imaged ROI is shown in figure 5.3; the wave paths are shown at the lower part of this figure, where the arrow indicates the position of the source.*
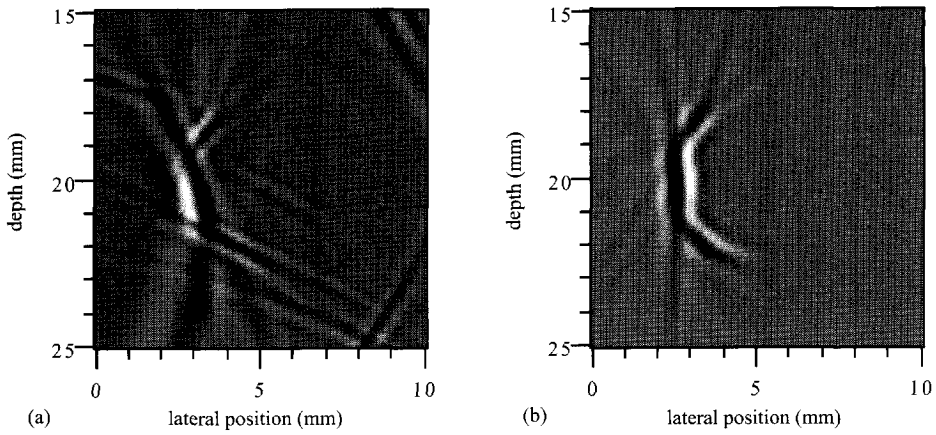
Figure 5.16: *The combined Multi-SAFT images of the cylindrical cavity of the acoustic model with stress-free top/bottom and absorbing left/right boundaries for a single-shot (a) and a multi-shot (b) experiment; the imaged ROI is shown in figure 5.3.*

6

Data-Acquisition Optimization

6.1 Introduction

Any ultrasonic (single-shot) data set recorded along a limited receiver aperture can be imaged, though the resulting image quality may not always be very good. In the previous chapters it has been demonstrated that, due to the source and receiver aperture limitation, the data-acquisition configuration should be optimized in order to obtain ultrasonic data which can be successfully imaged by the Multi-SAFT inversion scheme. A number of optimizations has already been mentioned and will be briefly summarized here.

By applying angled shear wave transducers, the occurrence of too many responses can be prevented and unambiguous combined Multi-SAFT images may be obtained (see chapter 5). When the applied source is strongly directive, it possible to insonify a single inhomogeneity according to a few specific wave paths. The applied receiver, however, should possess a very wide beam in the image plane in order to receive responses from as many directions as possible. Yet, the beam width of the receiver should be narrow perpendicular to the image plane to avoid responses originating from outside the image plane to be recorded.

When the pulse-echo data-acquisition configuration is applied, the source and receiver will be physically housed in one single transducer. This implies that the different directivity characteristics of the source and receiver, required to optimize the data-acquisition as described above, can only be realized when two separate (slightly inclining) transducers are built together to fit into a single housing (so-called *SE-transducer*) (Krautkrämer and Krautkrämer, 1977). Yet, as the source is not located at a fixed position, the insonification of the inhomogeneity cannot remain optimum during scanning. For this reason and because of the poor imaging performance for forward scattering wave fields, the pulse-echo data-acquisition configuration is not found to be particularly fit for Multi-SAFT imaging and the pitch-catch configuration is preferred.

In order to obtain a good image quality, the optimizations described above will generally not suffice in the case of limited apertures. There are still two very important parameters that should

be optimized as well. The first one concerns the position(s) of the source within the available inspection aperture. The influence of the source position(s) within a limited aperture on the image resolution will be discussed in sections 6.2 and 6.3 for a very important type of inhomogeneity: the vertically oriented defect. The second parameter is the reflectivity of the scattering inhomogeneity to be imaged, which will be discussed in section 6.4. Finally, section 6.5 will describe how both diffraction and reflection responses should be employed for good Multi-SAFT imaging results.

6.2 Imaging Limited Aperture Data

6.2.1 Vertically oriented defects

The vertically oriented defect is a planar[1] inhomogeneity which is oriented perpendicularly to the inspection surface and is generally considered dangerous to a construction. In case it reaches the surface of the object it will be called *surface-breaking*, making it even more dangerous. Therefore, it is important that vertically oriented defects are identified and properly characterized. Conventional SAFT has not been very successful in imaging this type of defect (see chapter 3), because of applying the pulse-echo configuration for data-acquisition. It will be shown, that when dealing with limited apertures the pitch-catch configuration will generally be more successful in imaging vertically oriented defects.

In practice, it is very important to be able to discriminate between, for instance, two vertically spaced diffractors and a vertically oriented planar defect. This classical problem is illustrated in figure 6.1. To accomplish this distinction, the spatial resolution in the depth direction (when imaging the responses of the indirect forward scattering wave path), as shown in chapter 3 for the
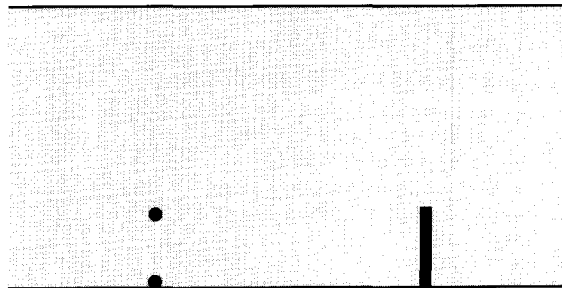
Figure 6.1: *The classical problem of discriminating between two vertically spaced diffractors and a vertically oriented planar defect.*

---

1   Planar defects will be considered to be perfectly smooth in this chapter, although in reality they may be rough as well (see chapter 7).

pulse-echo image, should be improved. In chapter 4 the spatial resolution to be expected has been shown with the aid of k_x-k_z images. Here a different approach will be presented.

When the responses of two vertically spaced diffractors are recorded at the same time along the entire available receiver aperture, i.e. the total travel times are always equal for the two diffractors, the inversion algorithm will surely not be able to image the two diffractors separately. Thus, a condition to b satisfied is that the responses of the two diffractors should be recorded separately in time, at least in a part of the receiver aperture.

6.2.2   Separated indications

The separation of responses in time can be expressed in the difference between the total travel times corresponding to the two diffractors. For two diffractors, spaced vertically by 5 mm, the so-called *travel-time difference* depends on the positions of the source and receiver, the depth of the two diffractors and the thickness of the object. In this section, only plane objects will be considered which do consequently not allow a vertically oriented defect to be insonified at normal incidence. Figure 6.2 shows a graph for the pulse-echo configuration of the travel-time difference of two diffractors (spaced vertically by 5 mm) at different depths as a function of source/receiver position for the indirect forward scattering wave path (1,0). It can be seen, that for all depths the separation between the responses is very small along the available aperture (with respect to a wavelet of 0.5 μs).

Figure 6.3 shows the forward scattering travel-time difference graph for the pitch-catch
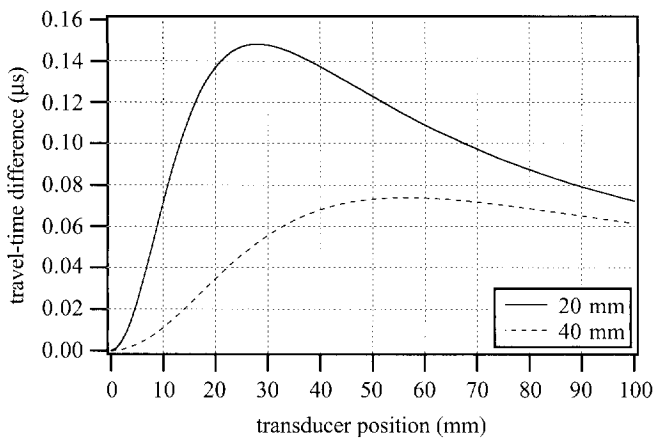
Figure 6.2: *The travel-time difference of two diffractors (spaced vertically by 5 mm) as a function of transducer position for the forward scattering (round-trip) wave path (1,0) in pulse-echo and for two different values of the plate thickness; the configuration is shown in figure 6.1 (c_s=3260 m/s).*
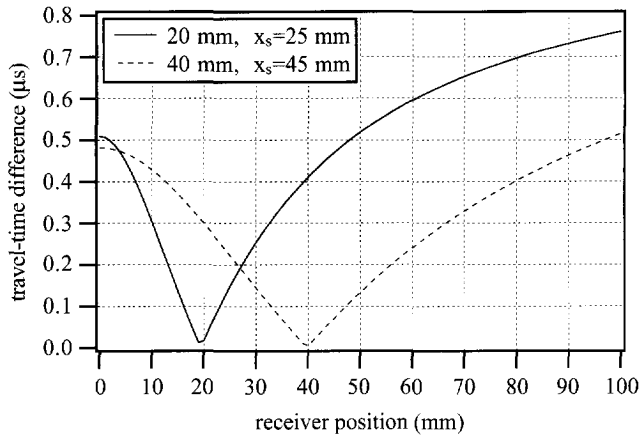
Figure 6.3: *The travel-time difference of two diffractors (spaced vertically by 5 mm) as a function of transducer position for the forward scattering wave path (1,0) in pitch-catch and for two different values of the plate thickness/source position; the configuration is shown in figure 6.1 (c_s=3260 m/s).*

configuration for the same 5 mm vertically spaced diffractors. The source is located at a fixed position and it can be seen, that the separation between the responses is much larger than for the pulse-echo configuration. The thicker the object, however, the smaller the separation, because the range of scattering angles will be reduced for the available inspection aperture. If the separation in time is larger than the length of the applied wavelet, the back-propagated responses can be imaged separately. However, imaging indications *separately* does not necessarily mean imaging *focused* indications. Therefore, a second condition has to be specified.

6.2.3 Focused indications

Focusing (in the x-z plane) will only occur when the spatial bandwidth of the recorded data is large enough in the k_x-direction as well as in the k_z-direction. It can be seen from the images in figure 4.6, that for the indirect forward scattering wave path in pulse-echo, the filled section of the (k_x,k_z) plane is mainly oriented in the k_x-direction. This implies that the spatial resolution will be high in the lateral direction, but low in the depth direction. This is confirmed by the imaging results of figure 3.17. It is very difficult to specify general conditions for good focusing, i.e. specifying the spatial bandwidth in the k_x- and k_z-directions. The extent to which the (k_x,k_z) plane should be filled can only be defined explicitly for certain specific situations.

Thus, the degree of focusing is determined by the range of k-values (spatial bandwidth), i.e. the range of recorded scattering angles. Not only the length of the receiver aperture is therefore important, but also its curvature. In figure 6.4 it is illustrated, that within an inspection aperture of fixed length more scattering information can be recorded when the aperture is curved. This can
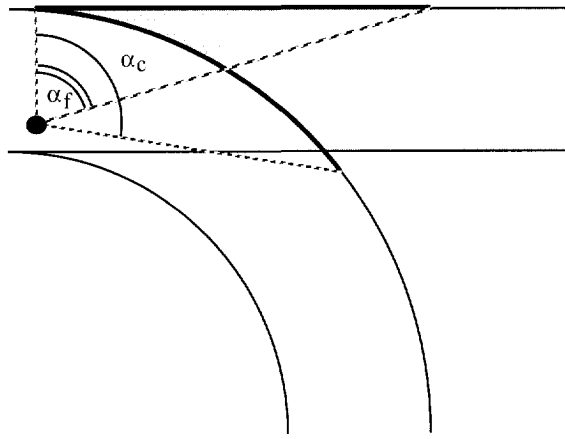
Figure 6.4: *Within an inspection aperture of fixed length (thick line) more scattering information can be recorded when the aperture is curved ($\alpha_c > \alpha_f$).*

also be demonstrated by calculating the actual recorded scattering angle for a diffractor at 15 mm depth as a function of receiver position (figure 6.5). The (1,0) images of two diffractors in 30 mm thick cylindrical pipes of 70 mm and 330 mm outer radius of figure 6.6 clearly illustrate the difference in spatial resolution.

6.2.4 A modelled example

An elastic numerical finite difference experiment has been performed for a flat plate with a vertically oriented slot (see figure 6.7) to demonstrate, that such an inhomogeneity can be imaged quite accurately in case the data-acquisition configuration has been properly optimized. The
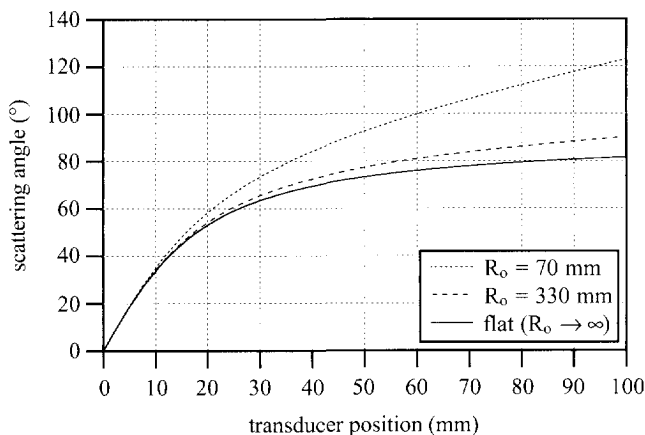
Figure 6.5: *The scattering angle from a point diffractor at 15 mm depth as a function of receiver transducer position for different values of the outer pipe radius.*

93
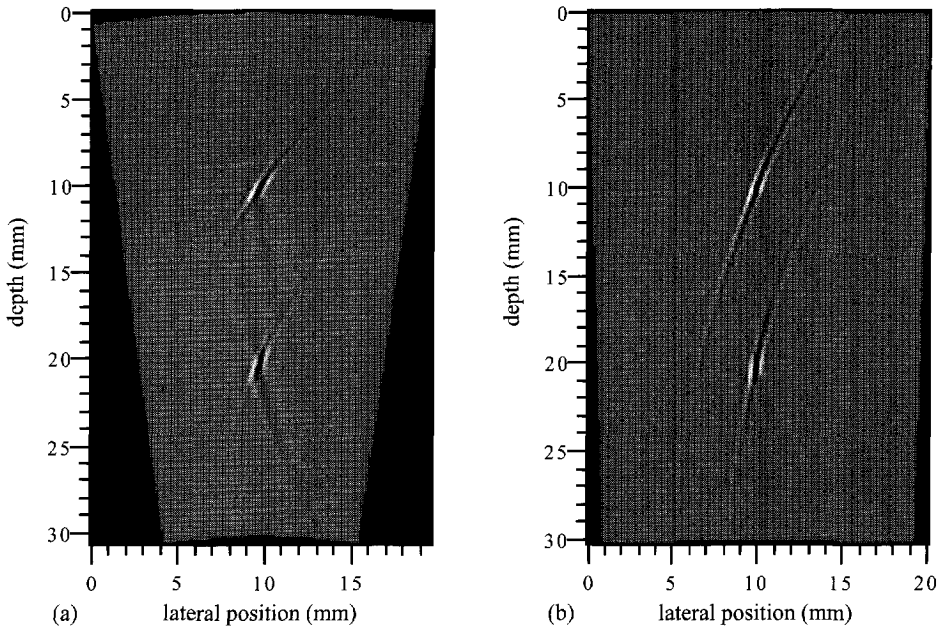
Figure 6.6: *The (1,0) images of two point diffractors in cylindrical pipes of 30 mm thickness and of 70 mm (a) and 330 mm (b) outer radius; the source has been located at 40 mm from the lateral position of the diffractors and the length of the receiver aperture has been 50 mm.*

thickness of the modelled steel plate is 40 mm and the height of the slot is 10 mm. A fixed source has been applied at x=40 mm and the receiver aperture runs from x=0 to x=80 mm, all with respect to the lateral position of the slot. The medium has been defined elastic with compressional and a shear wave velocities of steel (c_p=5900 m/s, c_s=3260 m/s). The top and bottom of the plate have been defined stress-free, while the left and right sides of the model have been made absorbing. The snapshots are shown in figure 6.8. The direct source wave field has been removed
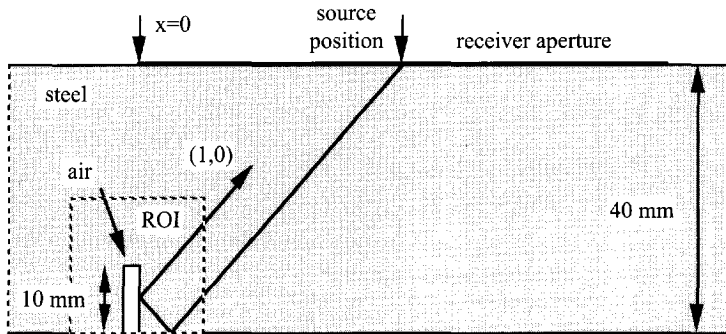
Figure 6.7: *The finite-difference model of the 10 mm high vertically oriented slot.*
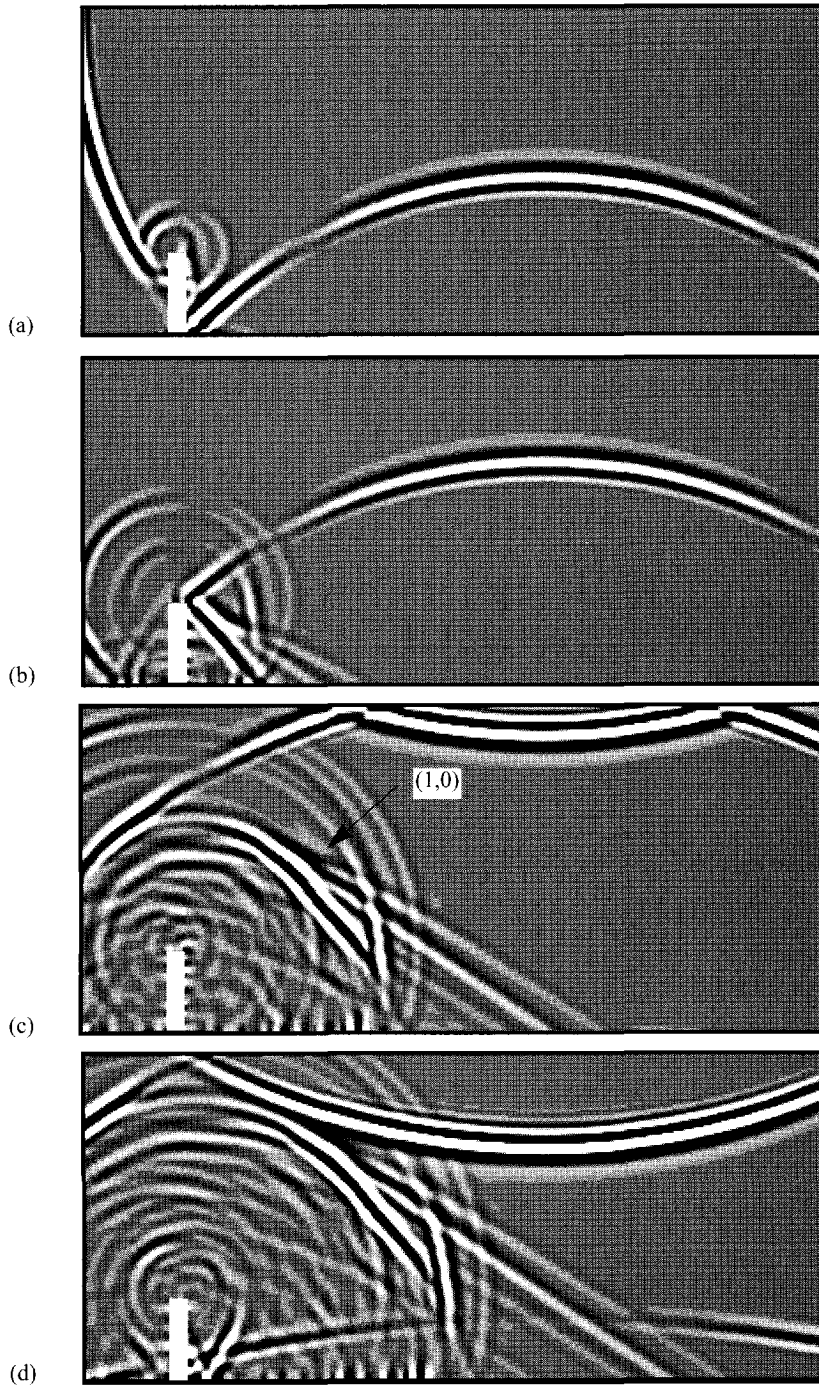
Figure 6.8: *The shear-wave snapshots, taken at 20, 22.5, 25 and 27.5 μs after triggering the source, of the elastic finite-difference modelling experiment involving a 10 mm high vertically oriented slot (see figure 6.7).*
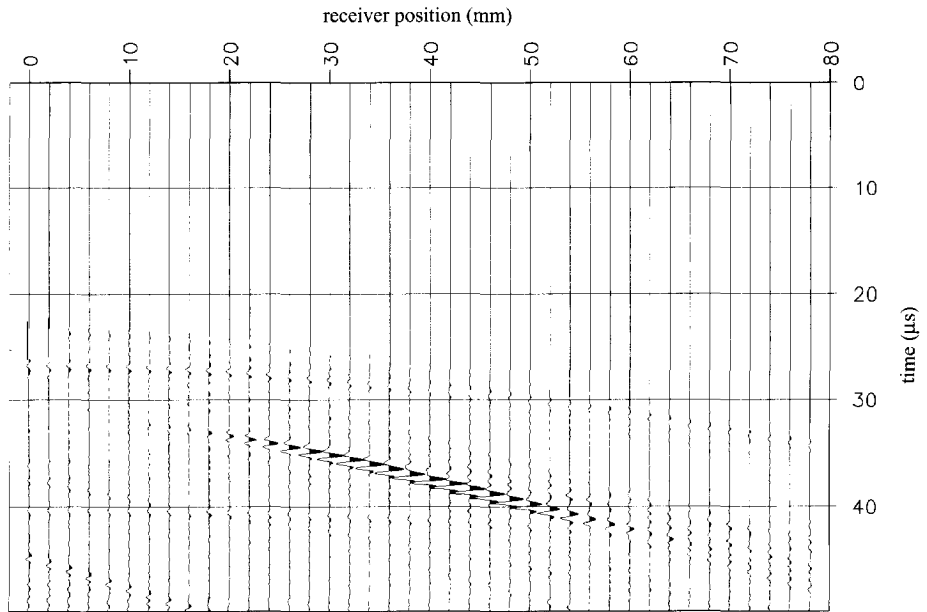
Figure 6.9: *The finite-difference modelled data of the 10 mm high vertically oriented slot (see figure 6.7).*

from the recorded data, which are shown in figure 6.9. The (1,0) wave path is used for imaging with Multi-SAFT and the resulting image is shown in figure 6.10, clearly indicating the 10 mm vertically oriented slot.

The results presented here make it fairly clear, that pitch-catch data-acquisition should be used in favour of the conventional pulse-echo configuration. Applying a fixed source and a scanning receiver will generally result in a sufficiently high spatial resolution for direct back scattering, as well as for indirect forward scattering wave paths. This does not hold only for vertically oriented defects, but for all arbitrarily orientated planar defects.

6.3 The Lateral Split Angle Configuration

6.3.1 Flat plate geometry

In the previous section it has been established that pitch-catch data-acquisition should be applied for Multi-SAFT imaging. This means, that the source should actually be located at a fixed position somewhere within the receiver aperture. Such a situation can be modelled successfully, though in practice it appears to be rather impracticable. The simple reason for this is, that the source transducer will obstruct the receiver transducer in its scanning along the inspection
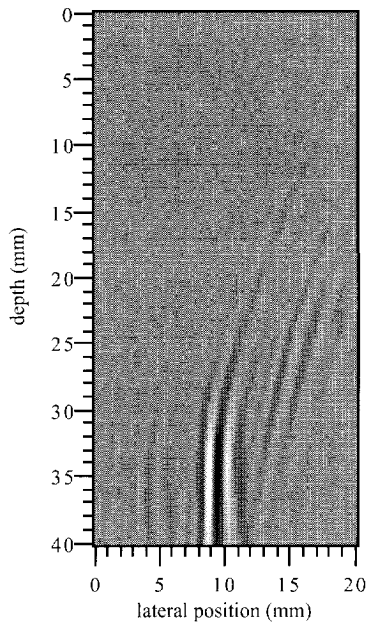
Figure 6.10: *The (1,0) image from the finite-difference modelled data of the 10 mm high vertically oriented slot.*

aperture. In this way a large part of the already limited aperture remains inaccessible for scanning and collecting ultrasonic data. In seismics, these missing data are known as *missing near offsets* and usually consist of a small percentage of the total amount of data being collected. In NDI, however, the *extra* aperture limitation due to the presence of the source transducer within the inspection aperture is quite unacceptable. To give an idea of dimensions, figure 6.11 shows a typical NDI situation with real transducers in proportionally correct dimensions.
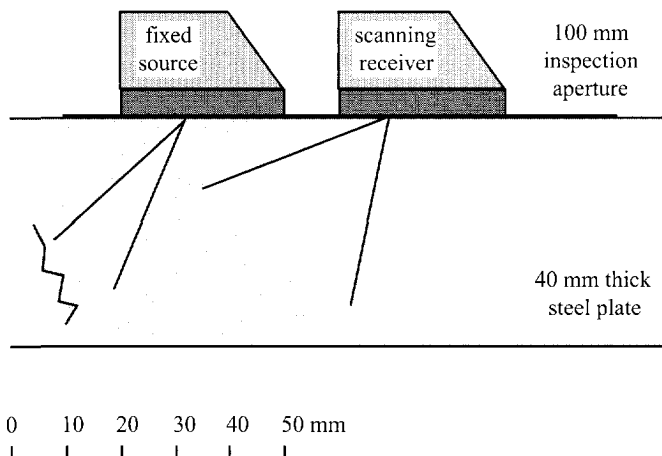
Figure 6.11: *A typical NDI situation with the transducers and object in proportionally correct dimensions.*
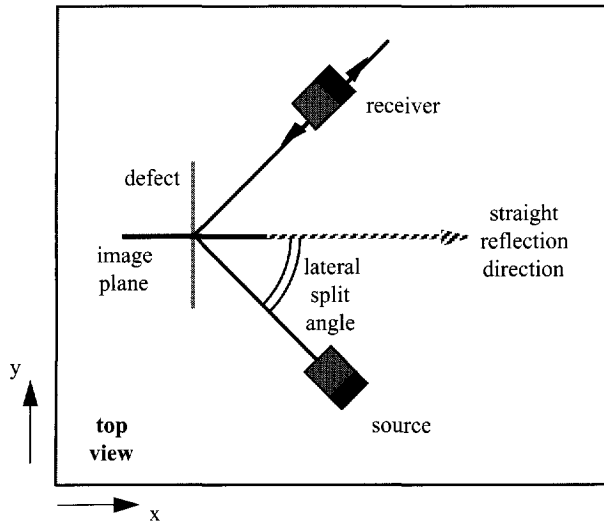
Figure 6.12: *The lateral split angle configuration; the defect is extending in the y-direction, which makes the straight reflection direction equal to the x-direction.*

To solve this problem the source transducer should be moved out of the scanning aperture. This can be accomplished by letting the source insonify the inhomogeneity from another angle. Such a configuration is shown in figure 6.12, where it is important to determine the *straight geometrical reflection direction* of the inhomogeneity with pulse-echo. This is the direction along the inspection plane in which a defect will reflect most of the incident energy back to the source (direction of the normal on the defect plane, projected on the inspection plane). The source and receiver transducers are both positioned under a same angle with respect to the straight geometrical reflection direction. This angle will be called the *lateral split angle* and this type of pitch-catch data-acquisition will be called the *lateral split angle configuration*. In this way, the receiver transducer can utilize the entire available inspection aperture and the source transducer can still be positioned such that the inhomogeneity is optimally insonified. It appears that the lateral split angle may be chosen arbitrarily, but it will be shown in section 6.5 that a proper choice of this angle may lead to a better Multi-SAFT imaging result.

The image plane is defined as the x-z plane in the straight geometrical reflection direction. When applying the lateral split angle configuration, the inversion process becomes pseudo three-dimensional and the y-coordinates have to be accounted for. The equations for the computation of the wave path length, as presented in chapter 4, do already contain the y-coordinates of both source and receiver transducers (equation (4.14)). These y-coordinates correspond to the distance from the image plane (defined as being y=0).

axial cross-section   radial cross-section
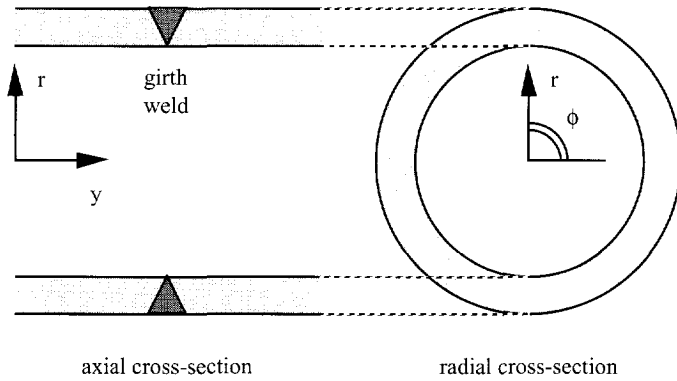
Figure 6.13: *When inspecting girth welds in cylindrical pipes, the image plane will generally be defined as the r-y plane.*

6.3.2 Cylindrical pipe geometry

For the cylindrical pipe geometry the image plane can have every possible direction with respect to the pipe's axis. In the commonly occurring situation of inspecting girth welds, the image plane will generally be defined as the r-y plane (see figure 6.13). The computation of indirect wave paths for cylindrical pipes will be always more time-consuming than for flat plates. For imaging in the r-y plane (constant ϕ, see figure 6.14 situation **A**), the indirect wave paths have only to be computed in a circular cross-section *for every depth level* (radius r) in the image plane, for every transducer position. This keeps travel-time computation reasonably fast and perfectly suitable for practical application. In the general situation, the indirect wave paths have to be computed *for every point* (radius r and angle ϕ) in the image plane, for every transducer position, because the angle ϕ between the transducer position and the image point is not a constant. This may be

axial cross-section   radial cross-section
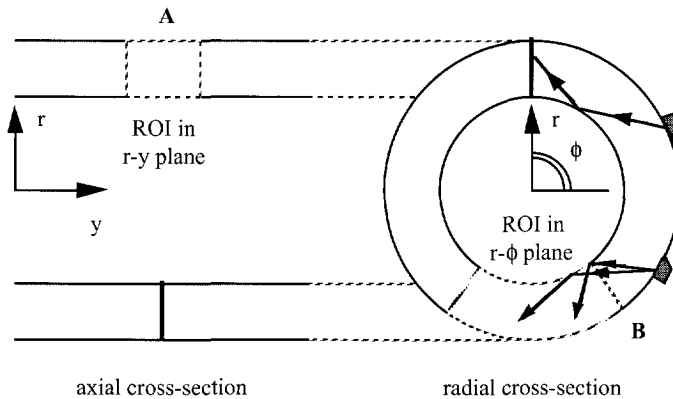
Figure 6.14: *Imaged ROI's oriented in the r-y plane (situation **A**) and in the r-ϕ plane (situation **B**).*
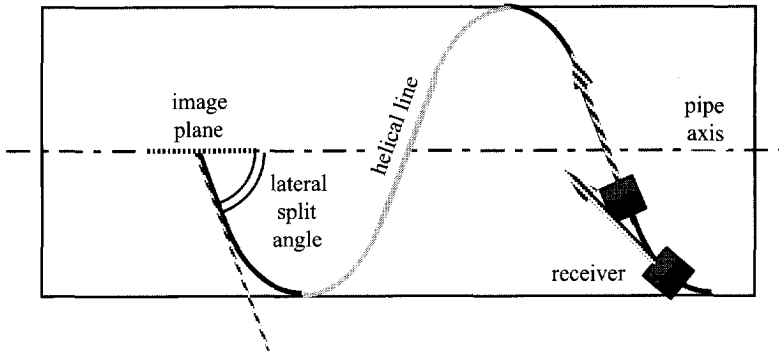
Figure 6.15: *Scanning along a helical line for the lateral split angle configuration on a cylindrical pipe surface.*

observed in the situation of imaging a part of the radial cross-section (r-ϕ plane), as shown in figure 6.14 situation **B**. Consequently, the computation of indirect wave paths will take even more processing time.

The scanning direction will be defined by the lateral split angle, just as for the flat plate geometry. The scanning aperture, however, will not be linear any more due to the cylindrical pipe geometry, except for scanning along the axial direction of the pipe. Scanning perpendicular to the axis of the pipe results in a circular aperture, but scanning in another direction will result into a *helical line* (see figure 6.15). During a helical-line scan the transducer remains at a constant (lateral split) angle with the pipe's axis (y-axis). This means, that a constant scan step of the transducer along the helical line implies a constant step in both the radial and axial directions. This keeps the algorithm for the computation of path lengths in cylindrical pipes very efficient.

By scanning the receiver transducer along a helical line, the receiver-beam direction will change with respect to the image plane. This effect is illustrated in figure 6.15. However, it should be realized that the scattered wave field will propagate in a helical direction around the cylindrical pipe, reflecting at inner and outer surfaces. Therefore, the receiver transducer will be able to record (indirectly) scattering responses propagating from the ROI along its entire helical scanning aperture, although the receiver transducer seems to be improperly directed.

6.4 Shear Wave Reflectivity

In chapter 2 it has been shown, that the energy to be imaged is proportional to the reflectivity of the scattering surface. Furthermore, in chapter 3 it has been stated, that defects in steel may generally be regarded as stress-free surfaces and in chapter 4 the use of angled shear wave transducers has been established. Thus, Multi-SAFT is considered to image shear wave

reflectivity at stress-free boundaries. Because compressional and shear waves are coupled according to the elastic wave theory (see chapter 2), the insonifying shear wave may be partly converted into a compressional wave upon reflection. These scattered compressional waves cannot be detected by the applied shear wave receivers and will therefore not contribute to the image.

To be able to anticipate on certain elastic reflectivity effects (such as mode-conversion), angle dependent shear wave reflectivity should be studied. If the orientation of an inhomogeneity is approximately known, both the source position and the lateral split angle should be chosen such that the reflectivity information is optimally recorded. For experiments with the lateral split angle data-acquisition configuration, as proposed in the previous section, both the source and the receiver are positioned symmetrically with regard to the straight geometrical reflection direction. Consequently, this three-dimensional set-up requires a three-dimensional evaluation of shear wave reflectivity. For the derivation of this shear wave reflectivity, a number of assumptions has been made:

1. considering only SV-wave source and receiver transducers;
2. regarding infinitely large smooth plane reflecting surfaces;
3. assuming defects in steel to have stress-free surfaces;
4. assuming incident plane waves.

6.4.1 Shear wave reflectivity at stress-free surfaces

In this section, the situation of a plane incident shear wave reflecting at a plane stress-free surface of figure 6.16 is considered. Such an incident shear wave may be decomposed into two orthogonally polarized shear waves (see chapter 2). One causes particle displacements in the y-direction, the other one in the x-z plane, with both displacements oriented perpendicularly to the
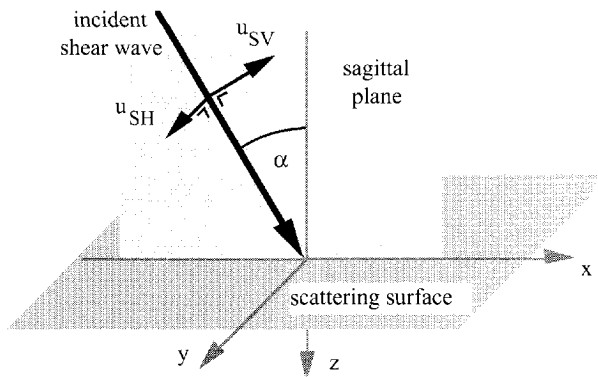
Figure 6.16: *The configuration of an incident shear wave on a plane stress-free surface.*

propagation direction. According to the definitions proposed in chapter 2, the particle displacement oriented in the y-direction, i.e. parallel to the reflecting surface, is designated horizontally polarized shear (SH). The particle displacement of the shear wave oriented in the x-z plane, i.e. perpendicular to the reflecting surface, is designated vertically polarized shear (SV). Notice, that the particle displacements of the SV component are oriented in the plane defined by the propagation direction and the normal on the inspection surface, which is called the *sagittal plane*.

To derive the angle dependent reflection coefficients of plane shear waves incident on a plane stress-free boundary, the corresponding boundary conditions have to be solved. This has already been done by many authors (Berkhout, 1987; Harker, 1988). For SH waves the incident and reflecting amplitudes are real and equal, which means that no mode-conversion takes place and there is no change of phase. SH waves are therefore called completely *uncoupled* from the P and SV waves. Consequently, the angle dependent reflection coefficient of SH waves at a stress-free surface is real and equals unity.

For SV waves the angle dependent reflection coefficient R_{SV} (based on the wave potentials, see chapter 2) reads (Harker, 1988):

$$R_{SV}(\alpha_s) = \frac{\left(1 - 2\sin^2 \alpha_s\right)^2 - 4\frac{c_s}{c_p}\sin^2 \alpha_s \cos \alpha_s \sqrt{1 - \left(\frac{c_s}{c_p}\right)^2 \sin^2 \alpha_s}}{\left(1 - 2\sin^2 \alpha_s\right)^2 + 4\frac{c_s}{c_p}\sin^2 \alpha_s \cos \alpha_s \sqrt{1 - \left(\frac{c_s}{c_p}\right)^2 \sin^2 \alpha_s}} \quad , \tag{6.1}$$

with c_p and c_s the compressional and shear wave velocity, respectively, and α_s the angle of incidence of the SV wave on the stress-free surface. This reflection coefficient may be written in terms of an amplitude R_{SV} and a phase φ_{SV}, according to the complex exponential function:

$$R_{SV}(\alpha_s) = |R_{SV}| \exp(i\varphi_{SV}) \quad . \tag{6.2}$$

As the compressional wave velocity c_p is always larger than the shear wave velocity c_s, the incident angle α_s will have a critical value above which the reflection coefficient becomes complex. This so-called *critical angle* α_c is defined by:

$$\alpha_c = \operatorname{asin}\left(\frac{c_s}{c_p}\right) \quad . \tag{6.3}$$

For values of the incident angle α_s below the critical angle $(\alpha_s < \alpha_c)$, the so-called *pre-critical reflection coefficient* is real $(\varphi_{SV} = 0)$ and only an amplitude modification $|R_{SV}|$ is introduced upon reflection at stress-free surfaces. For the amplitude factor it always holds that $|R_{SV}| \leq 1$, as a part of the shear wave energy may be converted into compressional waves.
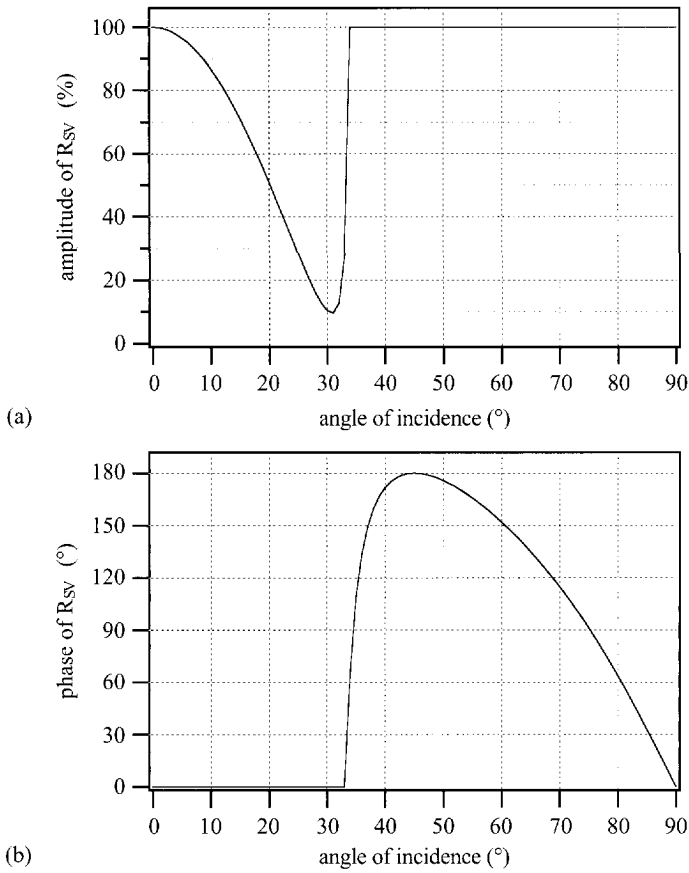
Figure 6.17: *The amplitude (a) and phase (b) of the SV wave reflection coefficient as a function of incident angle for plane stress-free surfaces of steel; $c_s=3260$ m/s, $c_p=5900$ m/s.*

For values of the incident angle α_s above the critical angle $(\alpha_s > \alpha_c)$, the so-called *post-critical reflection coefficient* will be complex and it will possess both an amplitude and a phase factor. The amplitude factor happens to be unity for SV wave reflection at stress-free surfaces, but the phase factor is a complicated expression of α_s and the wave velocities.

Thus it may be observed, that the angle dependent reflection coefficient of SV waves on a stress-free boundary will introduce *either* an amplitude change *or* a phase change, depending on the value of the incident angle. The amplitude and phase of the SV wave reflection coefficient are shown in figure 6.17 (for steel with $c_p=5900$ m/s and $c_s=3260$ m/s, according to (6.1)). Near the critical angle of incidence, which is in this case approximately 33°, the graphs of both the amplitude and phase feature a large change in value.

6.4.2   Shear wave polarization effects

In NDI-practice, shear waves are mostly generated by using mode-conversion of compressional waves at the interface between a (perspex) wedge and the (steel) object (see chapter 3). Therefore, the shear waves generally applied are shear waves which are polarized in the sagittal plane, defined by the propagation direction and the normal on the inspection surface. Such waves will be called SV waves *with respect to the inspection surface*. As long as the normal of the reflection (defect) plane is oriented in the same plane as the normal of the inspection plane, only SV wave reflectivity has to be considered.

When a lateral split angle configuration is used, as is generally the case for practical Multi-SAFT inspection, insonification and scattering take place in three dimensions. This implies, that the shear waves, being SV waves with respect to the inspection surface, may be differently polarized with respect to the reflection surface of the inhomogeneity. The insonifying shear wave may be decomposed *at the reflection surface* into a local SV and SH component (Lovelace, 1980). The angle between the incident shear wave and its local SV component will be called the *decomposition angle* χ. The decomposition angle is a function of the lateral split angle, the angle of incidence and the orientation of the reflection plane with respect to the plane inspection surface. This is shown in figure 6.18 for an arbitrarily lateral split angle γ, reflection-plane orientation (*tilt angle*) ξ, angle of incidence α, insonification angle β, and corresponding decomposition angle χ (requiring a highly developed sense for stereometry...)[2].

The process of pre-critical shear wave reflection at a stress-free surface is illustrated in figures 6.19a-c in terms of particle displacement vectors, where the vertical and horizontal directions in the figure indicate, respectively, the amplitude of the vertically (SV) and horizontally (SH) polarized components *with respect to the inspection surface*. An incident shear wave (SV_{1in}), which is pure SV with respect to that surface, is decomposed into local SH and SV components (SH_{2in} and SV_{2in}) at the reflection surface (figure 6.19a).

After pre-critical reflection, the amplitude of the local SH component will remain unchanged, but the amplitude of the local SV component will have been reduced, for instance, 50% due to mode-conversion (figure 6.19b). The reflecting local SH and SV components (SH_{2ref} and SV_{2ref}) are *in-phase* and compose a *total* reflecting shear wave (S_{2ref}), which contains an SV component (SV_{1ref}) that may be recorded at the surface of the object by an SV transducer (figure 6.19c). Clearly, the amplitude of the recorded SV component is *less* than 50% reduced (with respect to the initially incident SV wave) due to the positive contribution of the reflecting SH component (SH_{1ref}).

---

2   A 3-D construction plan is provided as an enclosure to this thesis in order to clarify the relation between the different angles and planes.
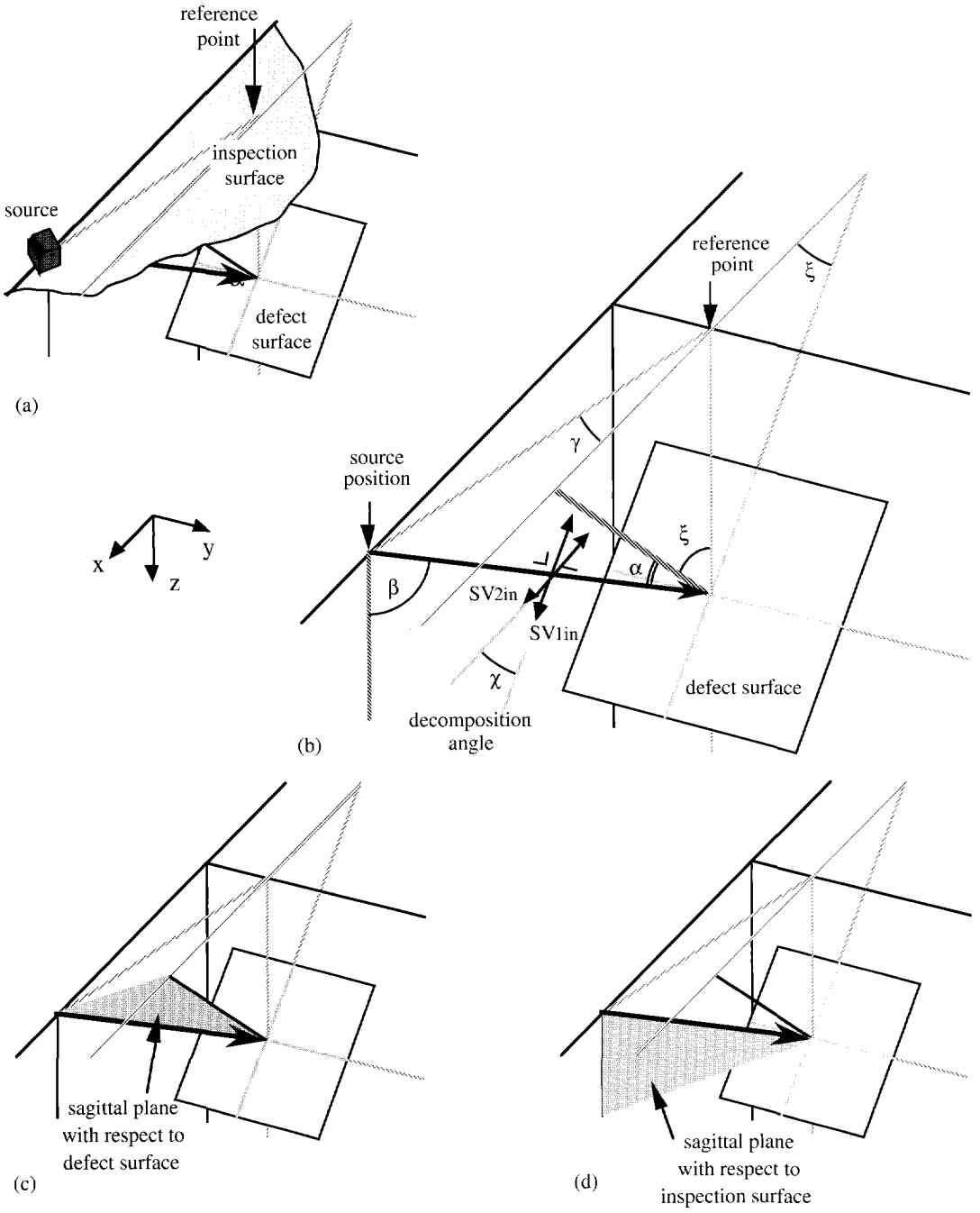
Figure 6.18: *The relation between the decomposition angle χ, the angle of incidence α, the insonification angle β, the tilt angle ξ and the lateral split angle γ for an incident SV wave from the inspection surface (SV_{lin}); χ is defined by the angle between the sagittal planes indicated in (c) and (d).*
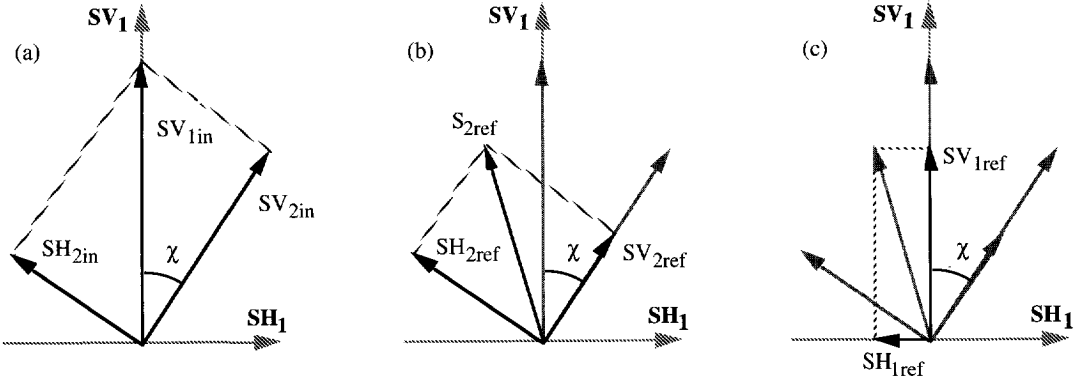
Figure 6.19: *Pre-critical shear wave reflection in terms of particle displacement vectors; the SV and SH wave components* with respect to the inspection surface *are indicated at the axes.*

When the angle of incidence α_s is post-critical, the SV component will be changed in phase upon reflection according to the reflection coefficient of an SV wave incident on a stress-free boundary given by equation (6.1). This also is illustrated in figures 6.20a-c in terms of particle displacement vectors. The incident shear wave (SV$_{1in}$), which is pure SV with respect to the inspection surface, is decomposed into local SH and SV components (SH$_{2in}$ and SV$_{2in}$) at the reflection surface (figure 6.20a). After post-critical reflection the amplitudes of the local SH and SV components (SH$_{2ref}$ and SV$_{2ref}$) will remain unchanged, but they will differ in phase. The phase of the local SV component (SV$_{2ref}$) will be changed here, for the sake of clearness, a 180° (figure 6.20b).
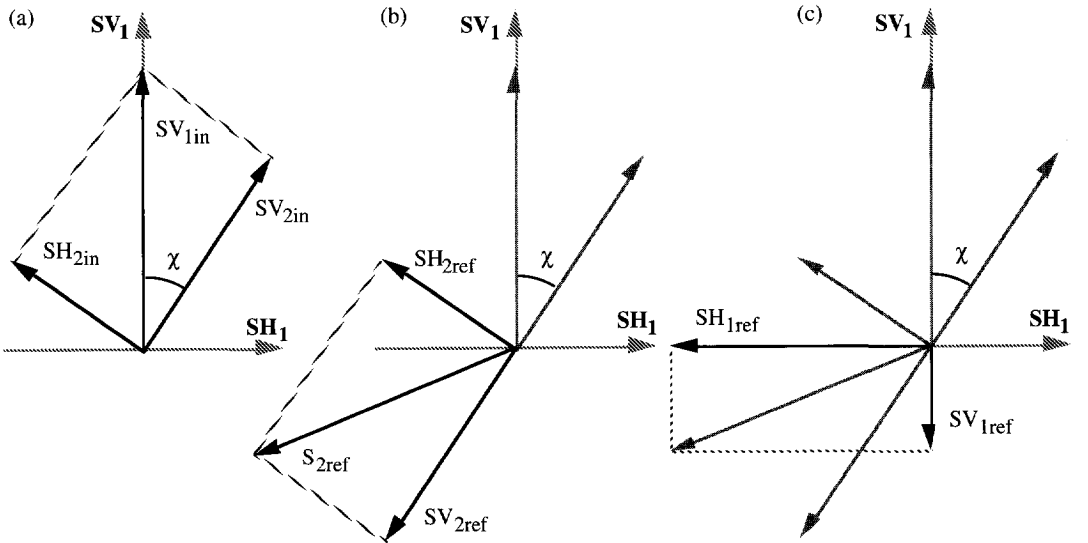
Figure 6.20: *Post-critical shear wave reflection in terms of particle displacement vectors; the SV and SH wave components* with respect to the inspection surface *are indicated at the axes.*

The reflecting local SH and SV components (SH_{2ref} and SV_{2ref}) have opposite phase and compose again a total reflecting shear wave[3] (S_{2ref}), which also contains an SV component (SV_{1ref}) which can be recorded at the surface of the object by a SV transducer (figure 6.20c). It can be seen from figure 6.20c, that the amplitude of the recorded SV component is reduced due to the phase change of the reflecting locally reflecting SV component with respect to the locally reflecting SH component, although 100% reflection of the incident shear wave did occur.

Figures 6.19 and 6.20 plainly illustrate that the effects of shear wave polarization on the amplitude of the recorded shear wave reflection response (SV component) cannot be intuitively predicted. Therefore, it is necessary to determine the shear wave reflectivity depending on both the lateral split angle and the angle of incidence on a stress-free reflection surface. This will result in the *general angle dependent SV wave reflection coefficient* $\Re$, describing the reflectivity of planar inhomogeneities *inside* the object for SV waves generated and recorded *at* the inspection surface.

6.4.3 General angle dependent SV wave reflectivity at stress-free surfaces

In appendix A the expression for the decomposition angle χ is derived:

$$\chi = \mathrm{acos}\left\{\left|\frac{\cos \xi - \cos \alpha \cos \beta}{\sin \alpha \sin \beta}\right|\right\} , \tag{6.4}$$

where for the angle of incidence α on the reflection plane holds:

$$\alpha = \mathrm{acos}\left(\cos \beta \cos \xi + \sin \beta \sin \xi \cos \gamma\right) . \tag{6.5}$$

Notice, that the decomposition angle is completely determined by the angle of insonification β (the angle of the incident wave vector with the normal on the *inspection* plane), the angle of incidence α (the angle of the incident wave vector with the normal on the *reflecting* plane), and the angle ξ between the normal vectors of the inspection and reflecting planes. Although the computation of these angles is not always very straightforward, as in the case of cylindrical pipe geometries for instance, expression (6.4) is generally valid for all incident SV (or SH) waves (polarization with respect to the inspection plane).

The decomposition of an incident shear wave into two orthogonal components SV and SH actually implies a coordinate transformation. As a result of this transformation, the reflectivity of

---

3   For arbitrary phase changes of the locally reflecting SV component, the total reflected shear wave will be elliptically polarized (SH and SV components of arbitrary different phases).

two different shear wave components have to be regarded separately. Thus, instead of a reflectivity matrix containing the reflectivity properties for incident SV waves only (R_{SV}), the reflectivity properties of SH waves should also be taken into account. This results in the following matrix formulation of the reflection process at a plane surface z_d ($\underline{P}^+$ and $\underline{P}^-$ describe the incident and reflected shear wave fields, respectively):

$$
\begin{pmatrix} \underline{P}_{SV}^-(z_d) \\ \underline{P}_{SH}^-(z_d) \end{pmatrix} = \mathbf{T}_\chi \, \mathbf{R}(z_d) \, \mathbf{T}_\chi \begin{pmatrix} \underline{P}_{SV}^+(z_d) \\ \underline{P}_{SH}^+(z_d) \end{pmatrix} ,
\tag{6.6}
$$

with the transformation matrix $\mathbf{T}_\chi$:

$$
\mathbf{T}_\chi = \begin{pmatrix} \cos \chi \; \sin \chi \\ \sin \chi \; \cos \chi \end{pmatrix} ,
\tag{6.7}
$$

and the reflectivity matrix $\mathbf{R}(z_d)$:

$$
\mathbf{R}(z_d) = \begin{pmatrix} \mathbf{R}_{SV}(z_d) & 0 \\ 0 & \mathbf{R}_{SH}(z_d) \end{pmatrix} .
\tag{6.8}
$$

Notice, that $\mathbf{R}_{SV}(z_d)$ and $\mathbf{R}_{SH}(z_d)$ are sub-matrices, each containing the reflectivity properties of the plane surface z_d for SV and SH waves, respectively, and that the matrix $\mathbf{R}_{SH}(z_d)$ equals I for plane stress-free surfaces. From equation (6.6) is can be seen, that the general angle dependent SV wave reflection coefficient $\Re$ equals $\mathbf{T}_\chi \, \mathbf{R}(z_d) \, \mathbf{T}_\chi$. Expressions for $\Re$ will be derived below.

For pre-critical angles of incidence, the general SV wave reflection coefficient $\Re_{pre}$ will be real and can readily be derived using figures 6.19a-c. The recorded SV wave is made up of two SV components (polarization with respect to the inspection plane), originating from the locally reflecting SH and SV waves (polarization with respect to the reflection plane). The amplitude of the recorded SV wave (SV_{1ref}) is simply the vector sum of the amplitudes of the reflected SV wave components ($\sin\chi SH_{2ref}$ and $\cos\chi SV_{2ref}$), which results in:

$$
\left| \Re_{pre}(\alpha,\chi) \right| = \sin \chi \; SH_{2ref} + \cos \chi \; SV_{2ref} = \sin^2 \chi + | R_{SV}(\alpha) | \cos^2 \chi ,
\tag{6.9}
$$

where $|R_{SV}|$ is the amplitude of the reflection coefficient for SV waves according to equation (6.1), and the incident shear wave amplitude is defined to be unity.

If the angle of incidence is larger than the critical angle, the amplitude of the locally reflecting SV wave (polarization with respect to the reflecting plane) is not altered, but its phase is changed upon reflection according to equation (6.1). Thus, for post-critical angles of incidence the general angle dependent SV wave reflection coefficient $\Re_{post}$ will be complex and the phases of the

locally reflecting components will have to be taken into account. When the amplitude of the incident shear wave is defined to be unity, again the recorded SV wave is made up of two SV components (polarization with respect to the inspection plane), originating from the locally reflecting SH and SV waves (polarization with respect to the reflection plane). Because of the phase change, the amplitude of the recorded SV wave (SV_{1ref}) is now the *weighted* vector sum of the amplitudes of the reflected SV wave components ($\sin\chi SH_{2ref}$ and $\cos\chi SV_{2ref}$). The detectable reflected SV wave can thus be written as:

$$\left| \Re_{post}(\alpha,\chi) \right| \exp\{j\,\omega t - \eta\} = \sin \chi \; SH_{2ref} \exp\{j\omega t\} + \cos \chi \; SV_{2ref} \exp\{j\,\omega t + \varphi_{SV}(\alpha)\}$$

$$= \sin^2 \chi \, \exp\{j\omega t\} + \cos^2 \chi \, \exp\{j\,\omega t + \varphi_{SV}(\alpha)\} \; , \qquad \qquad , (6.10)$$

where ω is the angular frequency, t is time, φ_{SV} is the phase change (according to the angle dependent reflection coefficient for SV waves), and η is the phase of the detectable reflected SV component (polarized with respect to the inspection surface). From this expression (6.10) the reflection coefficient $\Re_{post}$ may be determined using the following relations.

If the sum of two sine-functions with a constant phase difference is expressed as:

$$C \sin \{\omega t + \eta\} = A \sin \{\omega t\} + B \sin \{\omega t + \varphi\} \; , \qquad \qquad (6.11)$$

it can be shown (Lovelace, 1980), that for the amplitude C holds:

$$C = \sqrt{(A + B \cos \varphi)^2 + B^2 \sin^2\varphi} \; , \qquad \qquad (6.12)$$

and for the phase η:

$$\eta = a\cos\left(\frac{A + B \cos \varphi}{C}\right) \; . \qquad \qquad (6.13)$$

For the amplitude of the general angle dependent SV wave reflection coefficient for post-critical angles $\Re_{post}$ can thus be written, using expressions (6.10), (6.12) and (6.13):

$$\left| \Re_{post}(\alpha,\chi) \right| = \sqrt{\left[\sin^2 \chi + \cos^2 \chi \cos \varphi_{SV} \right]^2 + \cos^4 \chi \sin^2 \varphi_{SV}} \; , \qquad \qquad (6.14)$$

and for its phase:

$$\eta(\alpha,\chi) = a\cos\left(\frac{\sin^2 \chi + \cos^2 \chi \cos \varphi_{SV}}{\left| \Re_{post}(\alpha,\chi) \right|}\right) \; . \qquad \qquad (6.15)$$

As there occurs no phase change for pre-critical reflections and no amplitude change for post-critical reflections for SV waves reflecting at stress-free boundaries, compendious expressions for the amplitude and phase of $\Re$ can be derived from equations (6.9), (6.14), and (6.15) which read:

$$\left| \Re(\alpha,\chi) \right| = \sqrt{ \left[\sin^2 \chi + \cos^2 \chi \left| R_{SV} \right| \cos \varphi_{SV} \right]^2 + \cos^4 \chi \ \sin^2 \varphi_{SV} } \quad , \tag{6.16}$$

and:

$$\eta(\alpha,\chi) = \mathrm{acos}\left(\frac{\sin^2 \chi + \cos^2 \chi \left| R_{SV} \right| \cos \varphi_{SV}}{\left| \Re(\alpha,\chi) \right|} \right) . \tag{6.17}$$

6.4.4   General angle dependent SV wave reflectivity of vertically oriented defects

Flat plate geometry

The important vertically oriented defect will be taken as an example to demonstrate the effects of general angle dependent SV wave reflectivity for data-acquisition with the lateral split angle configuration. For this type of defect indirect wave paths should be employed for imaging (see section 6.2). Using the definitions of the insonification angle β, the lateral split angle γ and the tilt angle ξ from the flat plate geometry of figure 6.18, the general angle dependent SV wave reflection coefficient will be evaluated in this section as a function of lateral split angle for the indirect forward scattering wave path reflecting at a vertically oriented defect (so: $\xi = 90°$).

The insonification angle β will be chosen to be 45° and 60° (corresponding to practical transducer angles) and the lateral split angle will range from 0° to 90°. The reflecting plane is assumed to be smooth and embedded in steel (c_p=5900 m/s, c_s=3260 m/s). In figures 6.21 and 6.22 the angle of incidence α, the decomposition angle χ and the amplitude and phase of the SV wave reflection coefficient $\Re$ are shown as a function of the lateral split angle γ for insonification angles of 45° and 60°, respectively. The amplitude and phase, resulting from pure SV wave reflection and not taking polarization effects into account, are also indicated in the graphs (dashed lines). Notice, that the *constant* phase change due to the back-wall reflection is not taken into account.

A number of interesting features may be observed from figures 6.21 to 6.22. For a 45° insonification angle, for instance, the angle of incidence is post-critical for all lateral split angles. Consequently, when polarization effects would be ignored, the amplitude of the reflecting SV wave (to be recorded at the inspection surface) would be expected to remain unchanged. The
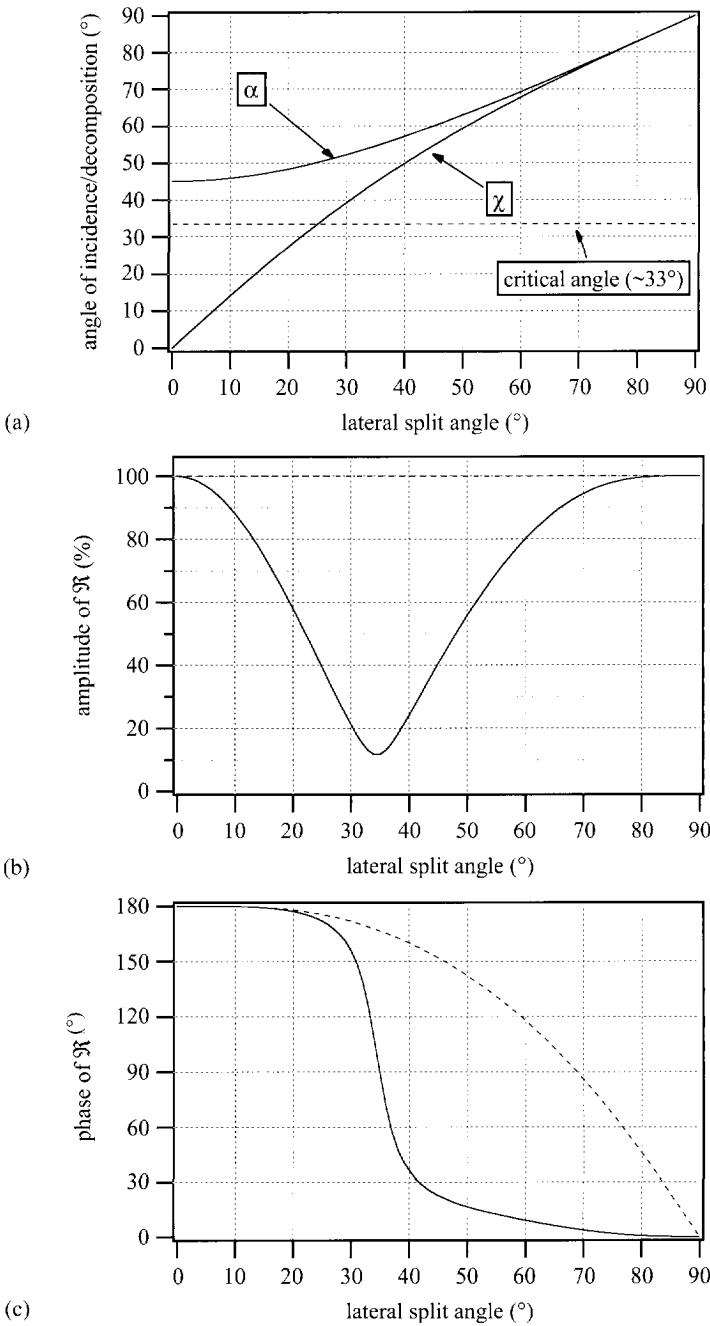
Figure 6.21: *The angles of incidence and decomposition (a), the amplitude (b) and phase (c) of the general SV wave reflection coefficient $\mathfrak{R}$, all as a function of lateral split angle for a vertically oriented defect and a 45° angle of insonification; the dashed curves in (b) and (c) indicate the relations in case polarization effects are not taken into account.*
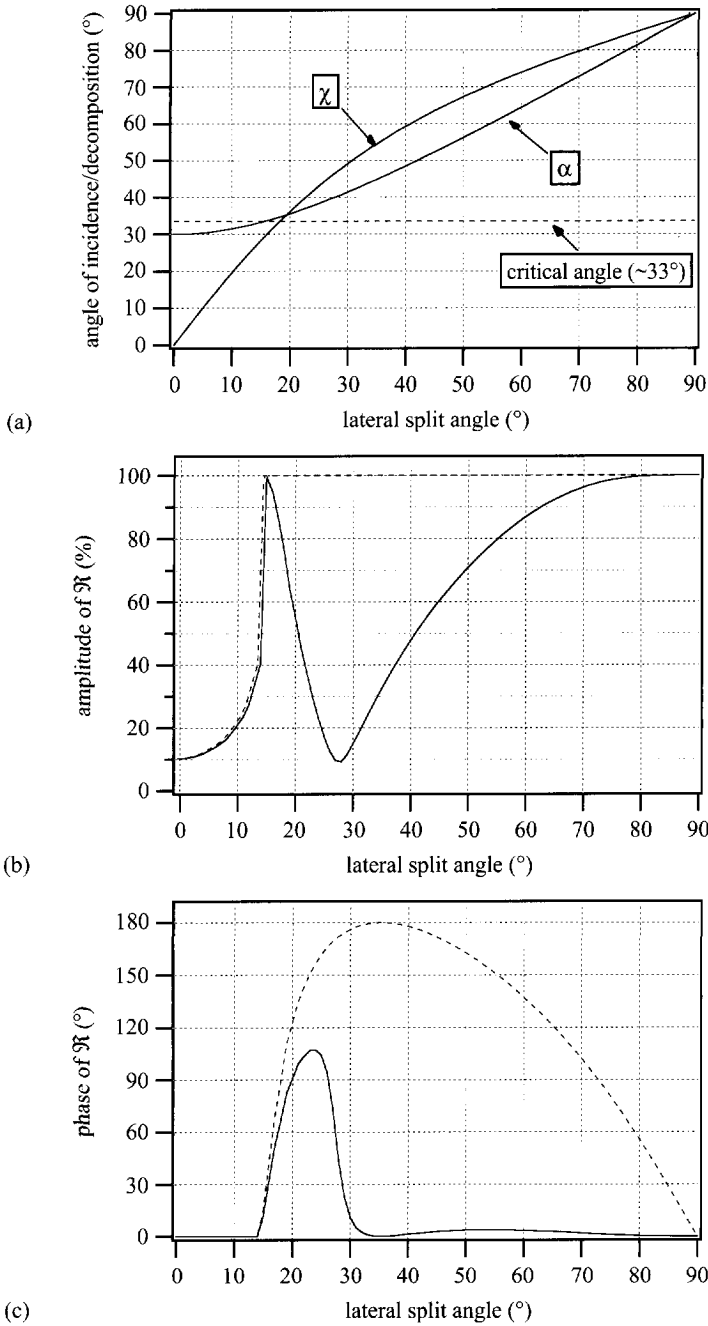
Figure 6.22: *The angles of incidence and decomposition (a), the amplitude (b) and phase (c) of the general SV wave reflection coefficient ℜ, all as a function of lateral split angle for a vertically oriented defect and a 60° angle of insonification; the dashed curves in (b) and (c) indicate the relations in case polarization effects are not taken into account.*
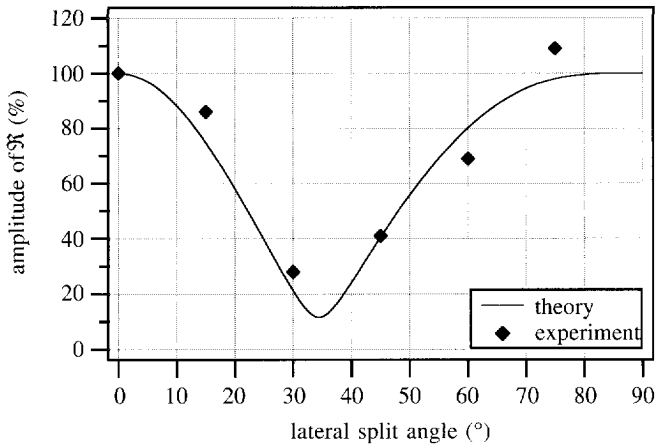
Figure 6.23: *The theoretical and experimentally determined amplitude of the general SV wave reflection coefficient $\Re$ as a function of lateral split angle for a vertically oriented defect and a 45° angle of insonification.*

effect of the decreasing amplitude of the (detectable) SV wave due to the phase changes may be clear for both insonification angles: the signal-to-noise ratio of the recorded data will be reduced drastically in some cases due to 'mode-conversion' between SV and SH, in spite of the fact that 100% reflection of the incident shear waves takes place.

For an insonification angle of 45°, the amplitude of the general angle dependent SV wave reflection coefficient has also been determined experimentally. The vertical side of a 40 mm thick steel plate was insonified via the back wall with six different lateral split angles (0°, 15°, 30°, 45°, 60° and 75°). The amplitude of the envelope of the recorded response was computed and graphically displayed in figure 6.23. It can be seen, that the measured points are in reasonable agreement with the theoretical curve. The amplitude for the 75° lateral split angle is somewhat too high, which is most likely due to the contribution of waves reflecting directly from the back wall to the receiver transducer.

Cylindrical pipe geometry

In the case of flat plate geometries, the general SV wave reflection coefficient as a function of lateral split angle can be *analytically* derived for the indirect wave path reflecting at a vertically oriented defect. However, for cylindrical pipe geometries its derivation is not very straightforward due to the more complex calculation of indirect wave paths (see chapter 4). As the tangent plane in the reflection point at the back wall is in general not oriented parallel to the tangent plane at the position of the source, which also holds for the source and receiver tangent planes, decomposition of polarized shear waves takes place three times: at the back wall of the pipe, at the defect plane
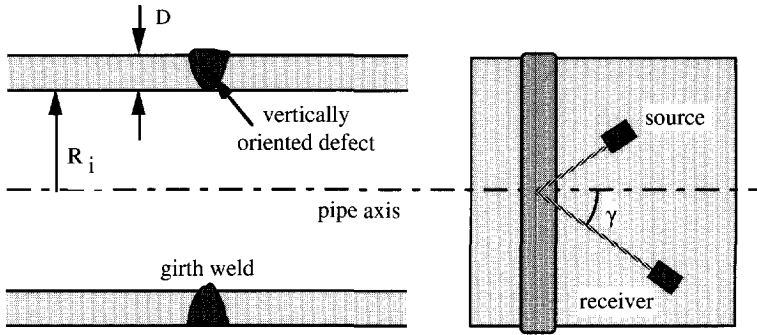
Figure 6.24: *The configuration for which the general SV wave reflection coefficient $\mathfrak{R}$ will be derived as a function of lateral split angle for a vertically oriented defect in a girth weld of a cylindrical pipe.*

and at the tangent receiver plane (for indirect (1,0) or (0,1) wave paths, as have to be employed for imaging vertically oriented defects).

The general angle dependent SV wave reflection coefficient will be derived for a smooth planar defect which is oriented perpendicularly to the back wall, with its surface in the plane perpendicular to the pipe's axis (see figure 6.24). This represents the typical situation of a vertically oriented defect in a girth weld. As already been mentioned, indirectly insonifying or scattering waves have to be employed to be able to image this kind of defect. The source will be positioned according to the lateral split angle configuration at a lateral split angle between 0° and 90°. The receiver will be located symmetrically at such a position that it properly receives the reflected SV waves. For clarity in the following derivation, the parameters (amplitude, phase, angle) will be denoted by the index '$_0$' if they correspond to the position of the source, by the index '$_1$' if they correspond to the point of reflection at the inner pipe's surface, by the index '$_2$' if they correspond to the position of the point of reflection at the vertically oriented defect, and, finally, by the index '$_3$' if they correspond to the position of the receiver.

In the cylindrical pipe situation, an insonifying shear wave is not only transformed according to equation (6.6) at the defect plane, but at the pipe's inner and outer surfaces as well. Therefore, a generated shear wave SV_0 (vertical polarization with respect to the source tangent plane) will be an arbitrarily polarized shear wave at the pipe's inner surface (back wall), where it reflects towards the vertically oriented defect (according to the (1,0) wave path). Thus, at the position of the defect a shear wave will arrive consisting of the two components SV_1 and SH_1, as the result of the first decomposition (angle χ_1) at the pipe's inner surface. Yet again, these SV_1 and SH_1 components can both be regarded as arbitrarily polarized shear waves at the position of the defect, where they will be reflected towards the pipe's outer surface. This means that, at the position of the receiver on the pipe's outer surface, a shear wave will arrive consisting of the four components SV_2, SH_2, SV'_2 and SH'_2, as a result of the second decomposition (angle χ_2) at the vertically

oriented defect. Once again, these components can all be regarded as arbitrarily polarized shear waves and each component will be decomposed (angle χ_3) into an SV and an SH component at the position of the receiver. This results into no less than eight components to be distinguished: SV_3, SH_3, SV'_3, SH'_3, SV''_3, SH''_3, SV'''_3, and SH'''_3.

All four reflected *SV components* will compose one detectable SV component at the position of the receiver. The amplitude and phase of this detectable SV wave will be derived here as a function of lateral split angle. From equations (6.6) and (6.7) it follows, that the amplitude of the locally reflecting SV and SH components SV_{2ref} and SH_{2ref} will contribute to the detectable SV component SV_{1ref} according to (see also equation (6.9)):

$$SV_{1ref} = SV_{2ref} \cos \chi + SH_{2ref} \sin \chi \ . \tag{6.18}$$

Thus, the incident shear wave SV_0 is decomposed into local SV and SH components SV_1 and SH_1 at the back wall according to equation (6.18):

$$SV_1 = SV_0 \cos \chi_1 \ , \tag{6.19a}$$

$$SH_1 = SV_0 \sin \chi_1 \ . \tag{6.19b}$$

In the following, the four detectable SV components (SV_3, SV'_3, SV''_3, SV'''_3) reaching the receiver will be written explicitly in terms of SV_0 (the amplitude of the incident SV wave) and the different decomposition angles χ_1, χ_2 and χ_3 with the aid of equations (6.18) and (6.19).

The first component SV_3 results from the local SV component SV_2, reflecting from the defect and generated by the local SV component SV_1, reflecting from the back wall:

$$SV_3 = SV_2 \cos \chi_3 = SV_1 \cos \chi_3 \cos \chi_2 = SV_0 \cos \chi_3 \cos \chi_2 \cos \chi_1 \ . \tag{6.20}$$

This component may be affected by either an amplitude reduction or a phase change from the first as well as the second reflection.

The second component SV'_3 results from the local SH component SH_2, reflecting from the defect and generated by the local SV component SV_1, reflecting from the back wall:

$$SV'_3 = SH_2 \sin \chi_3 = SV_1 \sin \chi_3 \sin \chi_2 = SV_0 \sin \chi_3 \sin \chi_2 \cos \chi_1 \ . \tag{6.21}$$

This component may be affected by either an amplitude reduction or a phase change from the first reflection only.

The third component SV''_3 results from the local SV component SV'_2, reflecting from the defect and generated by the local SH component SH_1, reflecting from the back wall:

$$SV''_3 = SV'_2 \cos\chi_3 = SH_1 \cos\chi_3 \sin\chi_2 = SV_0 \cos\chi_3 \sin\chi_2 \sin\chi_1 \ . \tag{6.22}$$

This component may be affected by either an amplitude reduction or phase change from the second reflection only.

The fourth component SV'''_3 results from the local SH component SH'_2, reflecting from the defect and generated by the local SH component SH_1, reflecting from the back wall:

$$SV'''_3 = SH'_2 \sin\chi_3 = SH_1 \sin\chi_3 \cos\chi_2 = SV_0 \sin\chi_3 \cos\chi_2 \sin\chi_1 \ , \tag{6.23}$$

and will not be affected by any amplitude reduction or phase change. All decomposition angles (χ_1, χ_2 and χ_3) can be computed from the (local) angles of insonification, incidence, and the tilt angle between the planes involved, according to equation (6.4). For the computation of the four SV components the amplitude of the incident wave SV_0 is defined unity. The phase changes will be computed with respect to the phase of this incident wave.

Thus, four SV components arriving at the position of the receiver, defined by equations (6.20) to (6.23), may be summed to make up one total detectable SV wave. Equation (6.11) is used to add the components SV_3 and SV'_3, as well as SV''_3 and SV'''_3, taking the phases into account. This will result into two SV components: SV_{31} and SV_{32}. Using equation (6.11) once again, the amplitude and phase of the final detectable SV component SV_{3tot} will be determined as a function of the lateral split angle γ.

The components SV_3 and SV'_3 have both been affected by either an amplitude reduction r_1 or a phase change η_1 from the first reflection (at the pipe's back wall). The SV_3 component, however, has also been affected by either an amplitude reduction r_2 or phase change η_2 from the second reflection at the defect. Therefore, the possible difference in amplitude or phase between these two SV components will be determined, respectively, by r_2 or η_2. Using equations (6.16) and (6.17), the amplitude $|\Re_{31}|$ and the phase η_{31} of the shear wave component SV_{31} can be computed.

From the two components SV''_3 and SV'''_3 only the first component has been affected by either an amplitude reduction r_2 or phase change η_2 from the second reflection (at the defect). Therefore, the possible difference in amplitude or phase between these two SV components will also be determined by r_2 or η_2. Using equations (6.16) and 6.17), the amplitude $|\Re_{32}|$ and the phase η_{32} of SV_{32} can be computed.

The components SV_{31} and SV_{32} have both been modified by an amplitude reduction and/or a phase change. The sum of the two components will result into a total amplitude $|\Re_3|$ and phase η_3 of the final detectable SV component. More general versions of equations (6.16) and (6.17), resulting from the sum of two sine functions having different amplitudes and phases, will be used:

$$\left| \Re(\alpha) \right| = \sqrt{\left[SV_a \cos \varphi_a + SV_b \cos \varphi_b \right]^2 + \left[SV_a \sin \varphi_a + SV_b \sin \varphi_b \right]^2} \ , \tag{6.24}$$

and:

$$\eta(\alpha) = a\cos\left(\frac{SV_a \cos \varphi_a + SV_b \cos \varphi_b}{\left| \Re(\alpha) \right|} \right) \ , \tag{6.25}$$

where SV_a and SV_b are the amplitudes of the two sine functions with phases φ_a and φ_b, respectively.

The amplitude and phase of the final detectable SV component have been computed for a vertically oriented defect (plane) with a smooth stress-free surface, for insonification angles of 45° and 60°, and for different values of the pipe radius. This has been done numerically (determining the decomposition angles) with the aid of specially developed software. The point of reflection at the vertically oriented defect has been chosen to be positioned half-way the thickness of the pipe, which has been set to 30 mm.

As indirect wave paths have to be employed – reflecting at the inner pipe's surface – the minimum feasible inner radius $[R_i]_{min}$ should be determined for each insonification angle. This is possible by modifying equation (4.15) and reads:

$$[R_i]_{min} = \frac{D \sin \beta}{1 - \sin \beta} \ , \tag{6.26}$$

with D the thickness of the pipe wall. Consequently, for an insonification angle of 45° the minimum inner radius is approximately 80 mm and for an insonification angle of 60° it is approximately 200 mm.

In figures 6.25 and 6.26 the amplitude and phase of the general SV wave reflection coefficient $\Re$ for the flat plate situation ($R_i \rightarrow \infty$) and the cylindrical situation of $R_i = 300$ mm have been plotted together with the curves for the smallest possible inner radius, for each insonification angle. It is remarkable, that in this case of a vertically oriented defect located half way a 30 mm thick pipe and with its normal parallel to the pipe's axis, the general SV wave reflection coefficient does not differ much with respect to the flat plate situation for a large range of inner radius values. This means, that (in this case) the curves of the (analytically computable) flat plate situation can be

(a)

(b)
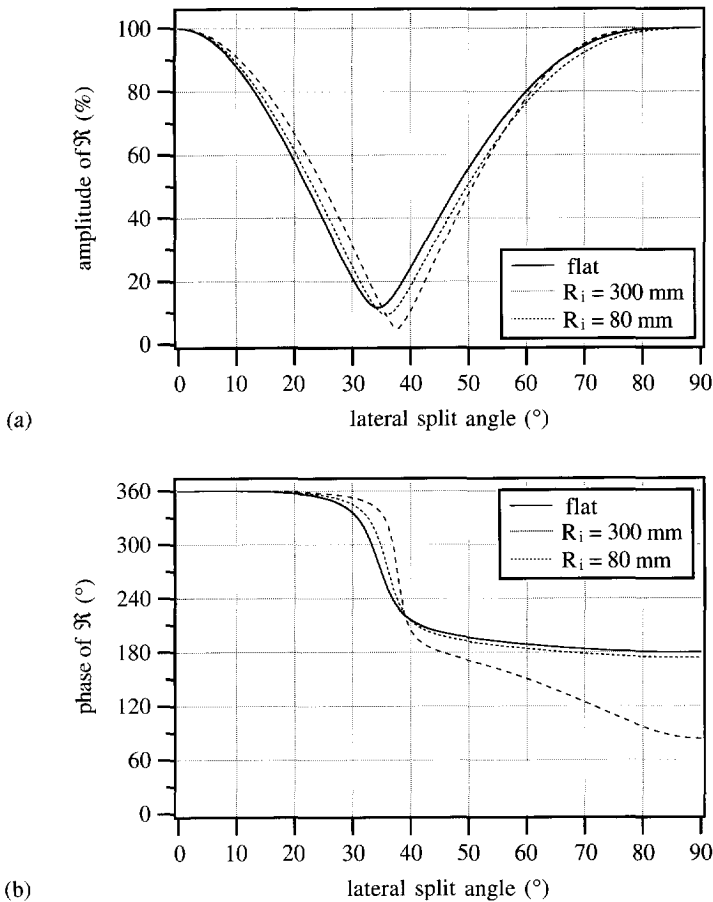
Figure 6.25: *The amplitude (a) and phase (b) of the general SV wave reflection coefficient $\Re$ as a function of lateral split angle for a vertically oriented defect in a girth weld of a cylindrical pipe and a 45° angle of insonification; the curves for two different values of the inner pipe radius are compared with the curve for the flat plate situation.*

regarded reasonably representative for the cylindrical situation.

In order to be able to understand the results of figures 6.25 and 6.26, the angles of incidence, the decomposition angles, and the amplitudes together with the phase changes of the final four SV components are shown in figures 6.27 and 6.28 for the 45° insonification angle and in figures 6.29 and 6.30 for the 60° insonification angle. Of course, the angle of incidence at the back wall in the flat plate situation is constant, its corresponding decomposition angle χ_1 zero, and the decomposition angles χ_2 and χ_3 are identical (simply named χ in the figures).
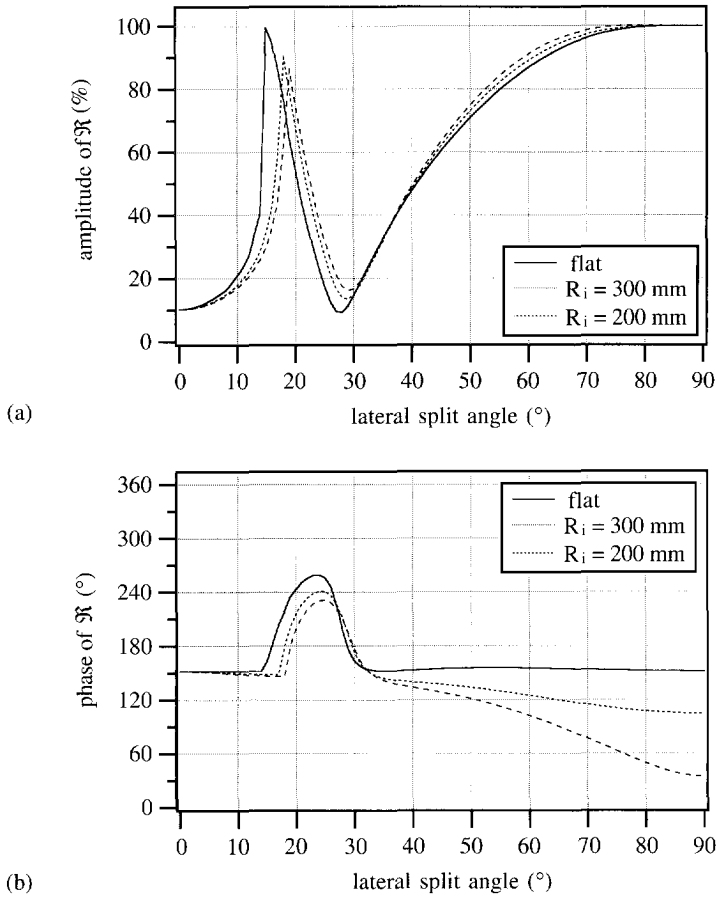
Figure 6.26: *The amplitude (a) and phase (b) of the general SV wave reflection coefficient $\Re$ as a function of lateral split angle for a vertically oriented defect in a girth weld of a cylindrical pipe and a 60° angle of insonification; the curves for two different values of the inner pipe radius are compared with the curve for the flat plate situation.*

The small changes of the curves for the amplitude and phase of the detectable SV component at the position of the receiver ($\Re_3$ and η_3) for different values of the inner radius can be explained from the small value of the first decomposition angle χ_1 and the fact that the angle of incidence α_2 deviates just a little from its value in the flat plate situation. This is because the tangent plane at the position of the reflection at the pipe's back wall makes a considerable tilt angle with the tangent plane at the position of the source, but it is tilted '*in transmission*' with respect to the normal at the source position (see figure 6.31a), causing the decomposition angle χ_1 to be small.

The reflecting defect plane makes a considerable tilt angle with respect to the tangent planes at

(a)

(b)

Figure 6.27: *The angles of incidence (a) and decomposition (b) as a function of lateral split angle for a vertically oriented defect in a girth weld of a cylindrical pipe with an inner radius of 300 mm and a 45° angle of insonification; the different indices refer to the reflections at different planes (back-wall, defect, inspection surface).*

which reflection takes place at the pipe's back wall and at which the receiver is positioned, but it is now tilted '*in reflection*' (see figure 6.31b), causing the decomposition angles χ_2 and χ_3 to be much larger. As an example, the relation between the decomposition angle and the tilt angle has been evaluated for an insonification angle of 45° and a lateral split angle of 30° for a flat plate geometry. Figure 6.31c shows clearly, that for reflection planes tilted in transmission (negative tilt angles) the decomposition angle is smaller than for reflection planes tilted in reflection (positive tilt angles). As may be expected from the small value of the first decomposition angle χ_1, the amplitude of the generated SH component at the back wall will be small and will not contribute much to the final (detectable) SV component. For the 60° insonification angle, the SV_3
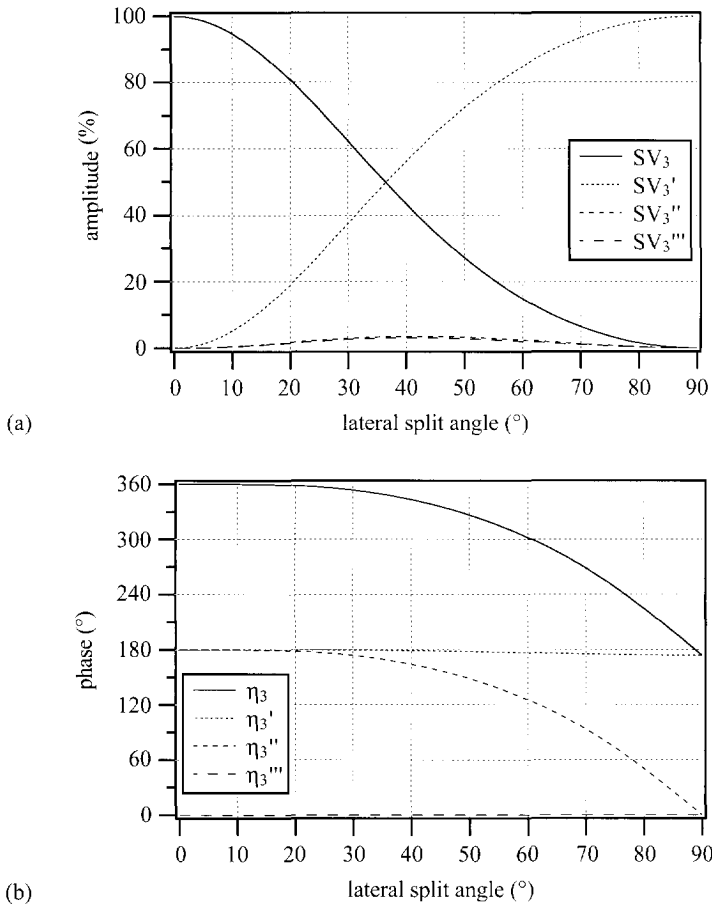
Figure 6.28: *The amplitudes (a) and phase changes (b) of the final four SV components as a function of lateral split angle for a vertically oriented defect in a girth weld of a cylindrical pipe with an inner radius of 300 mm and a 45° angle of insonification; the different indices refer to the reflections at different planes (back-wall, defect, inspection surface).*

component is clearly affected by an amplitude change caused by mode-conversion at the surface of the defect for a range of lateral split angles (compare figures 6.28 and 6.30).

In this section it was shown, that vertically oriented plane defects may be insonified with SH as well as SV waves by applying real wedge transducers in a lateral split angle configuration. This can be very important for imaging partially closed cracks[4]. When a crack is partially closed due to possible stresses in the material, SV waves will hardly be reflected by the closed part of the crack

---

4   Here, *partially* closed cracks are considered, as completely closed cracks are not likely to be detected by conventional ultrasonic inspection methods.
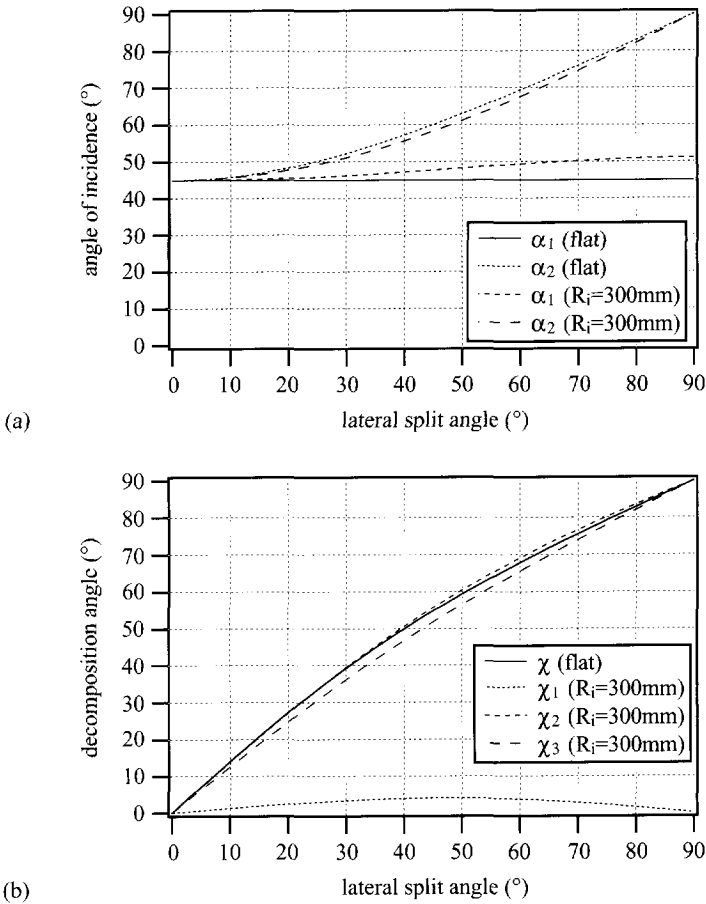
(a)

(b)
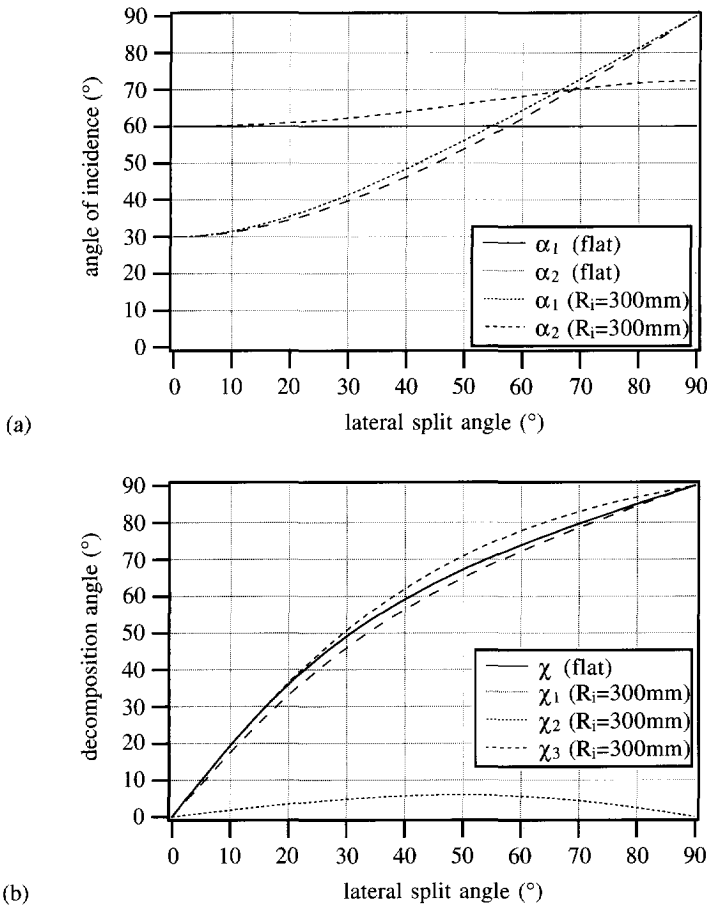
Figure 6.29: *The angles of incidence (a) and decomposition (b) as a function of lateral split angle for a vertically oriented defect in a girth weld of a cylindrical pipe with an inner radius of 300 mm and a 60° angle of insonification; the different indices refer to the reflections at different planes (back-wall, defect, inspection surface).*

surface. For SH waves, however, these closed parts possess a considerable reflectivity due to the discontinuity of shear stresses at the crack surface. Thus, the closed parts of a partially closed crack may also imaged by making use of the contribution of the locally reflecting SH wave component to the detectable SV wave at the inspection surface by real wedge transducers in a lateral split angle configuration.
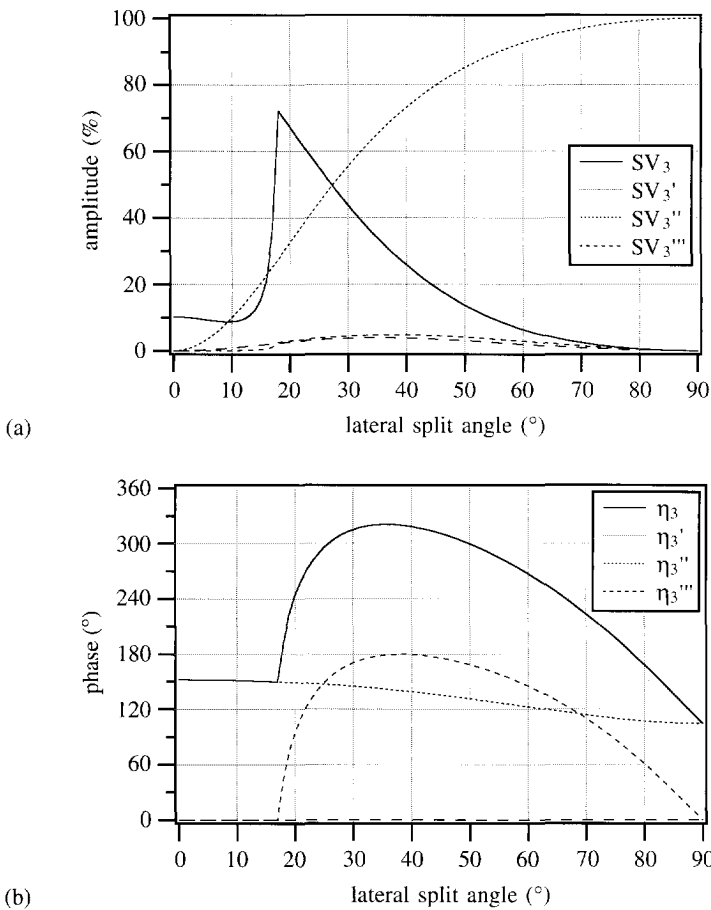
Figure 6.30: *The amplitudes (a) and phase changes (b) of the final four SV components as a function of lateral split angle for a vertically oriented defect in a girth weld of a cylindrical pipe with an inner radius of 300 mm and a 60° angle of insonification; the different indices refer to the reflections at different planes (back-wall, defect, inspection surface).*

6.5 Combining Diffraction and Reflection Images

6.5.1 Choosing wave paths for imaging

In order to be able to image an inhomogeneity, of course, its scattering wave field should be recorded. As mentioned earlier, the scattered wave field for planar inhomogeneities will be strongly directional. Therefore, it is very important to arrange the source position and receiver aperture in such a way, that the reflected wave field can actually be recorded. Due to the limitation
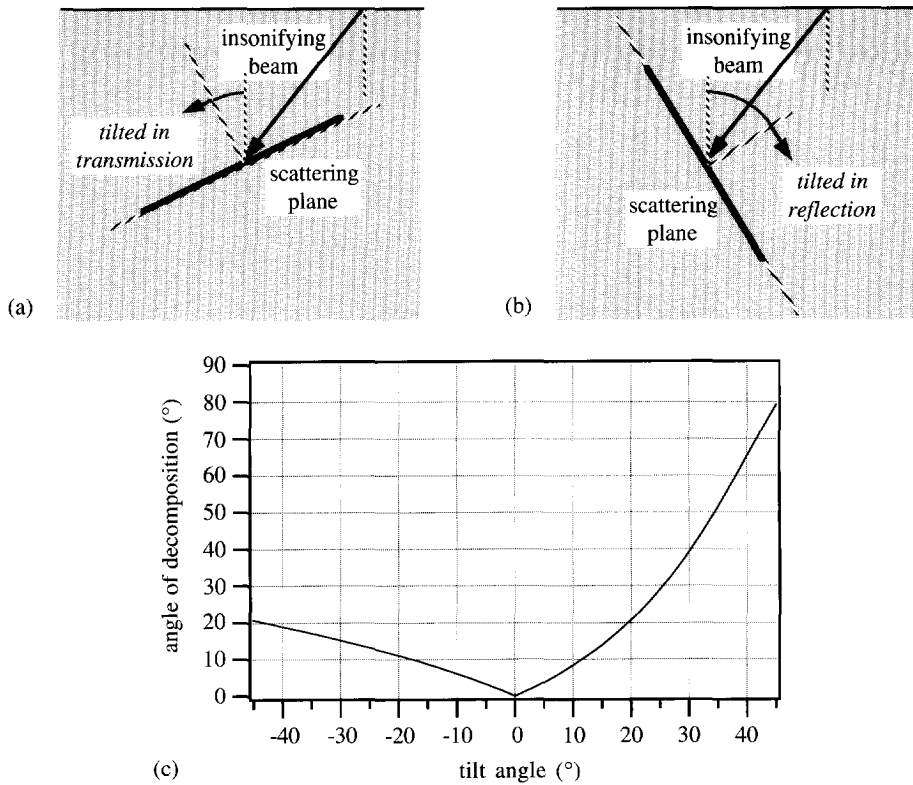
Figure 6.31: *The defect plane may be tilted* in transmission *(a) or* in reflection *(b); for transmission tilt angles (negative values) the decomposition angle is smaller than for reflection tilt angles (positive values), as shown in the graph (c) for a 30° lateral split angle and a 45° insonification angle on a flat plate.*

single-sided lack of penetration

lack of side wall fusion

slag inclusion

cracking
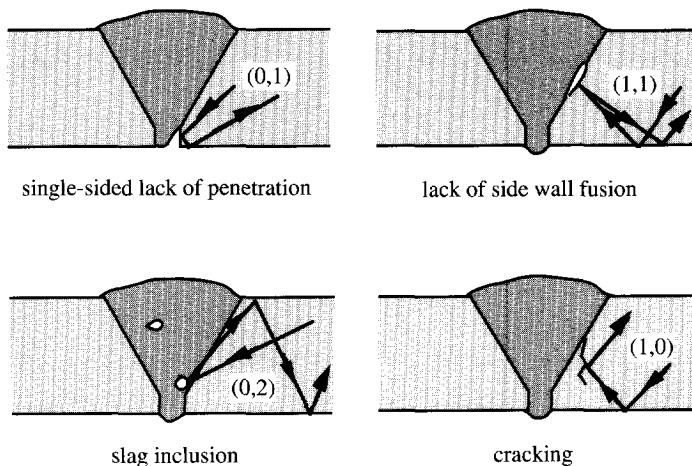
Figure 6.32: *A number of examples of typical defect orientations for which different wave paths have to be employed.*

of the receiver aperture and the angle dependence of the transducers, direct as well as indirect wave paths have to be applied in most cases and the data-acquisition configuration should be carefully optimized.

The directional source should insonify the inhomogeneity as completely as possible. In some cases, different source positions have to be applied in order to be able to insonify the entire defect. Using the a priori knowledge on the weld geometry, the orientation of a planar inhomogeneity may be estimated, for instance, using conventional pulse-echo inspection. In figure 6.32 a number of examples of defect orientations are given for which different wave paths have to be employed for imaging. In practice, determining which wave path contains the most (reflection) information will sometimes be a process of trial and error. Planar defects are usually imaged by using the reflection wave path, which may be direct or indirect, depending on the orientation of the planar defect. The image quality, however, will never be absolutely perfect due to the limited receiver aperture and the extremities of the inhomogeneity (indicating its size) can therefore not be determined accurately from the image. This is shown in figure 6.33a using Multi-SAFT on a modelled 3 mm high vertically oriented defect at 20 mm depth in a 30 mm flat steel plate.

Apart from a *reflected* wave field, the planar defect will also scatter a *diffracted* wave field originating from its extremities. This can also be observed from the snapshots of figure 6.8. The diffracted waves do not possess such strong directivity like the reflected waves. Therefore, the diffracted waves may propagate along other wave paths and may be recorded separately at the inspection surface. Imaging the diffraction responses (by employing another wave path for imaging) will result in an image of the extremities of the planar inhomogeneity. This is shown in
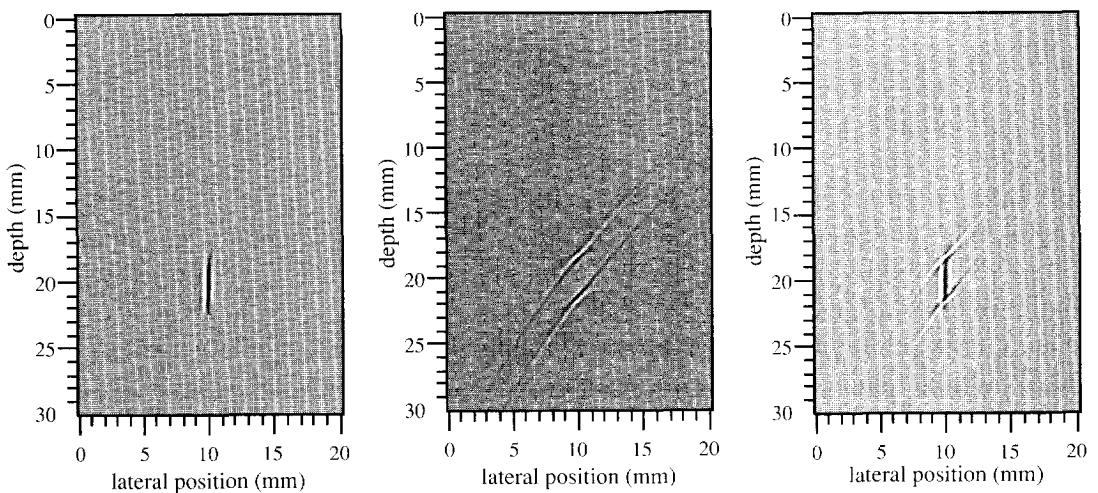
Figure 6.33: *The modelled reflection image (a), diffraction image (b) and combined Multi-SAFT image (c) of a 3 mm high vertically oriented defect.*

figure 6.33b for the vertically oriented defect and it is evident that the size of the defect can still not be determined accurately from this image. By applying the Multi-SAFT principle and combining both reflection and diffraction images, the desired image resolution can be accurately obtained (see figure 6.33c).

6.5.2 Lateral split angle optimization

As demonstrated in the previous section, both diffraction as well as reflection responses should be used for imaging, if possible[5]. It has also been mentioned, that diffraction responses have a much lower amplitude than reflection responses. This causes a problem when recording both reflection and diffraction responses in practice, for the dynamic range of the applied A/D-converter is limited and the amplitudes should not be clipped (causing severe distortion when transforming the data into the frequency domain). Thus, in practice the dynamic range of the sampled diffraction responses will not be sufficiently high to enable their employment for imaging.

However, in section 6.4 it was shown that the amplitude of the reflection response may – for certain orientations of the planar inhomogeneity – be reduced by adjusting the lateral split angle. It is assumed, that the amplitude of the diffraction responses is not affected by changes in polarization, i.e. the diffraction coefficient remains unchanged[6]. For the situation of the limited dynamic range in practice, the optimum lateral split angle will therefore be the value corresponding to an acceptable minimum of the amplitude of the reflection response. When this angle is determined (which requires the orientation of the planar inhomogeneity to be known), then the reflection as well as the diffraction responses will be sampled with sufficiently high dynamic range and both can be employed for imaging. This will be demonstrated in chapter 8, where experimental results will be presented.

In this last section, a number of important results have been presented. In the first place, it has been demonstrated that, in case the inspection aperture is limited, employing both reflection and diffraction responses is necessary in order to obtain a sufficiently high image resolution. Secondly, by making use of polarization effects in order to obtain both reflection and diffraction images it has been demonstrated that the knowledge of the general shear wave reflectivity can be of great importance. Of course, optimizing the data-acquisition configuration according to that reflectivity is only possible when the orientation of the planar inhomogeneity is (approximately) known. Fortunately, this a-priori knowledge is often available in practice. Finally, it has been made plausible that for an estimation of the general shear wave reflectivity at vertically oriented defects in girth welds of pipes the relations for the flat plate geometry can be used.

---

5   Diffraction will only be present in case the inhomogeneity possesses sharp extremities.
6   This has not been verified, although it may be concluded from experiments; in literature it seems that only diffraction coefficients have been determined for the 2-D case.

7

Accuracy of Multi-SAFT Imaging

7.1 Introduction

In this chapter the influence of different disturbing phenomena on the imaging result is evaluated. The influence of the presence of interfering responses, such as uncorrelated noise and responses from other wave paths, will be described. The influence of various errors in the imaging parameters, such as the wave velocity or the source position, will be discussed with the aid of a point diffractor model. The influences of the medium characteristics which are not accounted for by Multi-SAFT, such as surface roughness and anisotropy of the back-ground medium, are studied as well. And finally, the problem of insufficient or incomplete insonification is addressed.

In order to illustrate the influence of various effects on the imaging result, certain models (configurations) have been chosen. When other models are used, the imaging results will generally differ. The general effect, however, can be illustrated with the aid of simple models like point diffractors (used for the evaluation of errors in imaging parameters) or a vertically oriented defect (used for studying the effects of surface roughness). The results presented in this chapter are not extensive and give only a general idea of the effects. Certain specific problems definitely require further study.

7.2 Influence of Interfering Responses

By optimizing the data-acquisition procedure, as has been described in chapter 6, the responses propagating along of a specific wave path may be recorded and imaged. The recorded ultrasonic data usually contain, apart from the desired responses, a number of other responses. These other responses may be due to scattering waves which propagated along another wave path, but they may also be due to *grain noise* of the medium or electronic noise caused by the measuring equipment.

As has been defined in chapter 3, the image quality depends on the image resolution and the image accuracy. The parameters influencing the image (spatial) resolution have already been

discussed. In this section the influence of the undesired *interfering* responses, which are treated by Multi-SAFT as having propagated along the desired wave path, on the imaging accuracy is described.

7.2.1 Uncorrelated noise

In every real ultrasonic data set responses will be present due to the electronic components of the recording equipment and due to material structure of the inspected medium. In case these responses are uncorrelated they will be regarded as *uncorrelated noise*. It has been mentioned in chapter 2 that the imaging procedure is actually a spatial averaging process, i.e. uncorrelated responses will generally not interfere constructively in the image. This implies, that the presence of uncorrelated noise at reasonable signal-to-noise levels (i.e. >15 dB) will hardly affect the imaging accuracy.

This can be demonstrated by comparing the imaged results from modelled data without noise and with a signal-to-noise ratio[1] of 5 dB (see figures 7.1 and 7.2). The model consists of one point diffractor at 30 mm depth. The responses of the direct wave path (0,0) have been modelled for a pitch-catch configuration with the source at x=30 mm and the receiver scanning with scan steps of 0.5 mm from x=0 to x=80 mm. The position x=0 corresponds to the lateral position of the point diffractor (see figure 7.3). It becomes clear from the images that the presence of uncorrelated noise does indeed not seriously affect the image accuracy. Due to the mentioned spatial averaging process, the signal-to-noise ratio in the image has been improved compared to that in the time-domain ultrasonic data.

For the measurements in low-carbon steel, as have been performed with the Multi-SAFT workstation described in Appendix C, the presence of noise has not been very disturbing as the signal-to-noise ratio of the recorded ultrasonic data did generally exceed 20 dB. A few experiments have been performed on cylindrical model defects in special 'hardware tool' steel (DOSTA 45; containing 0.45% C, 0.25% Si and 0.65% Mn). The shear waves in this type of steel are strongly attenuated due to grain scattering and the signal-to-noise ratio is low (<10 dB). Yet, the imaging result is quite good and does not differ much from the image resulting from a measurement in low-carbon steel. The images are shown in section 8.2.3 of chapter 8.

7.2.2 Correlated noise

The presence of responses, which propagated along other wave paths than the one that is being chosen for imaging, can lead to spurious indications in the image. These responses are regarded as

---

1   The signal-to-noise ratio is defined as being the difference in logarithmic level between the strongest frequency component contained in the data and the noise frequency band.
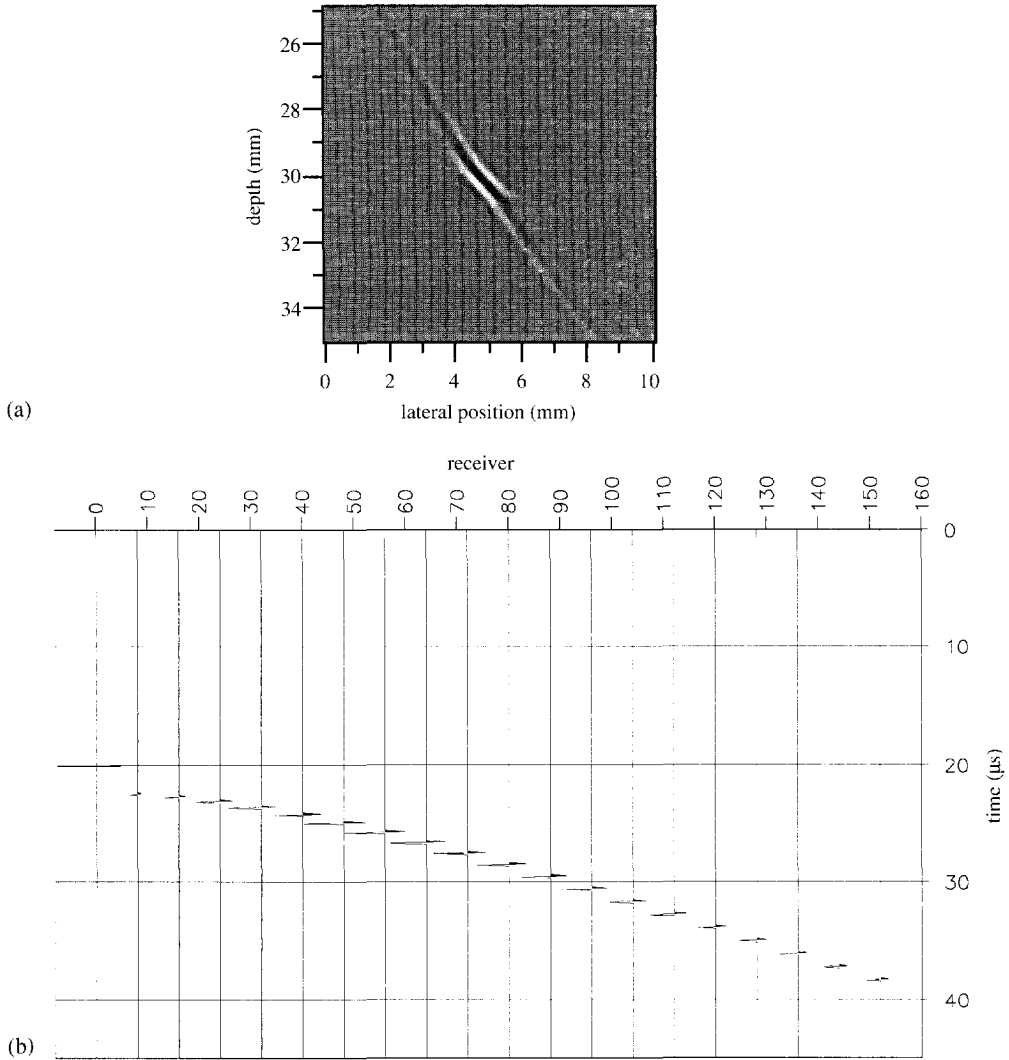
Figure 7.1: *The image (a) of a point diffractor from noise-free modelled data (b); the model is shown in figure 7.3.*

correlated noise. The extent to which these indications will affect the image accuracy depends on a number of conditions. The more difference in travel time there exists between the desired and undesired response, the larger the distance between the true and false indications in the image. This means, that the false indication may not even be located in the imaged ROI and will therefore not affect the image accuracy at all.

The more the relation between the travel time and the receiver position (shape of the (x,t)-hyperbola) of the undesired response differs from that of the desired response, the less the false
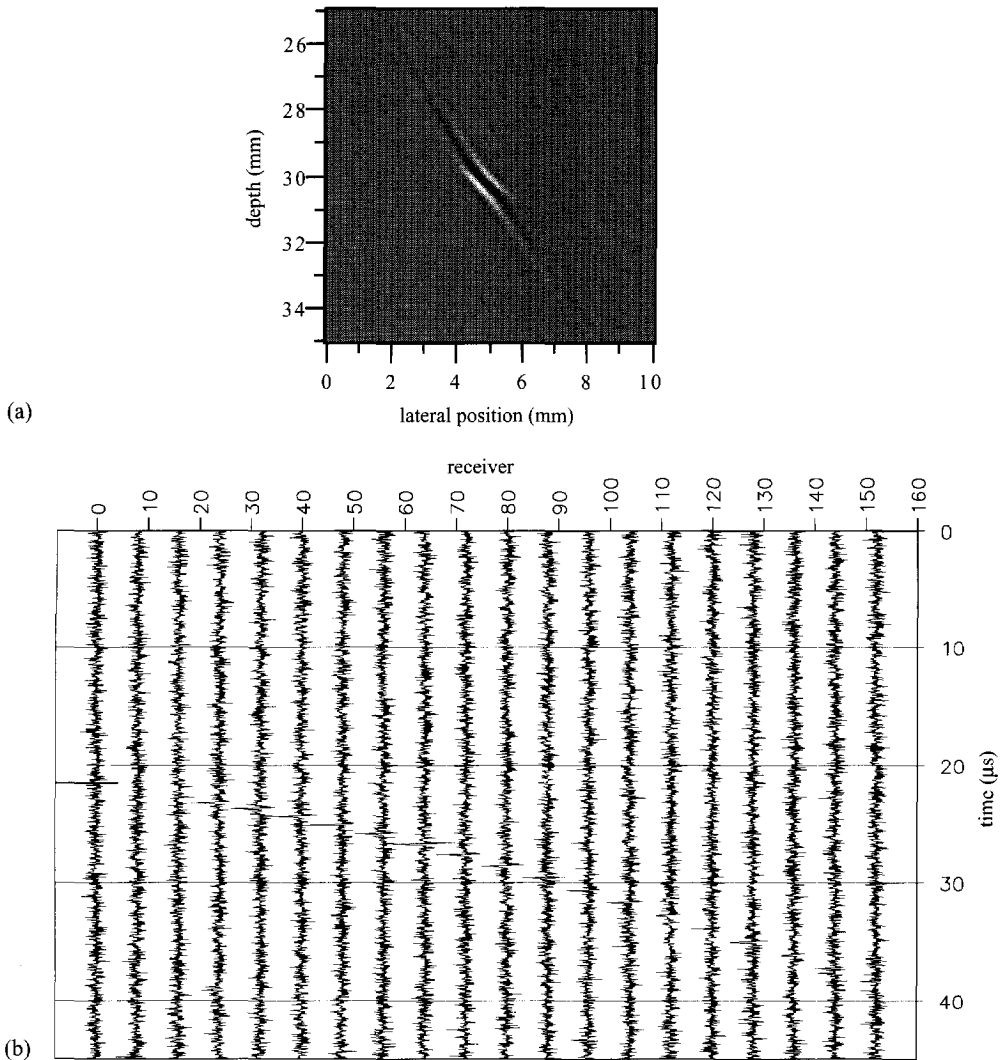
Figure 7.2: *The image (a) of a point diffractor from modelled data with a signal-to-noise ratio of 5 dB (b); the model is shown in figure 7.3.*

indication will be focused. This is a logical consequence of the summing procedure by SAFT of time samples along different hyperbolas (for a certain wave path, for each point in the ROI). It may be illustrated by a modelled example using the same model as described in the previous section, only the source is positioned at x=55 mm. The back wall is now defined at a depth of 40 mm. The hyperbolas of the responses of wave paths (0,0) and (0,1) are quite different, as can be observed from the modelled data (figure 7.4). When imaging for the (0,0) wave path the undesired (0,1)-response will not be focused very well.
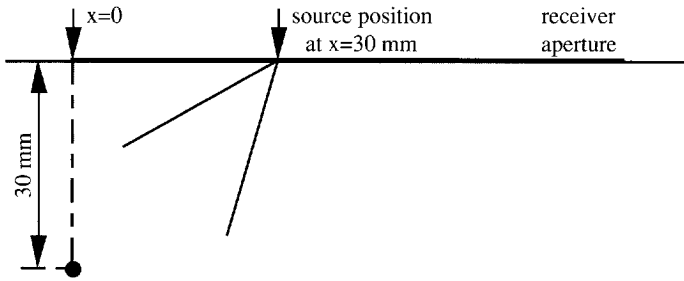
Figure 7.3: *The model used for the noise-free and noisy data of figures 7.1b and 7.2b.*

However, when the hyperbolas of the (0,0) and (1,0) wave paths are compared, it can be observed that they have exactly the same shape (figure 7.4). This is caused by the fact, that the pitch-catch configuration is applied, i.e. a fixed source position. By changing the source wave path from (0) to (1) and leaving the receiver path unchanged, the total travel time for the response of the point diffractor will only be increased by a constant. The image for the (0,0) wave path therefore features a false indication close to the true indication, caused by the (1,0) responses, as is shown in figure 7.5a.
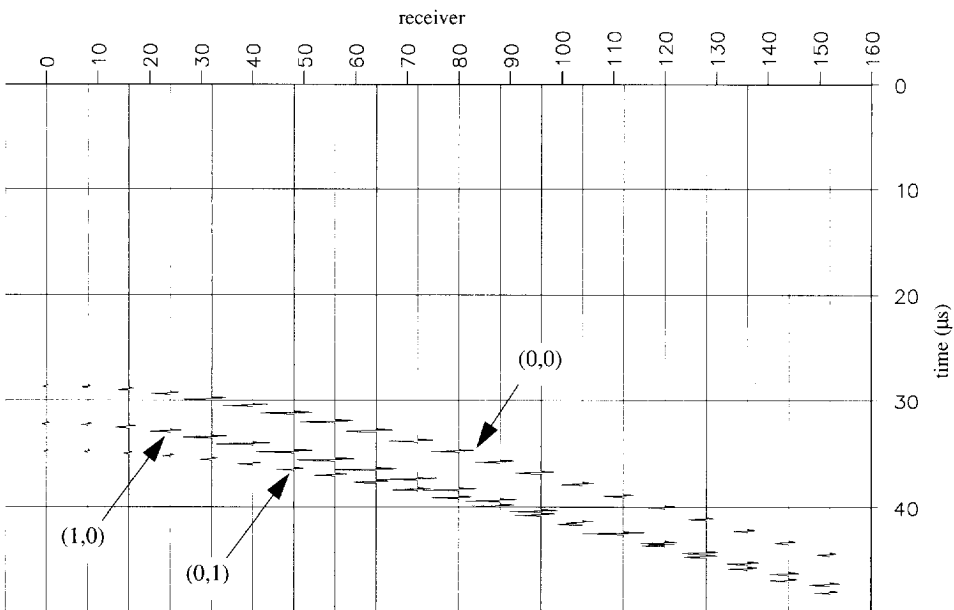
Figure 7.4: *The modelled data for a diffractor at 30 mm depth in a steel plate of 40 mm thickness; the (0,0), (1,0) and (0,1) responses are indicated.*

131
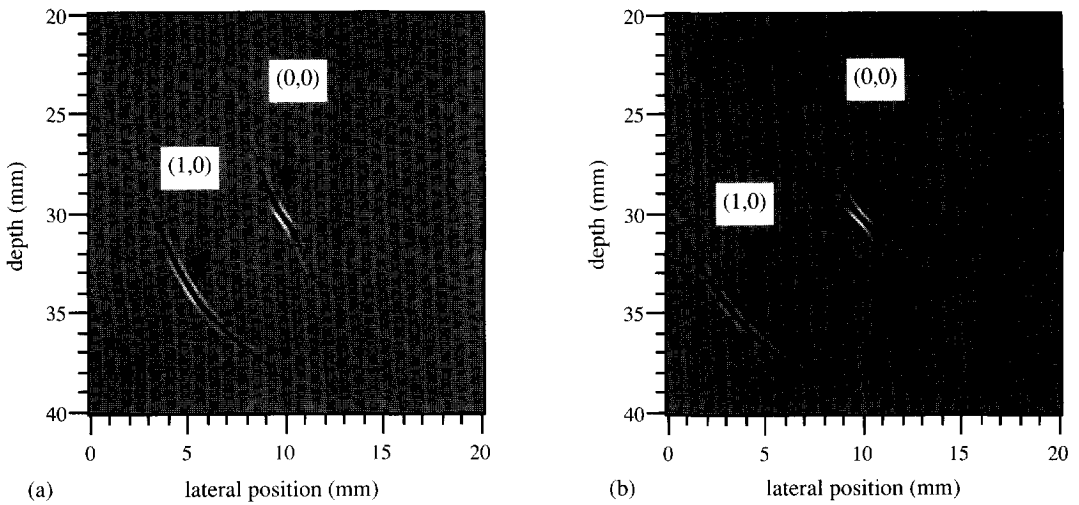
Figure 7.5: *The (0,0) images of a point diffractor modelled for a pitch-catch configuration with the source at x=30 mm (a) and x=55 mm (b) featuring spurious indications caused by the (1,0) responses.*

In practice, the source position will be chosen in such a way that responses from only a few different wave paths will be present. For vertically oriented defects these are typically the (1,0) and (1,1) wave paths in case the source beam is strongly directed towards the back wall for indirect insonification of the defect. The wave paths that would interfere with these (1,0) and (1,1) paths are the (0,0) and (0,1) paths, which are hardly contained in the data due to the optimization of insonification (directive source beam). Therefore, in practice the undesired responses from other wave paths will in general not affect the image accuracy very much.

Yet, in order to discriminate between true and false indications, two experiments involving two different source positions have to be performed. By comparing the two resulting images it will be observed, that the false indication has changed its position while the position of the true indication has remained stationary. This is illustrated by the (0,0) image in figure 7.5b (source at x=55 mm) when it is compared with the (0,0) image of figure 7.5a (source at x=30 mm).

7.2.3 Other interfering responses

There remain still a number of other types of interfering responses, namely: the response from a scatterer out of the image plane, the response due to interaction between different scatterers, the response due the typical geometry of the inspected object, and the response due to a S-P-S mode-conversion. The hyperbola of the latter response will generally differ so much from any chosen shear wave path that it may be considered not to affect the image accuracy. Moreover, this type of response will rarely be recorded in practice.
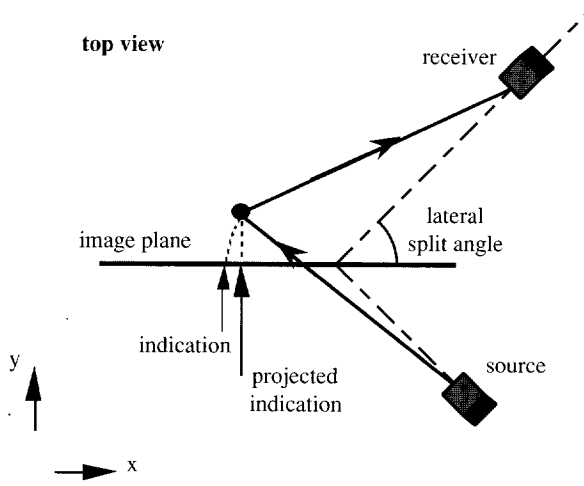
Figure 7.6: *The indication caused by an out-of-plane scatterer deviates just slightly from the (projected) location of that scatterer.*

A scatterer located out of the image plane will only influence the image accuracy if it is insonified *and* its responses are recorded. Because of the strongly directional source applied in combination with a narrow beam width of the receiver in the image plane, the amplitudes of most of the out-of-plane responses will be reasonably suppressed. However, they may occur in practice and as can be seen from figure 7.6, such a response will generally lead to an indication very close to the (projected) location of the out-of-plane scatterer.

The response, which has reflected at different parts of an inhomogeneity or at more than one inhomogeneity, cannot be processed properly. These so-called *multiple scattering responses* may
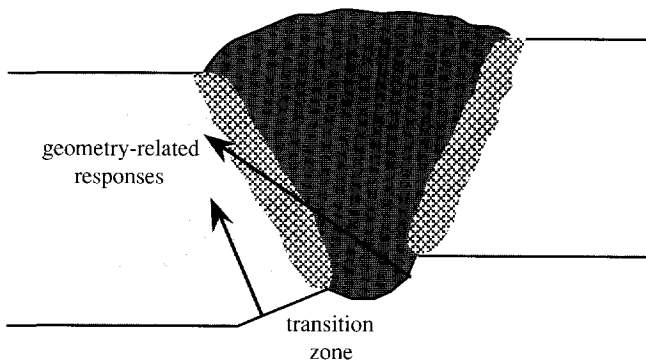
Figure 7.7: *A V-shaped weld in high-low with a transition zone; due to the irregularly shaped boundaries of the object spurious responses will be recorded.*

very well be contained in the data and will lead to spurious indications. This can be seen from the (1,1) image of two vertically oriented defects in section 8.2.2 of chapter 8.

Scattering responses from the geometrical boundaries of the object will generally not be recorded due to the applied data-acquisition configuration (in reflection) and the directivity of the receiver transducer. However, when the object is irregularly shaped at the position of the ROI, as may be the case for certain weld configurations (Shankar et al., 1991), then scattering responses from the geometrical boundaries will be recorded. A special situation is shown in figure 7.7, where two plates have been welded in a high-low situation with a transition zone. When the shape of the weld is accurately known, then the false defect indications can be identified and the image accuracy will not be affected. In practice, irregularities in the object geometry will often lead to false calls with conventional ultrasonic inspection.

For all the interfering responses described in this section it still holds, that their false indication in the image can be distinguished from the true indication by performing another experiment involving another source position, as explained in the previous section.

7.3 Influence of Errors in Imaging Parameters

In this section the extent will be evaluated to which errors in the imaging parameters, such as the thickness of the object or the wave velocity, will affect the image accuracy. To keep the evaluation unambiguous, only one error will be introduced per imaging process. The imaging parameters which are related to spatial dimensions will be called *geometrical parameters* and involve the transducer positions and the object thickness. The imaging parameters which are related to the travel time of a response will be called *propagation parameters* and involve the wave velocity of the medium and the wedge delay time.

The model that is used to evaluate the influence of errors in the imaging parameters on the image accuracy is shown in figure 7.8. It is a 40 mm steel plate (c_s=3260 m/s) with two point diffractors at 20 and 30 mm depth. The source position has been located at x=55 mm and the receiver position ranges from x=0 to x=100 (with a scan step of 1 mm), all with respect to the lateral position of the point diffractors (see figure 7.8). The insonification has been optimized for the indirect wave paths (1,0) and (1,1), and consequently the presence of other responses in the data is being ignored. The effects of errors in the imaging parameters on the imaging accuracy is different for forward and back scattering wave paths and therefore both the (1,0) and (1,1) responses will be imaged in the following sections. Figure 7.9 shows the correctly focused images for the (1,0) and (1,1) wave paths.
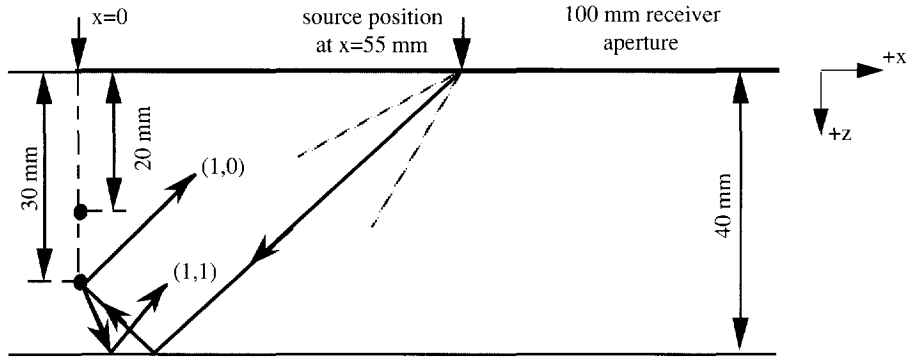
Figure 7.8: *The model that is used to evaluate the influence of errors in the imaging parameters on the image accuracy.*

The evaluation is done for the flat plate geometry. For cylindrical pipe geometries the effects are approximately the same (Lorenz, 1991). However, the difference in path length of a direct (0) path and an indirect (1) path is somewhat smaller for cylindrical pipes than for flat plates. This yields that the travel time differences between the direct and indirect responses will be smaller, which may result into a slightly better focus of false indications for a decreasing pipe radius. Of course, the influence of such an error will be different in other situations (other source and receiver positions, other defects), but the general effects can be illustrated.

Figure 7.9: *The (1,0) image (a) and (1,1) image (b) of the two point diffractors of the model shown in figure 7.8.*

135

7.3.1   Errors in geometrical parameters

To evaluate the effect of an error in the position of the source and the receiver aperture, the modelled data has been imaged with an error of +2 mm (i.e. 2 mm further away from x=0 than the correct position). Figures 7.10 and 7.11 show the images focused with the errors in, respectively, the source and receiver aperture position. It can be seen from the image of figure 7.10, that the error in the source position results in a very small (<1 mm) displacement of the indications, which are hardly out of focus. The (positive) error in the position causes the calculated path lengths to the diffractors to be slightly larger than the actual wave path. Consequently, the indications are displaced in the positive depth direction (+z-direction) for the (1,1) wave path and in both the positive lateral direction (+x-direction) and the –z-direction for the (1,0) wave path. The displacements are smaller than 1 mm.

For the error in the receiver aperture it can be seen from the images in figure 7.11 that the indications are displaced in both the +x-direction and the –z-direction for the (1,1) wave path and in the both the +x- and +z-directions for the (1,0) wave path. The displacement is in the order of the error introduced (~2 mm) and the (1,0) indications are slightly out of focus while the focus of the (1,1) wave path is hardly affected. The difference between the displacements resulting from the error in the position of the source and the receiver aperture is caused by the fact, that the error

Figure 7.10: *The (1,0) image (a) and (1,1) image (b) of the two point diffractors of the model shown in figure 7.8 for an error of +2 mm in the source position.*

Figure 7.11: *The (1,0) image (a) and (1,1) image (b) of the two point diffractors of the model shown in figure 7.8 for an error of +2 mm in the position of the receiver aperture.*

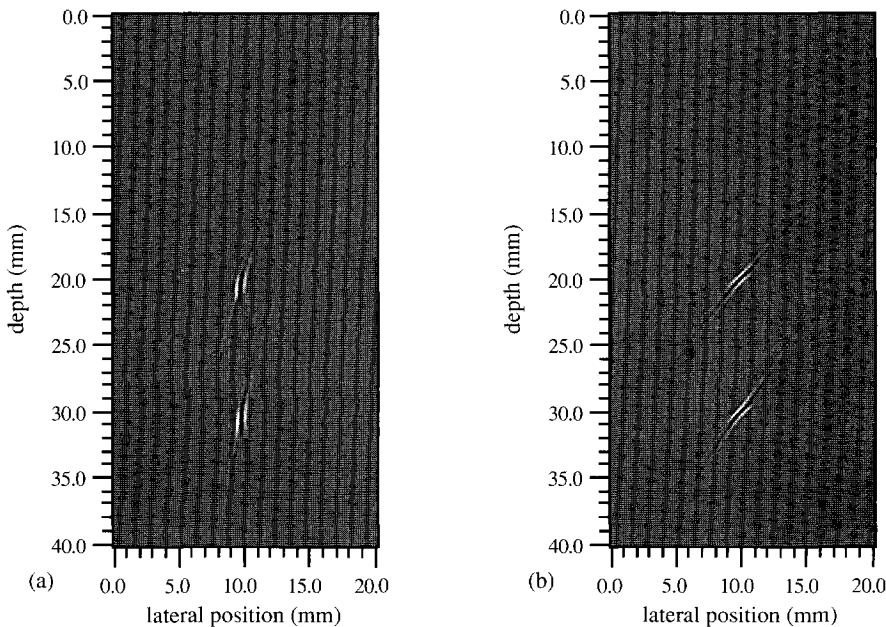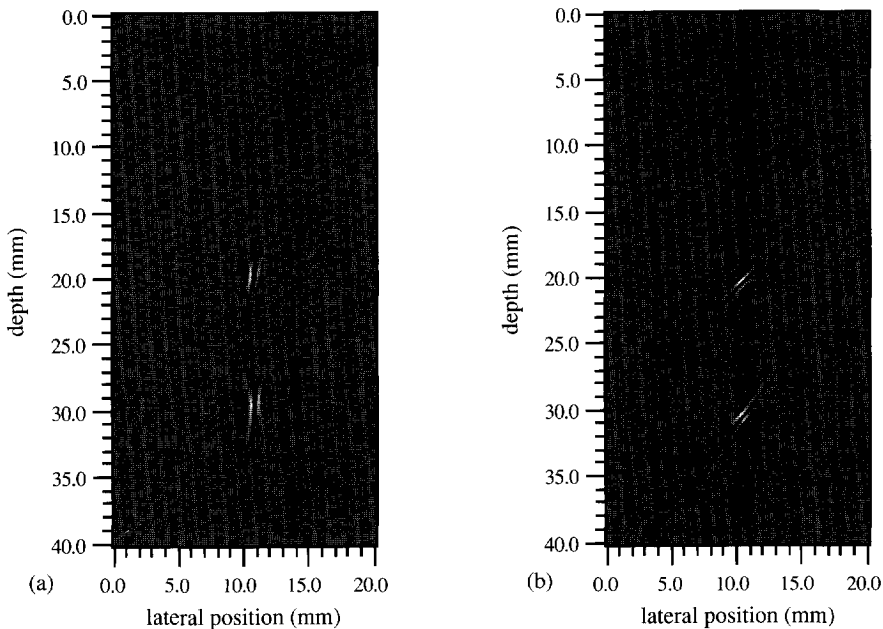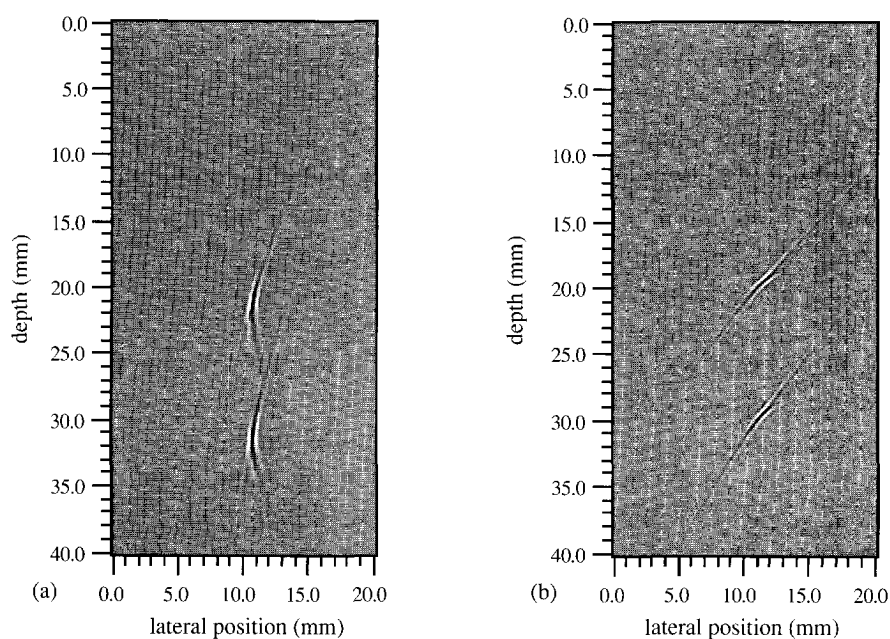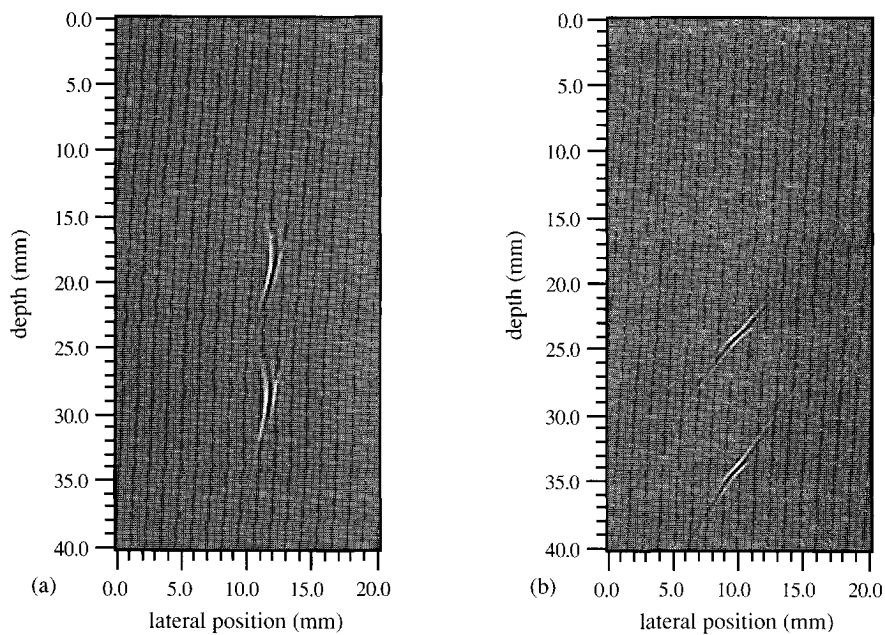**Figure 7.12:** *The (1,0) image (a) and (1,1) image (b) of the two point diffractors of the model shown in figure 7.8 for an error of +2 mm in the thickness of the plate.*

137

in the source position introduces a travel time error which is constant, while for each receiver position the relative travel time error is different.

When an error of +2 mm is introduced to the thickness of the plate (i.e. the plate is thought to be 2 mm thicker than in reality) then the images of figure 7.12 are the result. From these images it can be observed that the (1,1) indications are hardly out of focus while the (1,0) indications are considerably out of focus. The (positive) error in the thickness causes the calculated path lengths to the diffractors to be slightly too large. The displacement of the (1,1) indications is in the +z-direction and approximately twice the introduced error (~4 mm). This is obvious for a back scattering wave path, as the inspection aperture is translated away from the diffractors in the z-direction by a distance of twice the error in the thickness. The (1,0) indications are displaced in the +x- and −z-direction by a distance in the order of the error introduced in the thickness of the object (~2 mm).

From the imaging results of figures 7.10 to 7.12 it can be concluded, that an error of +2 mm in the source position hardly affects the image accuracy. The influence of such an error in the position of the receiver aperture is slightly larger and approximately proportional to the magnitude of that error. The effect of an error of +2 mm (5%) in the thickness of the plate causes large displacements being proportional to the error introduced for the (1,0) forward scattering wave path and proportional to twice the introduced error for the (1,1) back scattering wave path. The focus of the indications is in general hardly affected for errors in the geometrical parameters, apart from the focus of the (1,0) indication, which is only considerably affected for the error in the thickness.

In this section, only the error in the position of the receiver *aperture* has been evaluated. In case a (normally distributed) error in the scan step is introduced, which may be due to improper scanning, the effect on the image will be slightly different. This is illustrated by the images of figure 7.13, where a variable scan-step error in the interval of ±0.5 mm and ±1.0 mm has been introduced for imaging the modelled data. Although the focus is just slightly affected for the ±0.5 mm error, the point diffractors are positioned correctly. In case the error lies in the range of ±1.0 mm the image focus strongly deteriorates. These effects will even be stronger for a pulse-echo configuration, because in that case the error in the scan step will be introduced for the receiver as well as for the source position.

From this section it can be concluded, that the plate thickness is the most critical geometrical parameter and should be measured as accurately as possible in practice in order to avoid the image accuracy to be strongly affected. It should also be noted, that an error in a geometrical parameter causes a relative travel time error, which decreases for increasing path length. For this reason, errors in geometrical parameters do not affect the focus of the indications very much.

Figure 7.13: *The (1,0) images (a,c) and (1,1) images (b,d) of the two point diffractors of the model shown in figure 7.8 for a variable receiver scan-step error of ±0.5 mm (a,b) and ±1.0 mm (c,d).*

7.3.2 Errors in propagation parameters

To evaluate the effect of an error in the wave velocity, the modelled data has been imaged with an error of +100 m/s (i.e. 100 m/s higher than the correct wave velocity; ~3%). The (positive) error in the wave velocity causes the calculated travel times to be slightly too small. The effect on the image of such an error is quite destructive, as can be seen from the images in figure 7.14. The indications have been displaced mainly in the –x-direction (~3 mm) and are considerably out of focus for both wave paths. This is due to the fact, that in for errors in propagation parameters the relative error in the travel time increases for increasing path length, while the it decreases for errors in the geometrical parameters.

An error of +1 µs in the total wedge delay time (1 µs longer than the correct value) has been introduced for imaging the modelled data. The (positive) error in the delay time causes the calculated travel times to be slightly too small. The effect on the images can be observed from figure 7.15. The (1,1) indications have been displaced slightly in the +x- and +z-directions (~1 mm) and remain reasonably in focus. The (1,0) indications have been displaced somewhat more in the +x- and –z-directions (~2 mm) and are considerably out of focus.

An error in the total wedge delay time may be caused by improper determination of this value
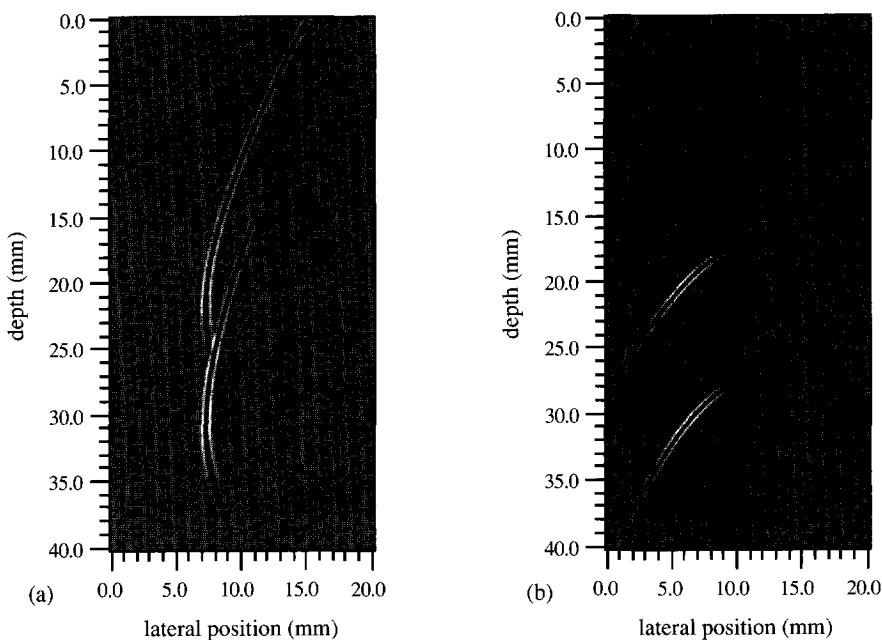
Figure 7.14: *The (1,0) image (a) and (1,1) image (b) of the two point diffractors of the model shown in figure 7.8 for an error of +100 m/s in the wave velocity.*

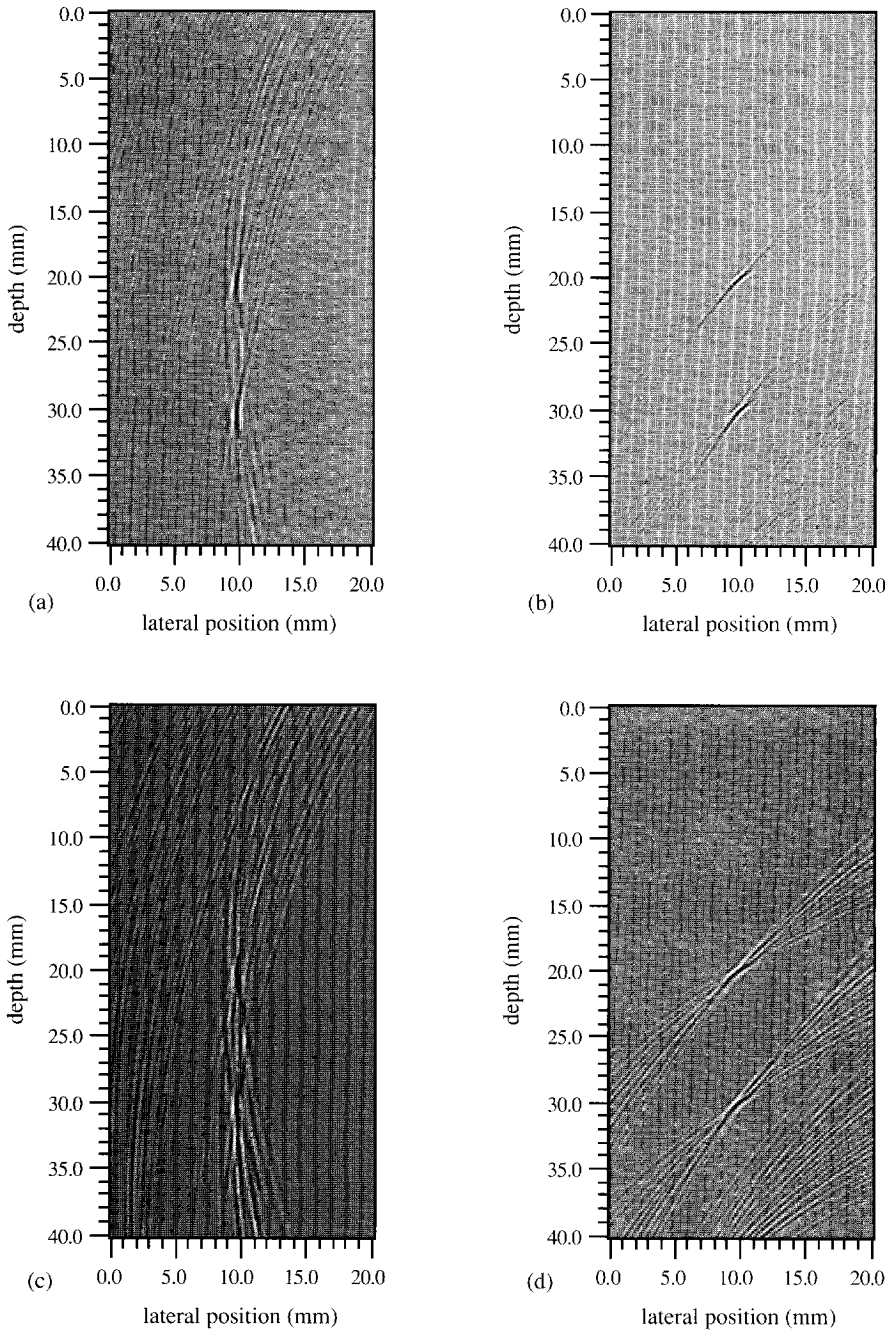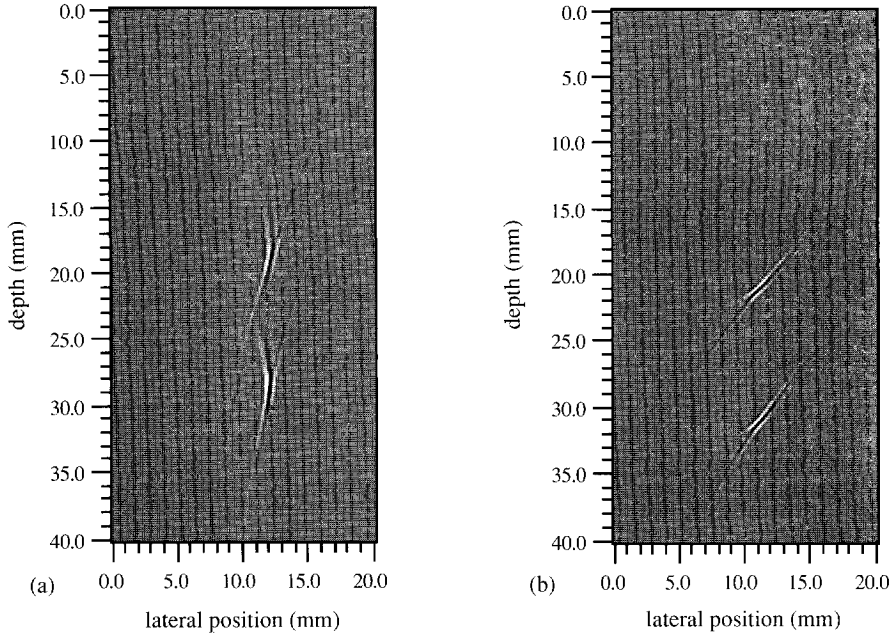**Figure 7.15:** *The (1,0) image (a) and (1,1) image (b) of the two point diffractors of the model shown in figure 7.8 for an error of +1 μs in the total wedge delay time.*

(calibration) or by the fact, that a fixed index point has been defined. As mentioned in chapter 4, the poiusition of the index point depends on the angle of insonification/reception according to Snell's law. To determine the wedge delay time error, a situation as shown in figure 7.16 is evaluated. A wedge transducer has an index point defined by the main direction of the beam in steel. The position of this index point defines also the constant wedge delay time τ. The response from a point diffractor at depth d is assumed to enter the wedge at the index point, but in reality it will enter the wedge at a slightly different position (see figure 7.16).

By applying a constant wedge delay time, the computed travel time t' of an ultrasonic response from the point diffractor at depth d in figure 7.16 to the piezo crystal will slightly differ from its real travel time t_r. This difference will be defined as a wedge delay time error $\Delta \tau$. The calculation of this wedge delay time error as function of the lateral (x-)offset of the transducer is described in Appendix B and the results are shown in figures 7.17 and 7.18 for a 45° and 60° wedge transducer and diffractors at 10, 30 and 50 mm depth[2].

The 45° wedge transducer has a bounded beam and is therefore assumed to receive responses only

---

2   For the calculation of the wedge delay time errors, the vertical distance of the piezo crystal to the interface is assumed to be 10 mm, which corresponds to the dimensions of real wedge transducers.
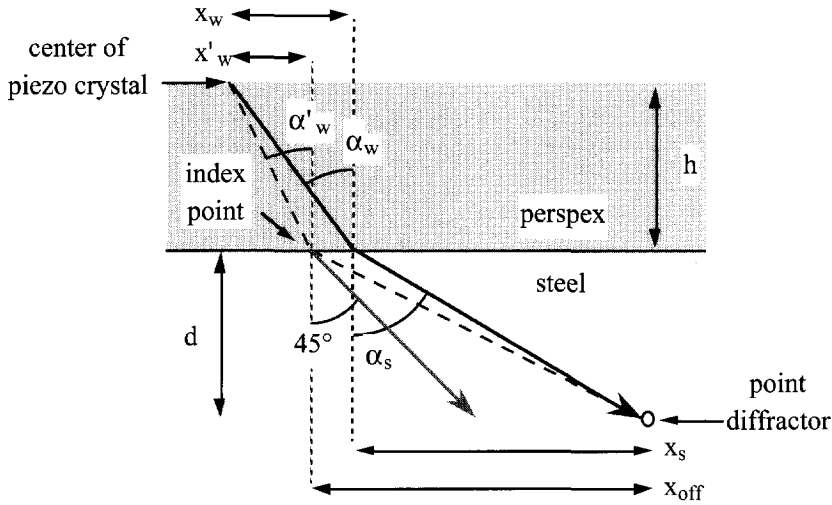
Figure 7.16: *The configuration for the evaluation of the influence of a fixed index point on the image accuracy.*

under an angle from $30°$ to $60°$. This means, that the responses will not be recorded along the entire aperture, as becomes apparent from the curves in the graph of figure 7.17. In figure 7.18 the wedge delay time errors for a $60°$ wedge transducer, assuming to receive responses under an angle from $45°$ to $75°$, are shown for diffractors at different depths. It can be concluded from these graphs, that the constant wedge delay time for a fixed index point will in most situations not lead to a noticeable reduction of the image accuracy, unless the defect is located *very* near the inspection surface. In such a situation, an indirect wave path has to be chosen for imaging.
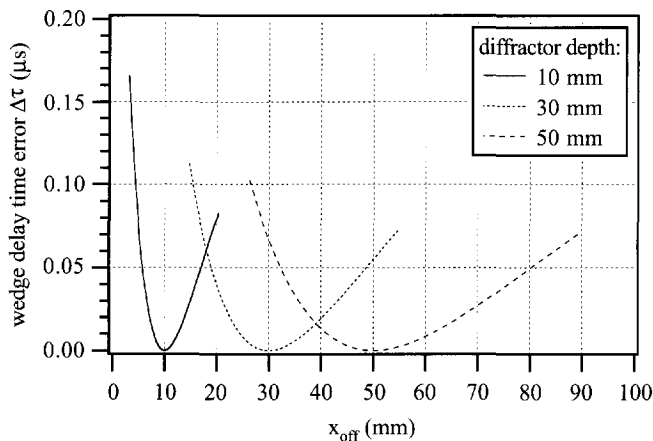
Figure 7.17: *The wedge delay time error $\Delta\tau$ resulting from assuming a fixed index point as a function of the x-offset between the index point and the lateral position of the point diffractor for a $45°$ insonification angle.*
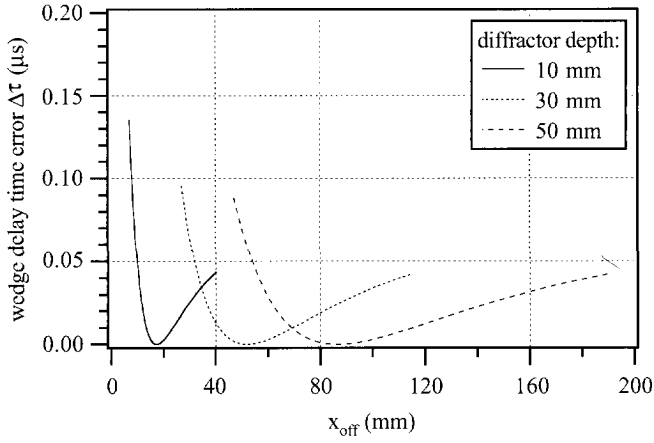
Figure 7.18: *The wedge delay time error $\Delta\tau$ resulting from assuming a fixed index point as a function of the x-offset between the index point and the lateral position of the point diffractor for a $60°$ insonification angle.*

Evaluating all the results presented in section 7.3, it can be concluded that errors in the imaging parameters affect the focus as well as the position of the indications. It may be observed, that the focus of the indications in the (1,0) images are slightly more affected than in the (1,1) images. This is due to the fact, that the spatial bandwidth of a forward scattering wave field (such as (1,0)) is smaller than of a back scattering wave field (such as (1,1)). Errors in the propagation parameters affect the image quality the most, as they cause a relative travel time error which increases for increasing path length. For variable scan-step errors larger than ±0.5 mm the image quality will be considerably deteriorated, because then the imaged back-propagated ellipses start to interfere destructively.

It is not surprising that the most critical imaging parameter is the wave velocity, as it plays a key role in the imaging process by transforming travel times into path lengths. The correctness of the applied wave velocity can be evaluated by observing the maximum amplitude in the image, when imaging for small deviations of its value. Optimum constructive interference is expected to occur for the correct value of the wave velocity, thus leading to a maximum amplitude of the indication in the image. Moreover, the correctness of the applied wave velocity can be checked by imaging the same scattering energy for two different wave paths, for instance (1,1) and (1,3) (as long as they are actually contained in the recorded data). The (1,1) and (1,3) indications should then overlap in the combined image in case the value of the applied wave velocity is correct. Such procedures, for instance, can be used in situations where the wave velocity cannot be determined accurately enough.

7.4 Influence of Medium Characteristics

The structure of the medium as well as the reflectivity characteristics of the object influence the propagation of shear waves. Changes in amplitude, phase and polarization may occur on reflection, not only at the surface of the inhomogeneity, but also at the object boundaries. Moreover, such changes can also be introduced during scanning (irregular surface or coupling problems). In this section the influence on the image accuracy of defect-surface roughness, as well as of inhomogeneity and anisotropy of the (back-ground) medium will be discussed.

7.4.1 Changes in amplitude, phase and polarization

During the data-acquisition process in a homogeneous (back-ground) medium the amplitude, phase and polarization of a source wavelet may be affected by the transducer coupling, by the reflection at the object boundaries and by scattering from the inhomogeneity. Changes in the amplitude (caused by attenuation and mode-conversion) will not affect the image accuracy, as long as the responses still have detectable amplitudes of course. Changes in the phase (caused by reflection and changes in polarization) will only affect the image accuracy in case they are not constant along the receiver aperture, i.e. when the phase change is depending on the receiver position. Position-dependent phase changes will result into a different constructive interference of the back-propagated responses during imaging.

This is illustrated in figure 7.19 for an experimental data set on a slag inclusion (see section 8.3.3 for details), where a gradual phase change from 0° to 40° is introduced along the 100 mm long
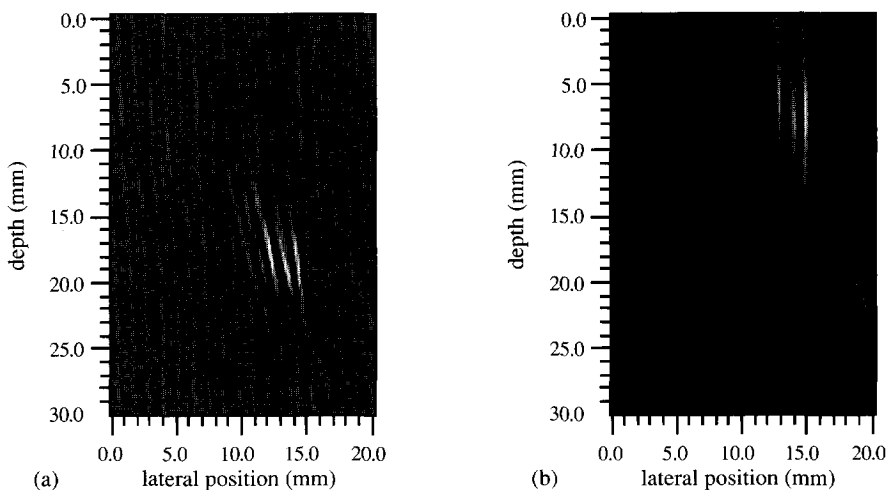
Figure 7.19: *The (2,1) images of a slag inclusion without (a) and with (b) introducing a gradual phase change of 40° along the receiver aperture.*

receiver aperture. The image still features the indication, but it is evidently mis-located when it is compared to the correct image.

The coupling layer should always be kept as thin as possible. In case the receiver transducer is scanned along the inspection aperture with a coupling layer of considerable thickness (>0.5 mm), the wave path length will change as a function of angle of incidence. This will cause an error in the total recorded travel time of the responses and will lead to unfocused and mis-located indications in the image (McGrath et al., 1989). The errors can be compared to errors in the wave velocity and should be avoided in practice by keeping the coupling layer thickness negligibly thin.

Phase changes at the object boundaries are not compensated for by Multi-SAFT. This does not give any problems in case those phase changes are (approximately) constant for every recorded direction, i.e. as long as the recorded responses are equally affected. For angles of incidence at a planar defect in the range close to the critical angle, the phase of the reflected shear wave may change quite considerably as a function of that angle of incidence, depending on the polarization effects (i.e. the value of the locally reflecting SH-component). However, the angle of incidence can often not easily be determined in practice due to the complexity of the 3-D data-acquisition configuration.

Thus, in case poorly focused indications are imaged, another experiment for a different source position should be performed in order to determine whether or not the poor focusing is the result of variable phase changes in the recorded responses. Combining multiple images resulting from responses of different wave paths, the additional phase changes caused by reflection at the object boundaries (~180°, see chapter 6) should be eliminated in order to keep the phase of the wavelet in the images constant for all wave paths.

7.4.2 Roughness of the reflecting surface

Roughness of the defect surface and object boundaries will mainly lead to a reduction of the amplitude of reflection responses and will increase the amount of diffracted energy, depending on the degree of roughness (see figure 7.20). Lord Rayleigh was the first to study wave scattering from rough surfaces (Rayleigh, 1877). His work lead to the so-called *Rayleigh criterion* for the definition of the degree of roughness of a surface. For monochromatic plane waves the Rayleigh criterion states that if the phase difference of any two reflecting rays is smaller than $\pi/2$, then the surface may be called 'smooth', otherwise it will be called 'rough'.

If this condition is averaged across the surface, according to Ogilvy (1991), then Δh may be replaced by σ, defined as the RMS of the distance deviation Δh from a perfectly smooth reference plane (see figure 7.21). Consequently, the degree of roughness is related to the applied wave
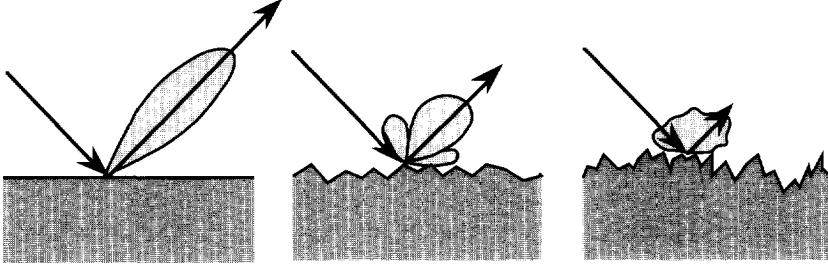
Figure 7.20: *Increasing roughness will lead to a decrease of reflection amplitude and an increase of diffracted responses.*

length λ, the incident angle α and the standard deviation σ. Based on these parameters, the Rayleigh criterion for smooth surfaces has been defined:

$$R_a = \frac{2\pi}{\lambda} \, \sigma \cos \alpha < \frac{\pi}{4} \, , \tag{7.1}$$

where R_a is known as the Rayleigh parameter.

The roughness of a surface also depends on the correlation length L_c, which controls the rate of change of surface height with distance along the surface. For surfaces with a Gaussian height distribution[3] the correlation function $C(R)$ may be defined as:

$$C(R) = \exp\left\{ -\frac{R^2}{L_c^{\,2}} \right\} \, , \tag{7.2}$$
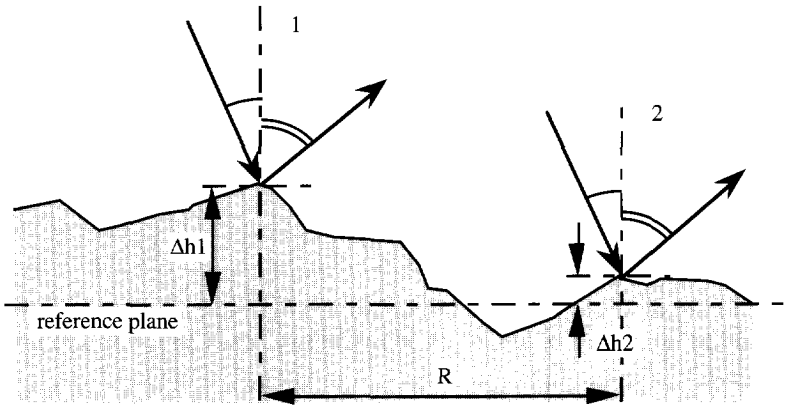
Figure 7.21: *The configuration for the derivation of the Rayleigh criterion.*

---

3   This is just an assumption to keep the mathematical description simple, for in practice many variations in correlation functions do exist.

with R the distance between two points along the surface. In equation (7.2) the correlation length L_c is defined as the distance over which the correlation function $C(R)$ falls by $1/e$.

With the aid of the finite difference modelling scheme the effects of defect roughness on the imaging result have been qualitatively evaluated for the case of a vertically oriented defect. The model is the same as described in chapter 4. A number of modelling experiments has been performed for defects with different roughness related to σ and L_c, as described in table 7.1 and denoted model A through F. The wave length of the central frequency component is approximately 2.5 mm. As a reference case, a perfectly smooth vertically oriented defect is also modelled (model F). The modelled crack-like defects are shown in figure 7.22, where it should be noted that the cracks of models A, B and C possess the same Rayleigh parameter. The value of the Rayleigh parameter is ~0.67 for a 45° angle of incidence and 2.5 mm wave length, which may be regarded as smooth ($<\pi/4$) according to equation (7.1).

Table 7.1: *The roughness of the different modelled crack surfaces and the corresponding RMS height deviation σ and the correlation length L_c.*

model	σ (μm)	L_c (μm)
A	375	250
B	375	125
C	375	500
D	125	250
E	750	250
F	0	–

From the models A, E and F the recorded B-scans and snapshots are shown in figure 7.23 to 7.25, where the deformation of the wavelets and the amount of scattering responses for increasing roughness can be clearly observed. The imaging results for all models of table 7.1 are shown in figure 7.26. It can be concluded that, although models A, B and C are considered to be 'smooth', the image quality clearly depends on the correlation length and may be quite poor. The dimensions of the crack of model C may be regarded as the most likely to be encountered in practice and it is obvious from its image in figure 7.26 that for an accurate defect characterization more insonification angles, i.e. more experiments are necessary. From the image of crack model B the vertically oriented defect is nicely reconstructed, although the (direct) scattering energy causes a strong false indication to the left of the crack tip. With the aid of more experiments, applying different insonification angles, the false indication should be identifiable.
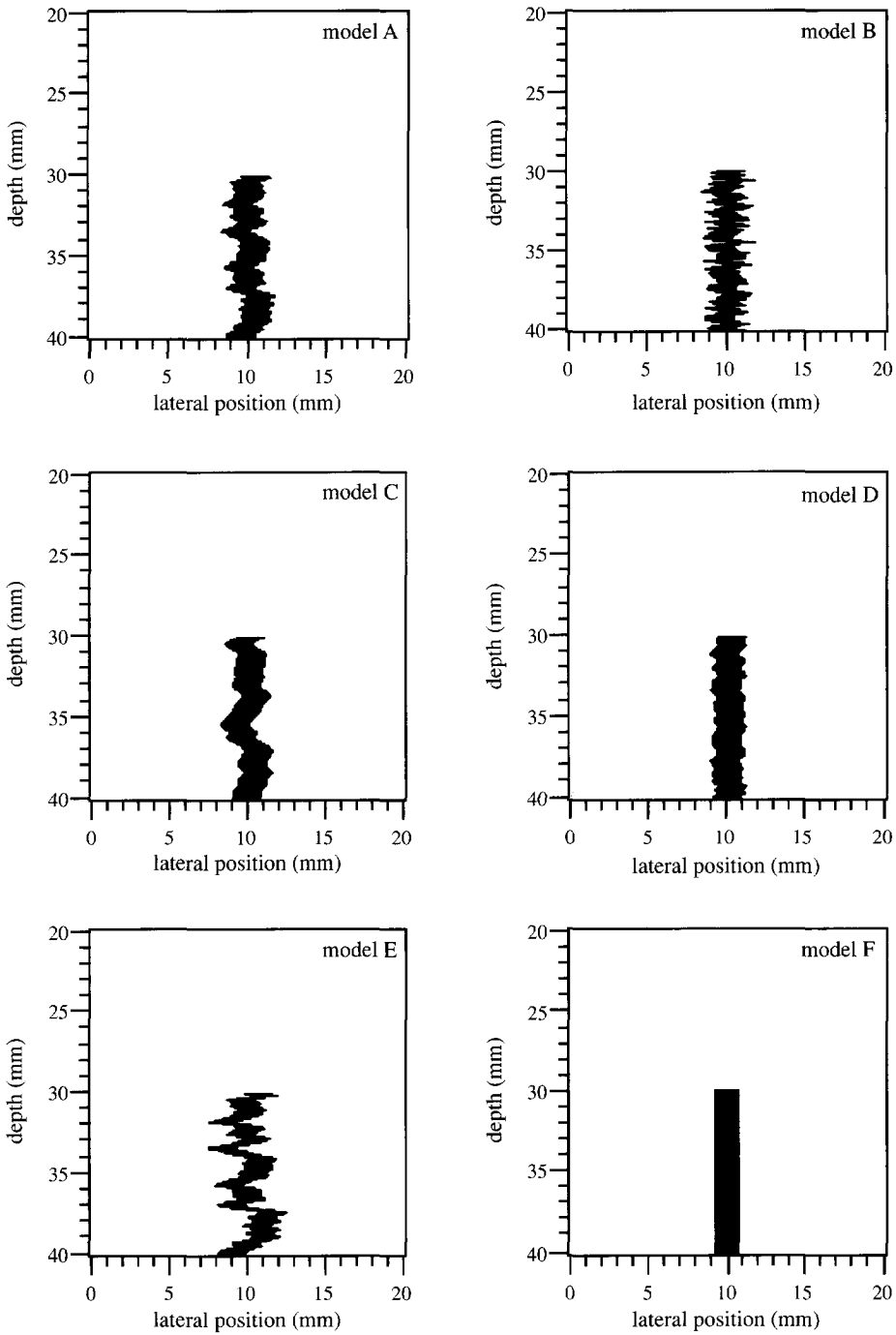
Figure 7.22: *The different modelled cracks, featuring different types of roughness (see table 7.1).*

(a)

(b)
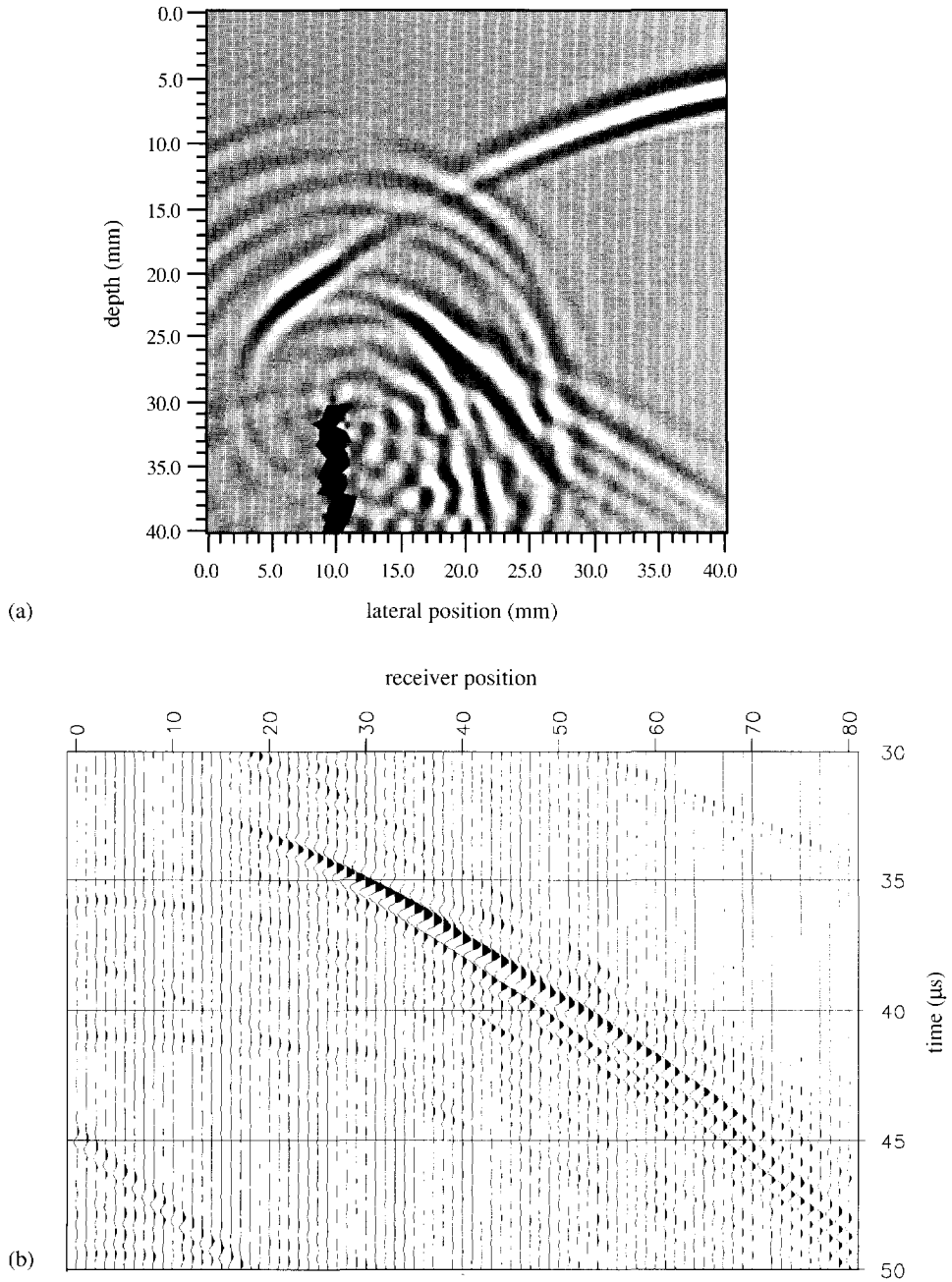
Figure 7.23: *A modelled snapshot (a) and a part of the B-scan data (b) of the reflection of an incident shear wave at a rough vertically oriented defect (model A, see table 7.1).*

(a)

(b)
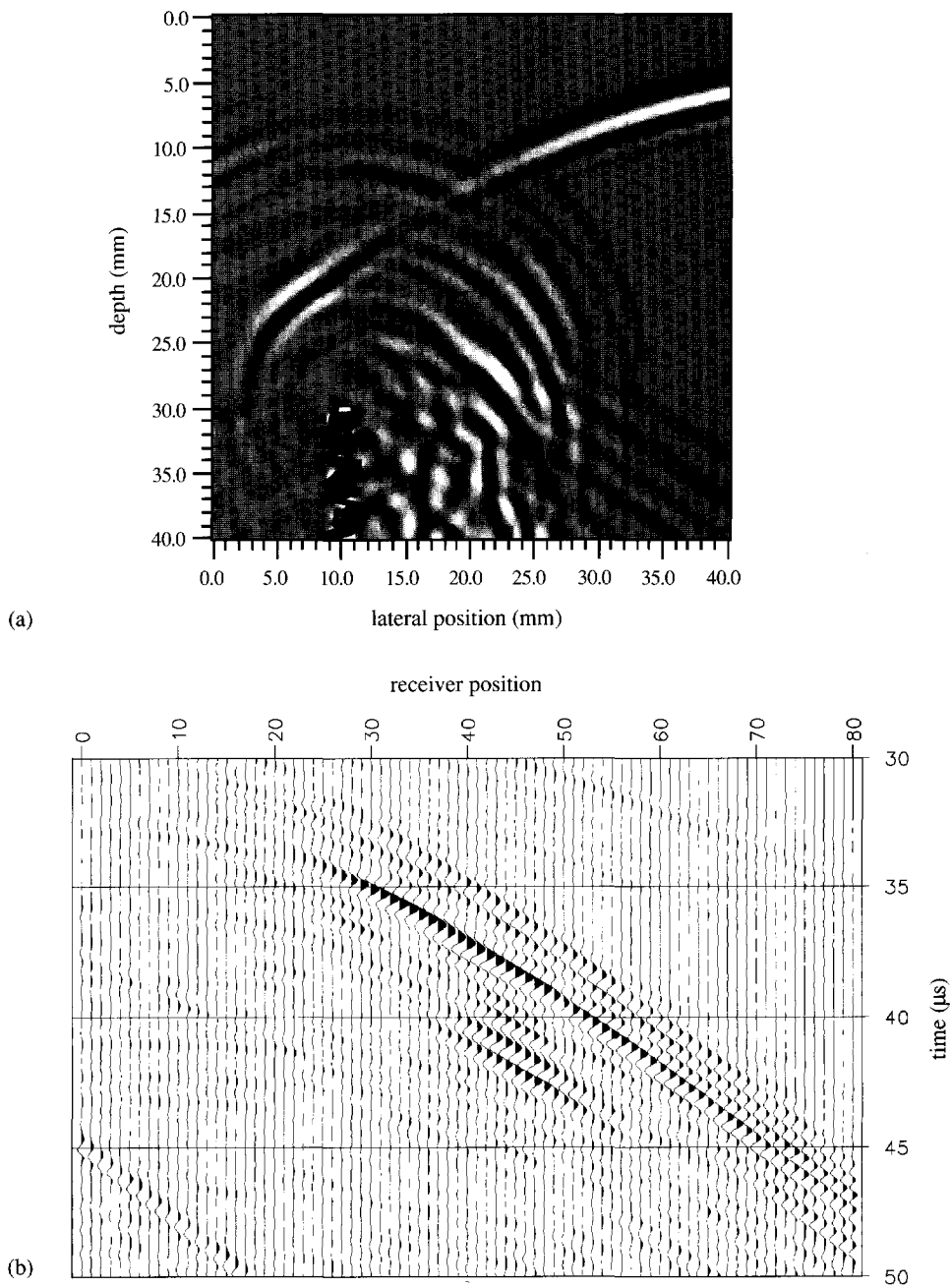
Figure 7.24: *A modelled snapshot and a part of the B-scan data of the reflection of an incident shear wave at a rough vertically oriented defect (model E, see table 7.1).*

(a)

(b)
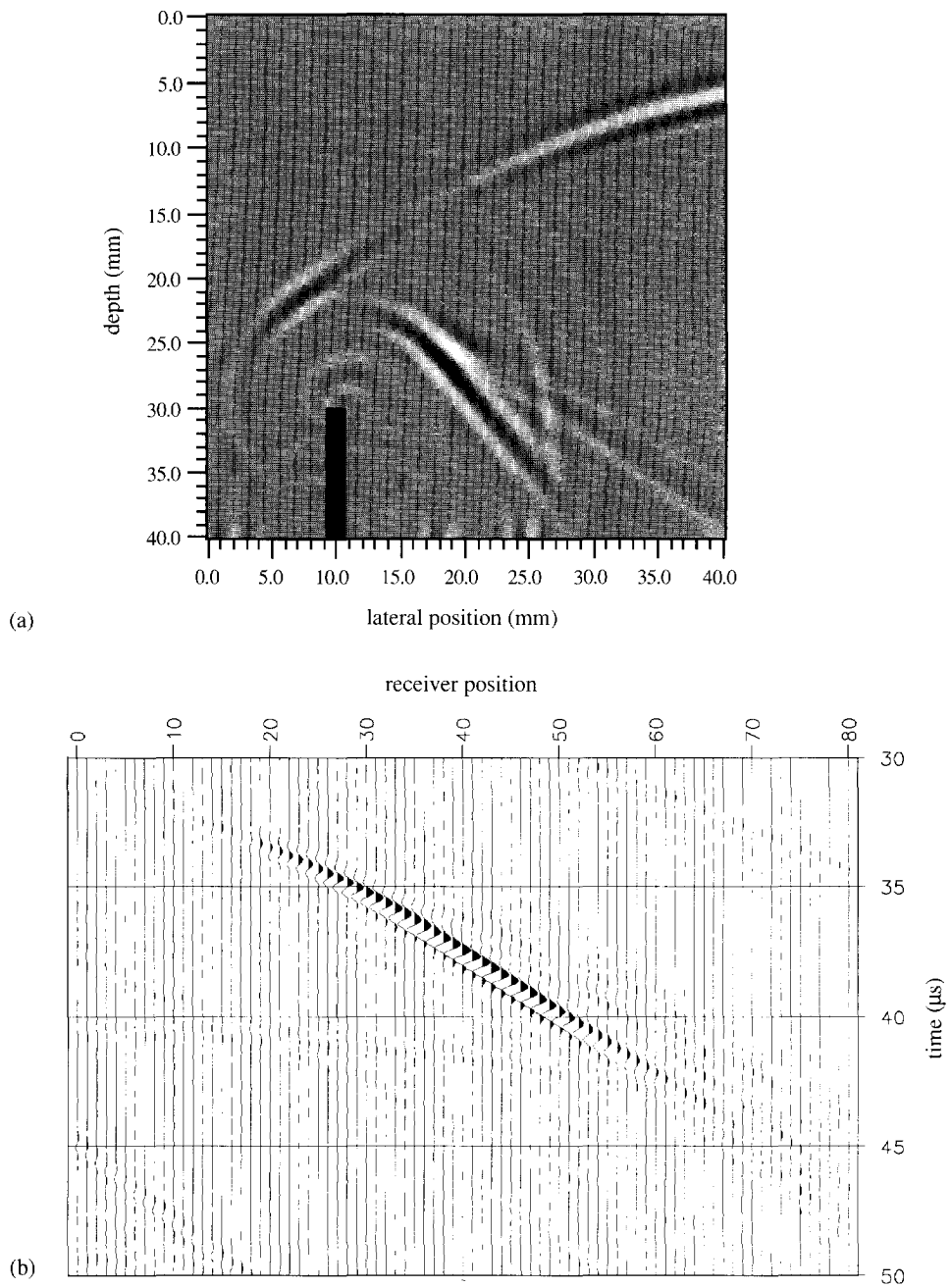
Figure 7.25: *A modelled snapshot and a part of the B-scan data of the reflection of an incident shear wave at a perfectly smooth vertically oriented defect (model F, see table 7.1).*
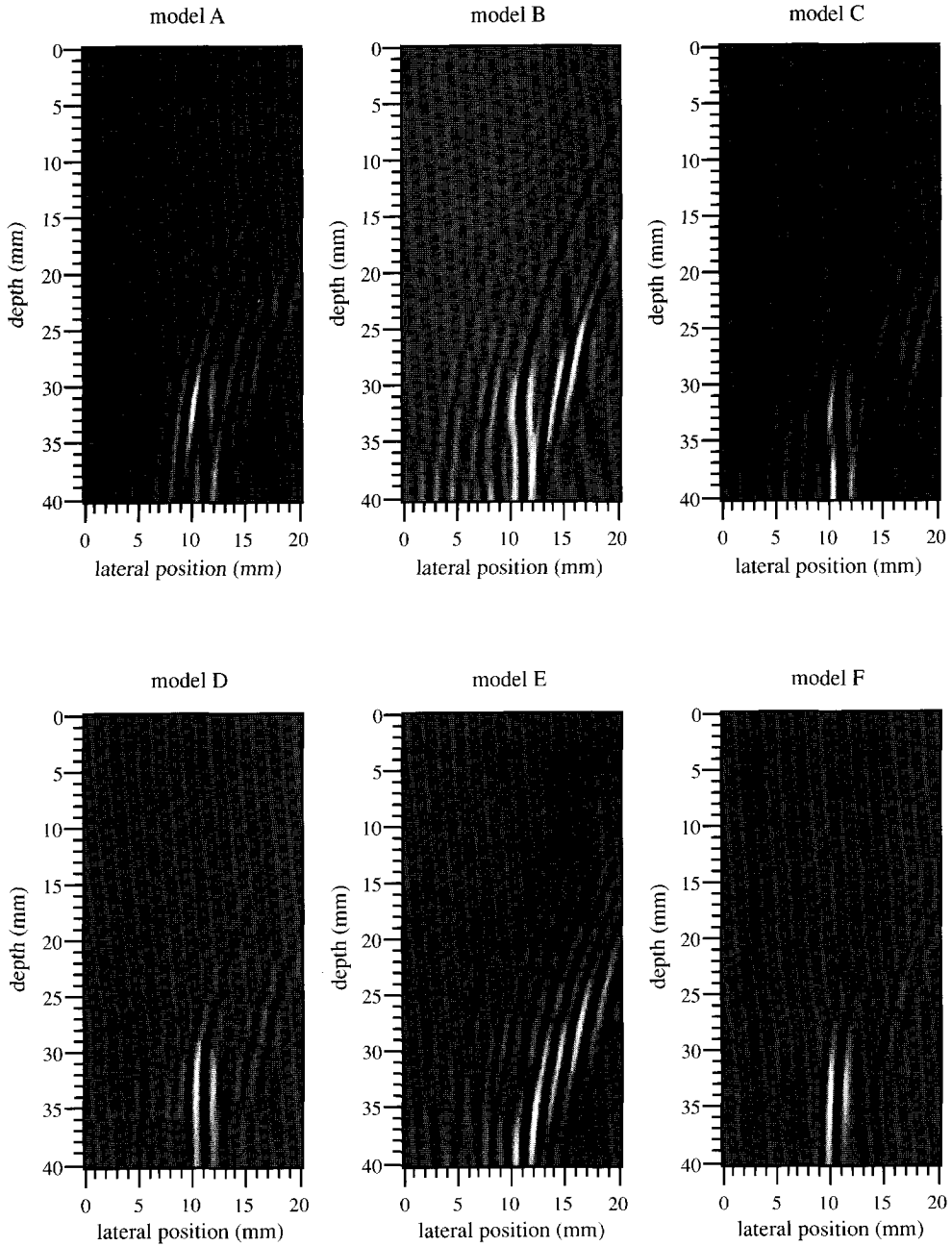
Figure 7.26: *The (1,0) images resulting from imaging the finite-difference modelled B-scan data of the reflection of an incident shear wave at vertically oriented defects of different degrees of roughness (see table 7.1).*

As roughness depends on wave length, the application of a low-pass frequency filter prior to imaging should reduce the measure of roughness and consequently the effects on the imaging results. In figure 7.27 the same images are shown as in figure 7.26, but the time-domain data has been low-pass filtered and the main wave length has almost doubled to 4.5 mm. The imaging results are clearly less affected by the roughness when compared to the perfectly smooth case. Thus low-pass filtering may increase the image accuracy, although it will decrease the image resolution...

7.4.3 Inhomogeneity and anisotropy

The Multi-SAFT algorithm has been developed for homogeneous isotropic back-ground media. Any inhomogeneity or anisotropy of this back-ground medium will lead to errors in the geometrically calculated wave path lengths. This will subsequently lead to errors in the total travel times and to loss of focus and mis-location of indications due to destructive interference. In case the inhomogeneity of the back-ground medium is caused by a distribution of very small local changes in the medium parameters (as is the case for the 'hardware-tool' steel as described in section 7.2.1), then the medium may be considered generally homogeneous. When the additives are distributed uniformly in the medium, an *average wave velocity* can determined. The image accuracy will then hardly be affected, although the signal-to-noise ratio will be reduced due to the extensive scattering loss.

Azimuthal anisotropy of the medium may be accounted for by determining the wave velocity in the directions in which the waves will propagate during data-acquisition. By applying the appropriate (average) *direction-dependent* wave velocity for imaging, the image accuracy will hardly be affected by the azimuthal anisotropy. As in practice the material will nearly always possess some anisotropy (due to the manufacturing process), it is important to determine the wave velocity in different directions to check whether or not the effects of anisotropy should be taken into account.

The most frequently encountered inhomogeneous and isotropic medium is the welded area. Its medium properties cannot be determined accurately and the responses that propagated a considerable distance through this welded area are not suited for imaging with Multi-SAFT. This will be illustrated in chapter 8, where a lack of interrun fusion in a weld is imaged. In such a situation only the presence of an inhomogeneity is revealed, but its characterization from the Multi-SAFT images is almost impossible.
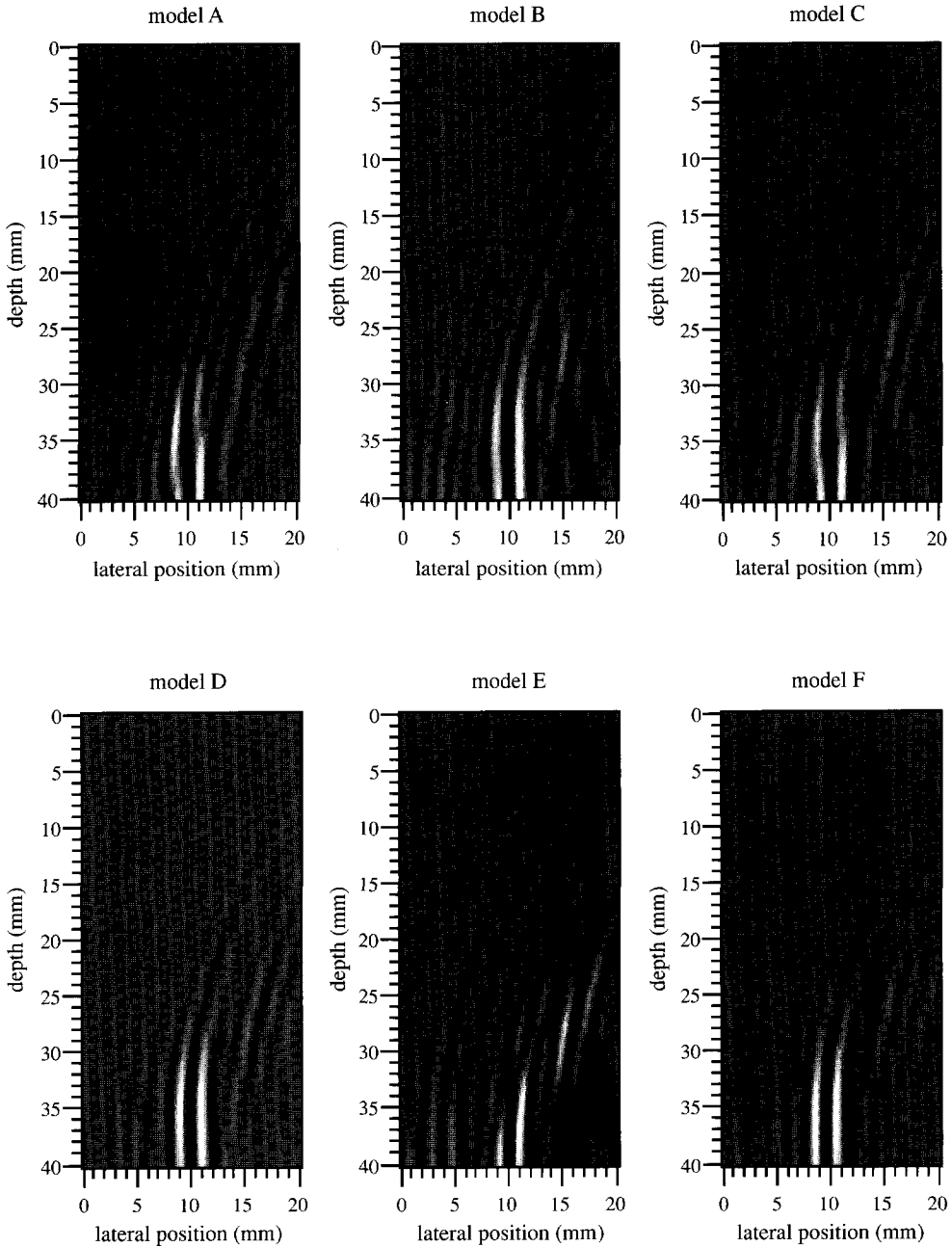
Figure 7.27: *The (1,0) images resulting from imaging the* low-pass filtered *finite-difference modelled B-scan data of the reflection of an incident shear wave at vertically oriented defects of different degrees of roughness (see table 7.1).*

7.5 Influence of Insufficient or Incomplete Insonification

It seems trivial to mention the situations in which inhomogeneities are insonified insufficiently or incompletely. Such situations are, however, often occurring in practice and the effects are generally not always recognized. Yet, the effects are obvious: the parts of the inhomogeneity which are insonified insufficiently or not at all will not appear as indications in the image, thus leading to an inaccurate imaging result.

In chapter 5 it has been demonstrated, that volumetrical defects (such as inclusions) can only be partly insonified, which makes *multi-path* or even *multi-shot* imaging absolutely necessary. In practice, a directive source with a narrow beam is applied in order to optimize the data-acquisition procedure, as has been described in chapter 6. This can easily lead to mis-interpretation of the imaging result, because the insonified part of an imaged ROI is not marked to indicate the part of the image which actually can be evaluated. In other words, in case certain parts of the imaged ROI are not (sufficiently) insonified, the absence of indications in those parts of the image does not imply that there are no inhomogeneities in that area. This is demonstrated using the model of figure 7.28 containing two point diffractors at different depths. The source is highly directive and will mainly insonify the lower diffractor. The imaging result (figure 7.29) clearly indicates this diffractor and the weak indication of the upper diffractor is easily overlooked. By applying a 15 dB clipping level for the representation of the image, both diffractors will become visible, although then also other (noisy) indications may appear.

In chapter 8 it will be shown, that when two weld defects are present in the same image plane, they can be imaged separately by performing different experiments (involving different source positions) in case the data-acquisition is carefully optimized. For inhomogeneities of sizes equal
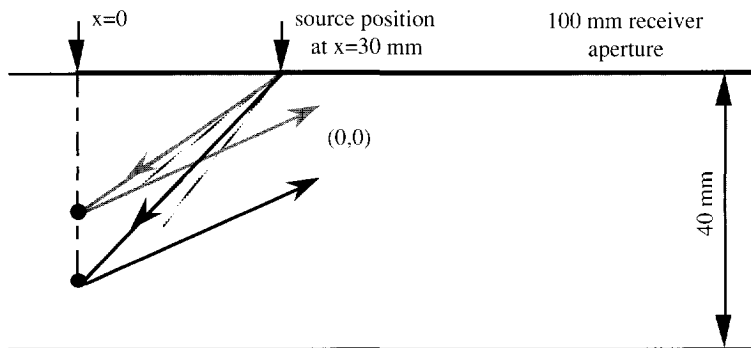
Figure 7.28: *The model of two point diffractors at different depths as used for the illustration of the effects of insufficient insonification.*
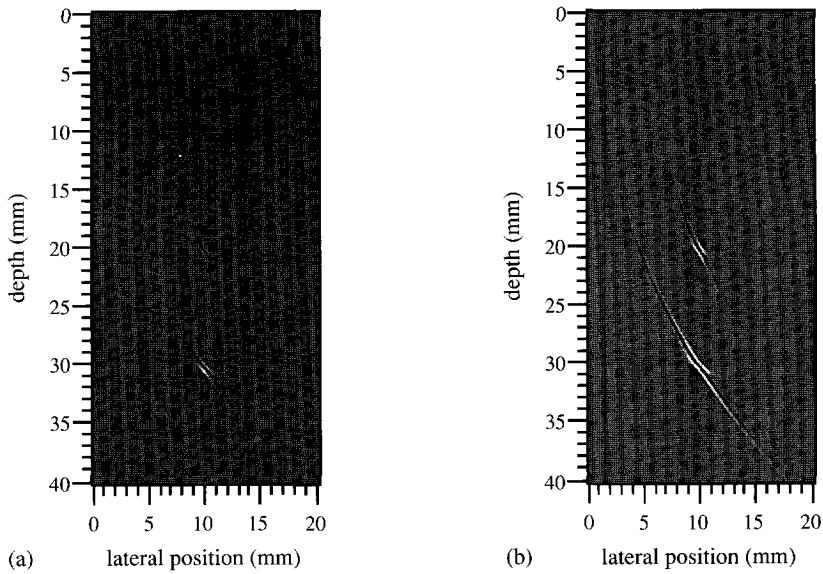
Figure 7.29: *The effects of insufficient insonification of two point diffractors at different depths (see figure 7.28); in the (0,0) image (a) the indication of the upper diffractor is easily overlooked and a 15 dB clipping level has to be applied (b) to reveal its presence more clearly.*

to or smaller than the source beam width, problems will generally not arise. When inhomogeneities are expected to be larger than the source beam width, more experiments with different source positions should be performed to ensure a good image accuracy. It should be noted, that the source beam width depends on both frequency and distance to the inhomogeneity.

8

Experimental Multi-SAFT Imaging Results

8.1 Introduction

In this chapter the Multi-SAFT imaging and characterization performance is evaluated. Section 8.2 will present the imaging results for artificial defects, i.e. simple machined slots and cylindrical holes in steel plates. These images will be compared with the imaging results obtained using the finite difference modelling scheme to verify the theoretically expected image quality and the assumptions made in chapter 4 regarding the Multi-SAFT algorithm. Multi-SAFT imaging results for real weld defects will be presented in sections 8.3 and 8.4. The weld defects are contained in special steel test objects and were intentionally generated by skilled welders. Various weld defects have been imaged in flat steel objects of approximately 13 and 30 mm thickness, featuring three different weld types (U-, X- and V-shaped). Section 8.4 will contain two Multi-SAFT imaging results for a defect in a girth weld of a steel pipe section of 14 mm thickness. Unless stated otherwise, the object have been made of low-carbon steel (mild steel, type Fe510).

The Multi-SAFT imaging results can be easily verified for the case of artificial defects. Although very accurate fabrication data is available on the positions and types of defects from the welders, destructive inspection would be the best way of verifying the imaging results for real weld defects. Unfortunately, the steel test plates of 30 mm thickness were made available by the Dutch Welding Institute NIL (Halkes and Terpstra, 1989) for the evaluation of Multi-SAFT inspection and could not be inspected destructively. The test plates and welded pipe sections of 13 mm and 14 mm thickness were specially constructed for the Multi-SAFT project. Therefore, they could be inspected destructively and photographs of the imaged cross-sections of the plate of 13 mm thickness containing weld defects will be compared to the corresponding Multi-SAFT imaging results.

All experiments have been performed using a specially developed Multi-SAFT workstation (see Appendix C for details) and a standard lateral split data-acquisition configuration. The source has been a directive 45° or 60° shear wave transducer, located at a fixed distance from a reference point on the inspection plane. This reference point usually corresponds to the expected lateral position of the inspected defect. The applied receiver has been a 45° or 60° wide-angle shear

wave transducer, scanned along a 100 mm aperture, starting at a certain distance from the reference point. Unless specified otherwise, a total of 101 A-scans of 2048 samples were recorded along the receiver aperture (scan step 1 mm), applying a sampling frequency of 25 MHz. For all experiments a lateral split angle of either 30° or 45° was applied. The total wedge delay has already been compensated for during recording of the data.

The Multi-SAFT images are all presented in linear grey-level plots, as it is found to be the most objective way of displaying. The use of false-color displays, for instance, can easily lead to subjective imaging, i.e. a certain color table may be chosen to emphasize correct indications and may even be used to manipulate the size of the indication as it is appearing in the image. Consequently, the wrong conclusions could be drawn from the imaging results.
One should always prevent imaging systems to become imagine systems...

8.2 Artificial defects

8.2.1. A 10 mm high vertically oriented slot

In chapter 6 the imaging of vertically oriented defects has been studied and a 10 mm high vertically oriented slot in a steel plate of 40 mm thickness has been imaged by applying the Multi-SAFT algorithm on data computed with the finite difference modelling scheme. The imaging result (figure 6.10) revealed the 10 mm high defect much better than the image obtained by conventional pulse-echo imaging, as shown in chapter 3 (figure 3.20). In order to verify the image quality obtained by using separate source and receiver transducers, the use of indirect forward scattering wave paths, as well as the assumptions made for the Multi-SAFT inversion scheme, a 10 mm high vertically oriented slot in a steel plate of 40 mm thickness has been experimentally imaged by Multi-SAFT. The configuration of the artificial defect is shown in figure 8.1.

A 45° source and 60° receiver have been applied in a 30° lateral split angle configuration. The reference point corresponds to the lateral position of the defect. The source has been positioned at 45 mm from that reference point, thus mainly insonifying the defect indirectly via the back wall, and the receiver aperture started at the reference point. The shear wave velocity has been measured and is approximately 3260 m/s. Figure 8.2 shows the recorded B-scan data. The strong forward scattering reflection responses are clearly recognized in the data. Comparing figure 8.2 with the modelled data of figure 6.9 shows a strong resemblance between the two data sets.

As the insonification is mainly indirect, the (1,0) and (1,1) wave paths have been employed for imaging with Multi-SAFT. The corresponding imaging results are shown in figure 8.3, where the reference position corresponds to the center of the images. The (1,0) image does resemble the
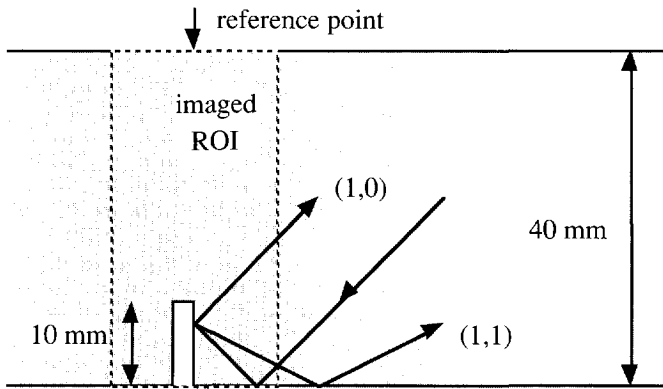
Figure 8.1: *The configuration of the 10 mm high vertically oriented defect.*
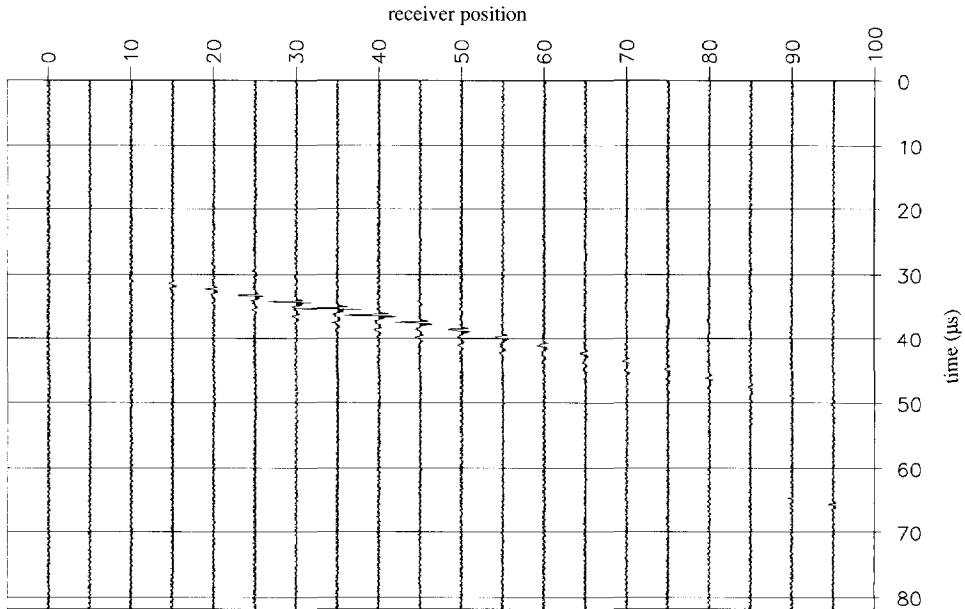
Figure 8.2: *B-scan data recorded from the 10 mm high vertically oriented defect.*

modelled (1,0) image of figure 6.10 very well, but features a slightly better image quality because of its larger temporal frequency bandwidth. The (1,1) image does not give an indication of the diffracting top of the slot, but features a false indication caused by the (1,0) responses instead. In spite of the fact, that the lateral split angle has been optimized to reduce the amplitude of the reflection responses, the diffraction responses probably are too weak to be imaged. Even when a 20 dB clipping level is applied, the diffraction indication is not clearly recognized (see figure 8.4). The fact, that the reflection responses are still too strong compared to the diffraction responses, is
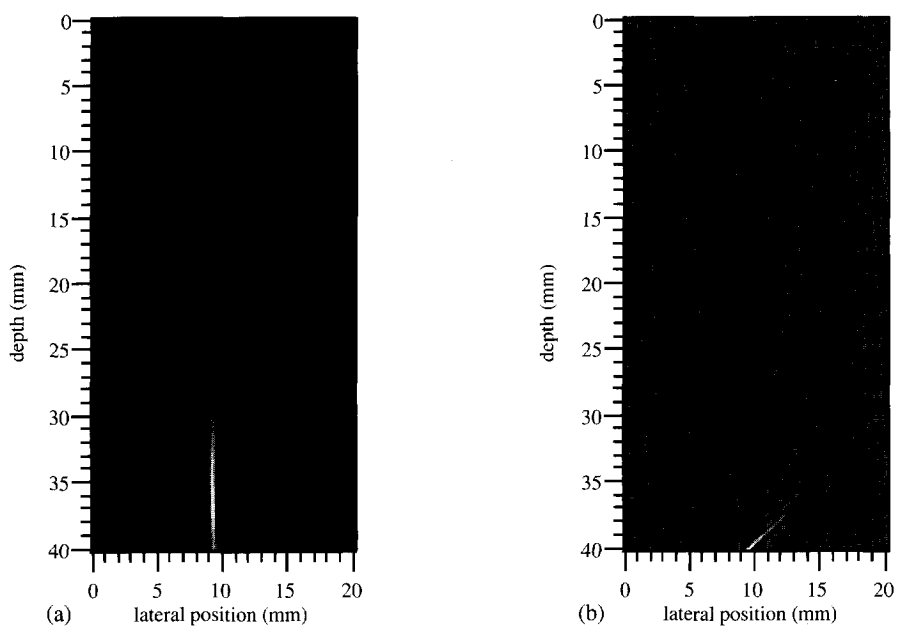
Figure 8.3: *The (1,0) image (a) and the (1,1) image (b) of the 10 mm high vertically oriented defect.*
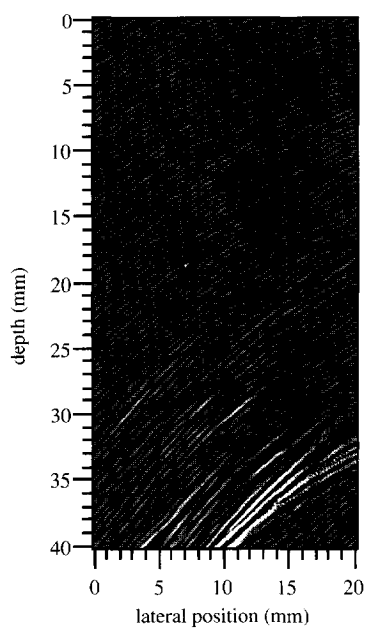
Figure 8.4: *The 20 dB clipped (1,1) image of the 10 mm high vertically oriented defect; the true (1,1) indication is marked in the image.*

presumably caused by the size of the defect. As will be demonstrated in the next section, smaller reflectors will cause the reflection responses to be less strong and will allow diffraction responses to be imaged.

The lateral position of the indication in the (1,0) image deviates slightly (less than 1 mm) from the real position, which is attributed to a combination of errors in the imaging parameters (wave velocity, the total wedge delay time, the positions of the source and receiver aperture, etc., see chapter 7). The height of the defect cannot be determined very accurately from the (1,0) image due to the limited inspection aperture and may be estimated slightly less than 10 mm (–3 dB point). The type, location and orientation of this surface-breaking planar defect becomes quite clear from the Multi-SAFT image. A time-of-flight-diffraction (TOFD) experiment could give additional information on the exact height of the defect.

8.2.2 Two 2 mm high vertically oriented defects

In a steel plate of 40 mm thickness, two slots parallel to the inspection surface have been machined (see figure 8.5). The slots are 2 mm wide and therefore result in two 2 mm vertically oriented defects. Except for the source position, the same data-acquisition configuration has been applied as for the Multi-SAFT inspection of the 10 mm high vertically oriented defect, as described in the previous section. A shear wave velocity of 3260 m/s has been measured. Two experiments have been performed with the source at 45 mm and 55 mm distance of the reference point, which approximately corresponded to the lateral position of the defects. The measured B-scan data of the experiments are shown in figure 8.6 and clearly feature the (1,0) reflection responses.

The (1,0) and (1,1) images of both experiments are shown in figures 8.7 and 8.8, where the
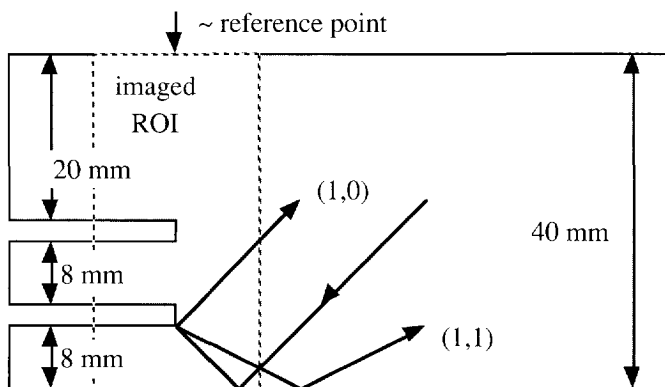
Figure 8.5: *The configuration of the two 2 mm high vertically oriented defects.*

(a)

(b)
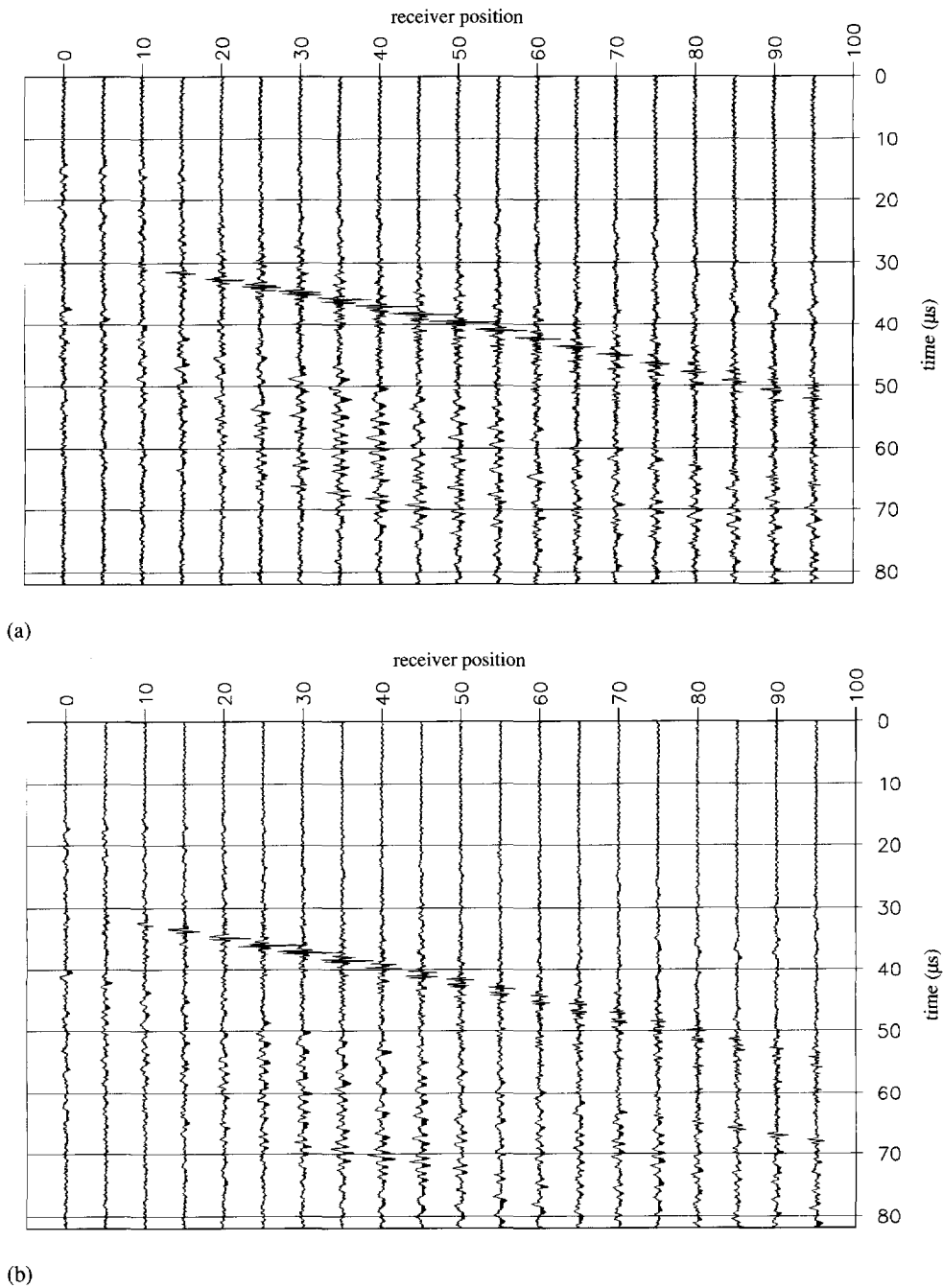
Figure 8.6: *B-scan data recorded from the two 2 mm vertically oriented defects for the source at 45 mm (a) and 55 mm (b).*
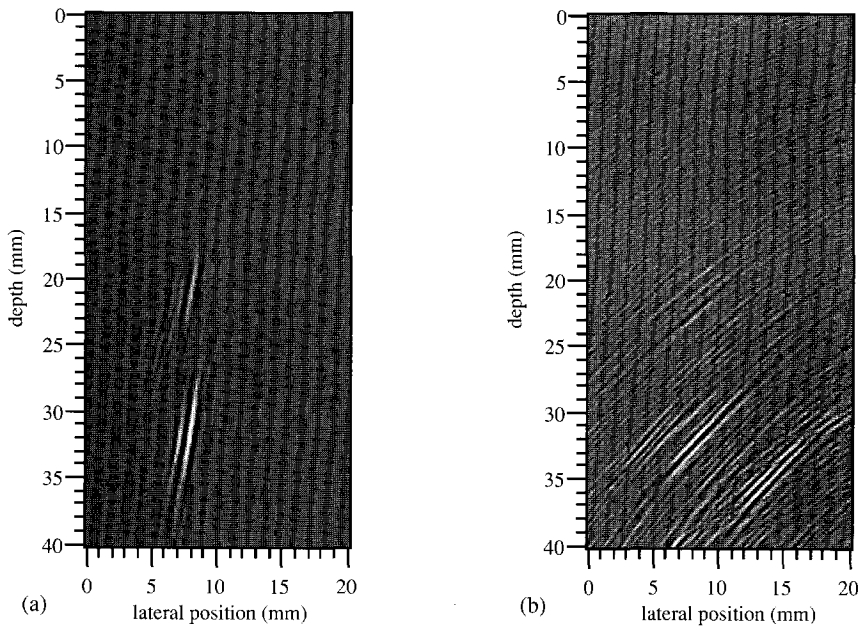
Figure 8.7: *The (1,0) image (a) and the (1,1) image (b) of the two 2 mm high vertically oriented defects for a source at 45 mm.*
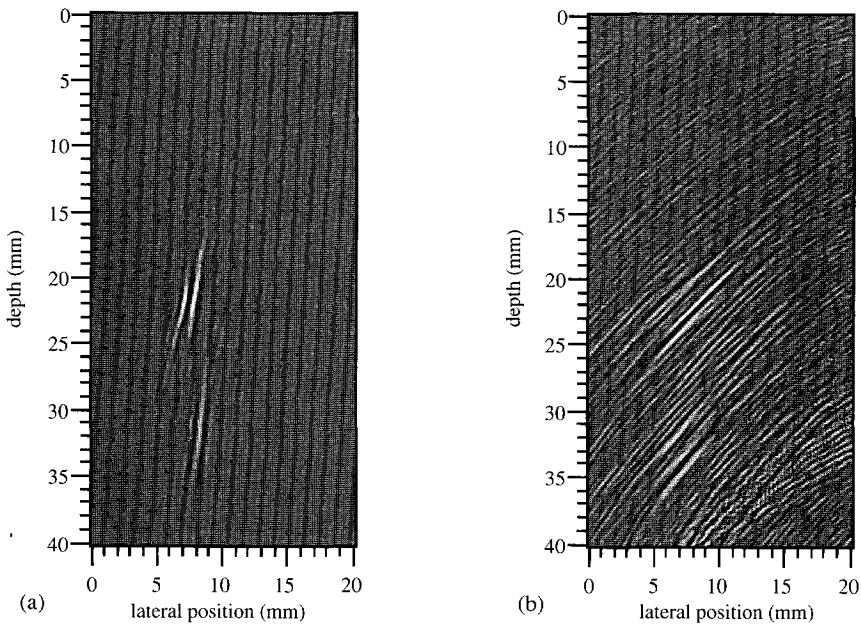
Figure 8.8: *The (1,0) image (a) and the (1,1) image (b) of the two 2 mm high vertically oriented defects for a source at 55 mm.*
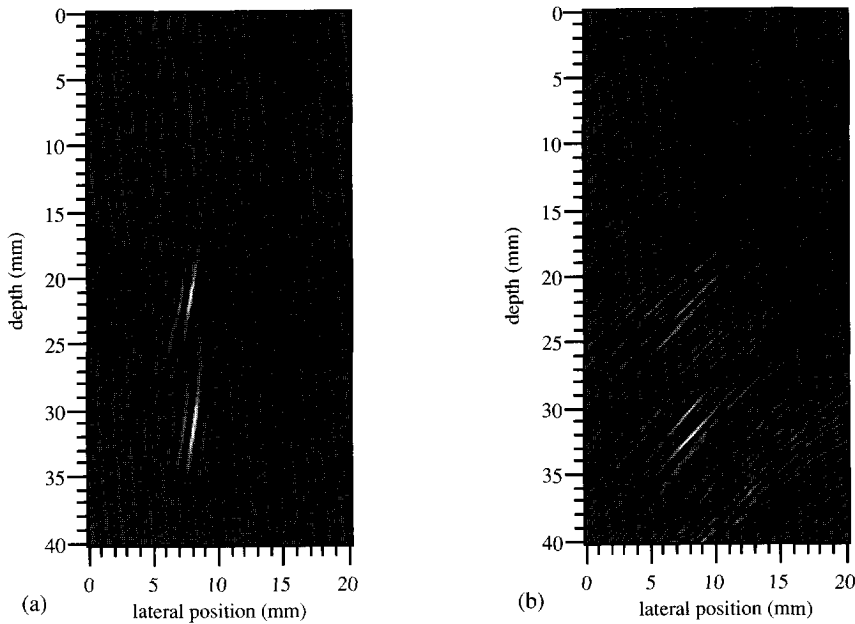
Figure 8.9: *The combined Multi-SAFT (1,0) image (a) and the (1,1) image (b) of the two 2 mm high vertically oriented defects from two different experiments; the indication due to internal scattering is marked.*

reference position corresponds to the center of the images. As may be expected from the geometry and insonification angle, the defect at 30 mm depth is best insonified when the source is positioned at 45 mm (figure 8.7a). Although a weak indication of the other defect is already visible, the directivity of the source clearly limits the region to be imaged (see remarks in section 7.4). Therefore, another experiment has been performed with the source positioned at 55 mm, insonifying the defect at 20 mm depth (figure 8.8a). For both experiments the (1,1) diffraction responses, although being very weak, could be imaged successfully (figures 8.7b and 8.8b).

The (1,0) reflection and (1,1) diffraction images have been combined for the two source positions, resulting in the images shown in figure 8.9. Notice the (very weak) spurious indications in the combined (1,1) diffraction image as the result of internally deflected insonification and/or scattering. The images of figure 8.9 illustrate that it is very well possible to combine images from different experiments, provided that the positions of the source and receiver aperture are accurately known.

Indications of both defects can now be recognized in the images and when the two images of figure 8.9 are superimposed on each other, the total combined Multi-SAFT image of figure 8.10 is the result. From this image the two vertically oriented 2 mm defects can readily be identified. Due to the combination of imaged diffraction and reflection responses, the type, orientation and
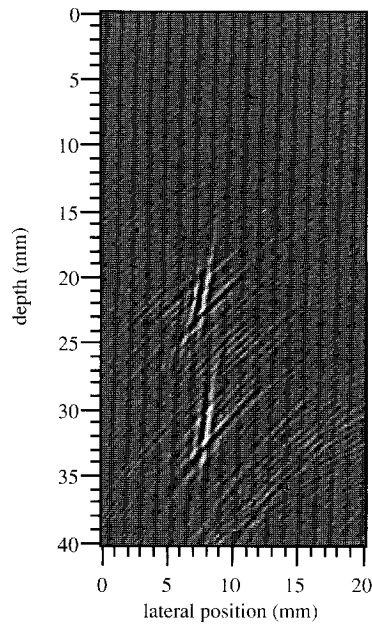
Figure 8.10: *The total combined Multi-SAFT image of the two 2 mm high vertically oriented defects from two different wave paths, from two different experiments.*

precise depth location (20-22 mm and 30-32 mm) of the two planar defects can be determined accurately from the image of figure 8.10.

8.2.3   Vertically oriented defects and cylindrical holes

The shape of a defect may be very important to determine, as a planar defect (with sharp extremities) is generally much more dangerous to a construction than a spherical defect. For this reason, four experiments have been performed on steel plates of 40 mm thickness which contained 2 mm and 4 mm (height/diameter) planar and cylindrical defects (see figure 8.11). The 2 mm defects were machined in low-carbon steel (c_s=3240 m/s) and the 4 mm defects in DOSTA 45 (c_s=3225 m/s), containing 0.45% C, 0.25% Si and 0.65% Mn. A 45° source transducer has been positioned at 60 mm from the reference position, corresponding approximately with the lateral position of the defects. Instead of 100 mm, the receiver aperture was 64 mm long and no less than 256 A-scans have been recorded. For all experiments a 45° receiver transducer has been applied in a 30° lateral split angle configuration.

The B-scan data for the 2 mm and 4 mm defects are shown in figures 8.12 and 8.13. By comparing the data sets for the cylindrical defects (figures 8.12a and 8.13a), it can be observed that the dataset recorded from the DOSTA 45 type of steel marks the presence of grain noise (see

section 7.1). Apart from the different noise levels, the two data sets for the cylindrical defects look very much the same. The B-scan data of the planar defects feature a much better signal-to-noise ratio and both feature approximately the same responses as well. Consequently, the size of the defects cannot be determined straight from the B-scan data.

The B-scan data have been imaged for the (1,0) and (1,1) wave paths and the Multi-SAFT imaging results are shown in figures 8.14 to 8.17. The combined Multi-SAFT image of the 2 mm diameter defect (figure 8.14c) clearly reveals the round shape of the defect, because of the presence of a creeping wave response (creeping along the surface of the defect) in the (1,0) (forward scattering reflection) image. The depth location of the defect (20 mm) can be determined very accurately, but its size cannot easily be extracted from the image. However, if one assumes that the position of the indication due to the creeping wave response in the (1,0) image corresponds to the back side of the hole (which is a sound assumption for 45° indirect insonification and small defects), the diameter of the cylindrical hole can be estimated accurately from the image.

From the combined Multi-SAFT image shown in figure 8.15c, the 2 mm vertically oriented planar defect can be easily recognized. Notice the resemblance with the image shown in figure 6.35, which is computed from data modelled with a very simple ray-tracing algorithm. The exact depth location of the defect (20 mm) can easily be determined from the image, as well as its size and orientation. The absence of an indication from a creeping wave response makes it plausible that the defect is planar rather than volumetric.

The lower signal-to-noise ratio of the B-scan data of the 4 mm diameter cylindrical defect does not really influence the image quality of the combined Multi-SAFT image shown in figure 8.16c. The indication of the creeping wave response is slightly weaker due to the grain scattering of the
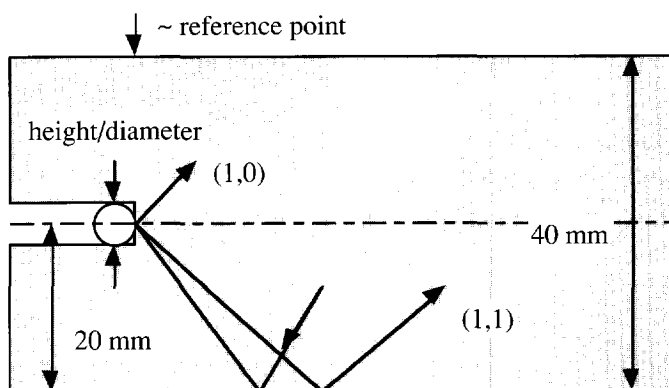
Figure 8.11: *The configuration of the vertically oriented defects and cylindrical holes.*

receiver position

(a)

receiver position

(b)
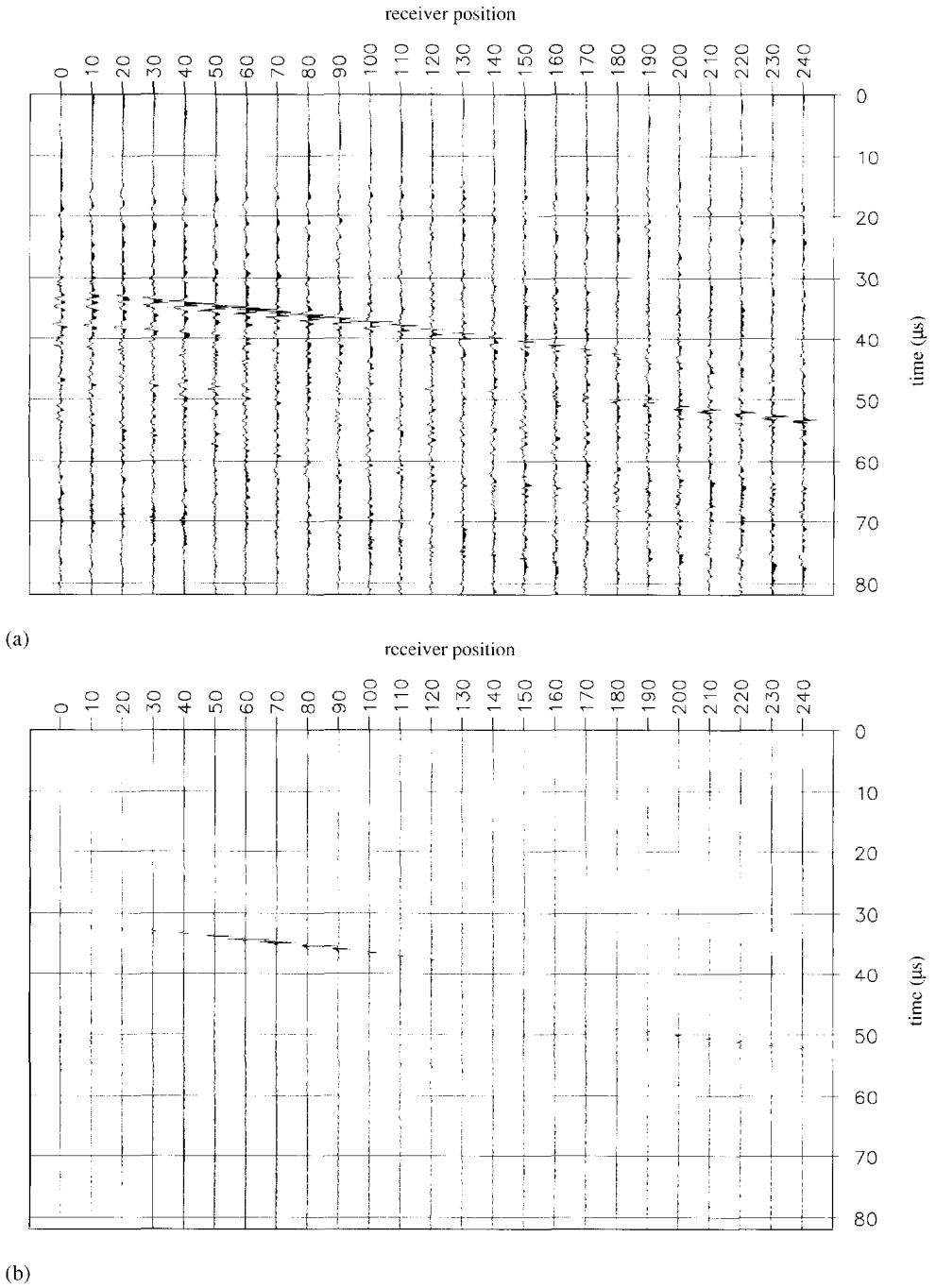
Figure 8.12: *B-scan data recorded from the 2 mm diameter cylindrical hole (a) and 2 mm high planar defect (b) in low-carbon steel .*

167

(a)

(b)
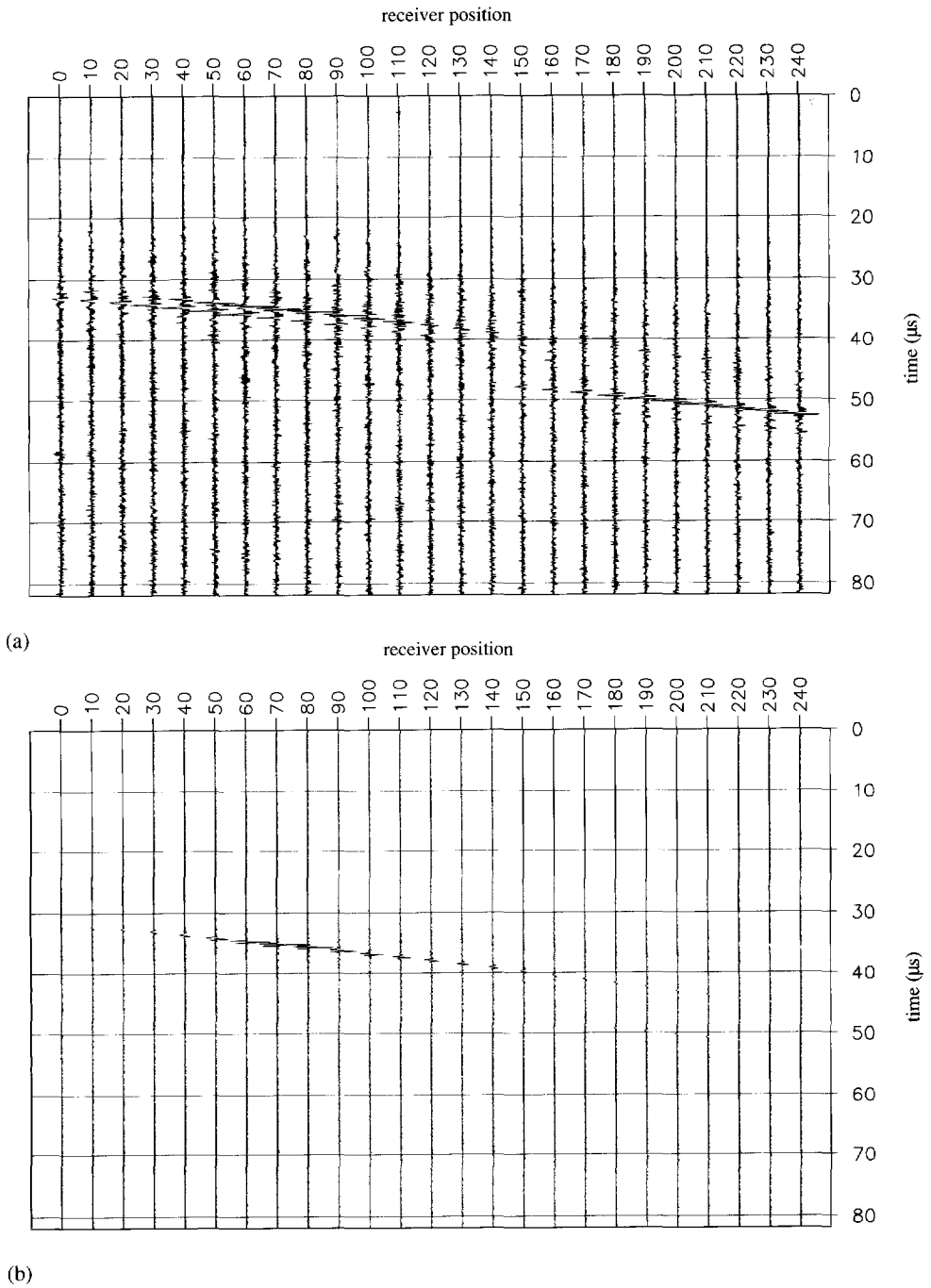
Figure 8.13: *B-scan data recorded from the 4 mm diameter cylindrical hole (a) and 4 mm high planar defect (b) in DOSTA steel .*
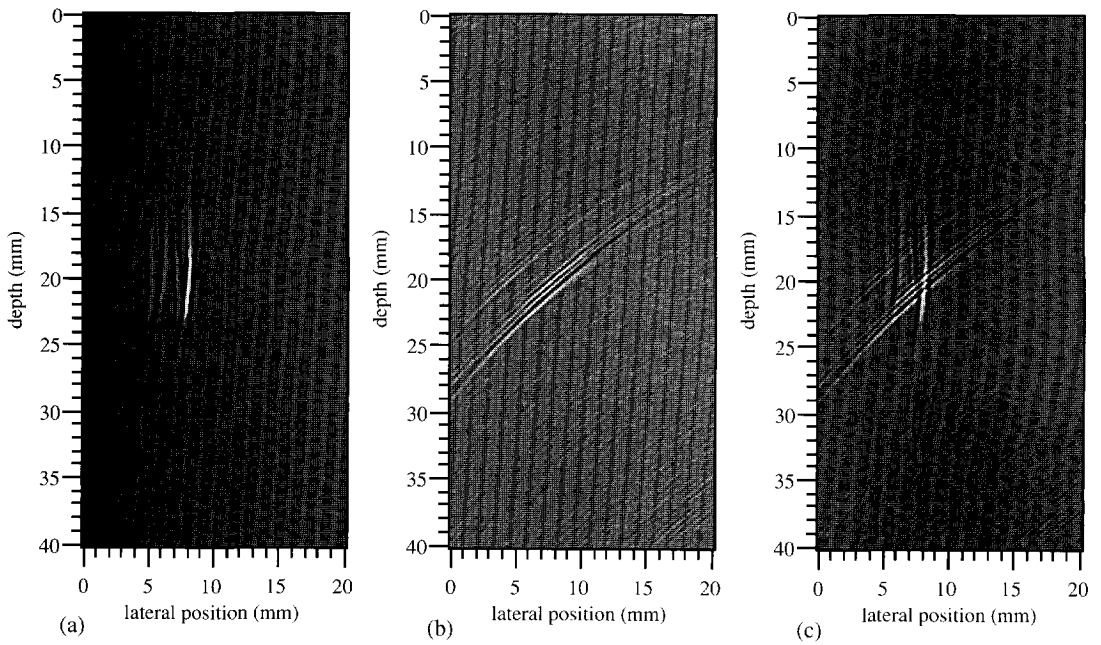
Figure 8.14: *The (1,0) image (a), the (1,1) image (b) and the combined Multi-SAFT image (c) of the 2 mm diameter hole in low-carbon steel.*
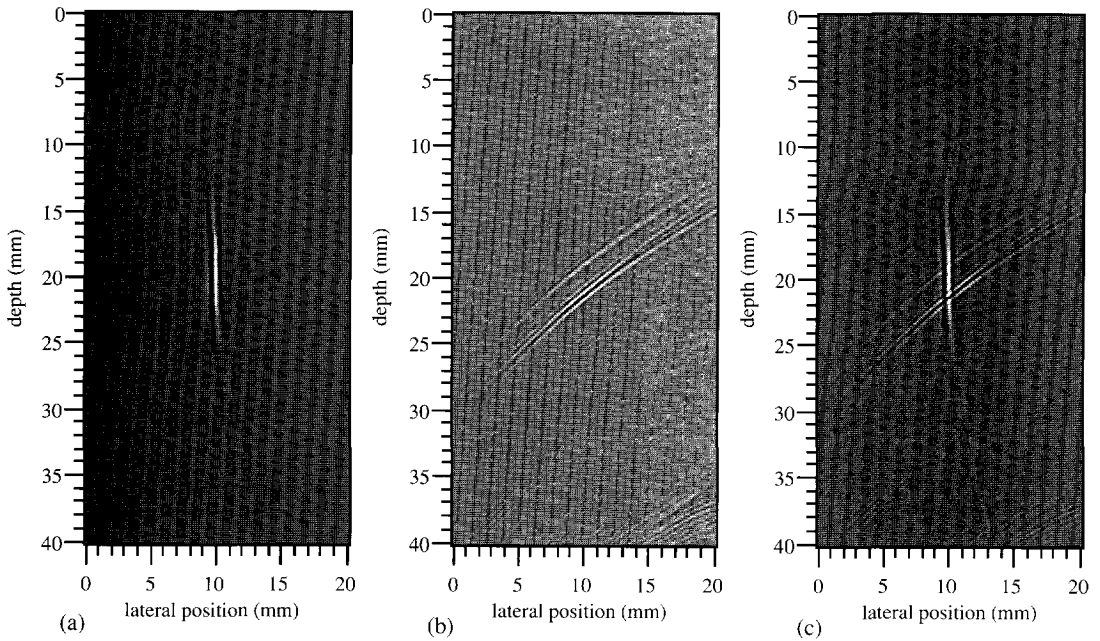
Figure 8.15: *The (1,0) image (a), the (1,1) image (b) and the combined Multi-SAFT image (c) of the 2 mm high planar defect in low-carbon steel.*
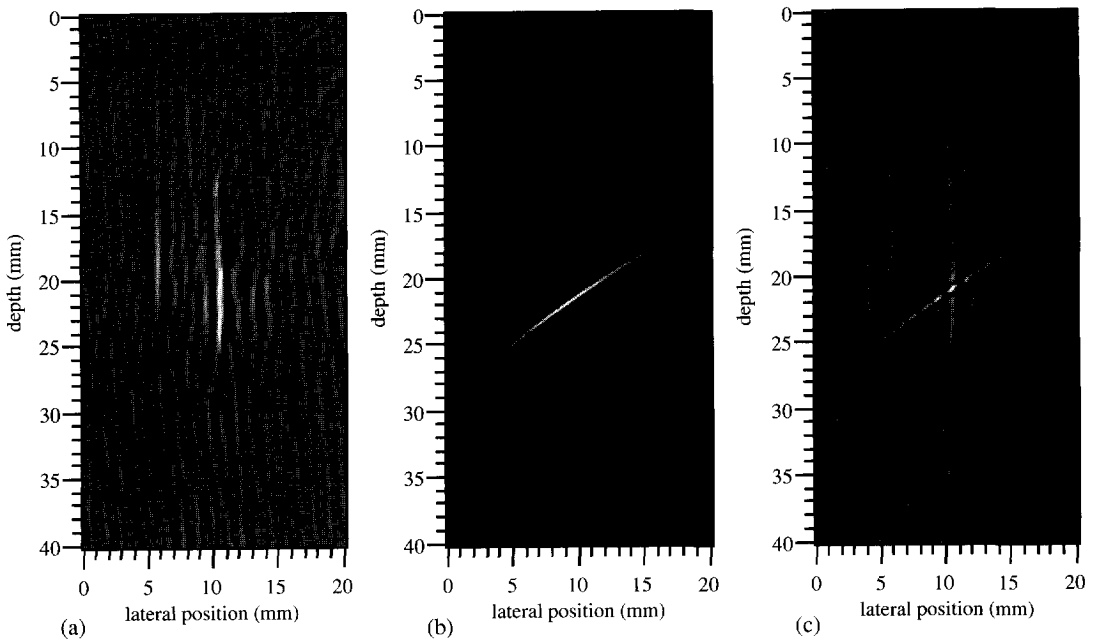
Figure 8.16: *The (1,0) image (a), the (1,1) image (b) and the combined Multi-SAFT image (c) of the 4 mm diameter hole in DOSTA steel.*
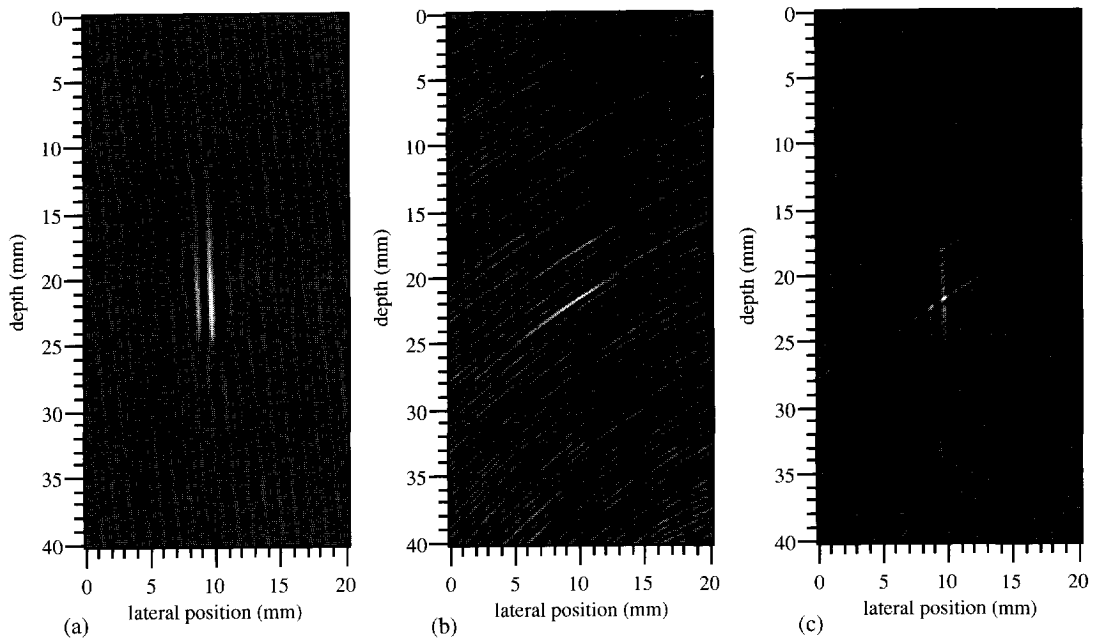
Figure 8.17: *The (1,0) image (a), the (1,1) image (b) and the combined Multi-SAFT image (c) of the 4 mm high planar defect in DOSTA steel.*

DOSTA 45 steel and the larger defect diameter. Still, the location and size of this defect can be extracted accurately from the image. The 4 mm vertically oriented planar defect can be identified from its combined Multi-SAFT image (figure 8.17c) as well. As the result of the larger reflecting surface and the grain scattering, the diffraction responses are weaker and cause the signal-to-noise ratio of the combined Multi-SAFT image to be slightly lower than for the 2 mm planar defect (figure 8.15c).

8.3 Real Weld Defects in Flat Plates

8.3.1 Lack of side-wall fusion in a U-shaped weld

A lack of side-wall fusion defect contained in a U-shaped weld has been inspected by Multi-SAFT. The weld joins two 30 mm steel plates and the exact configuration is shown in figure 8.18. The defect has a height of 6 mm, extends laterally from 11 to 12 mm from the center of the weld and is located at 9 mm depth, all according to the fabrication data. A 60° source transducer has been positioned at 85 mm from the reference point (corresponding approximately to the lateral position of the defect). The receiver aperture started at 35 mm and a 60° receiver transducer has been applied in a 30° lateral split angle configuration. The measured shear wave velocity is approximately 3300 m/s. The B-scan data is shown in figure 8.19, from which the (1,0) reflection and (1,1) diffraction responses are clearly visible.

The (1,0) and (1,1) images, as well as the combined Multi-SAFT image are shown in figure 8.20. The center of the weld is located at the left side of the image. From the combined Multi-SAFT image (figure 8.20c) the location and height of the indication have been determined. The values

Figure 8.18: *The configuration of the U-shaped weld.*
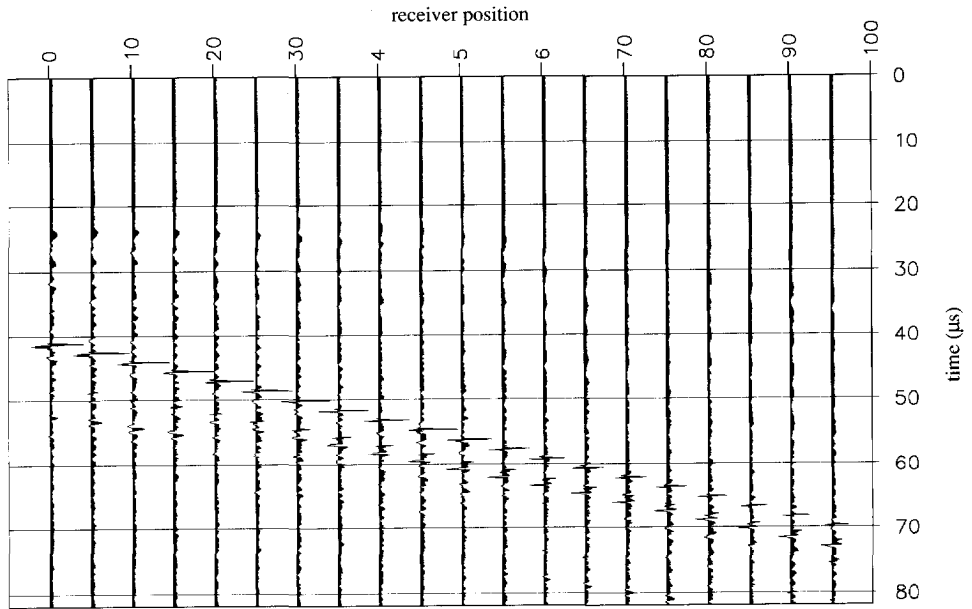
Figure 8.19: *B-scan data recorded from a lack of side-wall fusion in a U-shaped weld.*

are shown in table 8.1 and compared with the fabrication data. Although the location of the indication differs slightly from the fabrication data, its height is equal to the given value. Figure 8.20d shows the combined Multi-SAFT image featuring the weld lay-out. From the location and orientation of the indication it can be concluded, that it will probably be a lack of side-wall fusion defect.

Table 8.1: *The comparison of the fabrication data with the defect characterization results from the Multi-SAFT inspection of a lack of side-wall fusion in a U-shaped weld.*

dimensions: (with respect to weld center)	lateral position (mm)	depth position (mm)	height (mm)
Fabrication data	11-12	6-12	6
Multi-SAFT inspection	9-11	7-13	6

8.3.2 Closed lack of penetration in an X-shaped weld

A *closed* or *transparent* lack-of-penetration defect in an X-shaped weld has been inspected by Multi-SAFT. The weld joins two 30 mm steel plates and the exact configuration is shown in figure 8.21. According to the fabrication data, the defect has a height of 6 mm, is positioned 1 mm from
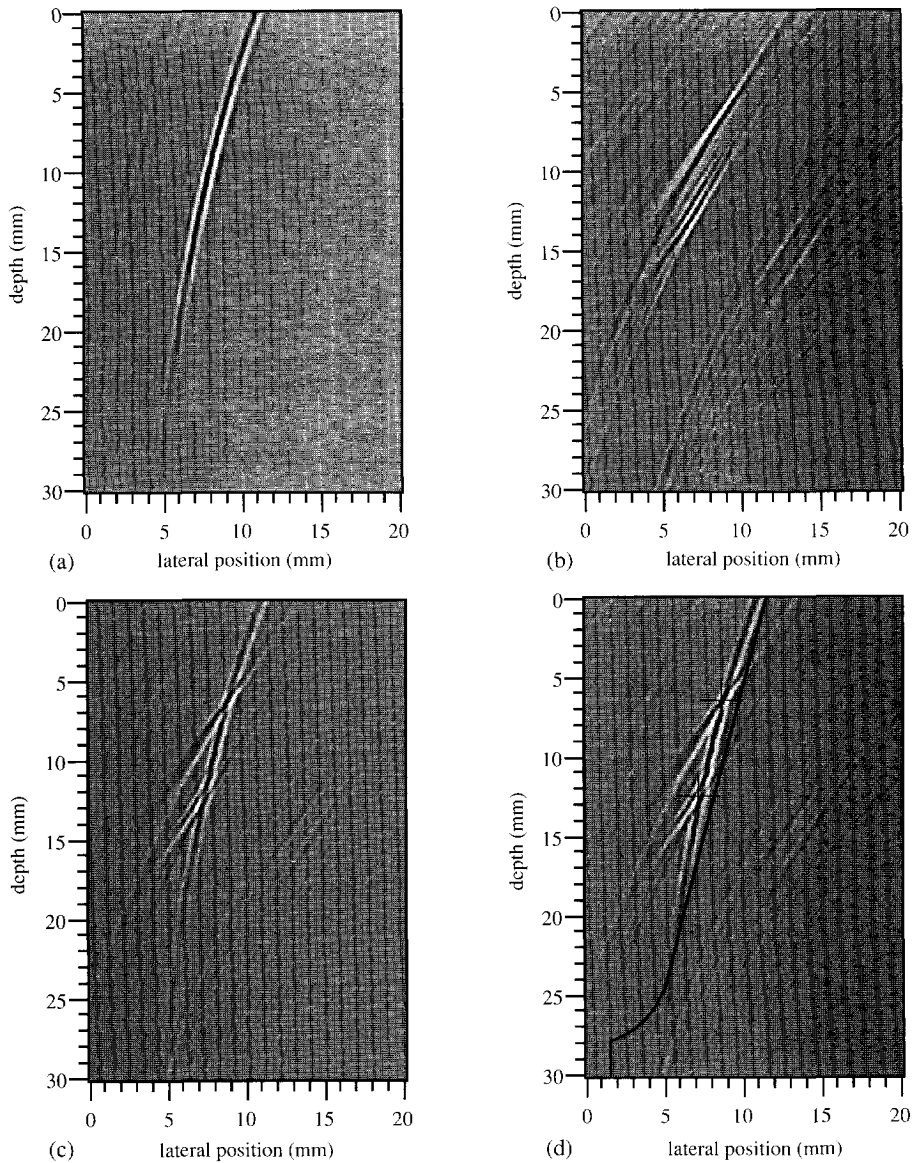
Figure 8.20: *The (1,0) image (a), (1,1) image (b), and combine Multi-SAFT image (c,d) of a lack of side-wall fusion in a U-shaped weld.*

the center of the weld at 15 mm depth. A 60° source transducer has been positioned at 80 mm from the reference point (corresponding approximately to the center of the weld). The receiver aperture started at 40 mm and a 60° receiver transducer has been applied in a 30° lateral split angle configuration. The measured shear wave velocity is approximately 3300 m/s. The B-scan
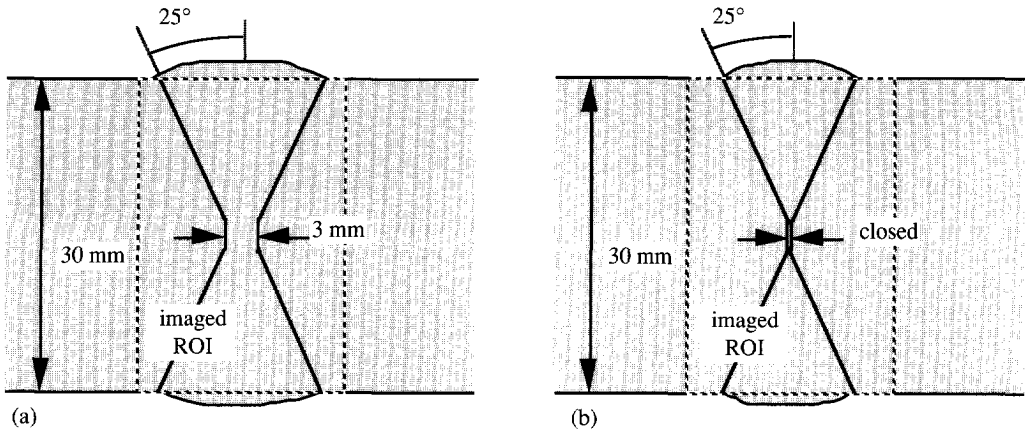
Figure 8.21: *The configuration of the X-shaped weld in the normal (a) and closed (b) situation.*
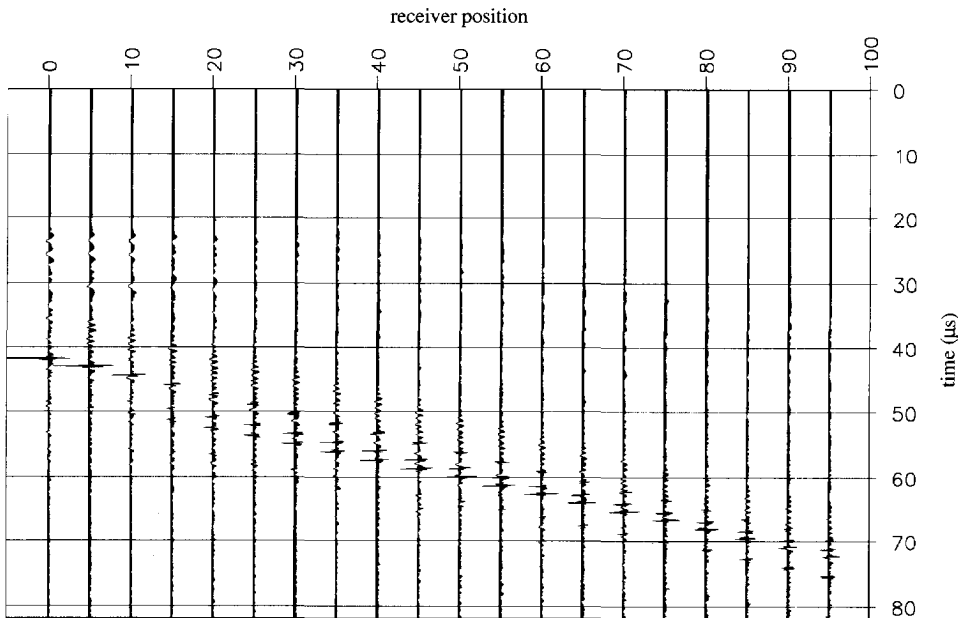
Figure 8.22: *B-scan data recorded from a closed lack-of-penetration defect in an X-shaped weld.*

data is shown in figure 8.22, from which the (1,0) reflection and (1,1) diffraction responses are easily identifiable.

The (1,0) and (1,1) images, as well as the combined Multi-SAFT image are shown in figure 8.23. The center of the weld is located in the center of the image. In spite of the fact, that the defect is

(partially) closed, it is clearly visible in the images. This is probably attained because of the locally reflecting SH-waves, for which the defect is much less transparent than for SV waves. From the combined Multi-SAFT image (figure 8.23c) the location and height of the indication have been determined. The values found are shown in table 8.2 and compared with the fabrication data. The location of the indication in the image differs slightly from the fabrication data, but its
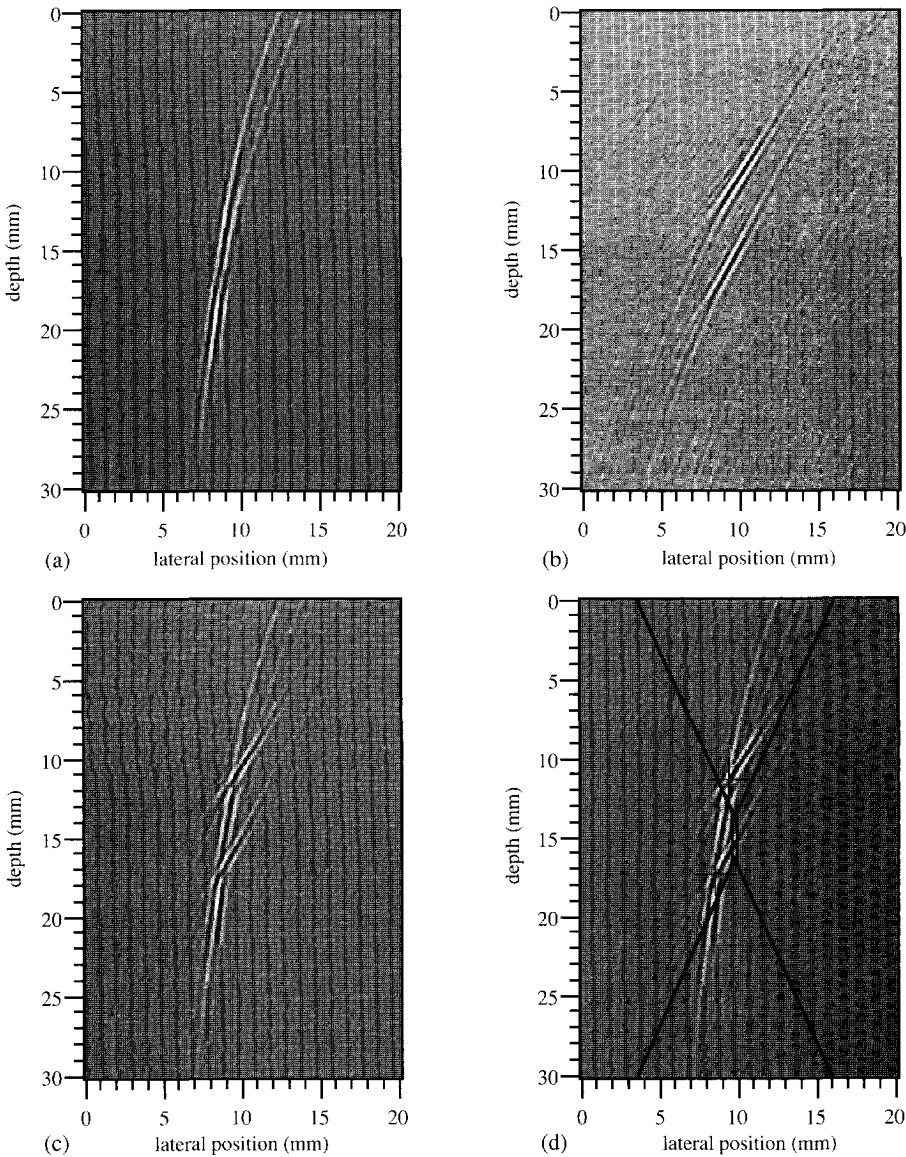
Figure 8.23: *The (1,0) image (a), (1,1) image (b) and combined Multi-SAFT image (c,d) of a closed lack-of-penetration defect in an X-shaped weld.*

height is equal to the given value. Figure 8.23d shows the combined Multi-SAFT image featuring the weld lay-out. From the location and orientation of the indication it can be concluded, that it will probably be a lack-of-penetration defect.

Table 8.2: *The comparison of the fabrication data with the defect characterization results from the Multi-SAFT inspection of a closed lack-of-penetration defect in an X-shaped weld.*

dimensions: (with respect to weld center)	lateral position (mm)	depth position (mm)	height (mm)
Fabrication data	1	12-18	6
Multi-SAFT inspection	−1	11-17	6

8.3.3 Slag inclusion in an X-shaped weld

A slag inclusion in an X-shaped weld has been inspected by Multi-SAFT. The weld joins two 30 mm steel plates and the exact configuration is shown in figure 8.21. The fabrication data give a defect with a height of 3 mm, extending laterally from 2 to 3 mm from the center of the weld at 18 mm depth. A 45° source transducer has been positioned at 75 mm from the reference point (corresponding approximately to the center of the weld). The receiver aperture started at 40 mm and a 45° receiver transducer has been applied in a 30° lateral split angle configuration. The measured shear wave velocity is approximately 3300 m/s. The B-scan data is shown in figure 8.24, from which a complex wave field – containing several responses – can be observed.

Because of the shape of the weld and the location of the defect, the insonification should preferably be according to a (0) or (2) wave path. As the source could not be positioned very close to the center of the weld due to the presence of the weld cap, the source has been located at longer distance and consequently only the (2,0) and (2,1) wave paths have been chosen for imaging. The (2,0) and (2,1) images, as well as the combined Multi-SAFT image are shown in figure 8.25, where the center of the image corresponds the center of the weld. The (2,1) image clearly features an indication from a creeping wave response, revealing the volumetrical nature of the defect. From the combined Multi-SAFT image (figure 8.25c) the location and height of the indication have been determined. These values are sh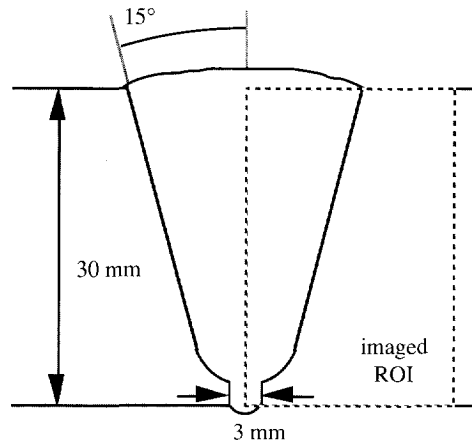own in table 8.3 to be compared with the fabrication data. The extension of the indication in lateral direction is slightly larger than given by the fabrication data due to the applied frequency band width, while the depth positions and heights correspond very well. Figure 8.25d shows the combined Multi-SAFT image featuring the weld lay-out. From the location and shape of the indication it can be concluded, that it will probably be a slag inclusion near the center of the X-shaped weld.

receiver position
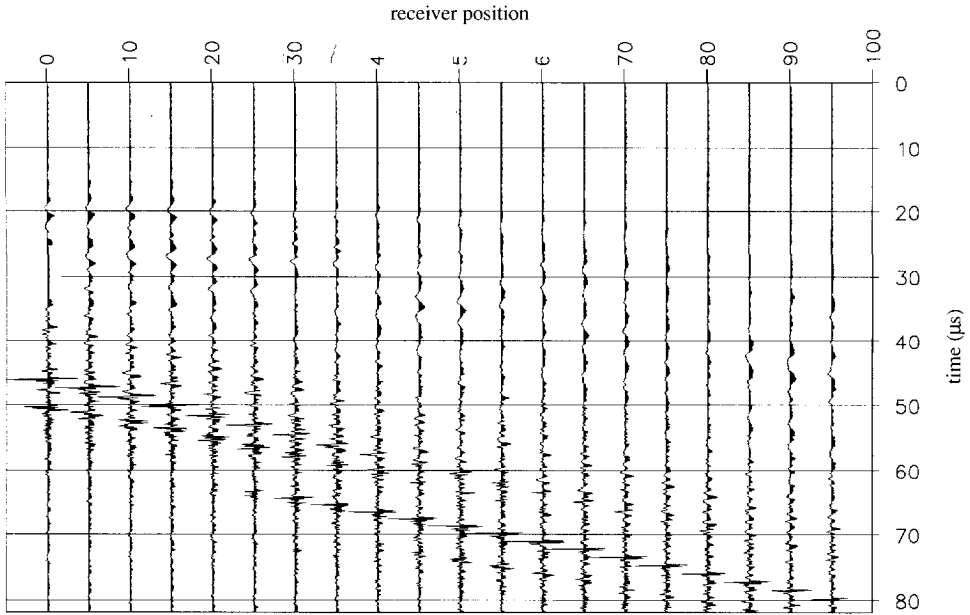
Figure 8.24: *B-scan data recorded from a slag inclusion in an X-shaped weld.*

Table 8.3: *The comparison of the fabrication data with the defect characterization results from the Multi-SAFT inspection of a slag inclusion in an X-shaped weld.*

dimensions: (with respect to weld center)	lateral position (mm)	depth position (mm)	height (mm)
Fabrication data	2-3	16.5-19.5	3
Multi-SAFT inspection	2-4	17-20	3

8.3.4 Lack of interrun fusion in an X-shaped weld

A lack of interrun fusion defect in an X-shaped weld has been inspected by Multi-SAFT. The weld joins two 30 mm steel plates and the exact configuration is shown in figure 8.21. From the fabrication data it follows, that the height of the defect is 3 mm, it extends laterally from 0 to 2 mm from the center of the weld, while it is located at 20 mm depth. A 60° source transducer has been positioned at 45 mm from the reference point (corresponding approximately to the center of the weld). The receiver aperture started at 45 mm and a 60° receiver transducer has been applied in a 45° lateral split configuration. The measured shear wave velocity is approximately 3300 m/s. The B-scan data is shown in figure 8.26, from which a complex wave field without distinctive responses can be observed.

177
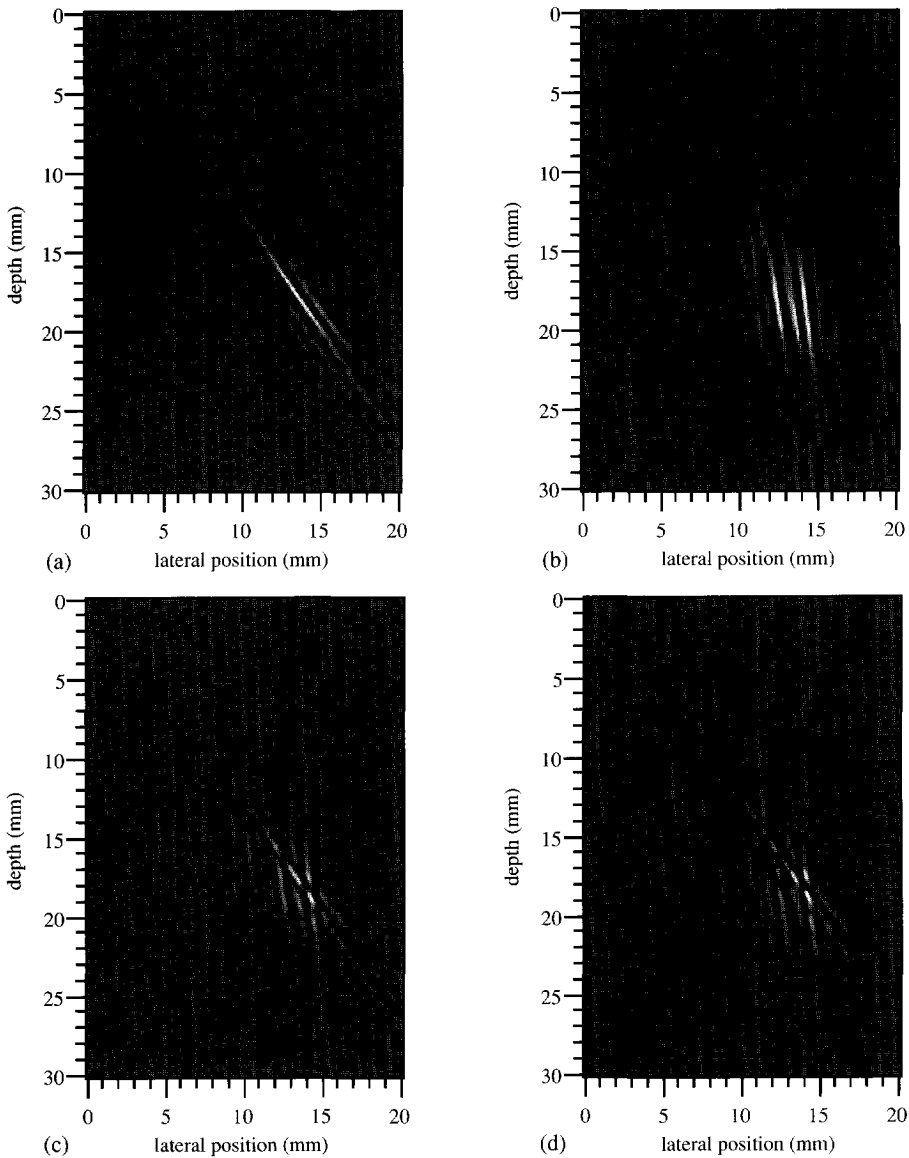
Figure 8.25: *The (2,0) image (a), (2,1) image (b) and combined Multi-SAFT image (c,d) of a slag inclusion in an X-shaped weld.*

A lack of interrun defect is embedded in the weld material and may be oriented approximately parallel to the inspection surface. This makes this type of defect very hard to image as no specific wave paths can be employed. The (1,1) and (0,2) images, as well as the combined Multi-SAFT image are shown in figure 8.27, where the center of the image corresponds the center of the weld. The images do not show very clear and bounded indications and the image quality may be
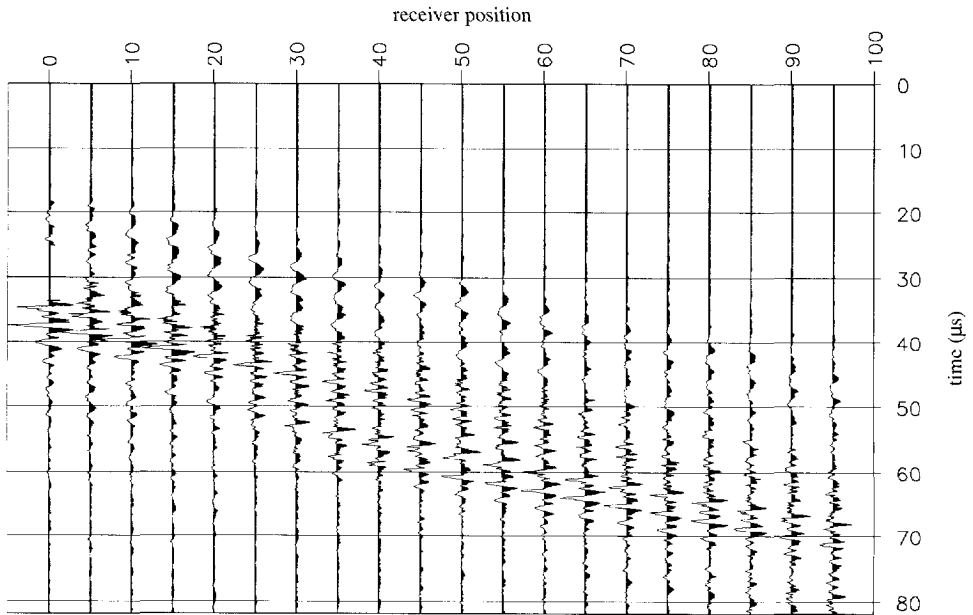
Figure 8.26: *B-scan data recorded from a lack of interrun fusion in an X-shaped weld.*

referred to as poor, probably due to the (anisotropic) nature of the weld material. From the combined Multi-SAFT image (figure 8.27c) the location and height of the indication cannot accurately be determined. Figure 8.27d shows the combined Multi-SAFT image featuring the weld lay-out. From the location of the indications and the poor image quality it is most likely to classify the defect as a lack of interrun fusion or slag inclusion.

8.3.5 External undercut at a V-shaped weld

An external undercut defect at the edge of the weld toe is usually detected by visual inspection. Its depth, however, cannot always be determined accurately, because the defect may extend further than is visible by means of lack of fusion or cracking. Therefore, such a type of defect in a V-shaped weld has been inspected by Multi-SAFT. The weld joins two steel plates of 12.8 mm thickness and the exact configuration is shown in figure 8.28. The measured shear wave velocity is approximately 3300 m/s. Because the preparation angle of the weld is 30°, the defect will be oriented accordingly and is optimally insonified for reflection responses by a 60° source. For a planar defect oriented in this way, the lateral split angle cannot be optimized such that the amplitude of the reflection responses are reduced compared to the amplitude of the diffraction responses (see figure 8.29). In order to obtain diffraction responses, a 45° source should be applied. Therefore, two experiments have been performed with two different insonification angles.
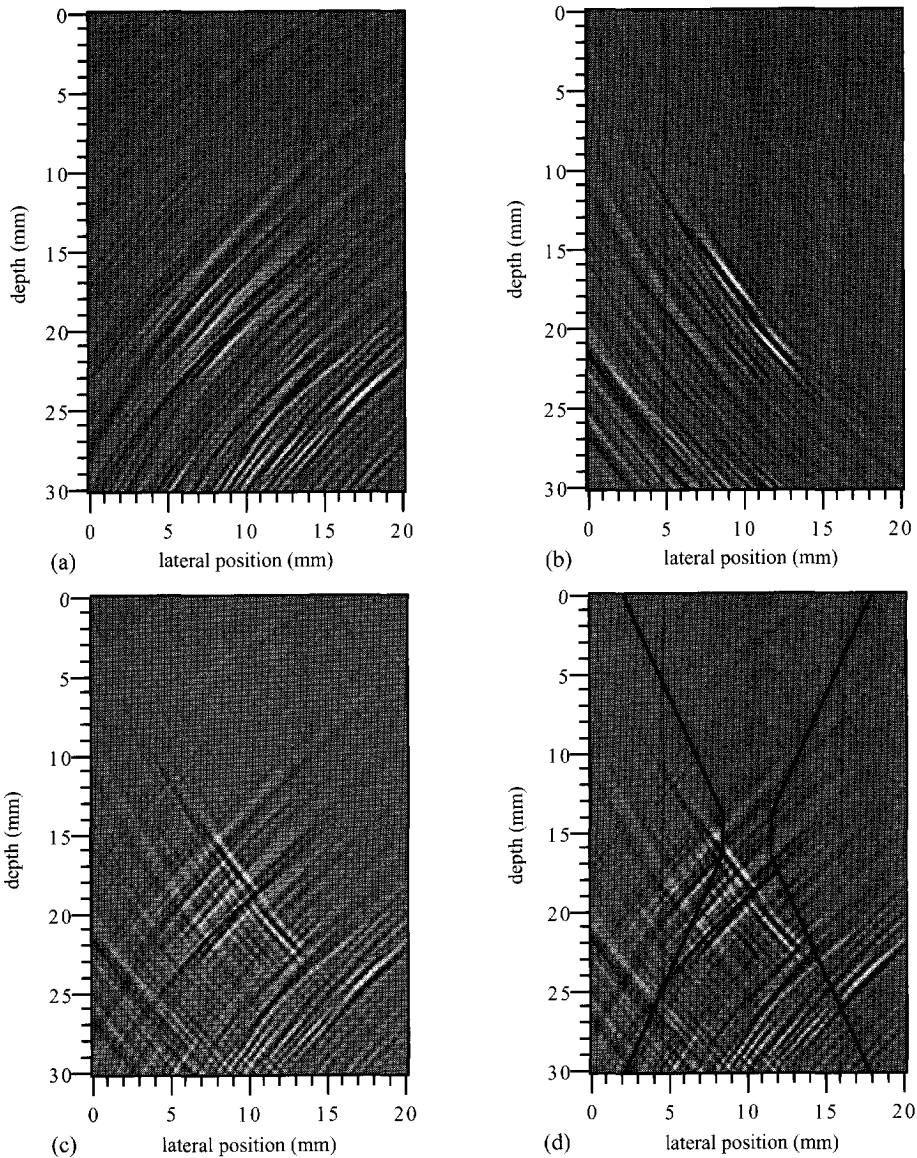
Figure 8.27: *The (1,1) image (a), (0,2) image (b) and combined Multi-SAFT image (c,d) of a lack of interrun fusion in an X-shaped weld.*

For the first experiment, a 60° source transducer has been positioned at 45 mm from the reference point (corresponding approximately to the lateral position of the defect). The receiver aperture started at 40 mm and a 60° receiver transducer has been applied in a 30° lateral split angle configuration. The B-scan data is shown in figure 8.30, from which a series of strong reflection responses can be observed. For the second experiment, a 45° source receiver has been positioned
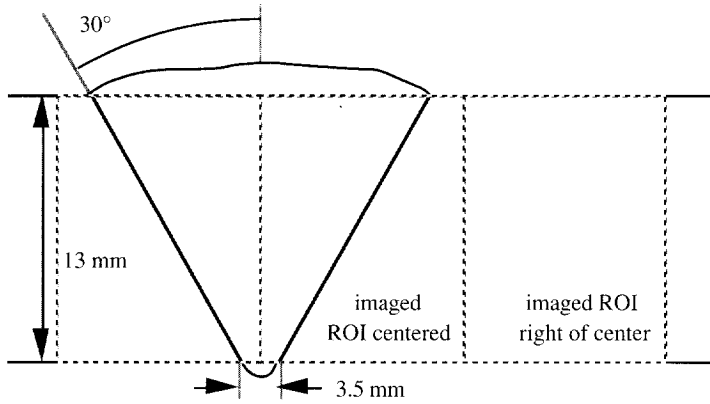
Figure 8.28: *The configuration of the V-shaped weld.*

at 25 mm from the reference point. The receiver aperture started at 45 mm and a 60° receiver transducer has been applied in a 30° lateral split angle configuration. The B-scan data is shown in figure 8.31, featuring a series of weak diffraction responses.

The most suitable responses to be imaged in this case are the ones corresponding to the (1,3) or (1,5) wave paths. In figure 8.32, the (1,3) image for the reflection responses (60° source experiment), the (1,5) image for the diffraction responses (45° source experiment) and their combined Multi-SAFT image are shown. The left of the image corresponds the center of the weld.
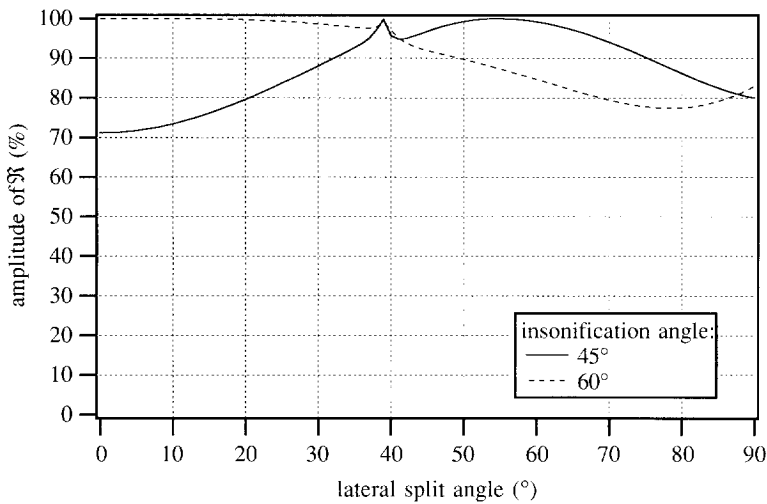
Figure 8.29: *The amplitude of the general SV wave reflection coefficient as a function of the lateral split angle for planar defects oriented at 30° with respect to the normal on the inspection surface and for a 45° and 60° insonification angle.*
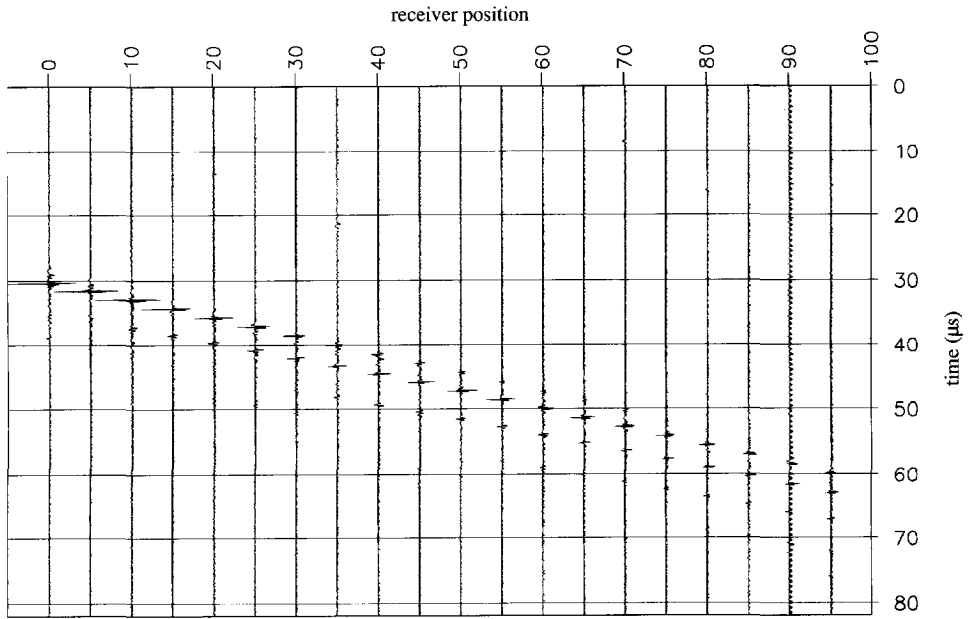
Figure 8.30: *B-scan data recorded from an external undercut at a V-shaped weld applying a 60° source.*
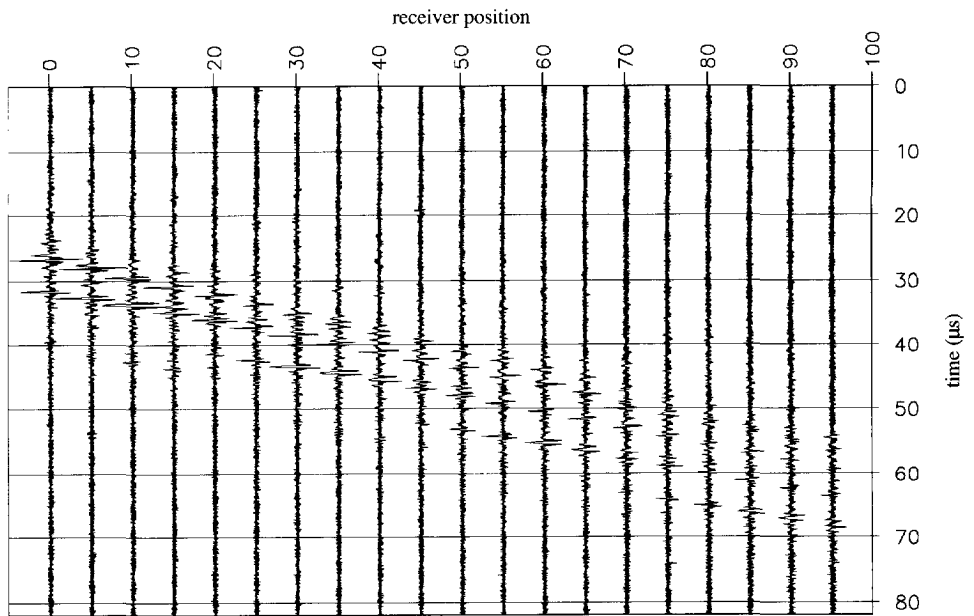
Figure 8.31: *B-scan data recorded from an external undercut at a V-shaped weld applying a 45° source.*
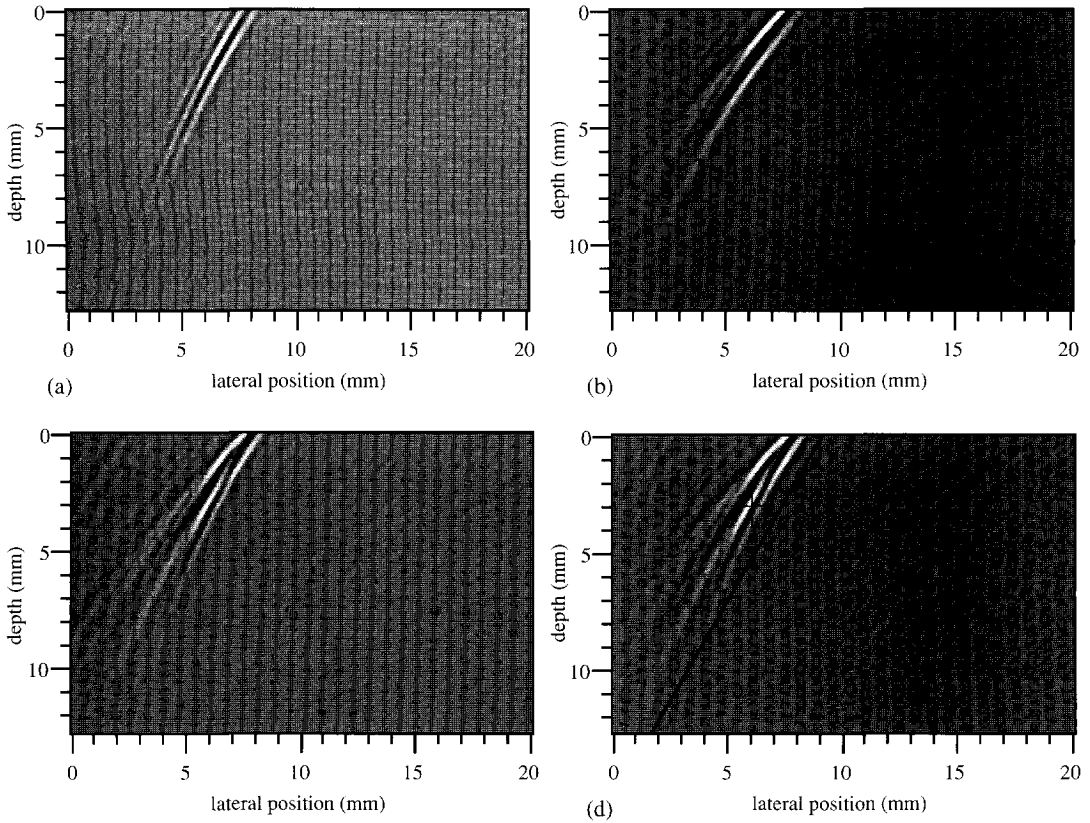
Figure 8.32: *The (1,3) image of the 60° source experiment (a), the (1,5) image of the 45° source experiment (b) and the combined Multi-SAFT image (c,d) of an external undercut at a V-shaped weld; imaged ROI right of center*

The reflection image (figure 8.32a) reveals clearly the surface-breaking defect, while the diffraction image (figure 8.32b) shows just barely the indication of the lower extremity of the defect. Combining the two images does not make the determination of the height of the defect much easier. Nevertheless, the location and height of the indication have been determined from the combined Multi-SAFT image (figure 8.32c) and are presented in table 8.4. The height has been determined by picking those points of the indication which are approximately −3 dB down compared to its maximum amplitude (*−3 dB height*). Figure 8.32d shows the combined Multi-SAFT image featuring the weld lay-out.

After the Multi-SAFT inspection, the weld has been inspected destructively and a photograph of the imaged cross-section is shown in figure 8.33. From this figure the precise location, orientation and height of the defect have been measured and presented in table 8.4 to be compared with the values extracted from the images. From the data of table 8.4 it may be concluded, that the location

of the defect is approximately correct, while its height is slightly overestimated. This is mainly caused by the fact, that the intersection of the reflection and diffraction indications is not very clear from the combined Multi-SAFT imaging result.

Table 8.4: *The defect characterization results from the Multi-SAFT and destructive inspections of an external undercut at a V-shaped weld.*

dimensions: (with respect to weld center)	lateral position (mm)	depth position (mm)	height (mm)
Destructive inspection	6.7-8.0	0-2.1	2.1
Multi-SAFT inspection	6-8	0-3	3
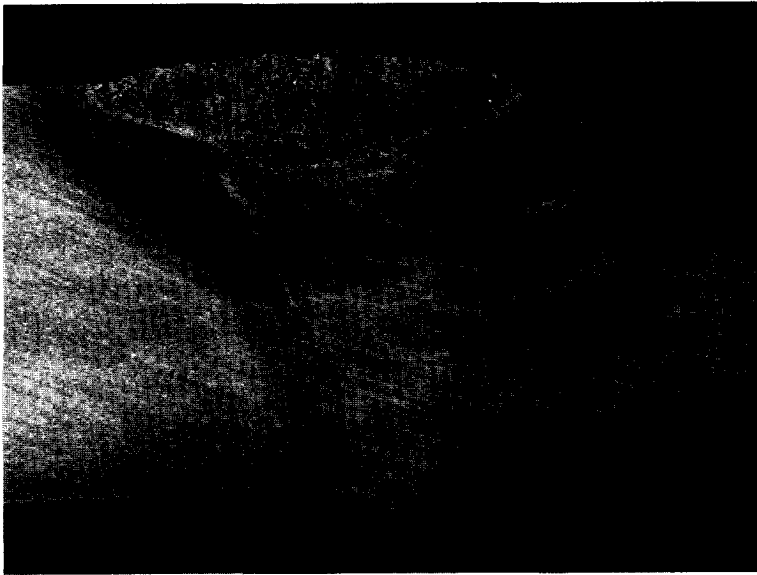
Figure 8.33: *Photograph of the imaged cross-section containing an external undercut at a V-shaped weld.*

8.3.6 Lack of side-wall fusion in a V-shaped weld

A lack of side-wall fusion defect in a V-shaped weld has been inspected by Multi-SAFT. The weld joins two steel plates of 12.8 mm thickness and the exact configuration is shown in figure 8.28. The measured shear wave velocity is approximately 3300 m/s. A 60° source transducer has been positioned at 35 mm from the reference point (corresponding approximately to the lateral position of the defect). The receiver aperture started at 45 mm and a 60° receiver transducer has been applied in a 30° lateral split angle configuration. The B-scan data is shown in figure 8.34, from

receiver position
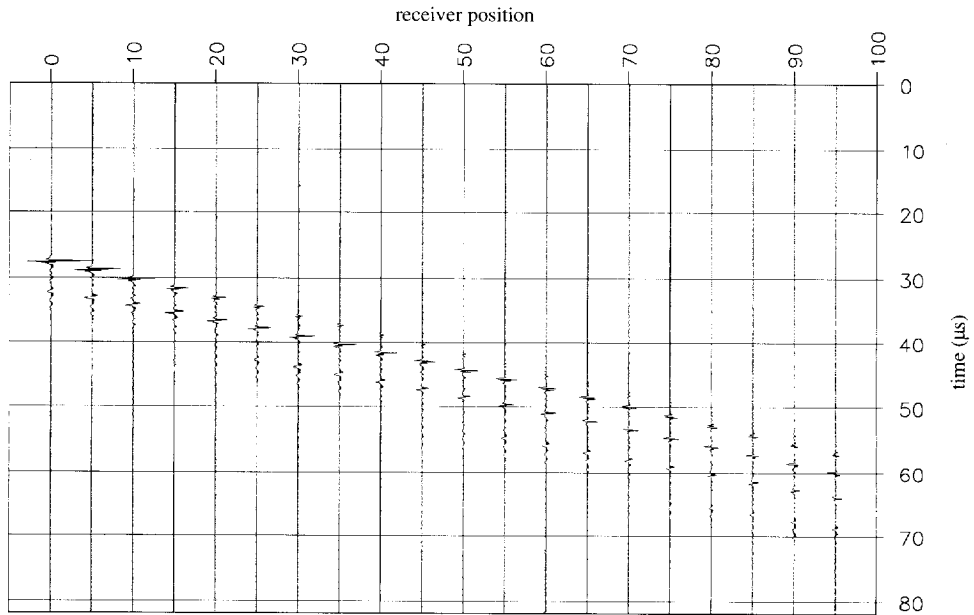
Figure 8.34: *B-scan data recorded from a lack of side-wall fusion in a V-shaped weld.*

which a number of multiple reflection responses can be recognized.

As the response of the (1,3) wave path is completely contained in the B-scan data, it has been employed for Multi-SAFT imaging and the result is shown in figure 8.35a. The center of the image corresponds the center of the weld. The location and −3 dB height of the indication have been determined from the Multi-SAFT image and are presented in table 8.5. Figure 8.35b shows

(a)   lateral position (mm)

(b)   lateral position (mm)

Figure 8.35: *The (1,3) image (a,b) of a lack-of-fusion defect in a V-shaped weld; imaged ROI right of center.*

the Multi-SAFT image featuring the weld lay-out. From the location and orientation of the indication in the image it can be concluded, that it is most likely a lack of side-wall fusion defect.

After the Multi-SAFT inspection, the weld has been inspected destructively and a photograph of the imaged cross-section is shown in figure 8.36. From this figure the precise location, orientation and height of the defect have been measured and presented in table 8.5 to be compared with the values extracted from the images. It appears that the height of the defect has been determined accurately, but that its depth location contains a small error, due to the fact that the −3 dB points of the indication do not necessarily have to correspond exactly to the positions of the extremities. A time-of-flight-diffraction (TOFD) experiment could give additional information on the exact height of the defect.

Table 8.5: *The defect characterization results from the Multi-SAFT and destructive inspections of a lack of side-wall fusion in a V-shaped weld.*

dimensions: (with respect to weld center)	lateral position (mm)	depth position (mm)	height (mm)
Destructive inspection	3.9-6.0	3.7-7.6	3.9
Multi-SAFT inspection	4-6	3-7	4
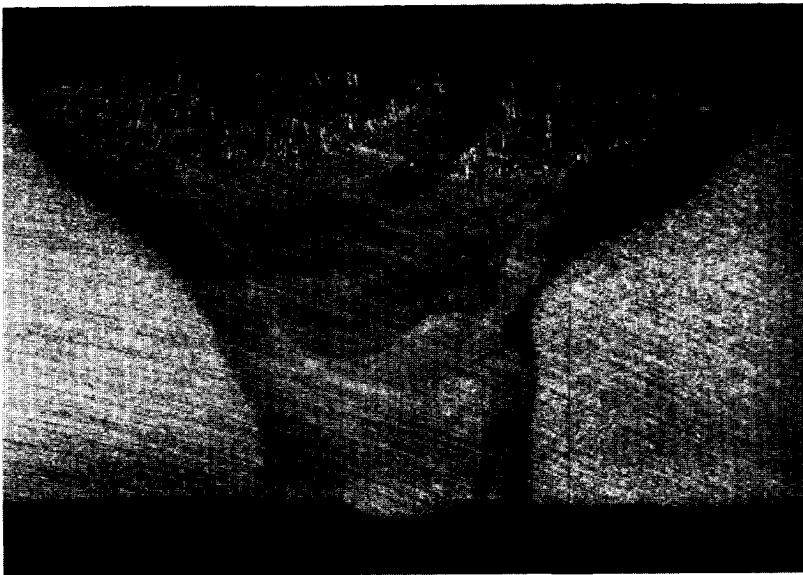
Figure 8.36: *Photograph of the imaged cross-section containing a lack-of-fusion defect in a V-shaped weld.*

8.3.7 Lack of penetration in a V-shaped weld

A lack-of-penetration defect in a V-shaped weld has been inspected by Multi-SAFT. The weld joins two steel plates of 12.8 mm thickness and the exact configuration is shown in figure 8.28. The measured shear wave velocity is approximately 3300 m/s. A 60° source transducer has been positioned at 65 mm from the reference point (corresponding approximately to the lateral position of the defect). The receiver aperture started at 40 mm and a 60° receiver transducer has been applied in a 30° lateral split angle configuration. The B-scan data is shown in figure 8.37, from which a number of multiple reflection responses can be recognized.

As the response of the (3,3) wave path is for the most part contained in the B-scan data, it has been employed for Multi-SAFT imaging and the result is shown in figure 8.38a. The center of the image corresponds the center of the weld. The location and –3 dB height of the indication have been determined from the Multi-SAFT image and are presented in table 8.6. Figure 8.38b shows the combined Multi-SAFT image featuring the weld lay-out. From the location and orientation of the indication in the image it can be concluded, that it is most likely a lack-of-penetration defect.

After the Multi-SAFT inspection, the weld has been inspected destructively and a photograph of the imaged cross-section is shown in figure 8.39. From this figure the precise location, orientation and height of the defect have been measured and these values are presented in table 8.6 to be
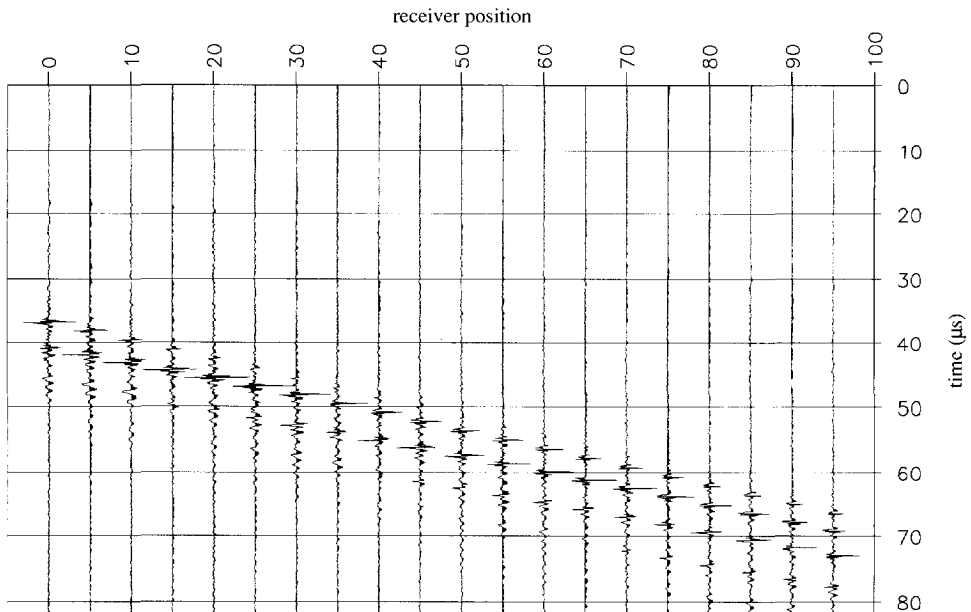
Figure 8.37: *B-scan data recorded from a lack-of-penetration defect in a V-shaped weld.*

(a)   lateral position (mm)   (b)   lateral position (mm)
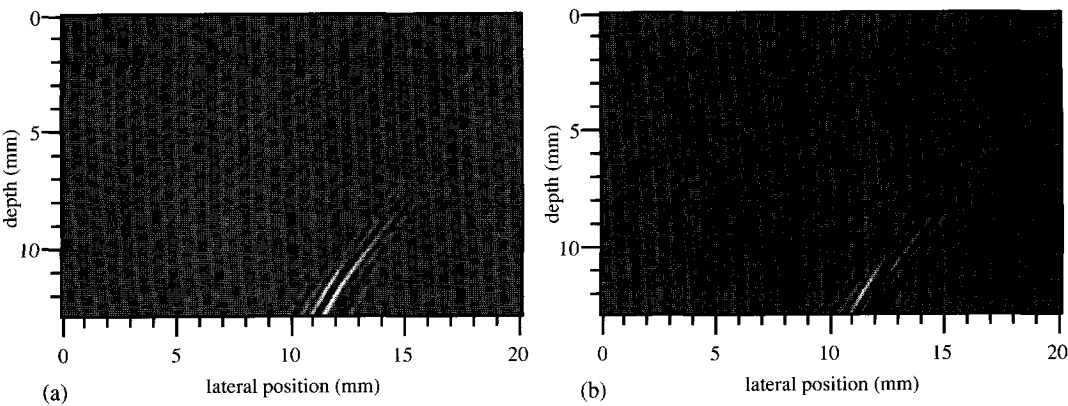
Figure 8.38: *The (3,3) image (a,b) of a lack-of-penetration defect in a V-shaped weld; imaged ROI centered.*

Table 8.6: *The defect characterization results from the Multi-SAFT and destructive inspections of a lack-of-penetration defect in a V-shaped weld.*

dimensions: (with respect to weld center)	lateral position (mm)	depth position (mm)	height (mm)
Destructive inspection	0.5-1.7	10.5-12.8	2.3
Multi-SAFT inspection	1-3	10-12.8	2.8
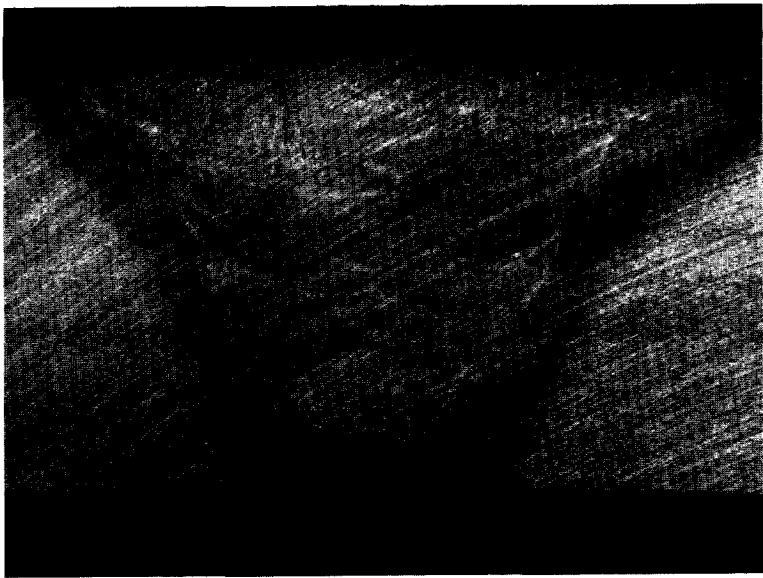
Figure 8.39: *Photograph of the imaged cross-section containing a lack-of-penetration defect in a V-shaped weld.*

compared with the values extracted from the images. Both the location and height determined with Multi-SAFT are not completely correct. As mentioned in the previous section, the positions of the diffracting extremities may be determined more accurately by performing a TOFD measurement.

8.3.8 Two weld defects at the same location in a V-shaped weld

In case two (or more) defects are present at approximately the same location in a weld, it becomes harder to interpret the ultrasonic responses by conventional means. Therefore, a Multi-SAFT inspection has been performed at a position in a weld which contained both a lack-of-penetration defect and a slag inclusion. The weld joins two steel plates of 12.8 mm thickness and the exact configuration is shown in figure 8.28. The measured shear wave velocity is approximately 3300 m/s. A 45° source transducer has been positioned at 45 mm from the reference point (corresponding approximately to the lateral position of the defect). The receiver aperture started at 45 mm and a 60° receiver transducer has been applied in a 30° lateral split angle configuration. The B-scan data is shown in figure 8.40, featuring a complex wave field.

The responses of both the (3,2) and (3,3) wave paths have been employed for Multi-SAFT imaging and the results is shown in figure 8.41. Figure 8.41c shows the combined Multi-SAFT
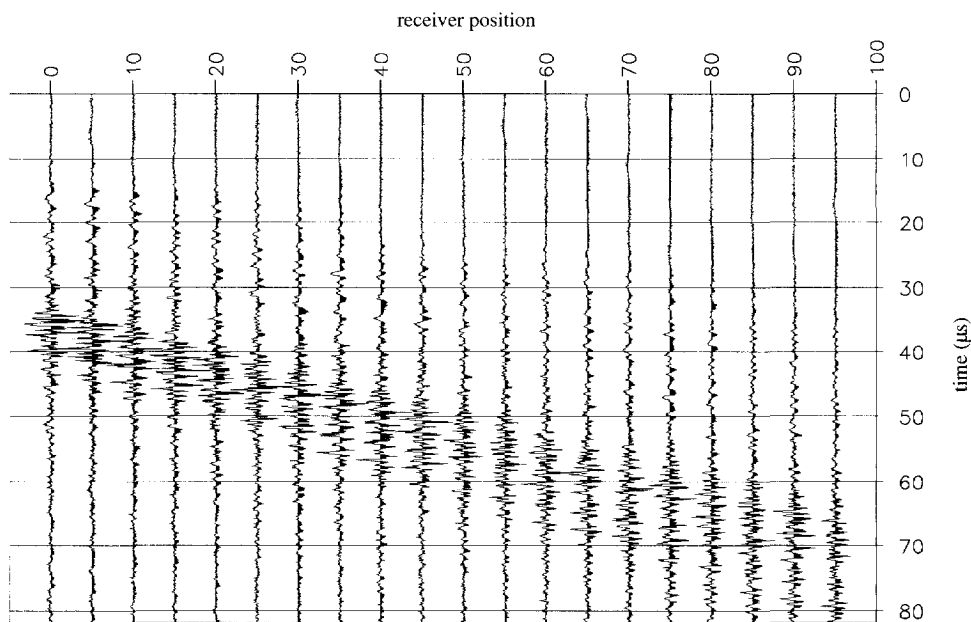
Figure 8.40: *B-scan data recorded from a slag inclusion and a lack-of-penetration defect together in a V-shaped weld.*
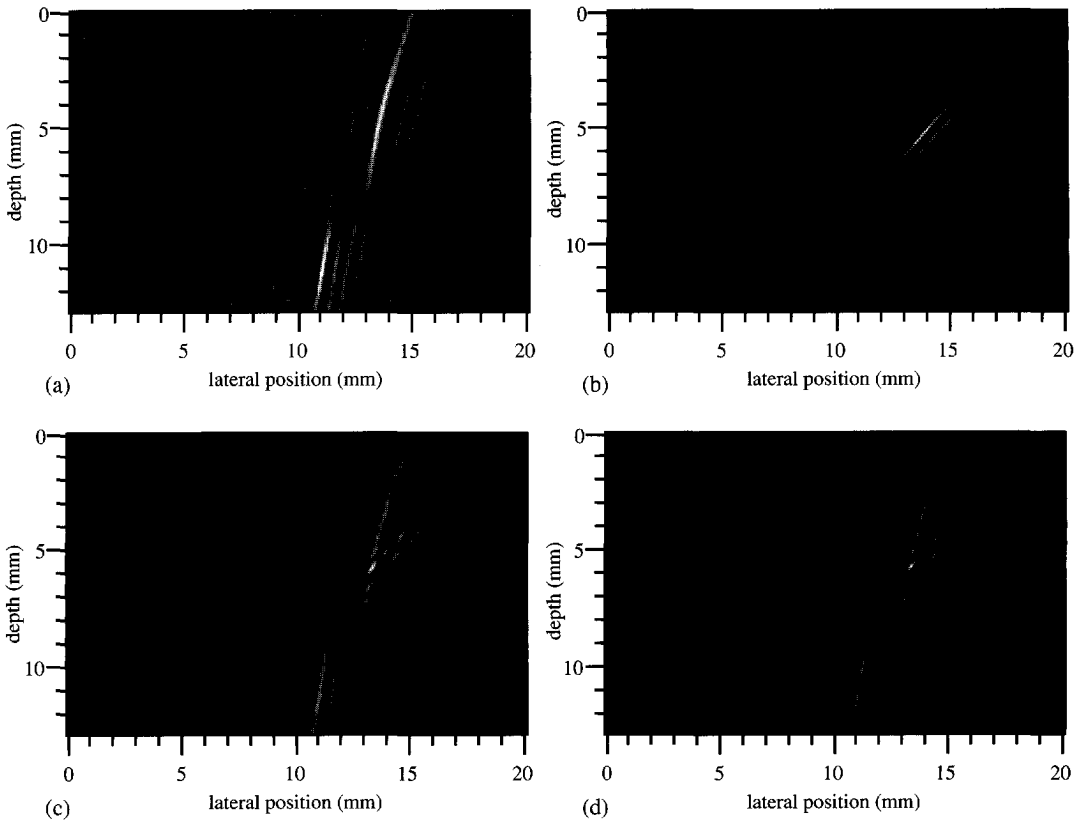
Figure 8.41: *The (3,2) image, the (3,3) image, and the combined Multi-SAFT image (c,d) of a slag inclusion together with a lack-of-penetration defect in a V-shaped weld; imaged ROI centered.*

image. The center of the image corresponds the center of the weld. The location and −3 dB height of the indications have been determined from the Multi-SA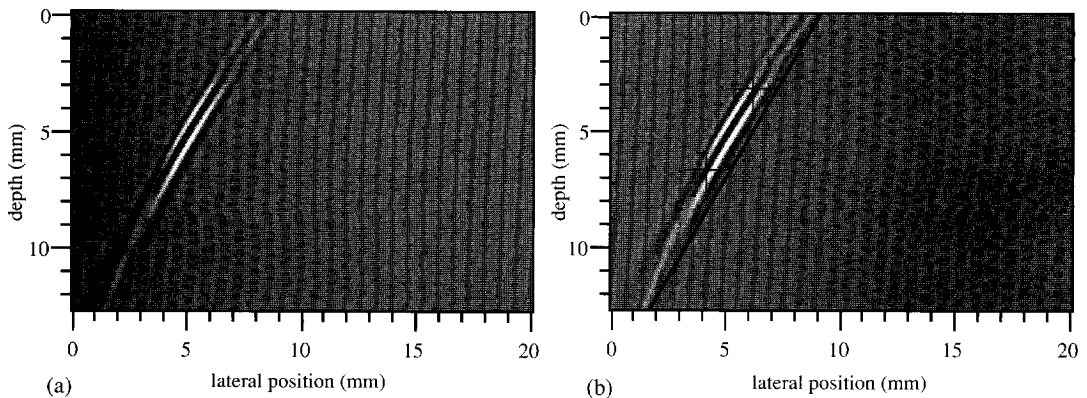FT image and are presented in table 8.7. Figure 8.41d shows the combined Multi-SAFT image featuring the weld lay-out. From the location and orientation of the indications in the image it can be concluded, that the upper one is most likely a slag inclusion. The lower indication could be either a lack-of-penetration defect or a slag inclusion.

After the Multi-SAFT inspection, the weld has been inspected destructively and a photograph of the imaged cross-section is shown in figure 8.42. From this figure the precise location, orientation and height of the defect have been measured and presented in table 8.7 to be compared with the values extracted from the images. The slag inclusion is small compared to the applied wave length (~1 mm) and therefore its height has been overestimated. The location of the slag inclusion, however, has been found quite accurately. As may be observed from the photograph shown in
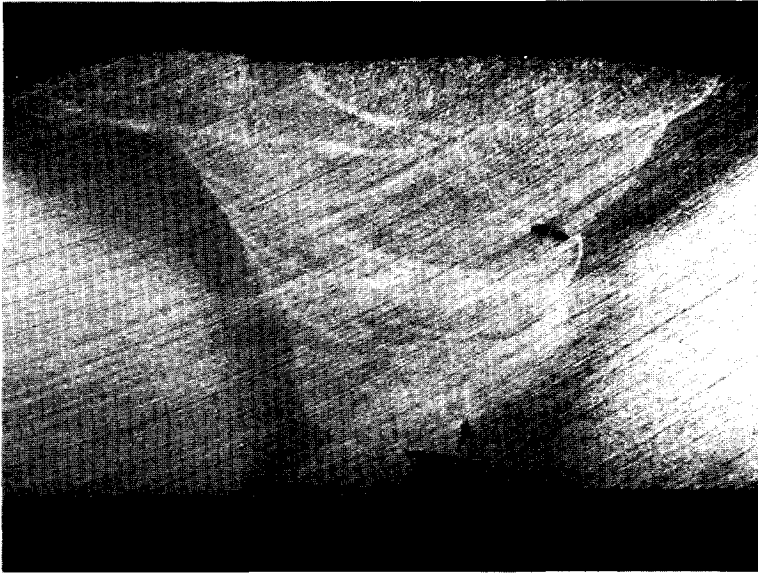
Figure 8.42: *Photograph of the imaged cross-section containing a slag inclusion together with a lack-of-penetration defect in a V-shaped weld.*

figure 8.42, the lack-of-penetration defect features something like an inclusion at its tip. This inclusion resulted in a strong forward reflection response (a (3,2) wave path), and lead to an incorrect interpretation of the indication and underestimation of the height of the defect.

Table 8.7: *The defect characterization results from the Multi-SAFT and destructive inspections of a slag inclusion and a lack of penetration in a V-shaped weld.*

dimensions: (with respect to weld center)	lateral position (mm)	depth position (mm)	height (mm)
Destructive inspection *slag inclusion*	2.7-3.7	4.7-5.1	0.4
Multi-SAFT inspection *slag inclusion*	3-5	4-6	2
Destructive inspection *lack of penetration*	0-0.7	10.5-12.8	3.3
Multi-SAFT inspection *lack of penetration*	1	10-12	2
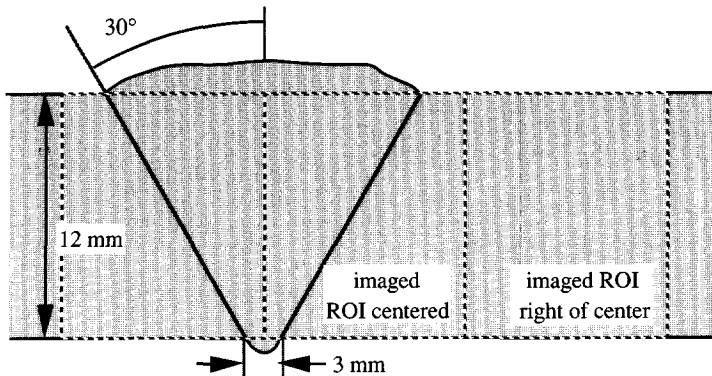
Figure 8.43: *The configuration of the V-shaped weld containing cracks.*

8.3.9 Cracks in a V-shaped weld

In chapter 7 it has been demonstrated, that rough or irregular planar defects (like cracks) are generally more difficult to image than smooth planar defects. To evaluate the performance of Multi-SAFT for crack-like defects, a test plate containing a V-shaped weld with a number of such defects has been made. The weld joins two NAXTRA steel plates of 12 mm thickness and the exact configuration is shown in figure 8.43. The measured shear wave velocity is approximately 3300 m/s. Two experiments have been performed on two differently oriented cracks (vertically and inclined). For the vertically oriented crack, a 60° source transducer has been positioned at 56 mm from the reference point. For the inclined crack, a 60° source transducer has been positioned at 65 mm from the reference point. In both cases, the reference point did correspond approximately to the lateral position of the defect. The receiver aperture started at 30 mm and a 60° receiver transducer has been applied in a 30° lateral split angle configuration. The B-scan data are shown in figure 8.44 and 8.45, from which can be observed that the signal-to-noise ratio is lower than for measurements on most other weld defects. This is caused by structure of the material (grain scattering) and the fact that cracks are less reflecting than smooth planar defects.

The vertically oriented crack has been imaged by employing the (3,4) forward-scattering wave path. The Multi-SAFT imaging result is shown in figure 8.46, where the left side of the image corresponds to the center of the weld. For the inclined crack, the (3,5) back-scattering wave path has been employed for imaging. The Multi-SAFT imaging result is shown in figure 8.47, where the center of the image corresponds to the center of the weld. The test plate was not yet destructively inspected at the time of writing this thesis. Therefore, the location and height of the indications, as may be extracted from the imaging results, could not be verified. However, the images of figures 8.46 and 8.47 clearly show that cracks can be imaged and that in both cases the defect has a (−3 dB) height of approximately 4 mm, which corresponds to the fabrication data.
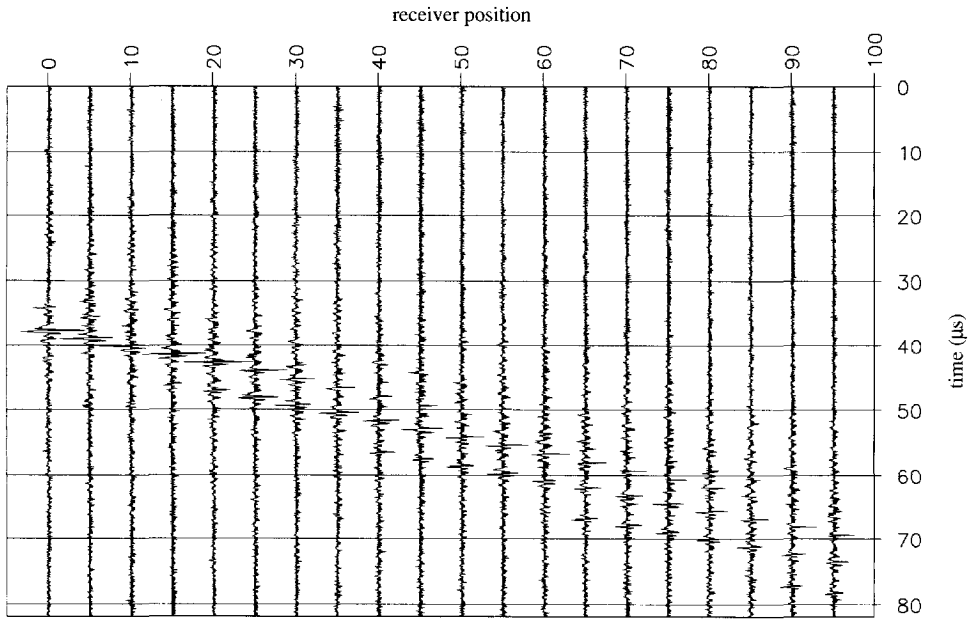
Figure 8.44: *B-scan data recorded from a vertically oriented crack in the heat-affected zone of a V-shaped weld.*

Figure 8.45: *B-scan data recorded from an inclined crack in a V-shaped weld.*

193
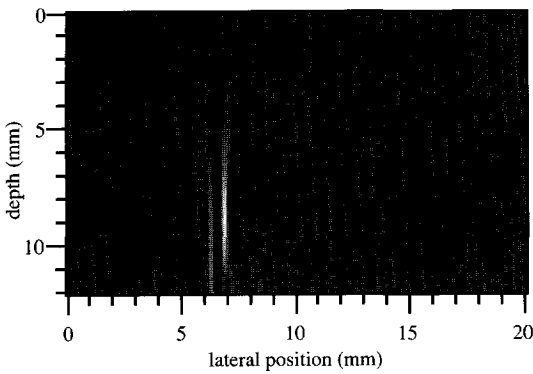
Figure 8.46: *The (3,4) image of a vertically oriented crack in the heat-affected zone of a V-shaped weld; imaged ROI right of center.*
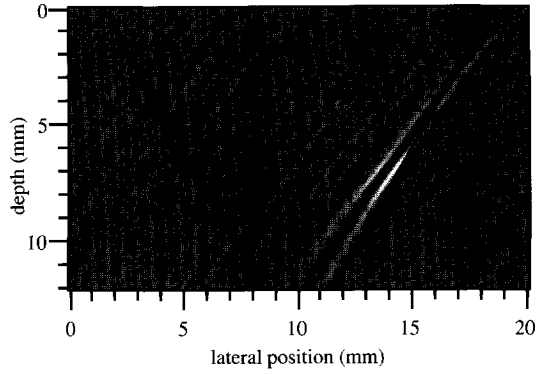
Figure 8.47: *The (3,5) image of an inclined crack in a V-shaped weld; imaged ROI centered.*

According to the location and orientation of both indications, the vertically oriented indication would be classified as cracking in the heat-affected zone and the inclined indication would probably be classified as a lack-of-fusion defect rather than a crack.

8.4 Real Weld Defects in Cylindrical Pipes

8.4.1 Lack of side-wall fusion in a V-shaped girth weld

A lack of side-wall fusion defect in a V-shaped girth weld has been inspected by Multi-SAFT. The weld joins two steel pipe sections of 14 mm thickness and the exact configuration is shown in figure 8.48. The inner radius of the pipe is 198 mm and the measured shear wave velocity is approximately 3300 m/s. A 60° source transducer has been positioned at 40 mm from the
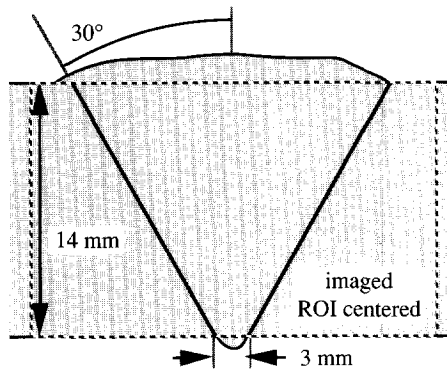
Figure 8.48: *The configuration of the V-shaped girth weld.*
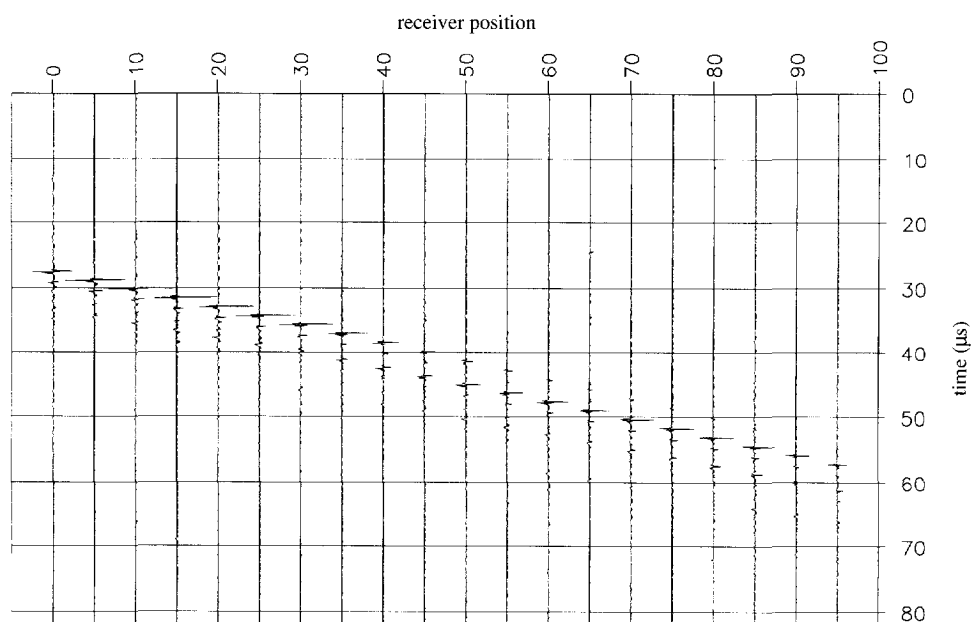
receiver position

Figure 8.49: *B-scan data recorded from a lack-of-fusion defect in a V-shaped girth weld.*

reference point (corresponding approximately with the lateral position of the defect). The receiver aperture started at 40 mm and a 60° receiver transducer has been applied in a 30° lateral split angle configuration. The B-scan data is shown in figure 8.49, from which a number of multiple reflection responses can be recognized.

As the response of the (1,1) wave path is the strongest and because the option of imaging of (3)-paths was not yet implemented for the cylindrical pipe geometry at the time of writing this theses, the (1,1) path has been employed for Multi-SAFT imaging and the result is shown in figure 8.50. The center of the image corresponds the center of the weld. The height of the indication has been determined by picking those points of the indication which are approximately −3 dB down compared to its maximum amplitude and is estimated to be about 3 mm (corresponding to the fabrication data). From the location and orientation of the indication in the image it can be concluded, that it is most likely a lack of side-wall fusion defect. The weld has not been inspected destructively.

The part of the pipe surface at which the inspection has taken place is visually not very curved. However, when the object is assumed to be a flat plate and the B-scan data is processed accordingly, the location of the indication will change as shown in figure 8.51. Although a defect in a girth weld may be identified correctly from the flat-plate image, its location may sometimes
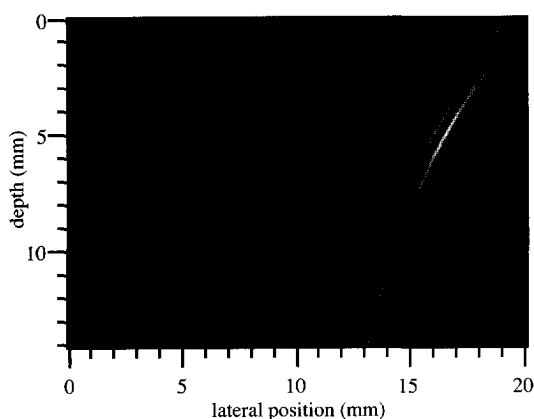
Figure 8.50: *The (1,1) image of a lack of side-wall fusion in a V-shaped girth weld; processed for the cylindrical pipe geometry.*
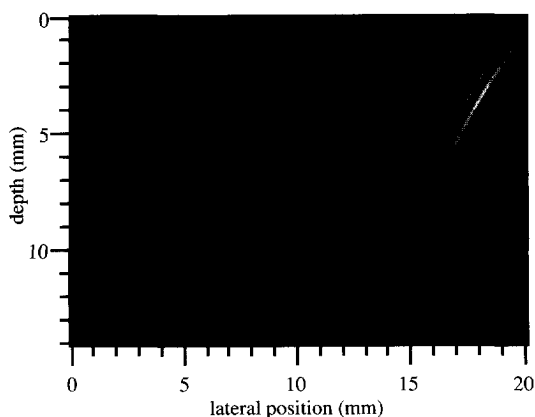
Figure 8.51: *The (1,1) image of a lack of side-wall fusion in a V-shaped girth weld; processed assuming a flat plate geometry.*

unjustly suggest that it is surface-breaking, for instance. Therefore, proper processing is preferred, taking the curvature of the pipe fully into account.

8.4.2 Cracking in a V-shaped girth weld

A small crack in a V-shaped weld has been inspected by Multi-SAFT. The weld joins two NAXTRA steel pipe sections of 14 mm thickness and the exact configuration is shown in figure 8.48. The inner radius of the pipe is 248 mm and the measured shear wave velocity is approximately 3300 m/s. A 60° source transducer has been positioned at 45 mm from the reference point (corresponding approximately to the lateral position of the defect). The receiver aperture started at 28 mm and a 60° receiver transducer has been applied in a 30° lateral split angle configuration. The B-scan data is shown in figure 8.52.

Although the (3,3) path should actually be chosen for imaging, the (1,1) path has been employed because the option of imaging (3)-paths was not yet implemented for the cylindrical pipe geometry at the time of writing this theses. The Multi-SAFT imaging result is shown in figure 8.53. The center of the image corresponds the center of the weld. The −3 dB height of the indication is estimated to be about 2 mm, although it should be 4 mm according to the fabrication data. The defect cannot uniquely be classified from the location and height of the indication. It could be planar (lack of fusion) as well as an inclusion (slag). Other experiments and/or other NDI techniques should be applied in order to be able to classify this defect properly. The weld has not been inspected destructively.
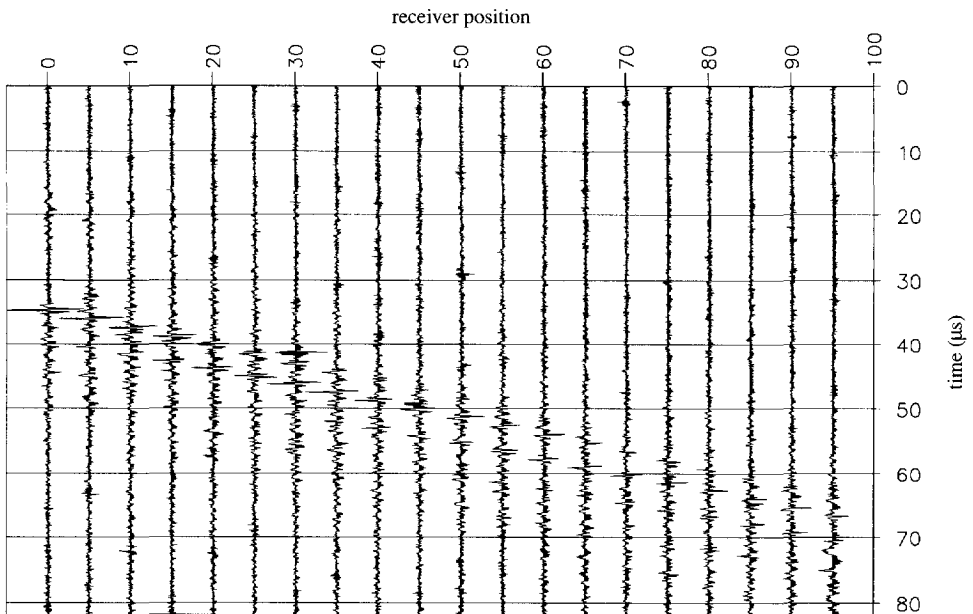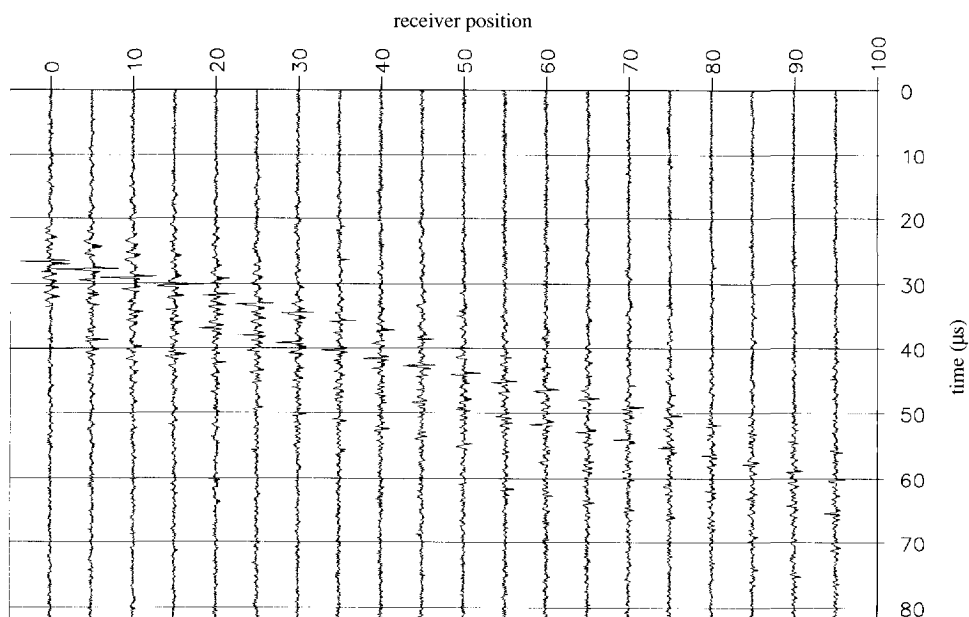
Figure 8.52: *B-scan data recorded from an inclined crack in a V-shaped girth weld.*
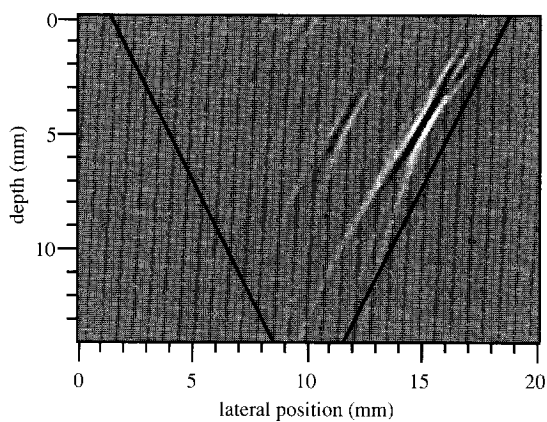
Figure 8.53: *The (1,1) image of an inclined crack in a V-shaped girth weld.*

197

8.5 Evaluation of Experimental Multi-SAFT Imaging Results

8.5.1 Image quality

The image quality is determined by both the image resolution and image accuracy. The image resolution is depending on the temporal and spatial frequency bandwidths. From the experimental imaging results it can be concluded, that the image resolution is limited mainly by the spatial frequency bandwidth and lies in the order of one wave length (approximately 1 mm for a center frequency of 3.3 MHz). For the images of the artificial defects, as described in section 8.2, this resolution seems sufficiently high. Yet, for a number of real weld defects a higher image resolution may improve the interpretability of the images. As the spatial frequency bandwidth generally cannot be increased (unless multiple experiments are considered), the temporal frequency bandwidth could be increased. Higher frequency components, however, will be more attenuated and internally scattered by the grain structure of the steel. Therefore, the increase of temporal frequency bandwidth will only improve the resolution in case the wave paths are short, i.e. for relatively thin (<15 mm) objects.

The image accuracy is mainly determined by the error in the location of the indication and by the presence of spurious indications. Through optimization of the insonification, not many (strong) spurious indications can be observed in the experimental imaging results. The location of the indication cannot always be determined accurately from the Multi-SAFT imaging results due to the limited inspection aperture (spatial frequency bandwidth). The combination of reflection and diffraction images, if possible, does improve the image accuracy considerably.

In general, the height of a defect is more accurately determined than its location. In most cases, the error in the height of the defect, as found from the experimental Multi-SAFT imaging results, is smaller than 1 mm and is apparently restricted by the image resolution. The error in the defect location ranges from 0 to 3 mm due to errors in the geometrical parameters and mainly depending on the type of defect. In case the exact position of the transducers could be measured more accurately during the inspection, for instance by applying special aids, the image accuracy could be improved further.

By comparing the imaging results computed from (finite-difference/ray-tracing) modelled data and measured data (figures 6.10 and 8.3 of the 10 mm high surface-breaking defect or 6.35 and 8.15 for the small vertically oriented defect) it can be concluded, that the experimental data-acquisition apparently has been optimal and that the assumptions made in chapter 4, regarding the applicability of the Multi-SAFT algorithm, do hold for these artificial defects.

By comparing two images with corresponding wave responses (like the (3,1) and (3,3) images) or

the maximum amplitude in two images computed with two different wave velocities, errors in the wave velocity have been easily discovered and eliminated. Consequently, most images feature nicely focused indications. Nevertheless, the accurate determination of both the wave velocity and the thickness of the object remain of vital importance. For instance, an error of 0.2 mm in the thickness will result in an error of approximately 1.2 mm when employing the (3,3) wave path.

In all cases, the signal-to-noise ratio of the B-scan data has been sufficiently high and did not give rise to confusing spurious indications in the images. The same holds for spurious indications from other responses present in the measured data. Apparently, undesired incoherent or coherent responses are successfully eliminated by the imaging (spatial averaging) process.

8.5.2 Characterization performance

Defect characterization involves the determination of the exact location, size/height, orientation and type/shape of a defect. From most of the experimental Multi-SAFT imaging results, as presented in the previous sections, the orientation and size/height of the defect could be determined accurately. The determination of the exact defect location was slightly less accurate. Apparently, the errors in the imaging parameters affect the location of an indication more than its size or orientation. Nevertheless, the approximate location of the indication in the image (with respect to the weld configuration) does give valuable information regarding the type of the defect. Hence, the type of the defect is in most cases determined successfully.

Of course, the characterization results obtained by Multi-SAFT can only be verified accurately in case destructive inspection of test objects has taken place. For the experiments described in sections 8.3.5 through 8.3.8 destructive inspection did actually take place. Yet, the destructive inspection of the test plate involved in these experiments (containing 15 weld defects) showed that the fabrication data are very accurate (error <1 mm) in most cases. This implies, that it really makes sense to compare the Multi-SAFT characterization data with the fabrication data in case destructive inspection is not possible. For the experiments involving cracks it is not sure if the fabrication data are accurate, because it is much more difficult to predict the size and orientation of a crack, which is induced during welding. Consequently, the crack-images merely demonstrate the possibility of imaging crack-like defects qualitatively.

Although the type of a defect may be identified correctly, its shape cannot always be determined from the Multi-SAFT images. And it often depends on the shape, rather than the type, whether or not a defect is classified as dangerous or not. A slag inclusion, for instance, may be harmless to the construction in case it is spherically shaped, but it may be quite harmful when it does possess sharp edges. With the aid of tomographical imaging the shape of a defect could be found quite easily. However, a measurement in practice along a limited inspection aperture does only provide

limited-resolution images from which the shape of the defect is not always clear. Therefore, other methods should be applied in conjunction with Multi-SAFT imaging to provide the additional information on defect shape. In the next chapter, an alternative method for defect shape determination by the application of neural networks is proposed.

9

Defect Characterization and Artificial Intelligence

9.1 Introduction

The term *'Artificial Intelligence'* was introduced about 30 years ago by J. McCarthy (Engelmore, 1987), who has continued to be one of the field's most important theoreticians. This field contains the subfields of knowledge-based systems (*expert systems*) and *neural networks*, and has primarily been a field of academic research. Problems which require some degree of human-like intelligence are tackled with Artificial Intelligence, although the actual approach depends on the type of problem.

Medical diagnostics, alarm processing and railway scheduling are problems for which data, rules and conditions may be gathered and assembled into a well-defined algorithmic structure, usually an expert system. Speech understanding and handwritten character recognition are tasks which cannot be easily solved by conventional techniques, since no precise algorithmic solution exists and therefore recognition, rather than computation, forms the basis of the solution. Recognition methods, such as neural network classification, operate by associating an unknown input pattern with previously encountered patterns and find the closest match.

In chapter 8 it has been shown that – due to the limited inspection aperture – the Multi-SAFT imaging result does not always allow an accurate determination of the shape of the defect. Especially when a creeping wave response is not present, a spherical defect is easily mistaken for a planar defect. This is illustrated, for instance, by the image of the slag inclusion shown in figure 8.25a. In practice, it is very important to know whether or not a defect possesses sharp extremities, as such a type of defect may considerably reduce the strength of a construction and may therefore be regarded as potentially dangerous.

Thus, the shape of the defect plays an important role and since it cannot be determined from the imaging result, the application of a neural network for defect-shape identification will be discussed. As a first step towards neural-network based defect characterization, the classification

of defects as either *'round'* or *'planar'* has been studied (Wielinga, 1992) and the results are presented in this chapter. The applied training and test data are modelled with the aid of a 2-D finite-difference scheme (Virieux, 1986; Van 't Veen et al., 1993). To check the results obtained with the modelled data, a number of real experiments has been carried out as well. At first, an explanation of the main principles and an overview of the existing methods and applications in NDI will be given.

9.2 Artificial Intelligence in Nondestructive Inspection

9.2.1 Main principles of expert systems and neural networks

An *expert system* consists of a knowledge base, which resembles a global data base containing facts, rules, relations, etc., and an inference engine, which interprets the knowledge and controls the problem solving procedure according to some strategy. There are two practical reasons for using expert systems: they can reduce costs and/or increase the overall quality of many decision-making tasks. For it should be realized: "Remember that crises and experts are almost never in the same place at the same time!" (Englemore, 1987). Expert systems provide less experienced personnel with expertise that is otherwise typically unavailable. Moreover, expert systems may be used to automate routine decision-making tasks, keeping accurate, consistent and complete records of their actions.

The human brain is processing information by means of interaction between many neurons to be able to interpret the signals perceived by its senses. A *neural network* is a modelled interaction between neurons and consists generally of three layers: a sensory or input layer, an association or hidden layer, and a response or output layer. Each layer has a certain number of units or neurons. Neurons in the same layer have no connection to each other and neurons in different layers have one-way connections. Such a network is called a *perceptron layered network* (Simpson, 1990) and is shown schematically in figure 9.1 for N input neurons and 2 output neurons.

Each neuron receives input signals from the neurons of a previous layer, which are multiplied by a certain weight value (representing the amount of activation an input signal causes). The neuron then calculates the total activation value, applies the input/output function and puts the result forward to the neurons of the next layer. The input/output function, transforming the activation value, is usually expressed by a threshold function or Sigmoid function (Freeman and Skapura, 1991) and is applied in order to get output values ranging between 0 and 1.

The activity of the network depends upon the characteristics of each neuron and the connections between them. In order to perform a classification process the inter-connecting weights have to be
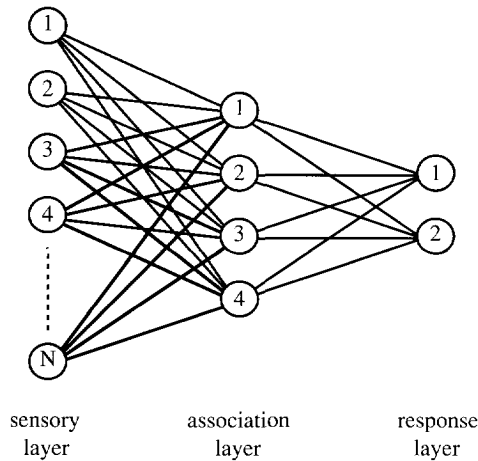
Figure 9.1: *The general structure of a perceptron layered network with N input neurons, 4 hidden neurons and 2 output neurons.*

set. For that purpose the neural network needs training, i.e. the network has to correct its connection weights little by little by gathering experience and comparing the output results with the correct answers. One of the most popular training methods is the *Backward Error Propagation* method (Freeman and Skapura, 1991), where the network computes some correction for each weight value from the error information during training.

The neural network, which will be used to evaluate the classification of planar and round defects in this chapter, will be a perceptron layered network of three layers with only one hidden neuron and two output neurons. The number of input neurons will depend on the type of input that will be used. The applied training method is the Backward Error Propagation method and the network has been implemented using the commercially available software package Neural Works Pro®.

9.2.2   Overview of existing methods and applications in NDI

The application of artificial intelligence in NDI has only recently been seriously considered practically feasible and since 1987 several publications can be found on this subject. About the development of expert systems in general and for NDI in particular, a nice overview is given by Engelmore (1987). McNab and Dunlop (1991a) give an introduction on information technology in NDI. At the Center for NDE at the Iowa State University, Ames USA, an expert system for flaw classification has been developed (Schmerr Jr. et al., 1987; Nugen et al., 1988). This so-called Flaw Expert (*FLEX*) system is designed to characterize flaws as either crack-like or volumetric from an inspection of ultrasonic scattering amplitudes, taken from multiple angles of insonification. The feature processing part characterizes the waveform with respect to a pre-

defined set of features (*knowledge base*), while the 'interpretation' part uses the presence or absence of these features to characterize the flaw with respect to type (*inference engine*). According to the papers the results are quite accurate, indicating a defect to be volumetric or crack-like with an accuracy better than 70%.

To allow discrimination between intergranular stress-corrosion cracking (*IGSCC*) and counterbores (ridges machined prior to welding to match unequel pipe-wall thicknesses) near welds, a knowledge-based ultrasonic examination assistant has been developed at the EPRI NDE Center, Charlotte USA (Shankar et al., 1991). It helps interpreting measured B-scan data using an expert system. A knowledge-based assistant has also been developed for a SAFT ultrasonic inspection system (Melton et al., 1987) in order to ensure that the SAFT inspection procedure is performed correctly and consistently, i.e. guiding an operator through a SAFT inspection.

Flaw classification and sizing through learning systems like neural networks have been firmly related to physics (Schmerr Jr. et al., 1988; Grabec and Sachse, 1989). In order to be able to define classification rules for an expert system, specific (discriminating) features have to be extracted from the ultrasonic data. Therefore, extensive studies have been performed on ultrasonic responses from defects in order to determine those specific features. These studies also include the (elastic) modelling of defect responses, for modelled data are often used as training data for neural networks.

Apart from the many different network structures and training methods, the input to the neural network ranges from statistical characteristics of the response (Baker and Windsor, 1989; Brown and DeNale, 1991; Song and Schmerr Jr., 1991), digitized time domain and/or frequency domain data (Ogi et al., 1990; Kitahara et al., 1991), to shapes of the response hyperbolas in B-, C- and D-scans (Hallam et al., 1990; McNab and Dunlop, 1991b; Woodcock et al., 1992). Surprisingly, regardless the type of input, 70-100% of the defect classification is claimed to be correct. In all cases, however, it is very important to apply the correct pre-processing of the raw data before using it as input for a neural network. A number of pre-processing techniques for digitized responses have been discussed by Berry et al. (1991).

The way a neural network operates has been already intensively studied in almost all work mentioned earlier. Especially Ogi et al. (1991) did study the influence of the different weight factors and the features the network seems to extract from the data. Also Wielinga et al. (1993) describe the adjustments of the weight factors during training and show that the final weights are related to the standard deviation of the average input values. In Kitahara et al. (1992) the first successful results have been presented on sizing of surface breaking defects.

9.3 Classifying Defects with Neural Networks

In this section the first step towards a full-scale evaluation of the application of neural networks for defect characterization will be described. This first step consists of determining the shape of a defect with neural networks, i.e. the classification of a defect as either planar or non-planar. In this chapter the network input will be directly extracted from the recorded (ultrasonic time-domain) wave field data, although it is plausible that the Multi-SAFT images could provide as good a basis for the extraction of network input. For simplicity, the defects to be classified will be either *round* (cylindrical) holes or horizontally oriented *planar* slots (with ends simulating vertically oriented defects, see figure 9.2).

9.3.1 Determining network input

As already described in the previous section, the success of neural defect classification is mainly determined by the type of network input (*input pattern*). This generally means, that appropriate pre-processing of the measured ultrasonic data has to be applied in order to obtain the best input data for the network. This pre-processing may consist of determining statistical parameters, filtering or transforming the data. Above all, the input data should possess those discriminating features needed for correct defect classification. In this section, the neural network classification performance for three different types of input will be evaluated.

The *time-domain response* and its *temporal amplitude spectrum* will be used as input, because the successful application of these types of input is extensively described in the literature. The response, used for the time-domain and temporal amplitude spectrum inputs, will be recorded at the geometrical reflection position (see figure 9.2). In the case of classifying a defect to be planar or non-planar (round), the discriminating information will obviously be contained in the directivity of the scattered wave field. Therefore, the *spatial amplitude spectrum* of the (filtered)
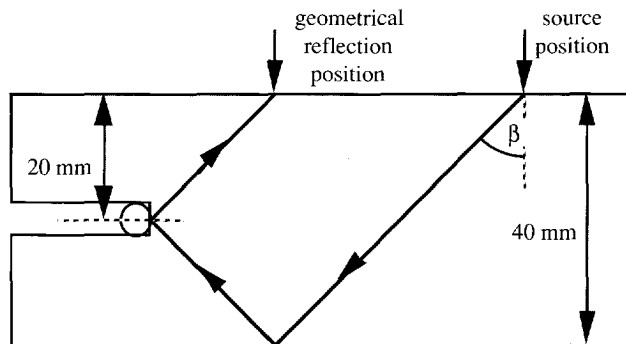
Figure 9.2: *The configuration of the round and planar model defects in low-carbon steel.*

B-scan data will also be applied as input for the network. A monochromatic spatial amplitude spectrum represents the plane-wave amplitude as a function of incident angle (with respect to the normal) on the receiver aperture. In order to obtain the spatial amplitude spectrum, the complete (filtered) B-scan is Fourier transformed with respect to time as well as to space (scanning direction) and is known as plane-wave decomposition. According to the literature studied in relation to this project, this type of input has never been applied for classification purposes before.

The discrete amplitude values of the different input patterns will directly be used as input values for the network, which may lead to a large number of input neurons to be defined for the neural network. The measured B-scan contains many responses and the correct response to be used (for every type of input) is determined by using its Multi-SAFT imaging result. From the indication in the image (obtained for a certain wave path) the arrival time in the recorded data can be computed by applying an *inverse-SAFT process*. The other responses contained in the recorded ultrasonic data should then be carefully filtered out to avoid undesired interference effects.

In practice, the time-domain response of a defect and its temporal amplitude spectrum will not only depend on the shape of the defect, but also on its orientation, on the employed wave path and on the transducer and surface characteristics (frequency contents, coupling). Thus, a neural network trained with the time-domain response or its temporal spectrum cannot be generally applied in practice, as the shape of the recorded wavelet is usually unknown and certainly subject to changes. The shape of the spatial amplitude spectrum for a single frequency, on the contrary, does not depend on the shape of the wavelet and may therefore be particularly suited for defect shape classification. However, the monochromatic spatial amplitude spectrum does depend on the directivity pattern of the receiver transducer. Yet, this directivity pattern may easily be determined and is not subject to serious changes in practical applications.

9.3.2 Modelled input data

In order to be able to study the neural network classification of defects, scattering data has been modelled using a finite-difference modeling scheme. Ultrasonic B-scan data of a series of models have been computed using the basic model as shown in figure 9.2. In order to strive after a network, which is not sensitive to changes in the size of the defects, round and planar defects have been defined for different sizes (length of the planar defect and diameter of the round defect). The sizes have been chosen to be 0.5, 1.0, 1.5, 2.0, 2.5, 3.0, 3.5, and 4.0 wave lengths with respect to the center frequency of 1 MHz in a medium with a (shear) wave velocity of 3260 m/s ($\lambda \approx 3.3$ mm).

In order to minimize the sensitivity of the network for changes in the insonification direction (orientation of the defects), scattering data for different angles have been provided. The

lateral distance
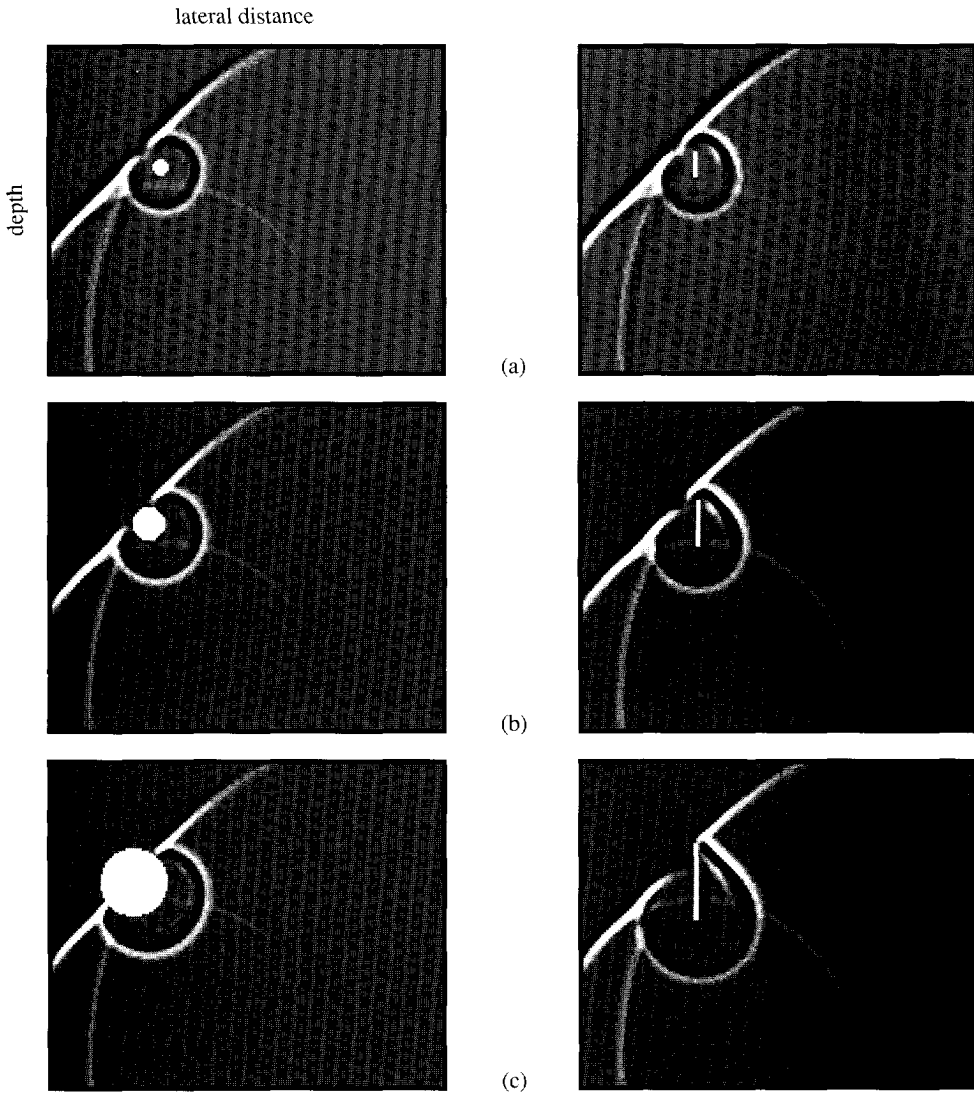
Figure 9.3: *The modelled snapshots showing the difference in acoustic scattering from round and planar defects of 1 λ (a), 2 λ (b) and 4 λ (c) diameter/height.*

insonification angles β have been chosen to be 34, 40°, and 45°. The first set of 48 B-scans has been computed by modelling an *acoustic* medium with a wave velocity of 3260 m/s, the second set by modelling an *elastic* medium with a compressional wave velocity of 5900 m/s and a shear wave velocity of 3260 m/s. In all cases absorbing boundaries have been applied at all sides and the insonifying plane wave is propagating upwards, corresponding to the (1,0) wave path. The defects have been modelled as stress-free boundaries. Snapshots of the scattering wave field from

lateral distance

depth

(a)

(b)

(c)
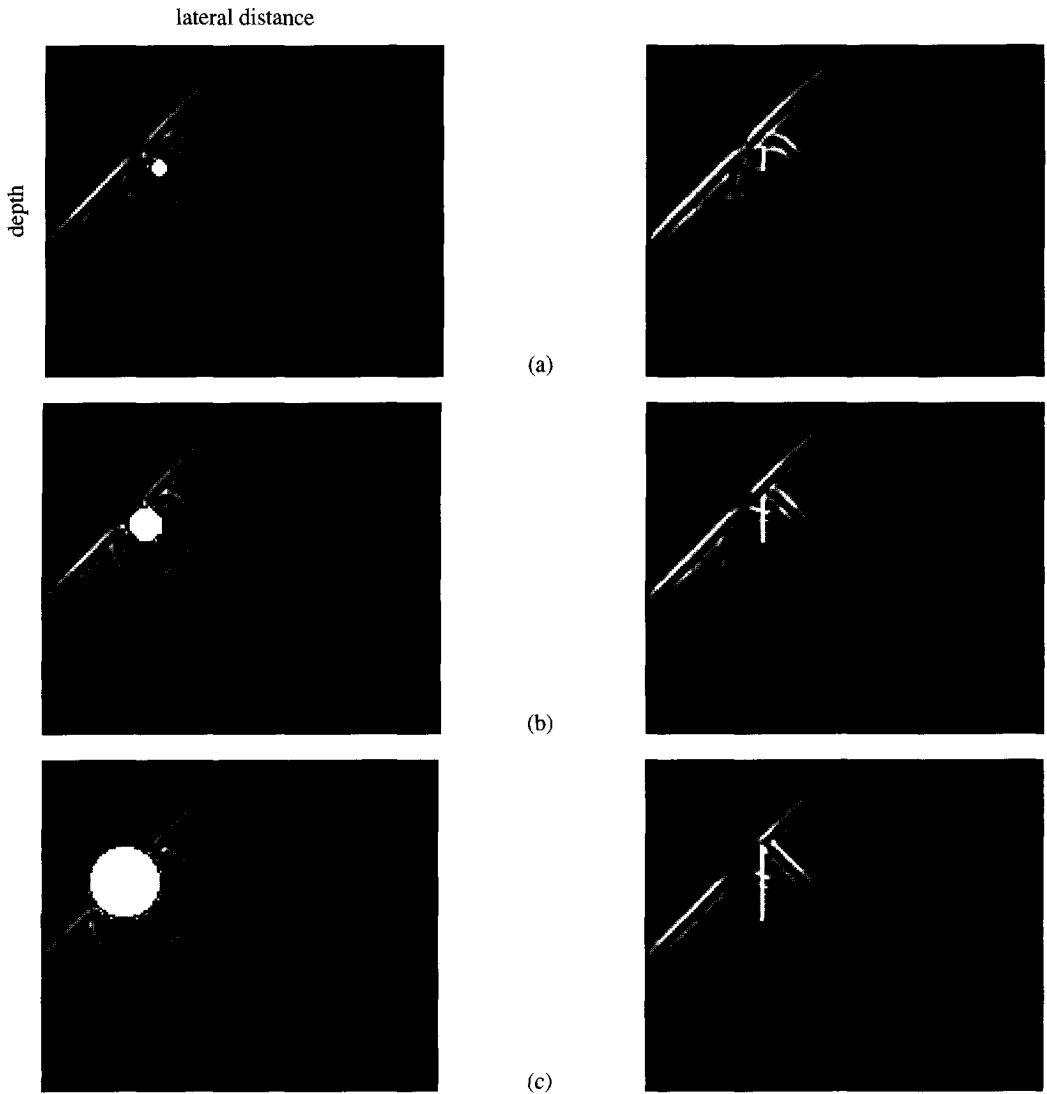
Figure 9.4: *The modelled snapshots showing the difference in elastic scattering from round and planar defects of 1 λ (a), 2 λ (b) and 4 λ (c) diameter/height.*

defects of different sizes are shown in figure 9.3 for the acoustic case and figure 9.4 for the elastic case. The difference in directivity of the scattering patterns for defects of different size and shape is quite obvious from these snapshots. Moreover, the difference between the acoustic and elastic situations becomes clear from the mode-conversion effects as may be observed in the elastic case.

For comparison, the network has been trained and tested with the modelled time-domain
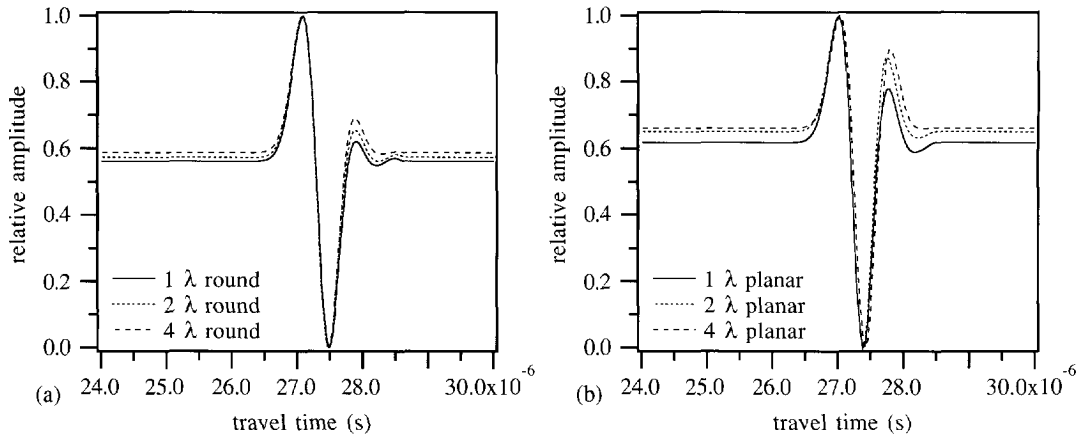
Figure 9.5: *The modelled acoustic time-domain responses for round (a) and planar (b) defects of different sizes.*

responses, the temporal and the spatial amplitude spectra[1]. They have all been presented to the network in a fixed number of points (the time-domain response centered around its maximum amplitude) and normalized between 0 and 1. This normalization is necessary to prevent the network to base the classification on absolute amplitude differences. Some of the input data extracted from the modelled acoustic data are shown in figures 9.5 to 9.7. It is easy to see differences between round and planar time-domain defect responses, as well as between their spatial amplitude spectra. However, the differences are less clear when comparing the temporal amplitude spectra.
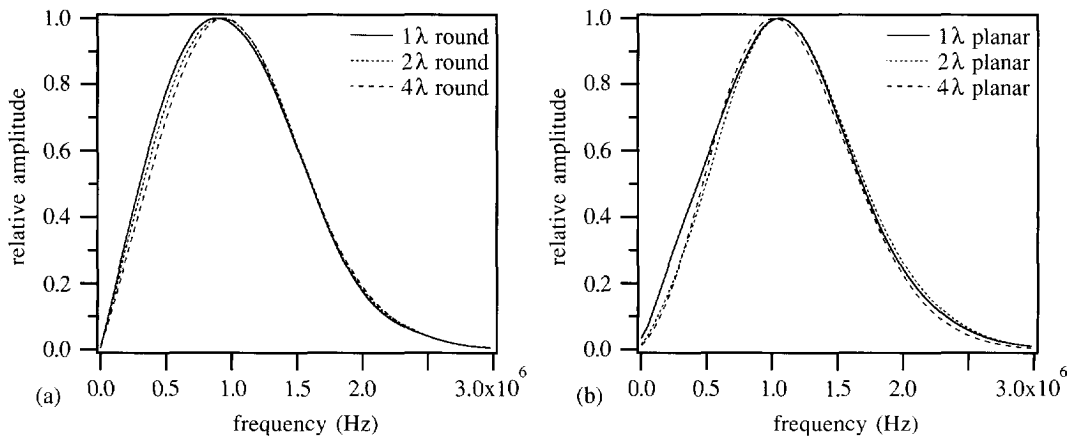
Figure 9.6: *The modelled acoustic temporal amplitude spectra for round (a) and planar (b) defects of different sizes.*

---

1   It has to be noted here, that the applied (modelled) receivers are almost *omni-directional*, i.e. almost equally sensitive for responses from all directions.
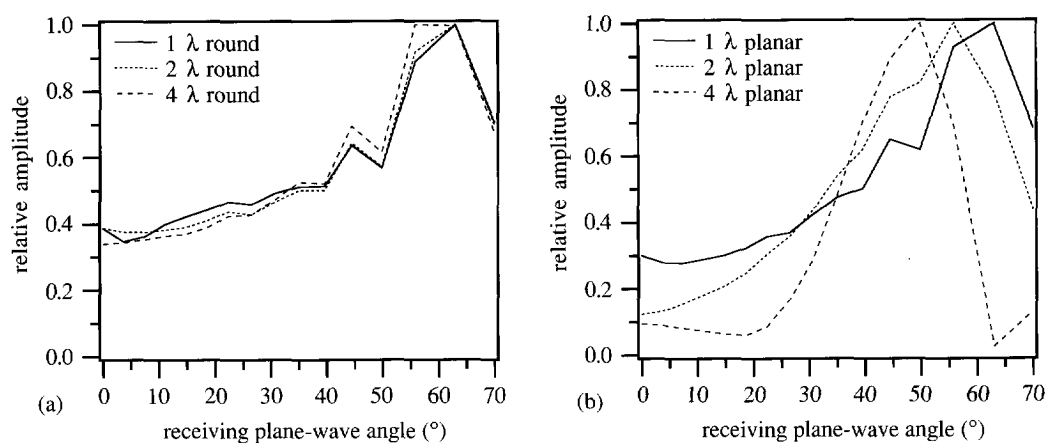
Figure 9.7: *The modelled acoustic spatial amplitude spectra for round (a) and planar (b) defects of different sizes.*

The neural network used for the evaluation study consists of a number of input neurons (64 for the time-domain response and the temporal amplitude spectrum and 16 for the spatial amplitude spectrum at 1 MHz), 1 hidden neuron and two output neurons. In Wielinga et al. (1993) it has been explained that this classification problem is simple enough to be handled by one single hidden neuron (linearly separable). This actually implies, that a properly designed statistical classifier should also be able to classify the different input patterns correctly. This again indicates, that the chosen types of input patterns obviously contain a considerable amount of discriminating information. Of course, the echo-acoustic response of a defect does represent its reflectivity, containing information on the structure and composition of the defect. In practice, the input patterns will probably contain less discriminating information due to the presence of noise and the beam pattern of the receiver transducer. In that case the neural network should possess more than one single hidden neuron in order to accomplish the classification task correctly. Besides, the classification of defects with trained neural networks will always be much faster than with statistical classifiers.

At first, the neural network has been trained and tested with all data for one and the same insonification angle to make sure that the network converged, i.e. that the input data does indeed possess distinct differences on which the classification may be based. Then the classification performance is determined by testing the trained neural network with new input patterns.

The classification results are given in a *matching percentage*, which is just the output value (sum of weights between 0 and 1)[2] of the neural network and does not equal a confidence level. For the

---

2   The output value is 1 when the input pattern corresponds 100% to the output class and 0 when it does not at all correspond to the output class.

output value an *acceptance level* of 0.85 has been defined, representing a threshold value above which an input pattern is assigned to a certain class. When the acceptance level is not reached by any of the two output values, the classification result will read *'undefined'*. In order to provide the network with consistent information for the learning process, the input patterns from the four smallest defects have been omitted during training. These small defects (small compared to the wave length of the 1 MHz center frequency) act mainly as diffractors, possessing a scattering directivity corresponding to that of small round defects, regardless of the shape of the defect (planar or not).

9.3.3 Input based on acoustic responses

Testing the network with the training data (without the four smallest defects) is called a *convergence test* and did result in a 100% correct classification for all types of network input and for all insonification angles combined to one single set. To test the *classification performance* of the neural network, it has been trained with the data from the insonification angles of 34° and 45° and tested with the data from the insonification angle of 40°. The spatial spectra have been computed for the 1 MHz center frequency and all acoustic test results are shown in figure 9.8. The test set contained 50% input patterns of round and 50% of planar defects. These test results are remarkable, as the round defects are all classified 100% correct for all three types of input, while on the other hand the planar defects are classified very inaccurately, except for the spatial spectra. The neural network seems to assume beforehand every input pattern to be a round defect and only classifies defects as planar when they are distinctly different from round-defect patterns.

As mentioned before, the smallest planar defects are classified as round defects because they act as diffractors for the wave length corresponding to the frequency used to compute the spatial spectra. In case a higher frequency (smaller wave length) is chosen for the spatial spectrum input,
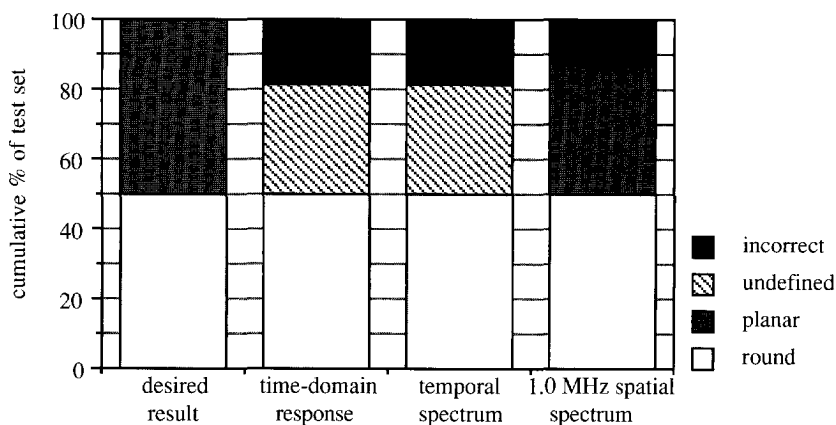
Figure 9.8: *The classification performance of the trained neural network for different acoustic input patterns.*
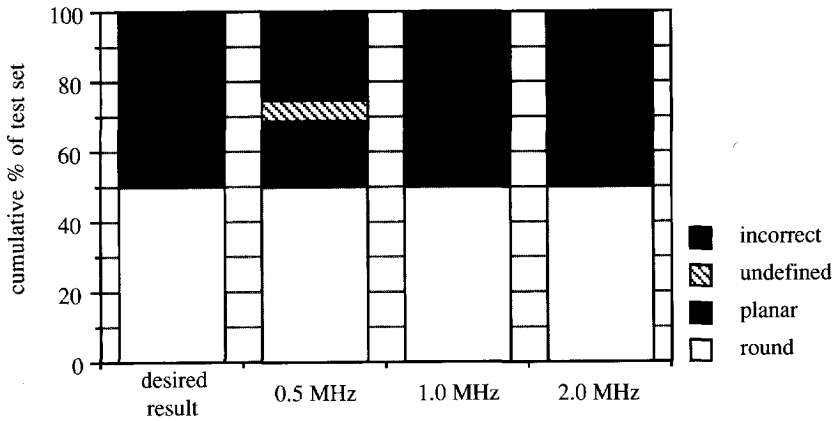
Figure 9.9: *The classification performance of the trained neural network for acoustic spatial spectra of different frequency components.*

the classification results for the smaller planar defects should improve. In figure 9.9 the classification performance is presented for the 0.5, 1.0, and 2.0 MHz spatial spectra of round and planar defects by a neural network trained with 1 MHz spatial spectra (without the two smallest defects). The classification results do indeed improve for a higher frequency (and become less accurate for a lower frequency). This implies, that classifying spatial spectra for different frequencies may also yield information on the size of the defect.

9.3.4 Input based on elastic responses

The same model of figure 9.2 has been used to model elastic scattering data from eight different sizes of round and planar defects. Elastic data contains more responses than acoustic data, because of the presence of creeping and mode-converted waves, so the scattering shear wave response may still be disturbed by other responses after isolation by narrow time-windowing. The same remarks hold here as for the acoustic models concerning the different input formats and the wave-length dependent classification for spatial spectra. The convergence test did overall result in almost 100% correct classification. Figures 9.10 and 9.11 present the results of the classification performance. The classification results of the elastic data show, that the network does not classify the round defects as distinctly as in the acoustic case, because the input data do contain more discriminating features. The results for the spatial spectra in this elastic case are comparable to those of the acoustic case.

9.3.5 Noise sensitivity

The classification performance has been evaluated with the aid of modelled elastic responses which do not contain any noise. This is not the case in practice and thus the networks classifying
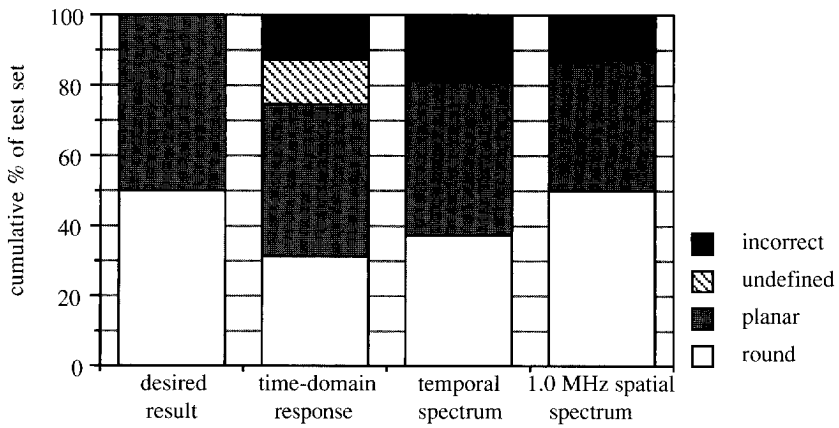
Figure 9.10: *The classification performance of the trained neural network for different elastic input patterns.*

performance has to be evaluated with input data from noisy responses. Therefore, random (approximately white) noise has been added in different amounts to the modelled elastic data (signal-to-noise ratios: 40, 30, 20, 10, 5 dB) and input patterns have been computed. The classification results are shown in figures 9.12 and 9.13 for the different signal-to-noise ratios. From these results it can be observed, that the spatial amplitude spectra are apparently less affected by the presence of noise than the other input types. This is probably caused by the fact, that the responses in the entire B-scan are employed for computing the spatial amplitude spectra (averaging the noise influence) and that the added noise does not possess any distinct directivity which could change the shape of the spatial amplitude spectrum severely.
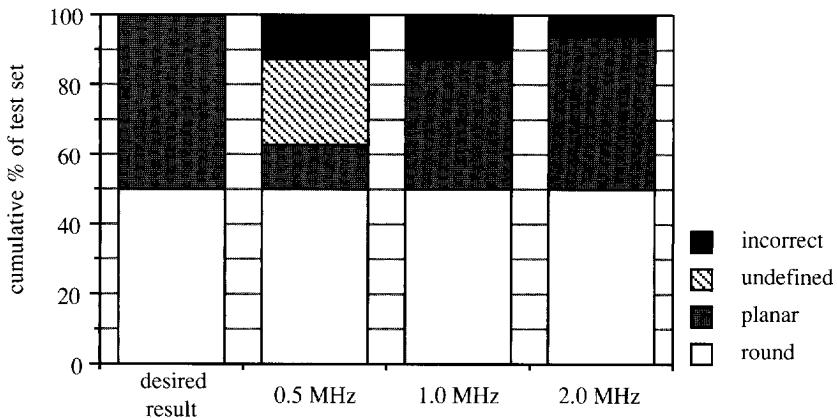
Figure 9.11: *The classification performance of the trained neural network for elastic spatial spectra of different frequency components.*

It can be concluded from the results presented in this section, that the spatial amplitude spectrum is obviously the most appropriate input pattern for the determination of defect shape by neural networks, as it is independent of the shape of the wavelet and less sensitive to the presence of noise. Therefore, the neural network classification performance of only this type of input will be evaluated in section 9.3.7 using experimental data.

9.3.6 Training analysis

The input data should contain discriminating features for the network to base its classification on. The larger the differences between the responses from a planar and a round defect, the faster a network will converge during training and also the more reliable the classification result will generally be. To study the extent of discriminating information, the RMS-error of the network output has been plotted as a function of the number of training cycles for all three types of input data and is shown in figure 9.14. Comparing these graphs it is quite evident, that in this case
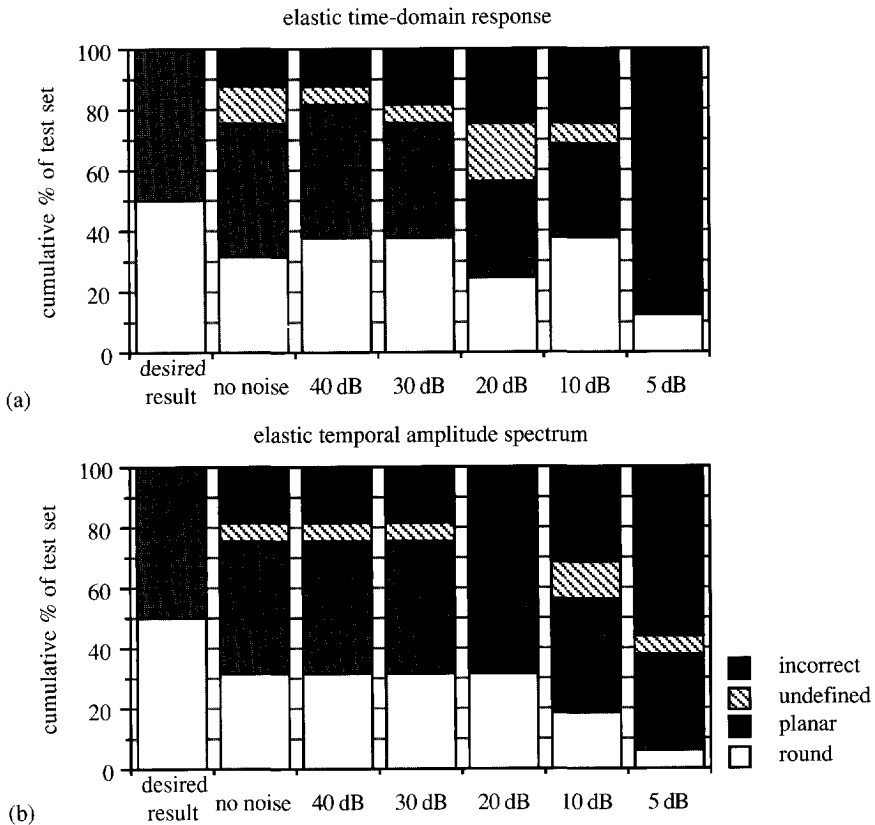
Figure 9.12: *The classification performance of the trained neural network for the elastic time-domain response (a) and its temporal frequency spectrum (b) for different values of the signal-to-noise ratio.*
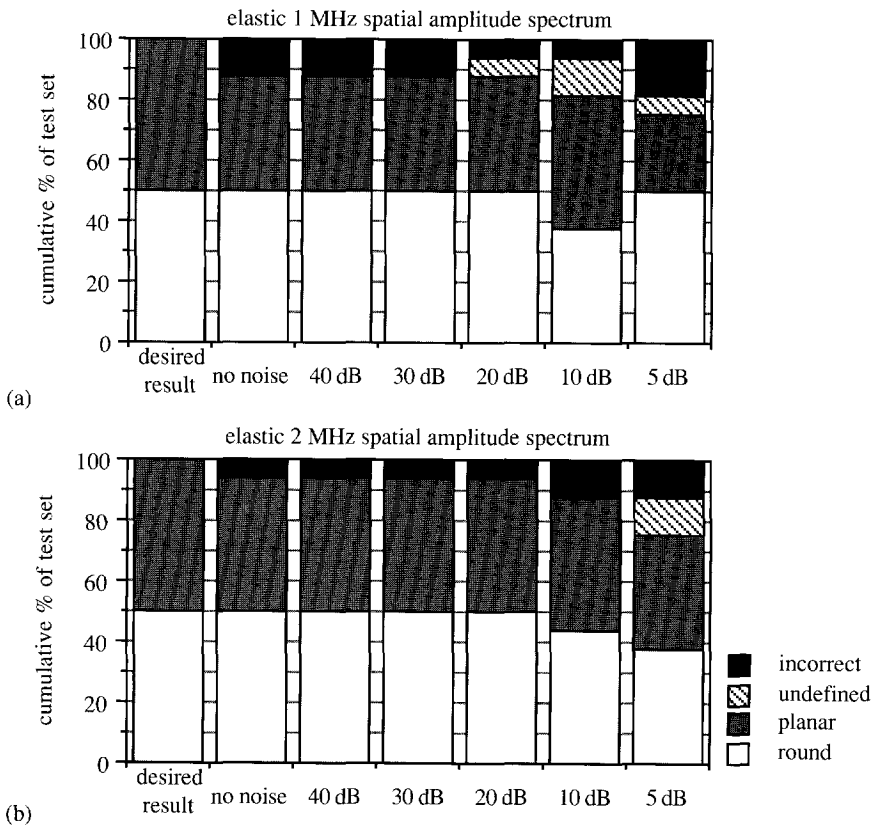
Figure 9.13: *The classification performance of the trained neural network for the elastic spatial amplitude spectrum of 1 MHz (a) and 2 MHz (b) for different values of the signal-to-noise ratio.*

(clean modelled input) the spatial amplitude spectrum contains the most unambiguous discriminating information for defect-shape classification.

The RMS-error is reduced during training by adjusting the hidden weights of the network. For the spatial amplitude spectrum of the modelled acoustic data, the evaluation of the hidden weights has been studied by Wielinga et al. (1993). They demonstrated, that for this relatively simple classification problem the weights initially converge to the *average difference* between the input values of round and planar defects, as shown in figure 9.15. This indicates again, that the input patterns are apparently linearly separable. Some statistical classifiers, like the nearest-neighbour classifier (Batchelor, 1974), use this average difference directly for the classification. Yet, a neural network adjusts its weights a little further in order to be able to correctly classify the more difficult (deviating) input patterns as well. This can be observed from figure 9.15, where the weight values have reached the average difference approximately after 860 training cycles and are adjusted to more pronounced values after 3600 training cycles (convergence). Theoretically, the
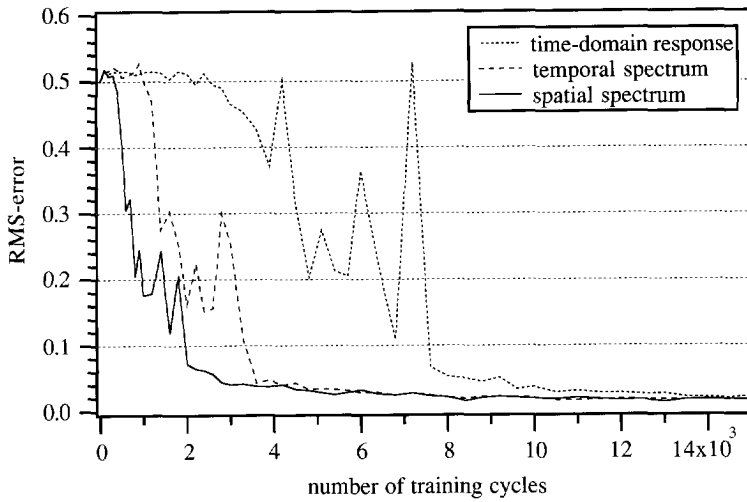
Figure 9.14: *The RMS-error of the neural network output during training as a function of number of training cycles for different types of input patterns.*

training time could be reduced for this simple example by adjusting the weights to the average difference values prior to training.

When the input patterns are not linearly separable and the network contains more than one hidden neuron, the study of the evaluation of the hidden weights is much more complicated. Although one hidden neuron may adjust its weights to the average difference of the input patterns, most of the hidden neurons seem to concentrate on particular features in the input patterns (peaks, zeroes).
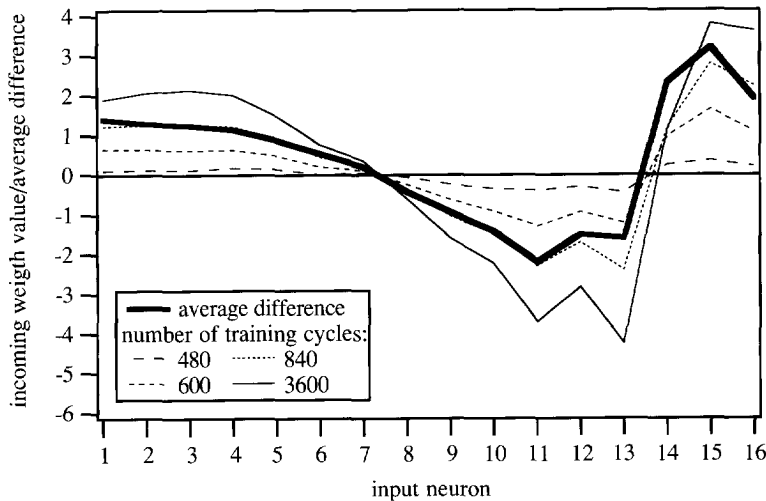
Figure 9.15: *The hidden weight for each input value after different numbers of training cycles; the average difference between the different input values of round and planar defects is indicated as well.*

This means, that the use of too many hidden neurons and a large number of training cycles may lead to the situation, that every training patterns is exactly remembered (stored in the hidden weights). This should be prevented at all times as it reduces the generalizing capacity of the network considerably.

9.3.7 Input based on experimental data

The model of figure 9.2 has been used for the fabrication of 40 mm thick steel test plates with round holes and horizontal slots (simulating vertically oriented planar defects). The diameter of the holes and the height of the slots have been chosen to be 2, 3, 3.5, 4, 4.5 and 5 mm. The center frequency of the broadband transducers is approximately 3 MHz, which results in a wave length of about 1 mm. Thus, the size of the smallest model defect is twice the applied wave length and there will be no problems with defects acting as diffractors only. For the experiments two sets of transducers have been applied, namely a 45° directive source with either a 45° or a 60° wide-angle receiver. The source position has been varied, resulting in actual insonification angles of 40°, 42.5° and 45°. The applied lateral split angle has been 60°.

The applied time window (to isolate the appropriate reflection responses) has been defined large enough not to affect the responses, consequently allowing other interfering responses to remain present in the data to some extent. The presence of other responses in the filtered data did result in a slight frequency dependency of the shape of the spatial amplitude spectra around the central frequency. Primarily for this reason, the amplitude spectra have been averaged over a small frequency band around the central frequency. For the sake of accuracy, the spatial spectrum input
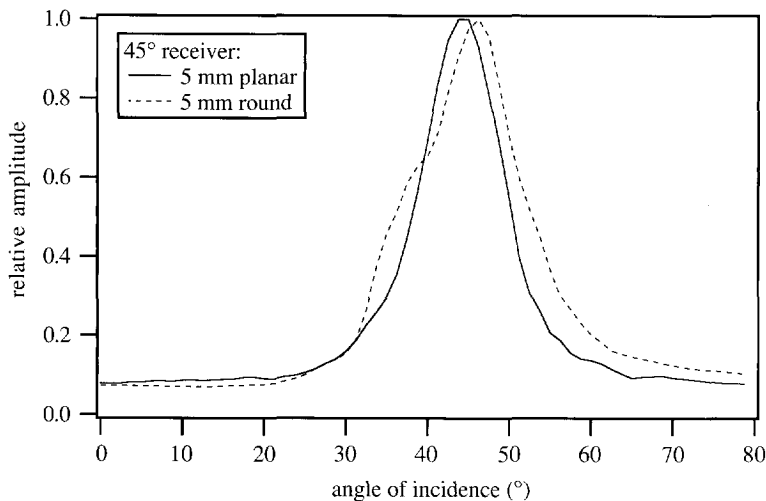
Figure 9.16: *The average spatial amplitude spectra of a round and planar defect for a 45° receiver as computed from experiments.*

patterns contain 64 points and consequently the neural network possesses 64 input neurons.

The 45° source and receiver have been applied to record the responses from the 2, 3, 4, and 5 mm model defects, for insonification angles of 40° and 45°, which have been used as training data (16 input patterns). Measurements from the 3.5 and 4.5 mm model defects have been used to test the classification performance of the neural network for the 45° wide-angle receiver (8 test patterns). Figure 9.16 shows some examples of the averaged spatial amplitude spectra of round and planar defects. It may be observed, that the difference in shape is less obvious than for the modelled experiments due to the directivity pattern of the receiver.

The 60° receiver has a wider beam and has been used together with the 45° directive source to generate a training set consisting of responses from the 2, 3, 4, and 5 mm model defects, for insonification angles of 40° and 45°. Ultrasonic responses from the same model defects for an insonification angle of 42.5° have been used to test the classification performance. The averaged spatial amplitude spectra of figure 9.17 illustrate the positive effect of a wider receiver beam. Moreover, by comparing figures 9.16 and 9.17 it is obvious that a neural network, trained for the spatial amplitude spectrum, is related to the directivity pattern of the receiver, because the shape of the 45° receiver round-defect spectrum is at least as narrow as the 60° receiver planar-defect spectrum.

Operating an acceptance level of 0.85, the test results for both data sets are 100% accurate, i.e. the test patterns have been all classified correctly without exceptions. Although the training and test sets do not contain many patterns and the model defects are perfect holes and slots, the
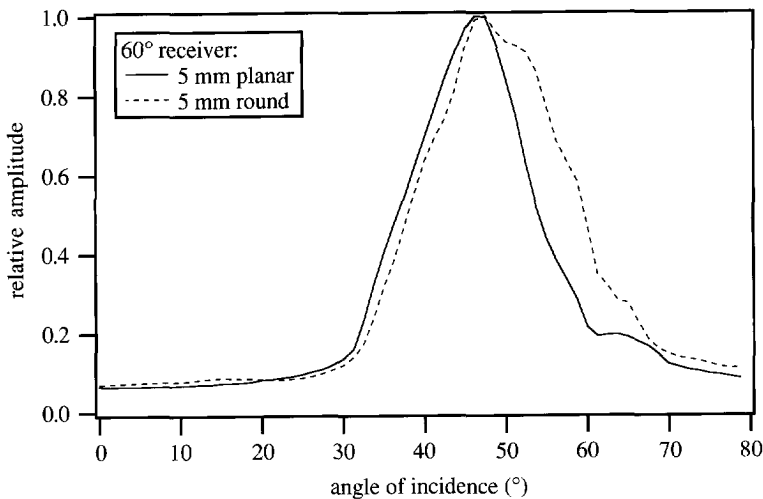
Figure 9.17: *The average spatial amplitude spectra of a round and planar defect for a 60° receiver as computed from experiments.*

application of neural networks to determine the shape of a defect from spatial amplitude spectra looks very promising. In some cases, as have been shown in chapter 8, the interpretation of an imaging result may require the application of an alternative technique, such as neural networks. Of course, more study and many more experiments involving real (weld) defects should be performed in order to come to a practical classification tool.

10

Conclusions and Discussion

10.1 Conclusions

In this thesis a 2-D ultrasonic imaging method for defect characterization in the field of nondestructive inspection of steel components is proposed. The method is based on the conventional Synthetic Aperture Focusing Technique (SAFT) and is called Multi-SAFT, because it employs multiple responses for the improvement of the image resolution. It has been shown, that the heuristically derived SAFT inversion algorithm equals a simplified version of the reflectivity imaging algorithm derived from general wave theory. The proposed imaging method is based on acoustic inversion operators and treats the recorded ultrasonic data in terms of different individual wave paths. It is important to notice that the Multi-SAFT algorithm can be applied to the different elastic wave components in case they can be assumed to be *uncoupled during propagation.*

The Multi-SAFT algorithm is designed explicitly for the application to homogeneous, isotropic media, such as most steel components in practice (without considering the welded region or special cladding layers). Because only structural information has to be extracted from the imaging results, the Multi-SAFT algorithm does not aim at *true amplitude* reflectivity. In the imaging process the elimination of propagation effects plays a central role and therefore the inversion process is more or less reduced to a geometrical problem in calculating wave path lengths. While the calculations of wave path lengths in flat plate geometries is very straightforward, they are quite complicated in cylindrical pipe geometries. In order to keep the imaging method as fast as possible, an efficient method for calculating wave path lengths in cylindrical pipe geometries is proposed.

From the analyses and experimental imaging results presented in this thesis it can be concluded, that:

- Multi-SAFT is typically a characterization method (not explicitly a sizing technique, like the Time-Of-Flight Diffraction technique) and should therefore be applied after detection of an inhomogeneity by a conventional inspection technique;

- the characteristics of an inhomogeneity can be determined from the Multi-SAFT imaging results, although the determination of defect shape is not always possible due to the limited image resolution; by applying neural networks on spatial amplitude spectra, computed from measured B-scan data, it has been demonstrated that the shape of a defect can be determined accurately in case perfectly round and planar defects are involved;

- in ultrasonic imaging for NDI the resolution is primarily restricted by the available spatial frequency bandwidth (i.e. the limited inspection aperture) and less by the temporal frequency bandwidth that can be applied; the spatial frequency bandwidth is increased considerably by employing multiple wave paths; by performing multi-source experiments the spatial frequency bandwidth can be increased even further;

- generally pulse-echo data-acquisition is not suitable for successful imaging of forward scattering (round-trip) responses and therefore separate source and receiver transducers should be applied;

- given a-priori knowledge on the location of an inhomogeneity, a directive shear-wave source transducer has to be applied at a fixed position for optimum insonification, while for optimum recording a wide-angle shear-wave receiver transducer has to be moved along the total available inspection aperture (pitch-catch data-acquisition);

- for the imaging of vertically oriented defects, using both reflection and diffraction responses, shear wave polarization effects can be employed successfully;

- the application of single-mode, bounded-beam transducers justifies the individual treatment of different elastic wave components and wave paths by the Multi-SAFT algorithm;

- in order to obtain a high image accuracy, the accurate determination of the wave velocity and total wedge delay time is most important; the quality of the experimental imaging results presented in this thesis demonstrate that this is very well possible;

- Multi-SAFT can be applied for the inspection of most weld defects, although the welded region cannot be considered homogeneous and isotropic.

The application of Multi-SAFT imaging for the characterization of defects in steel components is attractive and feasible, because:

- Multi-SAFT imaging can be applied as an in-service inspection technique; its results provide important information on the exact location and orientation, and in some situations also on the

size and shape of a detected inhomogeneity; this information cannot be obtained in such detail by other NDI techniques;

- with the information on the inhomogeneity provided by Multi-SAFT, acceptance standards do not have to be based on such unreliable features as signal amplitudes; they can be directly based on the information needed for a proper fitness-for-purpose analysis by fracture mechanics;

- measuring ultrasonic B-scans with a source transducer at a fixed position and manual movement of the receiver transducer with the aid of a mouse scanner is very easy, flexible and inexpensive, because no complex automated scanning system is required; the inspection procedure – including data-acquisition and data-processing – may be reduced to less than 30 minutes in case special dedicated scanning devices are applied;

- the application of Multi-SAFT is not necessarily restricted to flat plate and cylindrical pipe geometries; complex shaped objects can be inspected as well, provided the geometry is accurately known.

10.2 Discussion

10.2.1 Further improvements

The evaluation of the experimental Multi-SAFT imaging results has shown that ultrasonic imaging in NDI can be improved considerably compared to the conventional pulse-echo SAFT results found in the literature. Furthermore, due to the relatively simple procedures of both data-acquisition and data-processing, Multi-SAFT is practical and attractive for application in the field. However, the characterization performance of Multi-SAFT is not yet perfect, especially when defect sizing is concerned. Although Multi-SAFT is typically a reflection imaging technique, it can be successful as a diffraction imaging technique as well by changing the positions of the source and receiver aperture. Time-of-Flight Diffraction Tomography, as has been described by (Capineri et al., 1992), is actually applying Multi-SAFT on time-of-flight data (lateral split angle equal to 180°). The employment of multiple diffraction responses may further improve the image quality and the reliability of the characterization.

The amplitudes are not handled correctly by the Multi-SAFT algorithm, because only structural information is extracted from the images. However, the exact imaging algorithm (as derived from wave theory in chapter 2) indicates how the amplitudes should actually be processed. Therefore, if necessary, the imaging performance can be improved and the material characteristics of the

scatterer may even be determined from the reflectivity information by handling the amplitudes correctly and performing parametric inversion on the imaging results (Berkhout and Wapenaar, 1993).

Multi-SAFT is only concerned with shear wave responses. In case other elastic wave components are generated and recorded, the imaging quality will probably not improve substantially, as the inspection aperture – and consequently the image resolution – still remains limited. In order to increase the spatial frequency bandwidth, multi-source experiments have to be performed and combined. The extension of 2-D Multi-SAFT to 3-D will increase the spatial frequency bandwidth as well and a better image quality may be expected. The price to be paid, particularly in inspection time, will be high and it is questionable if it is worth all the effort in regular NDI.

Multi-SAFT has been applied to homogeneous and isotropic media only. For the successful application of ultrasonic imaging to more complex media, such as cladded pressure vessels and austenitic steel components, Multi-SAFT has to be extended to handle the propagation effects in inhomogeneous and anisotropic media. Although this will make the Multi-SAFT algorithm more complex and less efficient, such an extension is very well feasible (Berkhout, 1985).

For Multi-SAFT to be accepted in NDI practice, numerous field studies and evaluations have yet to be performed. It is also very important to realize, that special acceptance standards have to be written in order to make the applicability of techniques as Multi-SAFT in the industry possible in future.

10.2.2 The role of modelling and artificial intelligence in NDI

Throughout this thesis use has been made of modelling techniques to study and illustrate different wave phenomena to improve the understanding of the underlying physical principles. Not only the sophisticated, time-and-memory consuming finite-difference modelling schemes (to be applied for very realistic modelling of elastic wave phenomena, see Van 't Veen et al. (1993)), but also simple and fast ray-tracing algorithms provide one with an important tool to be applied for the development and improvement of ultrasonic NDI techniques. With the increasing computational possibilities the application of modelling can probably be extended from studies in research towards the evaluation of measurements in the field. The role of modelling wave phenomena in NDI will therefore become more and more important in the future and will certainly lead to a further improvement of the interpretation of inspection results.

In chapter 9 of this thesis a first exploratory study has been presented on the application of artificial intelligence (AI) methods in NDI. It should be realized that the classification of defect shape by neural networks is only one of the many conceivable applications of AI in NDI. The

results of this limited study already indicate that a number of intrinsic features of AI methods, such as adaptivity and speed of operation, are very attractive to NDI. For instance, AI methods can be applied in automated systems for the interpretation of NDI results of many standard inspection procedures. For instance, expert systems have already been developed for the interpretation of X-ray films (Montini et al., 1992).

The fields of NDI and AI have just recently met and a lot of knowledge has still to be shared, while many prejudices have to be put behind. Nevertheless, it is believed that the application of AI methods will improve the *reliability* of the interpretation of NDI results in future. Hopefully, part of this thesis will contribute to this development.

Appendix A

Derivation of the Decomposition Angle for Polarization
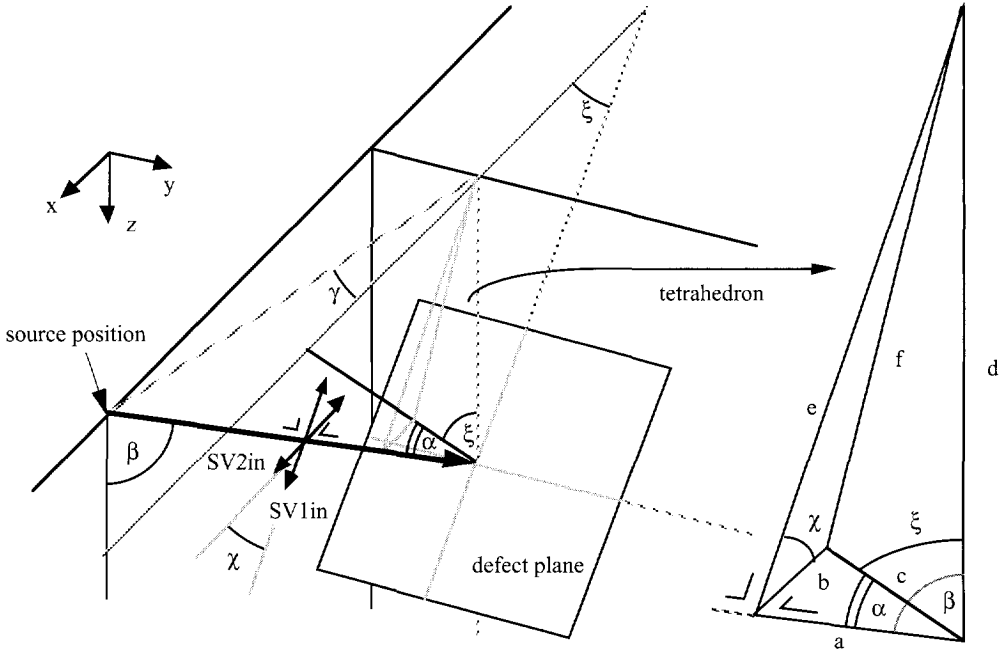
Figure A.1: *The decomposition angle χ in relation to the tilt angle ξ, the insonification angle β, the lateral split angle γ, and the angle of incidence α; the tetrahedron as indicated, is used to derive the expression for the decomposition angle.*

Using the tetrahedron indicated in figure A.1, the decomposition angle χ may be expressed by:

$$f^2 = b^2 + e^2 - 2\,be\,\cos\chi \ , \tag{A.1}$$

from which follows:

$$\cos \chi = \frac{b^2 + e^2 - f^2}{2\,be} \,, \tag{A.2}$$

where b and e may be written as:

$$b = d \cos \beta \tan \alpha \,, \tag{A.3}$$

$$e = d \sin \beta \,. \tag{A.4}$$

For f can be written:

$$f^2 = c^2 + d^2 - 2cd \cos \xi \,, \tag{A.5}$$

and with:

$$c = \frac{d \cos \beta}{\cos \alpha} \,, \tag{A.6}$$

this leads to:

$$f^2 = \left(\frac{d \cos \beta}{\cos \alpha}\right)^2 + d^2 - \frac{2\,d^2 \cos \beta \cos \xi}{\cos \alpha} \,. \tag{A.7}$$

Using (A.2), (A.3), (A.4) and (A.7), the expression for the decomposition angle χ is given by:

$$\chi = \mathrm{acos} \left\{ \left| \frac{\cos \xi - \cos \alpha \cos \beta}{\sin \alpha \sin \beta} \right| \right\} \,, \tag{A.8}$$

where α is the angle of incidence on the defect plane:

$$\alpha = \mathrm{acos} \left(\cos \beta \cos \xi + \sin \beta \sin \xi \cos \gamma \right) \,, \tag{A.9}$$

and γ is the lateral split angle.

The three-dimensional configuration shown in figure A.1 is not easy to interpret. Therefore, a 3-D reconstruction of this configuration can be made with the aid of a construction plan, which can be found as an enclosure to this thesis. The construction plan is shown in figure A.2 on a smaller scale and the instructions for the construction are given below. The angle between the components SV_{1in} and SV_{2in} is the decomposition angle.

I.   Cut out the whole figure with a pair of scissors.
      Cut the heavily dotted line (indicated with the pair of scissors) from *a* to *b*.

II.   The strips *A*,*B* and *C* should be folded away from you (outside corner).
      The strip *D* should be folded towards you (inside corner).
      The strip *E* should not be folded.

III. Fold the figure over the lines *1* and *2* away from you.
      Fold the figure over the line *3* and *4* towards you.
      Fold the figure over the lines *5*, *6* and *7* away from you.

IV.   Connect strip *A* with glue to the back of the inspection plane along the line indicated by *A'*.
      Then connect the strips *B* and *C* at the back of the sides indicated by *B'* and *C'*.
      Now strip *D* has to be connected to the back of *D'* such that the plane of strip *D* is oriented along the indicated dotted line. Finally connect strip *E* to the side of the defect plane indicated by *E'* and the model is ready.

Figure A.2: *A scaled version of the construction plan of the 'Lorenz model', which can be found as an enclosure to this thesis.*

Derivation of the Wedge Delay Time Error

Figure B.1: *The configuration of wave paths for a wedge transducer with fixed index point.*

The derivation is performed for a perspex wedge transducer with a fixed index point and a $45°$ angle in steel ($\alpha'_s = 45°$). The center of the piezo crystal is located at a distance h above the perspex-steel interface, while a point diffractor is located at depth d in the steel medium. The angle α'_w of the wave path in the wedge for $\alpha'_s = 45°$ is determined using Snell's law:

$$\alpha'_w = \operatorname{asin}\left(\frac{c_w}{c_s} \sin 45°\right) , \tag{B.1}$$

with c_w the compressional wave velocity in the perspex wedge (2680 m/s) and c_s the shear wave velocity in steel (3260 m/s).

Using figure B.1, the constant wedge delay time τ is defined as the propagation time from the index point to the piezo crystal:

$$\tau = \frac{h}{c_w \cos \alpha'_w} . \tag{B.2}$$

By applying a constant wedge delay time, the computed travel time t' of an ultrasonic response from the point diffractor at depth d in figure B.1 to the piezo crystal will slightly differ from its real travel time t_r. This difference will be defined as a wedge delay time error $\Delta\tau$.

For the real travel time t_r can be written:

$$t_r = \frac{h}{c_w \cos \alpha_w} + \frac{d}{c_s \cos \alpha_s} \ , \tag{B.3}$$

with α_w the angle of the wave path in the wedge, which is related to the angle α_s according to Snell's law.

The travel time for a fixed index point can be written as:

$$t' = \tau + \frac{\sqrt{(x_{off})^2 + d^2}}{c_s} \ , \tag{B.4}$$

with the lateral distance between the index point and the position of the point diffractor x_{off} (see figure B.1):

$$x_{off} = d \tan \alpha_s + h \tan \alpha_w - h \tan \alpha'_w \ . \tag{B.5}$$

In chapter 7 (figures 7.17 and 7.18) the wedge delay time error $\Delta\tau$ will be given as a function of x_{off} for a beam width of $30°$.

Appendix C

The Multi-SAFT Workstation

The experiments presented in chapter 8 have been performed with the Multi-SAFT workstation. This workstation consists of data-acquisition as well as processing facilities and is based upon a 386 25 MHz personal computer of type Intel 302, with a 80387 co-processor and 8 Mb internal memory. In this appendix the different components of the Multi-SAFT workstation will be described and the inspection procedure will be explained.

C.1 Data-Acquisition

C.1.1 Scanning facilities and transducers

In order to keep the data-acquisition process simple, flexible, fast and inexpensive, *manual* scanning of the receiver transducer is preferred. For the SAFT-algorithm to work properly, it is very important that the position of the scanning receiver transducer is accurately known. This has been accomplished by applying the MWS-4 scanner, manufactured by the Force Institute in Copenhagen, Denmark. The MWS-4 scanner is a mouse-like device, which can be used to make linear scans (see figure C.1). The receiver position is tracked by the scanner's wheels, which are connected to an optical decoder. The smallest scan step is 1/16 of a mm and the relative positioning accuracy over a large number of scan steps is better than 95%.

During scanning TTL-pulses are sent by the scanner to a tacho-interface board in the workstation. This tacho-interface, specially developed by TPD-TNO, triggers the source as well as the A/D-converter when a pre-defined number of TTL-pulses, corresponding to a given scan step, has been received. The scanning velocity is mainly determined by the measured-data display program and is approximately 10 A-scans of 2048 points per seconds. The A/D-converter is a SONIX STR*8100A, which is mounted on a board and is able to sample the data with 8 bits up to 100 MHz. Because the A/D-converter has a very fast I/O (~3 Mb/s), the amount of data that can be collected per second by manual scanning in practice is not limited by the A/D-converter.

The MWS-4 scanner is designed to be applied on plane inspection surfaces or in the radial
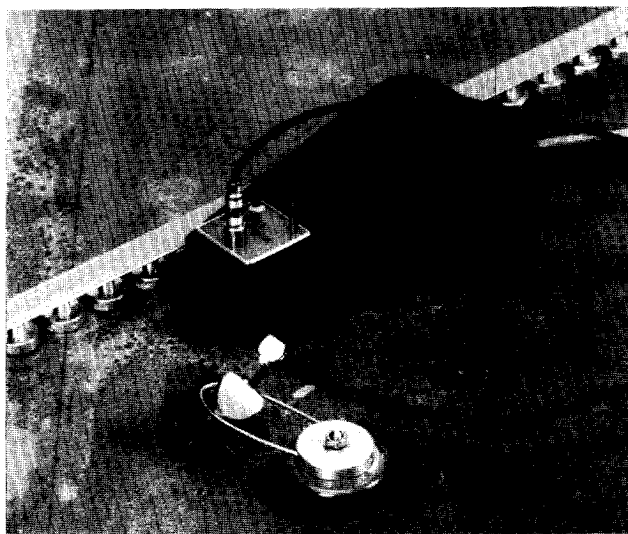
Figure C.1: *The data-acquisition configuration on a flat plate with the MWS-4 mouse scanner.*

direction of slightly curved pipes (minimum diameter 500 mm). As the lateral split configuration requires the scanner to be moved in arbitrary directions along a pipe's surface, a special manual pipe scanner (MPS-1) has been designed and constructed in cooperation with the TNO Product Centre. Figure C.2 shows the manual pipe scanner which has a special adapter for curved surfaces. The adapter is shown in figure C.3. The main difference between the MWS-4 and the
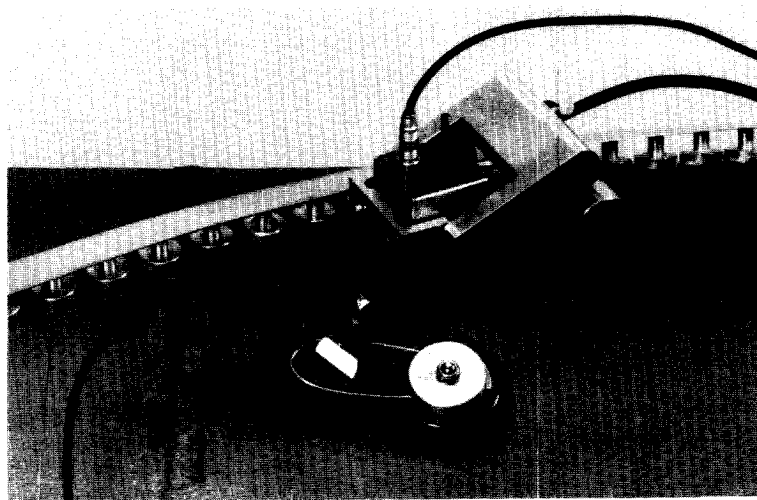
Figure C.2: *The data-acquisition configuration on a cylindrical pipe section with the MPS-1 mouse scanner.*

MPS-1 is that the latter has only one single tracking wheel positioned in-line with the center of the transducer, which enables the MPS-1 to be moved around a pipe's surface in every possible direction. The smallest scan step of the MPS-1 is 1/12 of a mm, the relative positioning accuracy is also better than 95%, and the pipe radius may be as small as 25 mm.

The MWS-4 and the MPS-1 scanners are applied to perform linear and helical scans, respectively. To ensure the scanner to be moved in the correct direction, a flexible guiding steel strip equipped with an array of permanent magnets for easy attachment to the inspection surface is applied. This guiding strip is shown in the figures C.1 and C.2 of the experimental data-acquisition configurations.

The applied source transducer is a standard Panametrics V536 (0.5 inch) 5 MHz snap-in P-wave transducer mounted on 45° or 60° wedges to generate shear waves in a directive beam (~8° –6 dB beam width). As the receiver should have a large beam width in the sagittal plane (with respect to the inspection plane) and a small beam width in the plane perpendicular to that plane (see chapter 6), a special set of 45° and 60° shear wave strip transducers were designed and manufactured by SONIMEX. Because the amount of wedge material has been kept to a minimum, reasonably sensitive shear wave transducers could be constructed with broadband frequency characteristics. The center frequency of the receiver transducers lies around 3.5 MHz and the –6 dB bandwidth is approximately 4 MHz. Figure C.4 shows the time and frequency response of the receiver strip transducer in pitch-catch with the Panametrics source transducer for a representative practical situation (lack-of-fusion defect). The –6 dB beam width is approximately 12° in the sagittal plane and 5° in the plane perpendicular to it.
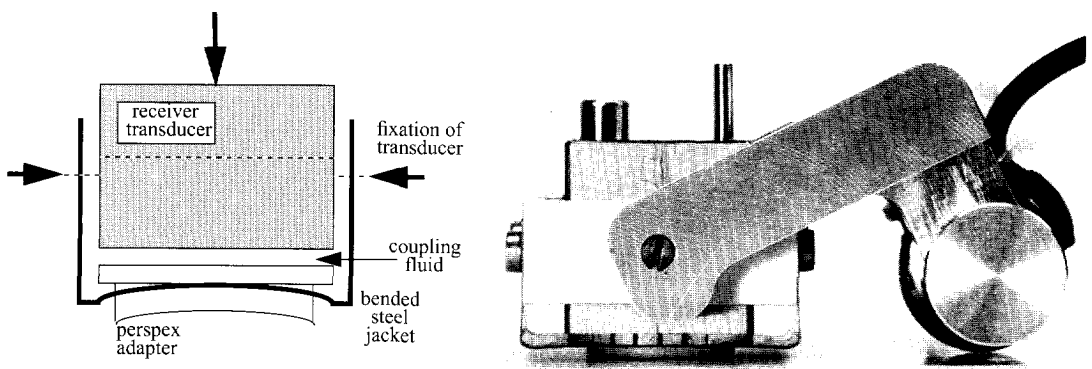
Figure C.3: *The MPS-1 mouse scanner with the special adapter for cylindrical pipe geometries; the bended steel casing presses the transducer on the round perspex adapter, which may be turned 360° to match the correct orientation of the receiver.*
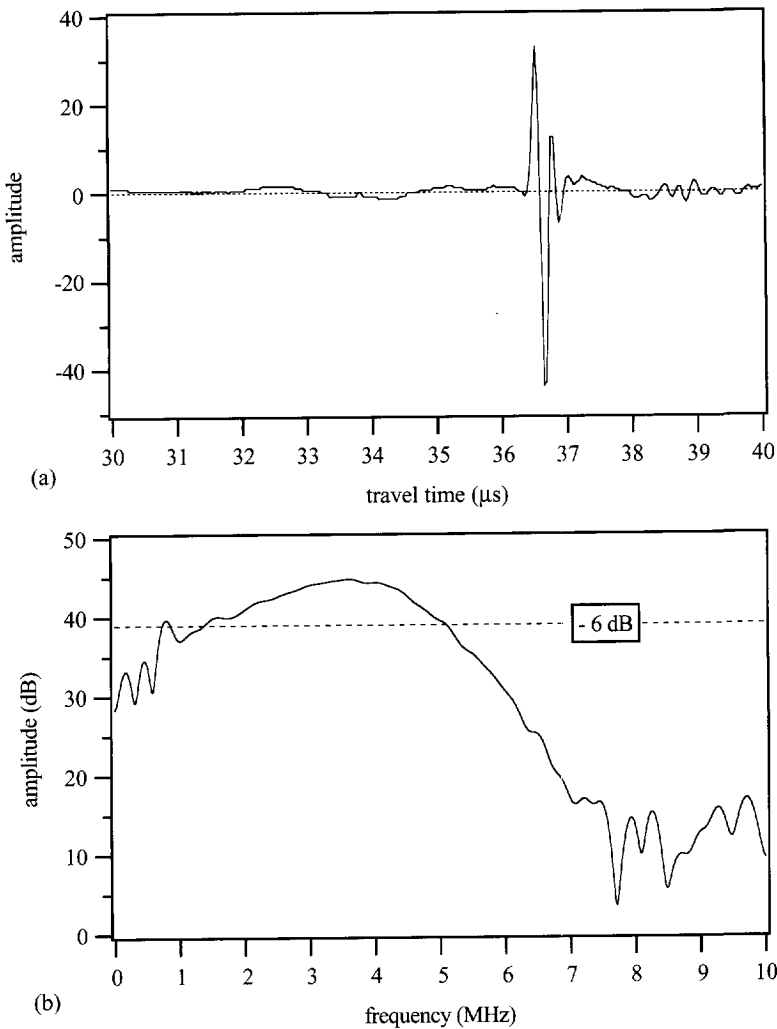
Figure C.4: *The time and frequency response of the shear wave receiver strip transducer in pitch-catch with a Panametrics V536 shear wave source transducer on a 60° wedge.*

C.1.2 The inspection procedure

Before Multi-SAFT is applied it is assumed, that the possible defect has already been detected and approximately located by conventional means of nondestructive inspection. The Multi-SAFT inspection procedure itself consists mainly of three steps. In the first place, the shear wave velocity of the material, the total wedge delay for the applied transducer set, the thickness of the object and (if the object has a cylindrical geometry) the outer radius have to be determined. Then

the position and possibly the orientation (straight reflection direction) of the inhomogeneity have to be determined by using the source transducer in pulse-echo mode. The information about the position and orientation will be used to position the source transducer optimally with respect to the inhomogeneity. When the source position, receiver aperture and lateral split angle are determined, the actual data-acquisition can take place.

The data-acquisition program has been written in TCL® (Technical Command Language) and is named ACQUIS. It consists of a menu, listing all the data-acquisition parameters, such as the sampling frequency, the number of data points and A-scans to be collected and the scan step to be applied. When the data-acquisition parameters are all set, the recorded-data display is invoked. By operating the scanner in 'free-running' mode, the source is triggered continuously regardless of the scanner's position. In this mode, the source signal amplitude and the receiver signal amplification can be adjusted in order to avoid overflowing of recorded responses somewhere along the scanning aperture.

When this has been done, the scanner is positioned at the start of the scanning aperture and the 'recording mode' is set. A total B-scan can now be recorded by simply moving the scanner along the scanning aperture. The recorded data is shown in grey-level display on-line during scanning and overflows will directly be displayed in red. In case overflows are recorded or A-scans are missed, the program will give a notification. Otherwise, the data can be stored or the same scan can be performed once again.

C.2 Multi-SAFT Imaging

C.2.1 Special software and hardware

The recorded B-scan data can be processed on the Multi-SAFT workstation with specially implemented software written in TCL. These programs are designed to make use of a Mercury array processor board (type MC3200 with 6 Mb internal memory, 20 MFlop), which is part of the workstation, but may be used without this special hardware. The two imaging programs are called FLATFOC for flat plate geometries and GIRTH for cylindrical pipe geometries. The latter program is designed to image rectangular cross-sections of girth welds in the axial direction of the pipe. Prior to imaging the data-acquisition and imaging parameters have to be set in a yank file. Such a yank file can be filled out with the aid of the programs YANK (in connection to FLATFOC) and YANKG (in connection with GIRTH).

C.2.2 Real-Time Focusing display and processing performance

The imaging program has to be started with a link to the properly filled out yank file. It will prompt the operator for some display parameters and will then start the imaging process. Each A-scan will be processed sequentially and will result in an individual image contribution. All these image contributions will be summed to make up the final imaging result. During processing of the A-scan data the imaged region may be displayed, showing step by step and in real time the evolution (focusing) of the indication(s) through the summation of A-scan image contributions. This mode will be called *Real-Time Focusing Display* (RTFD).

The total processing time depends on the dimensions of the recorded B-scan and the imaged region, as well as on the use of the Real-Time Focusing Display, and is slightly different for flat plate and cylindrical pipe geometries. To give an idea of the processing times achieved with the Multi-SAFT workstation (using the array processor), some values are given in table C.1. The computing performance of the programs for flat plate and cylindrical pipe geometries are almost identical. The average computing time per A-scan of 2048 points and an image of 100 by 100 points is approximately 0.6 s and the pre-processing of the B-scan data (100 A-scans) takes about 28 seconds. From table C.1 it can be concluded, that the use of the Real-Time Focusing Display does slow down the imaging process to some extent, but waiting for the final imaging result will be more pleasant while watching the focusing process actually taking place.

The imaging results can always be displayed by the program DISP_IT, which also gives the maximum pixel value in the image. DISP_IT is able to display two images at the same time for comparison and has a hard-copy option which generates a post-script file of an image to be sent to a printer. In order to be able to apply the Multi-SAFT principle, the program ADDING can be used to normalize and superimpose different images.

Table C.1: *The processing times of the Multi-SAFT workstation with the array processor for a B-scan consisting of 100 traces of 2048 samples and an imaged region of 100 by 100 points.*

number of records	RTFD	processing time (s)
50	off	58
100	off	88
100	after every 8	110
100	all	225

References

Achenbach, J.D., 1973, "Wave propagation in elastic solids", North-Holland/American Elsevier, Amsterdam.

Alterman, Z., 1968, J. Phys. Earth, Vol. 16, p. 113.

Auld, B.A., 1973, "Acoustic fields and waves in solids", Wiley Interscience.

Baker, A.R. and C.G. Windsor, 1989, "The classification of defects from ultrasonic data using neural networks: The Hopfield method", NDT International, Vol. 22, nr. 2.

Barna, B.A. and J.A. Johnson, 1983, "Imaging and characterization of defects with digital signal processing of ultrasonic data", in: Proceedings of Review of Progress in QNDE, Thompson and Chimenti (Eds), Plenum Press, New York.

Batchelor, B.G., 1974, "Methods of pattern classification", in: Practical approach to pattern classification, Plenum Press, London.

Berkhout, A.J., 1984, "Seismic resolution", Geophysical Press Ltd., London.

Berkhout, A.J., 1985, "Seismic migration; imaging of acoustic energy by wave field extrapolation", Elsevier Science Publishers B.V., Amsterdam.

Berkhout, A.J., 1987, "Applied seismic wave theory", Elsevier Science Publishers B.V., Amsterdam.

Berkhout, A.J., 1993, "A unified approach to acoustical reflection imaging; part I: The forward model", J. Acoust. Soc. Am., to be published.

Berkhout, A.J. and C.P.A. Wapenaar, 1993, "A unified approach to acoustical reflection imaging; part II: The inverse problem", J. Acoust. Soc. Am., to be published.

Berry, D., L. Udpa and S.S. Udpa, 1991, "Classification of ultrasonic signals via neural networks", in: Proceedings of Review of Progress in Quantitative NDE 1990 (10), Thompson and Chimenti (Eds), Plenum Press, New York.

Born, M., and E. Wolf, 1975, "Principles of optics", Pergamon Press.

Brown, L.M., and R. DeNale, 1991, "Classification of ultrasonic defect signatures using an artificial neural network", in: Proceedings of Review of Progress in Quantitative NDE 1990 (10), Thompson and Chimenti (Eds), Plenum Press, New York.

Bruck, D., M. Fischer, K.J. Langenberg, et al., 1982, "Comparison of different synthetic aperture reconstruction algorithms", in: Proceedings of IEEE-Ultrasonic Symposium 1982, B.R. McAvoy (Ed), IEEE, Piscataway (NJ).

Burch, S.F., 1987, "Comparison of SAFT and two-dimensional deconvolution methods for the improvement of resolution in ultrasonic B-scan images", Ultrasonics, Vol. 25, September 1987.

Capineri, L., H.G. Tattersal, J.A.G. Temple, et al., 1992, "Time-of-flight diffraction tomography for NDT applications", Ultrasonics, Vol. 30, nr. 5.

Chinn, D.J. and H.A. Dieterman, 1993, "Generalized ray theory and its application to long-distance ultrasonic testing", in: Proceedings of IUTAM '92 Symposium on Inverse Problems.

Corl, P.D., G.S. Kino, C.S. DeSilets, et al., 1978, "A digital synthetic focus acoustic imaging system", in: Proceedings of Acoustical Imaging 8, A.F. Metherell (Ed), Plenum Press, New York.

De Bruin, C.J.M., 1992, "Linear AVO inversion by prestack depth migration; imaging angle dependent reflectivity as a tool for litho-stratigraphic inversion", PhD. thesis, Delft University of Technology.

De Jong, E.C.J.N. and U. Stelwagen, 1992, "Feasibility of laser/EMAT ultrasonics for contactless wall thickness measurements", TNO Institute of Applied Physics, TPD-HAI-RPT-92-89.

Doctor, S.R., T.E. Hall and L.D. Reid, 1986, "SAFT - The evolution of a signal processing technology for ultrasonic testing", NDT International, Vol. 19, nr. 3.

Engelmore, R.S., 1987, "Artificial intelligence and knowledge based systems; origins, methods and opportunities for NDE", in: Proceedings of Review of Progress in Quantitative NDE 1986 (6), Thompson and Chimenti (Eds), Plenum Press, New York.

Euler, L., 1768, "Instructiones Calculi Integralis", St. Petersburg.

Flaherty, J.J., K.R. Erickson and V.M. Lund, 1967, "Synthetic aperture ultrasonic imaging systems", U.S. Patent 3,548,642.

Fortunko, C.M., R.E. Schramm, J.C. Moulder, et al., 1984, "Electromagnetic-acoustic-transducer/synthetic aperture system for thick-weld inspection", National Bureau of Standards, Technical Note 1075.

Freeman, J.A. and D.M. Skapura, 1991, "Neural networks: Algorithms, applications and programming techniques", Addison-Wesley Publishing Company, Reading (MA).

Grabec, I. and W. Sachse, 1989, "Experimental characterization of ultrasonic phenomena by a learning system", Journal of Applied Physics, Vol. 66, nr. 9.

Green, E.R., 1989, "Worst-case defects affecting ultrasonic inspection reliability", Materials Evaluation, Vol. 47, December 1989.

Green, E.R., 1990, "The effect of equipment bandwidth and center frequency changes on ultrasonic inspection reliability: modeling and experimental results", in: Proceedings of Review of progress in QNDE, Thompson and Chimenti (Eds), Plenum Press, New York.

Halkes, C.J. and S. Terpstra, 1989, "Ontwerp en fabricage proefplaten voor NIL-NDO project 2e fase", Dutch Welding Institute (NIL), report NDO 89-18.

Hall, T.E., S.R. Doctor and L.D. Reid, 1987, "A real-time SAFT system applied to the ultrasonic inspection of nuclear reactor components", in: Proceedings of Review of progress in QNDE 6, Thompson and Chimenti (Eds), Plenum Press, New York.

Hallam, N.J., N. Woodcock and A.A. Hopgood, 1990, "A knowledge based system for defect detection and characterization", in: Application of artificial intelligence in engineering V, Vol. 2 Manufacturing & planning, Springer-Verlag, Berlin.

Halmshaw, R., 1987, "Non-destructive testing", Edward Arnold, UK.

Hamlin, D.R., 1985, "Program for field validation of the synthetic aperture focusing technique for ultrasonic testing", Southwest Research Institute, report NUREG/CR-4078.

Harker, A.H., 1988, "Elastic waves in solids; with applications to nondestructive testing of pipelines", Adam Hilger, Bristol.

Harumi, K., F. Suzuki and T. Saito, 1973, J. Acoust. Soc. Am., Vol. 53, p. 600.

Kitahara, M., J.D. Achenbach, Q.C. Guo, et al., 1991, "Depth determination of surface breaking cracks by a neural network", in: Proceedings of Review of Progress in Quantitative NDE 1990 (10), Thompson and Chimenti (Eds), Plenum Press, New York.

Kitahara, M., J.D. Achenbach, Q.C. Guo, et al., 1992, "Neural network for crack-depth determination from ultrasonic backscattering data", in: Proceedings of Review of Progress in Quantitative NDE 1991 (11), Thompson and Chimenti (Eds), Plenum Press, New York.

Krautkrämer, J. and H. Krautkrämer, 1977, "Ultrasonic testing of materials", Springer-Verlag, Berlin.

Langenberg, K.J., 1987, "Applied Inverse Problems for Acoustic, Electromagnetic an Elastic Wave Scattering", in: Basic methods of tomography and inverse problems, Sabatier (Ed), Adam Hilger, Bristol.

Langenberg, K.J., M. Berger, Th. Kreutter, et al., 1986, "Synthetic aperture focusing technique signal processing", NDT International, Vol. 19, nr. 3.

Lorenz, M., 1988, "Opto-acoustical inspection of thin layers", MSc. thesis, Delft University of Technology.

Lorenz, M., 1990, "3rd Semi-Annual Report on SAFT-III Project", internal report TNO-Institute of Applied Physics, Delft.

Lorenz, M., 1991, "5th Semi-Annual Report on SAFT-III project", TNO-Institute of Applied Physics, Delft, report TPD-HAI-RPT-91-70.

Lörtzer, G.J.M., 1990, "An integrated approach to lithological inversion", PhD. thesis, Delft University of Technology.

Lovelace, J., 1980, "Polarization effects in shear wave testing", Materials Evaluation, December 1980.

Mayer, K., 1990, "Ultraschallabbildungsverfahren: Algorithmen, Methoden der Signalverarbeitung und Realisierung", PhD. thesis, Univerity GH Kassel.

McGrath, B.A., R.K. Chapman and I. Einav, 1989, "A study of changes in ultrasonic probe performance due to the thickness of the couplant layer", in: Proceedings of 28th Annual British Conference on NDT, Brook and Hanstead (Eds), Pergamon Press, Oxford.

McNab, A. and I. Dunlop, 1991a, "Information Technology - IT in NDT", British Journal of NDT, Vol. 33, nr. 12.

McNab, A. and I. Dunlop, 1991b, "AI Techniques applied to the classification of welding defects from automated NDT data", British Journal of NDT, Vol. 33, nr. 1.

Melton, R.B., S.R. Doctor, T.T. Taylor, et al., 1987, "SIIA: A knowledge-based assistant for the SAFT ultrasonic inspection system", in: Proceedings of Review of Progress in Quantitative NDE 1986 (6), Thompson and Chimenti (Eds), Plenum Press, New York.

Monchalin, J.P., 1986, "Optical detection of ultrasound", IEEE Transactions on Ultrasonics, Ferroelectrics & Frequency Control, Vol. UFFC-33, nr. 5.

Montini, G., M.G. Bordini, F. Boschetti, et al., 1992, "EXACT: an expert system for real-time X-ray image analysis and classification of weldings", in: Proceedings of 13th WCNDT, Hallai and Kulcsar (Eds), Elsevier Science Publishers B.V., Amsterdam.

Nugen, S.M., K.E. Christensen, L.S. Koo, et al., 1988, "FLEX - An expert system for flaw classification and sizing", in: Proceedings of Review of Progress in Quantitative NDE 1987 (7), Thompson and Chimenti (Eds), Plenum Press, New York.

Ogi, T., M. Notake and Y. Yabe, 1991, "Application of neural network to classification of defects: basic study of weights", in: Proceedings of Review of Progress in Quantitative NDE 1990 (10), Thompson and Chimenti (Eds), Plenum Press, New York.

Ogi, T., M. Notake, Y. Yabe, et al., 1990, "A neural network applied to crack type recognition", in: Proceedings of Review of Progress in Quantitative NDE 1989 (9), Thompson and Chimenti (Eds), Plenum Press, New York.

Ogilvy, J.A., 1991, "Theory of wave scattering from random rough surfaces", Adam Hilger, Bristol.

Ozaki, Y., H. Sumitani, T. Tomoda, et al., 1988, "A new system for real-time synthetic aperture ultrasonic imaging", IEEE Transactions on Ultrasonics, Ferroelectrics & Frequency Control, Vol. 35, nr. 6.

Randall, C.J., 1988, "Absorbing boundary condition for the elastic wave equation", Geophisics, Vol. 53.

Rayleigh, Lord, 1877, "The theory of sound", MacMillan, New York.

Reynolds, W.N. and R.L. Smith, 1984, J. Phys., Vol. D 17.

Rietveld, W.E.A., 1988, "Full elastic modelling for non-destructive evaluation; a finite-difference approach", MSc. thesis, Delft University of Technology.

Runge, C., 1908, Z. Math. Phys., Vol. 56, p. 225.

Schmerr Jr., L.W., C.P. Chiou and A. Sedov, 1988, "Equivalent flaw sizing: a unified approach", in: Proceedings of Review of Progress in Quantitative NDE 1987 (7), Thompson and Chimenti (Eds), Plenum Press, New York.

Schmerr Jr., L.W., K.E. Christensen, and S.M. Nugen, 1987, "Development of an expert system for ultrasonic flaw classification", in: Proceedings of Review of Progress in Quantitative NDE 1986 (6), Thompson and Chimenti (Eds), Plenum Press, New York.

Schmitz, V., W. Müller and G. Schäfer, 1986a, "Imaging with HOLOSAFT", in: Proceedings of Acoustical Imaging 14, Ridder, Van der Wal and Berkhout (Eds), Plenum Press, New York.

Schmitz, V., W. Müller and G. Schäfer, 1986b, "Practical experiences with L-SAFT", in: Proceedings of Review of progress in QNDE 5, Thompson and Chimenti (Eds), Plenum Press, New York.

Seydel, J., 1982, "Ultrasonic synthetic aperture focusing techniques in NDT", in: Research techniques in nondestructive testing, Sharpe (Ed), Academic Press, London.

Shankar, R., R. Williams, and M.J. Avioli Jr., 1991, "Knowledge-based ultrasonic examination assistant", Materials Evaluation, October 1991.

Silk, M.G., 1984, "Ultrasonic transducers for nondestructive testing", Adam Hilger, Bristol.

Simpson, P.K., 1990, "Artificial neural systems: foundations, paradigms, applications and implementations", Pergamon Press.

Song, S.J. and L.W. Schmerr Jr., 1991, "Ultrasonic flaw classification in weldments using neural networks", in: Proceedings of Review of Progress in Quantitative NDE 1990 (10), Thompson and Chimenti (Eds), Plenum Press, New York.

Thomson, R.N., 1984, "A portable system for high resolution ultrasonic imaging on site", British Journal of NDT, May 1984.

Tielsch, H., 1967, "The sense and nonsense of weld defects", Monticello Books, Lake Zürich (IL).

Van 't Veen, P.P., M. Lorenz and L.F. van der Wal, 1993, "Application of a finite-difference modelling scheme for ultrasonic defect characterization", in: Proceedings of Review of Progress in Quantitative NDE 1992 (12), Thompson and Chimenti (Eds), Plenum Press, New York.

Van Dijk, G.M., R. Hunik, U. Stelwagen, et al., 1988, "Ultrasoon onderzoek met SAFT-beeldreconstructie", Dutch Electric Power Institute (KEMA), report 98001-IND-53 CSV-88-038.

Van Dijk, G.M., R. Hunik, U. Stelwagen, et al., 1989, "Ultrasonic imaging with zero-offset synthetic aperture focusing technique", in: Proceedings of WCNDT 1989, Boogaard and Dijk (Eds), Elsevier Science Publishers B.V., Amsterdam.

Vandenbroek, C., M.B. Elzinga, J.R. Frederick, et al., 1980, "Synthetic aperture ultrasonic imaging in metals", in: Proceedings of First International Symposium on Ultrasonic Materials Characterization 1978, Berger and Linzer (Eds), National Bureau of Standards Special Publication 596.

Virieux, J., 1986, "P-SV wave propagation in heterogeneous media: Velocity-stress finite-difference method", Geophysics, Vol. 51.

Wapenaar, C.P.A. and A.J. Berkhout, 1989, "Elastic wave field extrapolation", Elseviers Science Publishers B.V., Amsterdam.

Wenk, S.A. and R.C. McMaster, 1987, "Choosing NDT: Applications, costs and benefits of nondestructive testing in your quality assurance program", ASNT Inc., USA.

White, R.M., 1963, "Generation of elastic waves by transient surface heating", J. Appl. Phys., Vol. 34, p. 3559.

Wielinga, T.S., 1992, "Classification of weld defects with neural networks", MSc. thesis thesis, Delft University of Technology.

Wielinga, T.S., E.J.H. Kerckhoffs, and M. Lorenz, 1993, "Towards the classification of spherical and planar weld defects with neural networks", Neural Network World, to be published.

Woodcock, N., N. Hallam, P. Picton, et al., 1992, "Interpretation of ultrasonic images of weld defects using a hybrid system", in: Proceedings of Neuro-Nimes 1991.

Based on the research presented in this thesis the following papers were or will be published:

Van der Wal, L.F., M. Lorenz and A.J. Berkhout, 1990, "A unified approach towards inverse problems in ultrsonic NDT", in: Elastic waves and ultrasonic nondestructive evaluation, Datta, Achenbach and Rajapakse (Eds), Elsevier Science Publishers B.V., Amsterdam.

Lorenz, M., L.F. van der Wal and A.J. Berkhout, 1990, "Improved imaging with Multi-SAFT", in: Proceedings of 1990 IEEE Ultrasonic Symposium, B.R. McAvoy (Ed), IEEE, Piscataway (NJ).

Lorenz, M., U. Stelwagen and A.J. Berkhout, 1991, "Imaging vertically oriented defects with Multi-SAFT", in: Physical Acoustics; Fundamentals and applications, Leroy and Breazeale (Eds), Plenum Press, New York.

Lorenz, M., L.F. van der Wal and A.J. Berkhout, 1991, "Ultrasonic imaging with Multi-SAFT: nondestructive characterization of defects in steel components", Nondestructive Testing and Evaluation, Vol. 6, p. 149-177.

Lorenz, M., L.F. van der Wal and A.J. Berkhout, 1992, "Ultrasonic characterization of defects in steel", in: Proceedings of 13th World Conference on NDT, Hallai and Kulcsar (Eds), Elsevier Science Publishers B.V., Amsterdam.

Lorenz, M., L.F. van der Wal and A.J. Berkhout, 1993, "Optimization of ultrasonic defect reconstruction with Multi-SAFT", in: Proceedings of Review of Progress in Quantitative NDE 1993 (13), Thompson and Chimenti (Eds), Plenum Press, New York.

Van 't Veen, P.P., E.J.M. Giling, M.Lorenz, et al., 1993, "Application of a finite-difference modelling scheme for ultrasonic defect characterization", in: Proceedings of Review of Progress in Quantitative NDE 1993 (13), Thompson and Chimenti (Eds), Plenum Press, New York.

Wielinga, T.S., E.J.H. Kerckhoffs, and M. Lorenz, 1993, "Towards the classification of spherical and planar weld defects with neural networks", Neural Network World, to be published.

Lorenz, M. and T.S. Wielinga, 1993, "Ultrasonic characterization of defects in steel using Multi-SAFT imaging and neural networks", NDT&E International, to be published.

Summary

When an inhomogeneity is detected in a steel component by conventional nondestructive inspection techniques, it may be desirable to characterize it in order to be able to perform a proper fitness-for-purpose analysis for the component under inspection. Such a characterization implies the accurate determination of the exact location, orientation, size and shape of the possible defect. Although several nondestructive inspection methods may be chosen for defect characterization purposes, it is found that ultrasonics offers the best potential, because an ultrasonic inspection is not confined to the near-surface region of the component and the technique may be operated while the component remains in service.

Since ultrasonic measurements do not directly provide the characteristic features of an inhomogeneity, some kind of processing of the ultrasonic data is required. In this thesis it has been evaluated to which extent ultrasonic imaging can be applied for the characterization of defects in steel components. After a general introduction, the ultrasonic imaging algorithm is derived from wave theory and compared with the heuristically derived Synthetic Aperture Focusing Technique (SAFT), which is found not to perform very well in practice. As a result from this comparison it is concluded, that the imaging performance can be improved particularly by increasing the spatial bandwidth of the ultrasonic data. This is achieved by employing multiple scattering responses for imaging, which actually implies the employment of multiple synthetic apertures. Therefore, the improved version of conventional SAFT is called Multi-SAFT.

A number of practical constraints on ultrasonic imaging are identified, which lead to a number of assumptions regarding the recorded responses, the medium to be inspected and the transducers applied in practice. It is explained that the assumptions are necessary in order to keep Multi-SAFT practicable and it is shown that the inversion problem is consequently more or less reduced to a geometrical problem. In relation to this, a very computational efficient algorithm is proposed for the calculation of indirect wave path lengths in cylindrical pipe geometries. Subsequently, a number of finite-difference modelling experiments are used to stress the importance of applying single-mode, bounded-beam transducers and to show the effects of inspection aperture limitation.

In the chapter on data-acquisition optimization it is shown why conventional (pulse-echo) SAFT is not capable of imaging, for instance, planar defects oriented perpendicular to the inspection surface. It is concluded, that separate source and receiver transducers have to be applied (pitch-catch) in order to provide sufficient image resolution in case forward scattering responses are employed. A modelled example illustrates that Multi-SAFT is perfectly suited for imaging so-called vertically oriented defects by applying a fixed source and a scanning receiver. To prevent the fixed source obstructing the scanning receiver in practice the lateral split angle configuration is defined.

Further optimization is achieved by using shear wave polarization effects, i.e. making use of the reflection characteristics of both SV and SH wave components. It is shown, that with the lateral split angle configuration the amplitude of the recorded SV reflection response can be reduced considerably in some cases, due to destructive interference of reflecting SV and SH wave components. Assuming the amplitude of the weaker diffracted responses to remain unchanged, it becomes possible to record both reflection and diffraction responses within the limited dynamic range of the measuring systems available in practice. By imaging both reflection and diffraction responses the combined image resolution may be improved significantly.

The influences of interfering responses, special medium characteristics and accidental errors in the imaging parameters on Multi-SAFT are evaluated in the chapter on the accuracy of the technique. It is found that the ultrasonic imaging process is not very sensitive to noise or to errors in the geometrical parameters, provided that the data-acquisition process has been carefully optimized. The propagation parameters, such as the wave velocity and the total wedge delay, should be determined as accurate as possible, since errors in these parameters may quickly lead to an intolerable reduction of the image quality. The effects of defect-roughness on the imaging result have only been studied qualitatively. However, it is indicated that up to a certain degree of defect-roughness the image quality remains reasonably acceptable.

The imaging and characterization performance of Multi-SAFT has been experimentally evaluated with the aid of special test samples containing artificial and real (weld) defects. In some cases the test samples could be destructively inspected and consequently the imaged cross-sections could be compared directly with the ultrasonic images. The experimental Multi-SAFT imaging results convincingly show that the practical assumptions mentioned above are generally valid and that the image quality is in most cases sufficiently high to allow accurate defect characterization.

Because even with Multi-SAFT the spatial bandwidth of the ultrasonic data still remains limited due to practical constraints, the shape of the defect cannot always be determined unambiguously from the imaging results. For this reason, the applicability of neural networks for the determination of defect-shape has been studied. Supported by modelled as well as experimental

results it has been demonstrated, that a properly trained neural network is able to determine very accurately whether a defect is round or planar in case the spatial amplitude spectrum is used as network input. For the computation of the spatial spectrum the right response is isolated from the rest of the recorded responses by utilizing the imaging results.

From the results presented in this thesis it may be concluded, that ultrasonic imaging with Multi-SAFT can be applied for the characterization of most types of defects in steel components. Because the data-acquisition and imaging processes have been kept relatively simple, the practical applicability of Multi-SAFT is believed to be feasible.

Samenvatting

Ultrasoon afbeelden ten behoeve van de karakterisatie van defecten in stalen componenten.

Wanneer een inhomogeniteit is gedetecteerd in een stalen component met behulp van conventionele niet-destructieve technieken kan het wenselijk zijn om die inhomogeneiteit te karakteriseren teneinde een juiste 'fitness-for-purpose' analyse uit te kunnen voeren voor de geïnspecteerde component. Zo'n karakterisatie houdt in dat de exacte positie, oriëntatie, grootte en vorm van het defect moeten worden vastgesteld. Ofschoon verscheidene niet-destructieve inspectiemethoden gekozen worden voor zulk een defectkarakterisatie biedt ultrasone inspectie de beste mogelijkheden, omdat het volledige volume van het object kan worden geïnspecteerd en omdat deze techniek kan worden toegepast op in-bedrijf-zijnde componenten.

Daar ultrasone metingen niet direct de karakteristieke eigenschappen van een inhomogeniteit opleveren moet een bewerking van de ultrasone data plaatsvinden. In dit proefschrift is bekeken in hoeverre ultrasoon afbeelden kan worden toegepast voor de karakterisatie van defecten in stalen componenten. Na een algemene inleiding wordt het ultrasone afbeeldingsalgorithme afgeleid met behulp van de golftheorie en vergeleken met de heuristisch afgeleide Synthetische Apertuur Focusserings-Techniek (SAFT), die in de praktijk niet goed blijkt te werken. Naar aanleiding van deze vergelijking wordt geconcludeerd, dat de afbeeldingsprestaties met name kunnen worden verbeterd door de spatiële bandbreedte van de ultrasone data te vergroten. Dit wordt bereikt door meervoudig verstrooide responsies te gebruiken voor het afbeelden, hetgeen eigenlijk het gebruik van meervoudige (multiple) synthetische aperturen inhoudt. De verbeterde versie van conventionele SAFT is daarom Multi-SAFT genoemd.

Er worden een aantal praktische beperkingen inzake ultrasoon afbeelden vastgesteld, die leiden tot een aantal aannames met betrekking tot de opgenomen responsies, het te inspecteren medium en de transducenten zoals die in de praktijk worden toegepast. Er wordt uitgelegd, dat de aannames noodzakelijk zijn teneinde Multi-SAFT hanteerbaar te houden en dat het inversie-probleem ten gevolge daarvan min of meer tot een geometrisch probleem wordt teruggebracht. In verband hiermee wordt een zeer efficiënt berekeningsalgorithme voorgesteld om de indirecte

golfpadlengtes in cylindrische pijpgeometriëen te bepalen. Vervolgens worden een aantal eindige-differentie modelleringsexperimenten aangewend teneinde het belang van het toepassen van transducenten met een begrensde bundelbreedte, die gevoelig zijn voor één golftype, te benadrukken en om de effecten van het beperken van de inspectie-apertuur te illustreren.

In het hoofdstuk over data-acquisitie optimalisatie wordt uitgelegd, waarom conventionele (puls-echo) SAFT niet in staat is om, bijvoorbeeld, vlakke defecten af te beelden die loodrecht staan ten opzichte van het inspectievlak. Er wordt geconcludeerd, dat gescheiden bron en ontvanger transducenten moeten worden toegepast (pitch-catch) om voldoende afbeeldingsresolutie te verkrijgen wanneer voorwaarts verstrooide responsies worden gebruikt. Een gemodelleerd voorbeeld toont aan, dat Multi-SAFT buitengewoon geschikt is voor het afbeelden van zogenaamde vertikaal georiënteerde defecten wanneer een vaste bron en een scannende ontvanger worden toegepast. Om te voorkomen dat in de praktijk de vaste bron de scannende ontvanger in de weg zal staan wordt de laterale split-hoek configuratie gedefiniëerd.

Een verdere optimalisatie wordt bereikt door gebruik te maken van polarisatie-effecten bij transversale golven, dat wil zeggen door de reflectie-eigenschappen van zowel SV- als SH-golven te benutten. Er wordt aangetoond, dat met behulp van de laterale split-hoek configuratie de amplitude van de gedetecteerde SV-reflectieresponsie in bepaalde gevallen aanzienlijk kan worden gereduceerd, doordat reflecterende SV- en SH-componenten destructief interfereren. Indien men aanneemt, dat de amplitude van de zwakkere diffractieresponsie onveranderd blijft, wordt het mogelijk om zowel reflectie- als diffractieresponsies op te nemen binnen het beperkte dynamische bereik van de meetsystemen, zoals die in de praktijk voorhanden zijn. Door zowel reflectie- als diffractieresponsies af te beelden kan de gecombineerde afbeeldingsresolutie significant worden verbeterd.

De invloed van interfererende responsies, speciale medium-eigenschappen en toevallige fouten in de afbeeldingsparameters op Multi-SAFT zijn geëvalueerd in het hoofdstuk over de nauwkeurigheid van de techniek. Er wordt aangetoond, dat het ultrasone afbeeldingsproces niet erg gevoelig is voor ruis of fouten in de geometrische parameters, op voorwaarde dat het data-acquisitieproces zorgvuldig is geoptimaliseerd. De propagatieparameters, zoals de golfsnelheid en de totale wigvertraging, moeten zo nauwkeurig mogelijk worden bepaald, daar fouten in deze parameters snel kunnen leiden tot een onacceptabele afname van de afbeeldingskwaliteit. De effecten van defect-ruwheid op het afbeeldingsresultaat zijn slechts kwalitatief onderzocht. Er wordt echter op gewezen, dat bij een zekere mate van defect-ruwheid de afbeeldingskwaliteit redelijkerwijs acceptabel blijft.

De afbeeldings- en karakterisatieprestaties van Multi-SAFT zijn experimenteel geëvalueerd met behulp van speciale testobjecten, waarin zich kunstmatige en echte (las-)defecten bevonden. In

bepaalde gevallen werden de test objecten destructief geïnspecteerd en dientengevolge konden de afgebeelde doorsneden direct worden vergeleken met de ultrasone afbeeldingen. De experimentele Multi-SAFT afbeeldingsresultaten tonen overtuigend aan, dat de hierboven genoemde praktische aannames in het algemeen gerechtvaardigd zijn en dat de afbeeldingskwaliteit in de meeste gevallen voldoende hoog is om een nauwkeurige defectkarakterisatie mogelijk te maken.

Daar zelfs met Multi-SAFT de spatiële bandbreedte van de ultrasone data nog beperkt blijft door de praktische beperkingen, kan de defectvorm niet altijd ondubbelzinnig worden vastgesteld uit de afbeeldingsresultaten. Daarom is de toepasbaarheid van neurale netwerken voor het bepalen van de defectvorm onderzocht. Ondersteund door gemodelleerde en experimentele resultaten wordt aangetoond, dat een goed getraind neuraal netwerk in staat is om zeer nauwkeurig te bepalen of een defect rond of vlak is, indien het spatiële amplitude spectrum wordt gebruikt als netwerk-invoer. Voor de berekening van het spatiële amplitude spectrum wordt de juiste responsie geïsoleerd van de overige responsies door gebruik te maken van de afbeeldingsresultaten.

Uit de resultaten, zoals die zijn weergegeven in dit proefschrift, kan worden geconcludeerd, dat ultrasoon afbeelden met Multi-SAFT geschikt is voor het karakteriseren van de meeste defecttypen in stalen componenten. Doordat de processen van data-acquisitie en afbeelden relatief eenvoudig zijn gehouden wordt de toepassing van Multi-SAFT in de praktijk mogelijk geacht.

Curriculum Vitae

Naam	Lorenz, Maarten
Geboortedatum	1 oktober 1962
Geboorteplaats	Rijswijk (Z-H)

OPLEIDING

1969-1975	Basisonderwijs te Rijswijk (Z-H)
1975-1977	VWO aan het Haags Montessori Lyceum te 's Gravenhage
1977-1981	VWO aan het Lodewijk Makeblijde College te Rijswijk (Z-H)
1981-1988	Technische Natuurkunde aan de Technische Universiteit Delft (oude stijl)

4^e-jaars werk: "Echo-akoestische slibdichtheidsbepaling", 5^e-jaars werk: "Opto-acoustical inspection of thin layers; the evaluation of a non-contacting and non-destructive testing method using laser techniques", beide uitgevoerd voor de Technisch Physische Dienst van TNO te Delft.

WERKERVARING

1988-1993	Wetenschappelijk medewerker bij de Technisch Physische Dienst van TNO te Delft.